Frascati Physics Series Vol. LVI (2012)
DARK FORCES AT ACCELERATORS
October 16-19, 2012

APEX: THE A PRIME EXPERIMENT AT JEFFERSON LAB

James Beacham
New York University (NYU), New York, NY

Abstract

APEX is an experiment at Thomas Jefferson National Accelerator Facility (JLab) in Virginia, USA, that searches for a new gauge boson (A') with sub-GeV mass and coupling to ordinary matter of $g' \sim (10^{-6} - 10^{-2})e$. Electrons impinge upon a fixed target of high-Z material. An A' is produced via a process analogous to photon bremsstrahlung, decaying to an e^+e^- pair. A test run was held in July of 2010, covering $m_{A'} = 175$ to 250 MeV and couplings $g'/e > 10^{-3}$. A full run is approved and will cover $m_{A'} \sim 65$ to 525 MeV and $g'/e > 2.3 \times 10^{-4}$.

1 Introduction

A U(1)$'$ extension of the gauge group of the Standard Model of particle interactions is a common feature of many theories. To have thus far evaded detection, the new gauge mediator, A', must either have a large, $\mathcal{O}$(TeV), mass or be very weakly coupled to ordinary matter. This second scenario can be tested at fixed target facilities such as the Thomas Jefferson National Accelerator Facility (JLab). APEX, The A Prime EXperiment, searches for an A' at JLab and is described in brief here. For a full description of the experiment see Ref. 1) and for a detailed description of the results of the test run see Ref. 2). The information in the current document also appears in a condensed form in Ref. 3).

2 Motivations

The Standard Model (SM) of particle interactions is described by the gauge group $\mathrm{SU}(3)_C \times \mathrm{SU}(2)_L \times \mathrm{U}(1)_Y$, where the forces are mediated by vector bosons. An extension of this model can have thus far evaded identification if the corresponding gauge boson is very weakly coupled to ordinary matter, with a coupling strength g' suppressed relative to the electromagnetic charge e by $\epsilon \equiv g'/e \sim 10^{-6} - 10^{-2}$ 4) (or, equivalently, $\alpha'/\alpha = \epsilon^2$). A new gauge boson, A', corresponding to a $\mathrm{U}(1)'$ extension of the SM can acquire an effective interaction with electromagnetism via kinetic mixing, where quantum loops of arbitrarily heavy particles provide a means by which the hidden $\mathrm{U}(1)'$ sector couples to the visible sector; see, e.g., Refs. 5, 6, 7).

In addition to the general interest in discovering an extension of the SM, a hidden gauge sector with a gauge boson with mass in the MeV to GeV range could address dark matter anomalies. The PAMELA experiment sees a positron excess but no antiproton excess, which could be explained by a sub-GeV mass hidden gauge boson coupling to dark matter and preferentially decaying into leptons. A similar scenario could explain the e^+e^- excesses seen by Fermi, ATIC, and HESS, and the effects observed by DAMA/LIBRA, INTEGRAL, CoGeNT, and others. A complete description of these possibilities is in Ref. 8).

Moreover, the anomalous magnetic moment of the muon could be explained by the existence of a sub-GeV mass A' with a weak effective interaction with the SM. The presence of this A' provides extra higher-order diagrams that contribute to the calculation of $(g-2)_\mu$ and can bring it into agreement with experimental measurements 8).

3 Existing Constraints

Aside from these suggestive motivations, the coupling strength and mass of the A' are not predicted. Thus, searches for this new gauge boson must be conducted over wide ranges of both. As a result, prior to 2009, the areas of parameter space probed by APEX were remarkably weakly constrained. Following the observation 8) that much of this range could be probed at existing experimental facilities, a renewed interest in such experiments has led to the current constraints and planned experimental sensitivities shown in Figure 1.

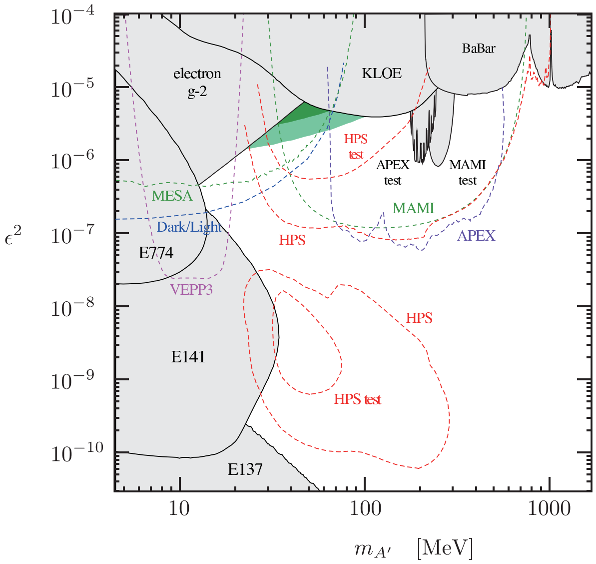

Figure 1: Existing and planned constraints in the $\epsilon - m_{A'}$ plane, as of late 2012. From 10).

The existing constraints in this range are from beam dump experiments and measurements of the $g-2$ of the electron, as well as a search for $\phi \to \eta A'$, $A' \to e^+e^-$ with the KLOE detector 9) and a search at BaBar for $\Upsilon(3S) \to \gamma\mu^+\mu^-$ that can be reinterpreted 8) as a limit on the coupling and mass of the A'. For a more comprehensive description of these constraints, see Ref. 10) and references therein.

As seen in Figure 1, APEX covers a large portion of this area of parameter space, from $m_{A'} \sim 65$ to 525 MeV and with coupling reach to $g'/e > 2.3 \times 10^{-4}$. A test run for APEX was performed in July of 2010 and demonstrated the feasibility of the full experiment.

4 APEX at Jefferson Lab's Hall A

APEX is designed to take full advantage of JLab's Continuous Electron Beam Accelerator Facility and the two High Resolution Spectrometers (HRSs) in Hall A. For the test run, an electron beam of energy 2.260 GeV and an intensity of up to 150 μA was used, incident upon a tantalum foil of thickness 22 mg/cm^2. The central momentum of each HRS was $\simeq$ 1.131 GeV with a momentum acceptance of ± 4.5%.

An A' is produced via a process analogous to photon bremsstrahlung and decays to an e^+e^- pair; thus, the A' signal will appear as a small, narrow bump in the invariant mass spectrum of e^+e^- pairs from background QED processes. The diagrams for signal and irreducible backgrounds are shown in Figure 2.

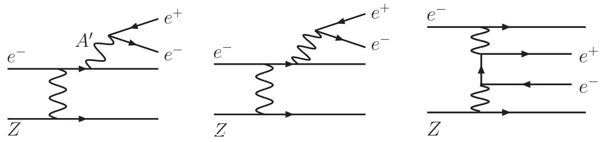

(a) (b) (c)

Figure 2: A' signal process (a) and irreducible QED backgrounds (b) and (c).

The opening angle Θ_0 of the e^+e^- pair is set by $m_{A'}$ and the incident electron beam energy as $\Theta_0 \sim m_{A'}/E_b \approx 5^\circ$, with no such expectation for the QED backgrounds. This motivates a symmetric HRS configuration with both spectrometer arms positioned far forward. To optimize sensitivity to A' decays, dipole septum magnets are placed between the target and the HRS aperture.

The Hall A HRSs consist of several different components to allow for the measurement of the position and momentum of charged particles to a high degree of accuracy. Vertical drift chambers, two orthogonal planes containing anode wires immersed in an argon-CO$_2$ mixture, allow for an accurate determination of the full 3D track of an incoming particle. The rate of electron singles for APEX ranges up to 5.8 MHz, and the APEX test run achieved a VDC rate of 5 MHz, higher than had ever been used in Hall A. Two separate sets of scintillators provide timing information, to identify coincident e^+e^- pairs. Online particle ID is provided by a gas Cherenkov detector and a lead glass calorimeter allows for further offline rejection of pion backgrounds.

Accurate determination of the momentum of a produced particle requires knowledge of the position of the particle at the target in addition to position as it enters the HRS. Since Hall A is used by several different experiments, a reliable method by which to calibrate optics is necessary. For the APEX test run, a method known as sieve-slit was used. A metal sieve with a characteristic pattern of holes drilled into it is placed just beyond the target enclosure, and elastic scattering events are collected during a calibration run. Since the position at the target is known very well, the pattern of incident particles that enter the VDC provide an optics matrix which is used for momentum calibration.

Excellent mass resolution is required to enable the identification of an A' resonance. The HRSs are designed to achieve high momentum resolution at the level of $\delta p/p \sim 10^{-4}$, providing a negligible affect upon the mass resolution. Angular resolution and multiple scattering in the target are the dominant contributions to the mass resolution, as shown in Table 1.

For the test run, APEX achieved a mass resolution of $\sigma \sim 0.85 - 1.11$ MeV, varying over the full $m_{A'}$ range.

mrad	Optics	Tracking	MS in target
σ(horiz)	0.11	∼0.4	0.37
σ(vert)	0.22	∼1.8	0.37

Table 1: Contributions to APEX mass resolution.

Reducible backgrounds were rejected using a combination of different triggers. These backgrounds include electron singles from inelastic or electron-nucleon scattering, pions from virtual photon decays, proton singles, accidental e^+e^- coincidences, and e^+e^- pairs from real photon conversions. The ratio of positron to charged pion production in the right HRS was greater than 1/100; this pion contribution was reduced online by a factor of 30 and the necessary rejection was achieved offline using both gas Cherenkov and calorimeter information.

The final event sample trigger for the test run required a double coincidence gas Cherenkov signal within a 12.5 ns window in each arm. The resulting data sample consisted of 770,500 true e^+e^- coincident events with 0.9% (7.4%) meson (accidental e^+e^- coincidence) contamination.

5 Bump Hunt / Resonance Search

The final data sample was analyzed as an invariant mass spectrum of e^+e^- pairs. A bump hunt for a small, narrow resonance was performed. A probability model of the form

$$P(m_{e^+e^-}|m_{A'},\sigma,S,B,a_i) = \frac{S\cdot N(m_{e^+e^-}|m_{A'},\sigma) + B\cdot Polynomial(m_{e^+e^-},a_i)}{S+B} \tag{1}$$

was used, where S is the number of signal events, N is a Gaussian distribution with width σ corresponding to the mass resolution, B is the number of background events, and the a_i are coefficients of a polynomial that encode the shape uncertainty on the background. This model formed the basis of a likelihood function and a test statistic, the profile likelihood ratio, that was then used to calculate p-values for the null hypothesis and upper limits on S.

A scanning-window approach was adopted, where a window around each $m_{A'}$ hypothesis is formed before performing a likelihood test. Based on extensive simulations, a 7th order polynomial and a 30.5 MeV window was chosen to maximize sensitivity and simultaneously minimize pull. The resonance search was performed on the invariant mass spectrum with 0.05 MeV binning and the procedure was repeated in steps of 0.25 MeV for each candidate A' mass.

6 Test Run Results

No significant excess was found over the invariant mass range of $m_{A'} = 175$ to 250 MeV; see Figure 3. The most significant excess was at 224.5 MeV with a p-value of 0.06%. Out of ∼1000 pseudoexperiments based on the test run data, 40% yielded a p-value at least as extreme as 0.06% somewhere in the mass range.

The upper limit on number of signal events, S, compatible with a background fluctuation at the 90% CL was translated into an upper limit on the A' coupling, α'/α, by exploiting the kinematic similarities between A' and γ^* production. The cross sections for the two processes are simply related 8) within a 1 MeV window around the A' mass, and thus the signal-to-background ratio is independent of detector acceptance in this mass window. Based on Monte Carlo simulations, the ratio f of the radiative-only cross section to the full QED background cross section varies linearly from 0.21 to 0.25 across the APEX mass range and, thus, all backgrounds can be normalized to the radiative background. The final expression relating S_{max} and $(\alpha'/\alpha)_{max}$ is

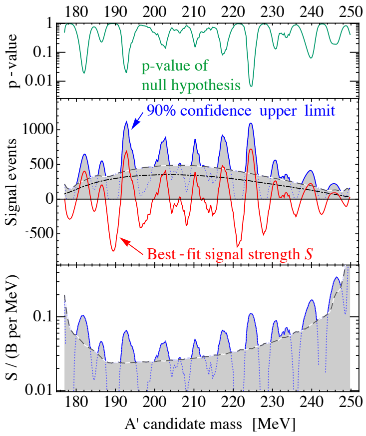

Figure 3: Results of the resonance search.

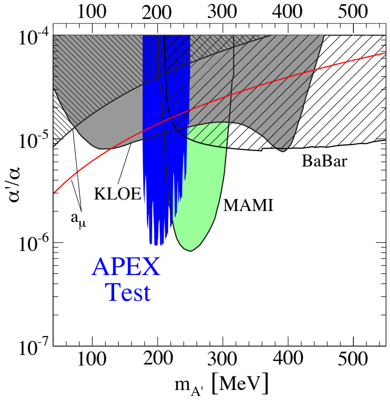

Figure 4: Upper limit on coupling.

$$\left(\frac{\alpha'}{\alpha}\right)_{max} = \left(\frac{S_{max}/m_{A'}}{f \cdot \Delta B/\Delta m}\right) \times \left(\frac{2N_{eff}\alpha}{3\pi}\right), \tag{2}$$

and the upper limit on coupling is shown in Figure 4.

7 Full Run Plans

The APEX full run is approved and will be ready to run when JLab switches on in 2014 after an upgrade of the beam energy from 6 to 12 GeV. The full run will take data for ∼34 days at four different energy and spectrometer settings, and will cover a larger mass range, $m_{A'}$ = 65 to 525 MeV, using a 50 cm long multifoil target. The full run statistics will be ∼200 times larger than the test run, allowing sensitivity to α'/α 1-2 orders of magnitude below current limits. A new optics calibration method is currently being tested and data acquisition rates are being improved, to allow for up to 5 kHz. A complete description of the full run is in Ref. $^{1)}$.

8 Acknowledgments

The author would like to acknowledge Rouven Essig, Philip Schuster, Natalia Toro, and Bogdan Wojtsekhowski, the APEX spokespeople, and Sergey Abrahamyan, Eric Jensen, Jin Huang, and Kyle Cranmer, the rest of the members of the core analysis team for the APEX test run, for their fruitful collaboration. Additional thanks are due the Hall A collaboration and the Jefferson Lab staff for their outstanding support.

References

1. R. Essig, P. Schuster, N. Toro and B. Wojtsekhowski, JHEP **1102**, 009 (2011) [arXiv:1001.2557 [hep-ph]].
2. S. Abrahamyan *et al.* [APEX Collaboration], Phys. Rev. Lett. **107**, 191804 (2011) [arXiv:1108.2750 [hep-ex]].
3. J. Beacham, Proceedings of the 8th Patras Workshop on Axions, WIMPs and WISPs, Chicago, July 18-22, 2012 [arXiv:1301.2581 [hep-ex]].
4. R. Essig, P. Schuster and N. Toro, Phys. Rev. D **80**, 015003 (2009).
5. B. Holdom, Phys. Lett. B **166**, 196 (1986).
6. P. Galison and A. Manohar, Phys. Lett. B **136**, 279 (1984).
7. M. J. Strassler and K. M. Zurek, Phys. Lett. B **651**, 374 (2007) [hep-ph/0604261].
8. J. D. Bjorken, R. Essig, P. Schuster and N. Toro, Phys. Rev. D **80**, 075018 (2009) [arXiv:0906.0580 [hep-ph]].
9. D. Babusci *et al.* [KLOE-2 Collaboration], [arXiv:1210.3927 [hep-ex]].
10. M. Endo, K. Hamaguchi and G. Mishima, Phys. Rev. D **86**, 095029 (2012) [arXiv:1209.2558 [hep-ph]].

Frascati Physics Series Vol. LVI (2012)
DARK FORCES AT ACCELERATORS
October 16-19, 2012

LIGHT DARK GAUGE BOSON SEARCHES IN ELECTROWEAK PROCESSES

T. Beranek
Institut für Kernphysik and PRISMA Cluster of Excellence
Johannes Gutenberg-Universität Mainz, D-55099 Mainz

Abstract

Extending the Standard Model of particle physics by an $U(1)$ group generates an additional gauge boson γ' which is known as hidden or dark photon. The hidden photon is able to interact with the electromagnetic current of the Standard Model. We study the exploration reach of various fixed target experiments searching for the hidden photon. Therefore we investigate the creation of a lepton pair induced by quasi-elastic scattering of an electron beam off a heavy nucleus (A,Z), i.e. $e(A,Z) \to e(A,Z)e^+e^-$ with a hidden photon γ' as signal and a virtual photon as background in the intermediate state. We compare our calculations with the data taken in the test run of the MAMI experiment. Predictions of the expected exclusion limits of the 2012 beam time at MAMI are presented. Furthermore, our analysis of rare kaon decays as possibility to constrain the γ' parameter space is presented.

1 Introduction

Recent observations of anomalies in astrophysical data 1) have motivated to consider extensions of the Standard Model of particle physics (SM) by including an additional $U(1)$ gauge group which could explain such anomalies 2). Though the idea to extend the SM by an additional $U(1)$ recently became popular, it did not rise up with these observations. In many well motivated SM extensions, e.g. from string theory, additional $U(1)$ groups appear naturally 3).
Extending the SM by such an $U(1)_D$ group generates an additional gauge boson γ' which is able to interact with the electromagnetic current of the Standard Model. Although this interaction is forbidden at tree level it is possible via kinetic mixing giving rise to an effective interaction Lagrangian

$$\mathcal{L}_{\text{int}} = i\,\varepsilon e\,\bar{\psi}_{\text{SM}}\,\gamma^{\mu}\,\psi_{\text{SM}}\,A'_{\mu},$$

where A' denotes the γ' field. Furthermore, ε is the kinetic mixing factor parameterizing the coupling strength relative to the electric charge e, and describes the interaction of the additional gauge boson with the electromagnetic current. The γ' may gain a mass $m_{\gamma'}$ which can be estimated to be in the range of 10 MeV to a few GeV, and the kinetic mixing factor $\varepsilon^2 = \alpha'/\alpha$ is predicted from various models to be in the range $10^{-12} < \varepsilon < 10^{-2}$ 4). The coupling of the γ' to SM particles and the predicted mass range allows for the γ' search by accelerator experiments at modest energies with high intensities. The proposal to search for the hidden gauge boson by fixed-target experiments 5, 6) motivated several experimental programs, e.g. by the A1 Collaboration at the MAMI accelerator in Mainz 7) as well as at the CEBAF facility at Jefferson Lab 8, 9). The A1 7) and APEX 8) experiments already have published first data. In these electron-hadron scattering experiments an electron beam is scattered off a nuclear fixed target, and a lepton-antilepton pair is created, which is detected. Using the measured invariant mass distribution, a bump search is performed. In the case, that no bump is seen, an exclusion limit for the γ' coupling ε^2 as function of its mass $m_{\gamma'}$ can be calculated, for which a precise knowledge of the background is crucial. Such precise study is the main subject of the first part of the present work 10). In the second part the possibility to constrain the γ' parameters from rare kaon decays is discussed 11).

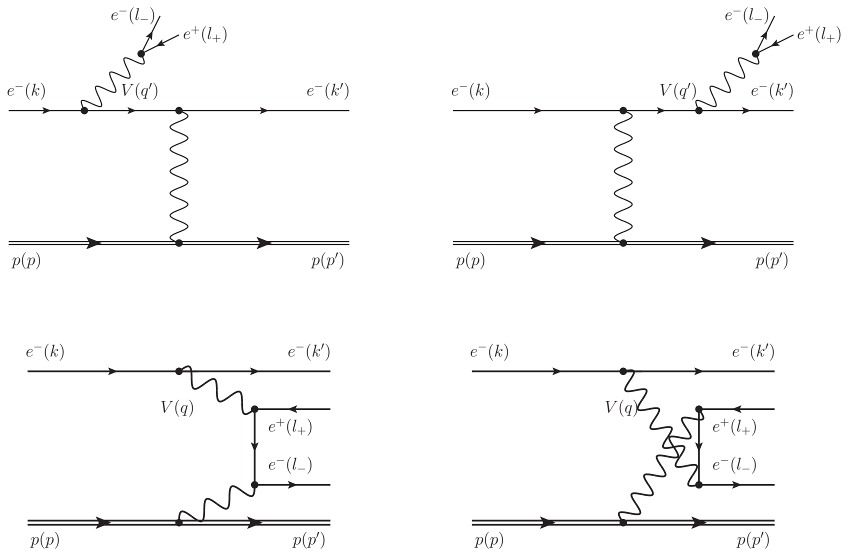

Figure 1: *Tree level Feynman diagrams contributing to the* $ep \to epl^+l^-$ *amplitude. Upper panel: exchange of the timelike boson* V *and a spacelike* γ *(TL). Lower panel: the spacelike boson* V *and a spacelike* γ *(SL). In addition to these direct (D) diagrams the exchange term (X), which consists of the same set of diagrams with scattered electron and electron of the* e^+e^- *pair exchanged, also contributes.*

2 Fixed target experiments

2.1 Calculation of the signal and background cross sections

The underlying diagrams for all fixed target experiments mentioned so far are shown in Fig. 1. We calculate this process exactly in leading order of QED and furthermore apply leading order radiative corrections of the corresponding elastic scattering process to obtain an estimate of these corrections, which reduce the cross section by an amount in the range of $10-20\,\%$.

The invariant amplitudes required for calculating the cross section can be read off from these Feynman diagrams. As in the two diagrams on the upper panel of Fig. 1 the intermediate boson V is timelike, we refer to this amplitude as TL. Correspondingly, we refer to the diagrams on the lower panel, where the

V is spacelike, as SL and their sum is denoted by SL + TL.
The isolated γ' production process is given by the coherent sum of the two TL diagrams on the upper panel of Fig. 1 while the background, resulting from the exchange of a virtual photon, is given by the sum over all diagrams, where the intermediate vector particle V in the TL diagrams is γ' and γ^*, respectively. We assign a finite decay width $\Gamma_{\gamma'}$ to the γ'.

In the case that the l^+l^- pair and the beam lepton are of the same species, as for the existing experiments, the same diagrams of Fig. 1 with the scattered (beam) electron and created electron of the pair exchanged also have to be taken into account. Therefore, we refer to the diagrams depicted in Fig. 1 as "direct" contribution and to those with exchanged final state electrons as "exchange" contribution, labeled by D and X, respectively.
The nucleus spin as well as contributions from the breakup channel and nuclear excitations can be neglected to good approximation. Effects due to the nucleus spin are suppressed by the large nucleus mass, which can be checked analytically. The inelastic contribution can be neglected since the momenta transferred to the nucleus are small.

The comparison with experimental data can be performed by integrating the obtained differential cross section over the experimental acceptances. To obtain the acceptance integrated cross section $\Delta\sigma$, which can be related to experimental count rates by multiplication with the luminosity, a non-trivial 8-fold integration is necessary.
The signal cross section $\Delta\sigma_{\gamma'}$ can be related to the direct TL cross section $\Delta\sigma_{\gamma}^{\mathrm{TL}}$ as given in Eq. (19) by Bjorken et. al. [5]

$$\frac{\Delta\sigma_{\gamma'}}{\Delta\sigma_{\gamma}^{\mathrm{TL}}} = \frac{3\pi}{2N}\frac{\varepsilon^2}{\alpha}\frac{m_{\gamma'}}{\delta m}. \tag{1}$$

Using this quantity one can calculate a limit on ε as

$$\varepsilon^2 = \left(\frac{\Delta\sigma_{\gamma'+\gamma}}{\Delta\sigma_{\gamma}} - 1\right)\frac{\Delta\sigma_{\gamma}}{\Delta\sigma_{\gamma}^{\mathrm{TL}}}\,\frac{2\,N\,\alpha}{3\pi}\,\frac{\delta m}{m_{\gamma'}}, \tag{2}$$

where the ratio $\Delta\sigma_{\gamma'+\gamma}/\Delta\sigma_{\gamma}$ is the (aimed) signal sensitivity, which has to be determined from the experiment. The ratio of the background cross section to the direct TL cross section $\Delta\sigma_{\gamma}/\Delta\sigma_{\gamma}^{\mathrm{TL}}$ has to be determined from theory.

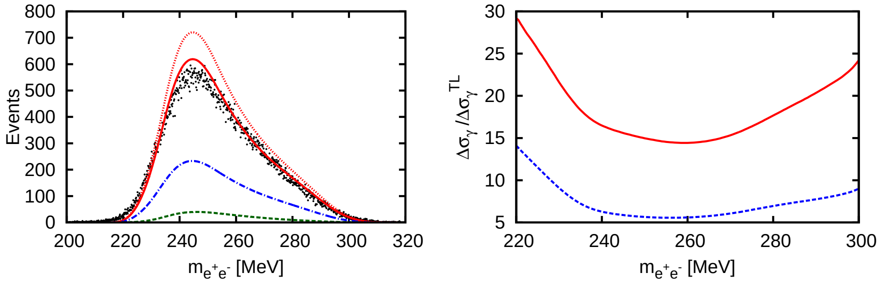

Figure 2: *Left panel: Comparison of theory calculations and experimental data for a* $m_{e^+e^-}$ *bin width of* $0.125\,\mathrm{MeV}$. *Black points: Data taken in a particular run of the MAMI 2010 experiment* [7]. *Solid curve: Theory calculation of the background cross section. Dotted curve: Theory calculation of the background cross section without radiative corrections. Dashed-dotted curve: Theory calculation of the direct SL + TL cross section. Dashed curve: Theory calculation of the direct TL cross section. Right panel: Solid (dashed) curve: Ratio of the background cross section* $\Delta\sigma_{\gamma,\,\mathrm{D+X}}$ *(*$\Delta\sigma_{\gamma,\,\mathrm{D}}$*) to the direct TL cross section* $\Delta\sigma_\gamma^{TL}$*, respectively.*

2.2 Comparison with data and predictions for MAMI

A first test run to proof the feasibility of a dedicated γ' fixed target search experiment has been performed at MAMI by the A1 Collaboration in 2010 [7]. A sample of the data taken in this experiment compared to our calculations can be seen in Fig.2.
For the comparison of the calculation and the data integrated luminosity of $\mathcal{L} = 41.4\,\mathrm{fb}^{-1}$ for the selected sample of events is used. A background contribution of around 5% was already subtracted in this sample, the systematic uncertainty in the luminosity from the knowledge of the thickness of the target foil is below 5%.

As seen on the left panel of Fig. 2, our calculation (solid curve) of the radiative background and the experimental data (points) are in good agreement. The influence of the radiative corrections is displayed by the solid and dotted curve on Fig. 2 which are calculated with and without radiative corrections, respectively.

One notices from the right panel of Fig. 2 (solid curve) that the ratio $\Delta\sigma_{\gamma,\,\mathrm{D+X}}/\Delta\sigma_\gamma^{\mathrm{TL}}$ smoothly varies between 15 and 25 for most of the invariant

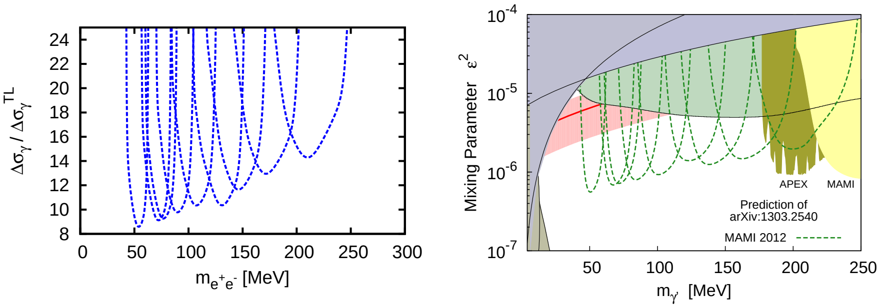

Figure 3: *Left panel: Combined plot of our result for the ratios* $\Delta\sigma_\gamma/\Delta\sigma_\gamma^{TL}$ *of each setting probed in the MAMI 2012 experiment, starting with the lowest beam energy on the left. Right panel: Predicted exclusion limits for the MAMI 2012 experiment.*

mass range. Neglecting the necessary contribution of the exchange term to the cross section, the ratio is lower by a factor of about 3 for the investigated range (dashed curve on the right panel of Fig. 2). The A1 Collaboration started a γ' search run at MAMI in 2012, probing the kinematics centered around $m_{e^+e^-} = 57 - 218\,\text{MeV}$, in which no signal of a γ' was found. In Fig. 3 a combined plot of our result for the ratio $\Delta\sigma_\gamma/\Delta\sigma_\gamma^{\text{TL}}$ is shown for each setting as function of the invariant mass $m_{e^+e^-}$. One obtains for the ratio a value of around $10 - 15$.

On the right panel of Fig. 3, the exclusion limits on ε^2 5, 7, 8, 12) are displayed: the shaded regions show existing limits, whereas the dashed curves show our predictions for the MAMI set of kinematics indicated by the dashed curve for an assumed integrated luminosity of around $10\,\text{fb}^{-1}$. Obviously, the MAMI 2012 will cover a large part of the $(g-2)$ welcome band.

3 Rare Kaon decays

In the following we will study the process $K^+ \to \mu^+\nu_\mu\gamma'$ as a possible signal from the dark sector (see Feynman diagram in Fig. 4) within the mentioned framework of kinetic mixing (model I) as well as in a model where the γ' couples only to the muon assuming an explicit breaking of gauge invariance 13) (model II). In a pioneering experiment 14) of the decay $K^+ \to \mu^+ +$ neutrals, only the

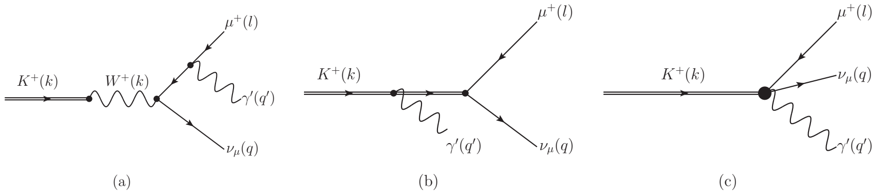

Figure 4: *Feynman diagram for the process* $K^+ \to \mu^+\nu_\mu\gamma'$.

charged muon is detected, excluding further charged particles or photons in the final state. Therefore it is convenient to express the decay rates as functions of the kinetic energy of the muon T_μ. In this experiment an upper bound for the branching fraction $\Gamma(K^+ \to \mu^+ + \text{ neutrals})/\Gamma(K^+ \to \mu^+\nu)$ of $2 \cdot 10^{-6}$ was found.

The SM background for invisible γ' decays results from the $K^+ \to \mu^+\nu_\mu\nu_l\bar{\nu}_l$ decays. Due to the applied experimental cuts a further background arising from radiative corrections to the 2-body decay $K \to \mu\nu_\mu$ can be neglected.

In order to obtain a dimensionless quantity, it is helpful to consider the ratio of these decay rates relative to the ratio of the 2-body decay $K^+ \to \mu^+\nu_\mu$. In order to obtain the experimental limits from these data the differential decay rate $\frac{d\Gamma}{dE_\mu}(K^+ \to \mu^+\nu_\mu\gamma')$ has to be folded with the detector efficiency $D(E_\mu)$ 14), i.e.

$$\tilde{R}(m_{\gamma'}) := \frac{\int \frac{d\Gamma}{dE_\mu}(K^+ \to \mu^+\nu_\mu\gamma')D(E_\mu)dE_\mu}{\Gamma(K^+ \to \mu^+\nu_\mu)}. \tag{3}$$

Since the kinetic mixing factor ε is a global factor of the amplitudes obtained from Fig. 4, one can rewrite $\tilde{R}\ (m_{\gamma'})\ =\ \varepsilon^2\ R\ (m_{\gamma'})$ and thus finds an upper bound for the allowed values of ε^2 as:

$$\varepsilon^2 < \frac{2 \cdot 10^{-6}}{R(m_{\gamma'})}. \tag{4}$$

In Fig. 5 (upper and middle panels) the differential decay rate for the signal process relative to the decay $K^+ \to \mu^+\nu_\mu$ is shown calculated within model I and II for the full phase space (left panels) and with applied corrections due to the given detector acceptance (right panels), according to the experimental set-up 14). One notices that within the kinetic mixing model (upper panels of Fig. 5) the inner bremsstrahlung contribution (IB) completely dominates the

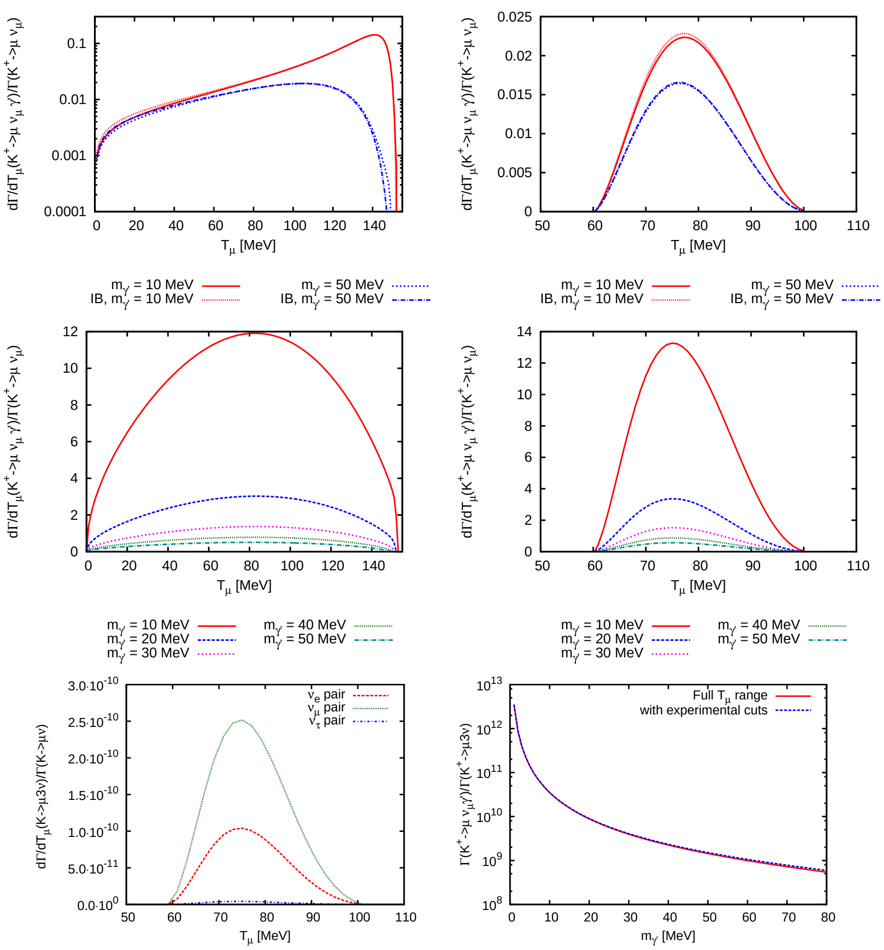

Figure 5: *Upper and middle panels: Ratio of* $\frac{d\Gamma}{dT_\mu}(K^+ \to \mu^+\nu_\mu\gamma')$ *and* $\Gamma(K^+ \to \mu^+\nu_\mu)$ *for various* γ' *masses for perfect detector efficiency (left panels) and for finite detector efficiency* 14) *(right panels) at* $\varepsilon^2 = 1$. *Upper panels: kinetic mixing model (model I); middle panels: model II, where the* γ' *only couples to the* μ^+. *Lower left panel: Standard Model background for different neutrino families using the detector efficiency function. Lower right panel: ratio of total decay rates* $\Gamma(K^+ \to \mu^+\nu_\mu\gamma')$ *at* $\varepsilon^2 = 1$ *relative to* $\Gamma(K^+ \to \mu^+\nu_\mu\nu\bar{\nu})$ *in model II.*

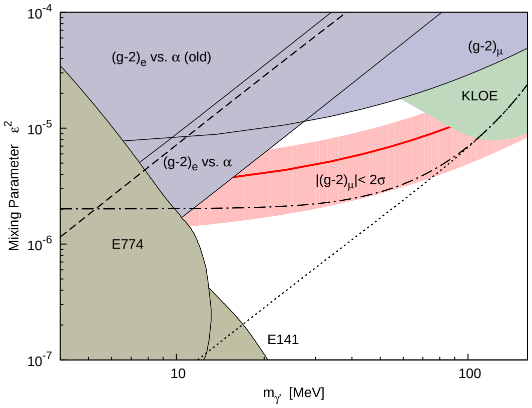

Figure 6: *Exclusion limits on the* γ' *parameter space (see text for further details). Dashed-dotted curve: bound calculated in the kinetic mixing model (model I) for an accuracy of the ratio* $\Gamma(K^+ \rightarrow \mu^+\nu_\mu\gamma')/\Gamma(K^+ \rightarrow \mu^+\nu_\mu)$ *of* 10^{-9}. *Dashed curve: result for the 1973 data* [14] *within model II, where the* γ' *only couples to the* μ^+. *Dotted curve: bound calculated in model II for an assumed improvement of the experimental accuracy by two orders of magnitude, i.e.* $2 \cdot 10^{-8}$.

result for the considered γ' mass parameters: comparison between IB curves and curves including the form factor dependence [15, 16]. Since in model II the gauge invariance is not required, the decay rate is enhanced by a factor of $1/m^2_{\gamma'}$ compared to model I. The expected SM background from the decay $K^+ \rightarrow \mu^+\nu_\mu\nu\bar{\nu}$ with the applied experimental cuts [14] is shown on the lower left panel.

As one can see from the lower right panel of Fig. 5, the total γ' decay rate (model II) $\Gamma(K^+ \rightarrow \mu\nu_\mu\gamma')$ calculated with $\varepsilon^2 = 1$ is about a factor of 10^9 larger than the decay rate to SM particles $\Gamma(K^+ \rightarrow \mu^+\nu_\mu\nu_l\bar{\nu}_l)$. This corresponds to an γ' signal, which will dominate over the expected SM signal for mixing factors down to $\varepsilon^2 \simeq 10^{-9}$. The calculated limits on the γ' parameter space are shown in Fig. 6. In this figure the colored regions again correspond to already excluded configurations of mass and coupling strength [17]. In this plot we have included the old as well as the new exclusion limits from $(g-2)$ of the electron compared to the fine structure constant α. One has to distinguish limits from searches with visible and invisible decay products. The exclusion limits in Fig. 6 are all obtained within the kinetic mixing framework were the γ' decay is assumed to be into SM leptons, except those from rare kaon decays in model I. In this work the bounds obtained from the kinetic mixing model (model I) correspond to searches with visible decay products. In experiments therefore the process $K^+ \to \mu^+\nu_\mu e^+e^-$, would be investigated e.g. by a search for peaks appearing over the known SM background. For invariant masses of the e^+e^- $m_{ee} < 2m_\mu$ the branching ratios $\Gamma(K^+ \to \mu^+\nu_\mu\gamma')$ and $\Gamma(K^+ \to \mu^+\nu_\mu e^+e^-)(m_{ee} = m_{\gamma'})$ after full phase space integration are equal. In model II the kaon decay to γ' is assumed to be invisible. Therefore the existing limits from direct searches in Fig. 6 do not exactly apply here. For reasons of simplicity we use the same figure to illustrate the numerical results of this calculation.

A possible bound for the kinetic mixing model is represented by the dash-dotted curve for an assumed experimental accuracy of the ratio $\Gamma(K^+ \to \mu^+\nu_\mu\gamma')/\Gamma(K^+ \to \mu^+\nu_\mu)$ of 10^{-9}. Furthermore, in Fig. 6 the bound obtained in model II and an estimate in which way the exclusion limits change due to an improvement in the experimental accuracy of the ratio $\Gamma(K^+ \to \mu^+\nu_\mu\gamma')/\Gamma(K^+ \to \mu^+\nu_\mu)$ by two orders of magnitude (dotted curve) are shown. Such an improved extraction might be achieved by new facilities, such as the NA62 experiment at CERN or rare kaon decay experiments at JPARC.

4 Conclusions

We have calculated the cross sections for the γ' fixed target experiments $e(A,Z) \to e(A,Z)l^+l^-$. We find, that our calculations for the electromagnetic background processes are in good agreement with the data taken at MAMI. This allows us to give accurate predictions for future exclusion limits as presented here for the new MAMI experiment, and we find, that the largest part of the $(g-2)_\mu$ welcome can be excluded.

Furthermore, we have investigated rare kaon decays as possibility to explore the γ' parameter space in the low mass region. We have shown, that the method used in this work may be suited to extend the existing limits within two models for the γ' coupling. For that purpose more precise data are necessary.

5 Acknowledgements

This work was done in collaboration with H. Merkel and M. Vanderhaeghen. This work was supported in part by the Research Centre “Elementarkräfte und Mathematische Grundlagen” at the Johannes Gutenberg University Mainz, the federal state of Rhineland-Palatinate, and in part by the Deutsche Forschungsgemeinschaft DFG through the Collaborative Research Center “The Low-Energy Frontier of the Standard Model” (SFB 1044), and the Cluster of Excellence “Precision Physics, Fundamental Interactions and Structure of Matter” (PRISMA). TB likes to thank Björn Walk for helpful discussions on GPU programming. Furthermore, we thank Achim Denig for useful discussions.

6 References

References

1. A. W. Strong *et al.*, Astron. Astrophys. **444**, 495 (2005). O. Adriani *et al.* [PAMELA Collaboration], Nature **458**, 607 (2009). I. Cholis, G. Dobler, D. P. Finkbeiner, L. Goodenough and N. Weiner, Phys. Rev. D **80**, 123518 (2009).

2. N. Arkani-Hamed, D. P. Finkbeiner, T. R. Slatyer and N. Weiner, Phys. Rev. D **79**, 015014 (2009). M. Pospelov and A. Ritz, Phys. Lett. B **671**, 391 (2009).

3. S. Weinberg, Phys. Rev. Lett. **40**, 223 (1978). L. B. Okun, Sov. Phys. JETP **56**, 502 (1982). B. Holdom, Phys. Lett. B **178**, 65 (1986). P. Fayet, Nucl. Phys. B **347**, 743 (1990). M. Pospelov, Phys. Rev. D **80**, 095002 (2009). S. Andreas, M. D. Goodsell and A. Ringwald, Phys. Rev. D **87**, 025007 (2013).

4. P. Fayet, Phys. Rev. D **75**, 115017 (2007). C. Cheung, J. T. Ruderman, L. -T. Wang and I. Yavin, Phys. Rev. D **80**, 035008 (2009). R. Essig, P. Schuster and N. Toro, Phys. Rev. D **80**, 015003 (2009). M. Goodsell, J. Jaeckel, J. Redondo and A. Ringwald, JHEP **0911**, 027 (2009).

5. J. D. Bjorken, R. Essig, P. Schuster and N. Toro, Phys. Rev. D **80**, 075018 (2009).

6. B. Batell, M. Pospelov and A. Ritz, Phys. Rev. D **79**, 115008 (2009). M. Reece and L. -T. Wang, JHEP **0907**, 051 (2009). B. Batell, M. Pospelov and A. Ritz, Phys. Rev. D **80**, 095024 (2009).

7. H. Merkel *et al.* [A1 Collaboration], Phys. Rev. Lett. **106**, 251802 (2011).

8. R. Essig, P. Schuster, N. Toro and B. Wojtsekhowski, JHEP **1102**, 009 (2011). S. Abrahamyan *et al.* [APEX Collaboration], Phys. Rev. Lett. **107**, 191804 (2011).

9. The Heavy Photon Search Collaboration (HPS), `https://confluence.slac.stanford.edu/display/hpsg/`. M. Freytsis, G. Ovanesyan and J. Thaler, JHEP **1001**, 111 (2010). Y. Kahn and J. Thaler, Phys. Rev. D **86**, 115012 (2012).

10. T. Beranek, H. Merkel and M. Vanderhaeghen, arXiv:1303.2540 [hep-ph].

11. T. Beranek and M. Vanderhaeghen, Phys. Rev. D **87**, 015024 (2013).

12. S. Andreas, C. Niebuhr and A. Ringwald, Phys. Rev. D **86**, 095019 (2012). D. Babusci *et al.* [KLOE-2 Collaboration], arXiv:1210.3927 [hep-ex].

13. B. Batell, D. McKeen and M. Pospelov, Phys. Rev. Lett. **107**, 011803 (2011).

14. C. Y. Pang *et al.*, Phys. Rev. D **8**, 1989 (1973).

15. J. Bijnens, G. Ecker and J. Gasser, Nucl. Phys. B **396**, 81 (1993).

16. A. A. Poblaguev *et al.*, Phys. Rev. Lett. **89**, 061803 (2002).

17. F. Archilli *et al.*, Phys. Lett. B **706**, 251 (2012). H. Davoudiasl, H. -S. Lee and W. J. Marciano, Phys. Rev. D **86**, 095009 (2012).

Frascati Physics Series Vol. LVI (2012)
DARK FORCES AT ACCELERATORS
October 16-19, 2012

HIDDEN PHOTONS IN BEAM DUMP EXPERIMENTS AND IN CONNECTION WITH DARK MATTER

Sarah Andreas
Deutsches Elektronen-Synchrotron DESY, Hamburg, Germany

Abstract

Hidden sectors with light extra U(1) gauge bosons, so-called hidden photons, recently received much interest as natural feature of beyond standard model scenarios like string theory and SUSY and because of their possible connection to dark matter. This paper presents limits on hidden photons from past electron beam dump experiments including two new limits from experiments at KEK and Orsay. Additionally, various hidden sector models containing both a hidden photon and a dark matter candidate are discussed with respect to their viability and potential signatures in direct detection.

1 Introduction

Gauge bosons of an extra U(1) symmetry in a hidden sector, so-called hidden photons, are well motivated since they arise naturally in string compactifications like the heterotic string or type-II string theories. Since the standard model (SM) is not charged under this new gauge group, there is no direct coupling and the interactions with the visible sector, and consequently the experimental constraints, are very weak. The hidden photon is additionally of great interest as it provides a solution to the discrepancy between the SM prediction of the muon anomalous magnetic moment and its experimentally measured value 1). Furthermore, models containing in the hidden sector a dark matter (DM) candidate which interacts with the visible sector via a light hidden photon have attracted much attention in the context of recent astrophysical observations 2, 3).

At low energies, the dominant interaction of the hidden photon γ' with the visible sector is through kinetic mixing with the ordinary photon. This can, for example, be generated from loops of heavy particles charged under both U(1)s 4). Integrating out those particles gives as an estimate for the size of the kinetic mixing the order of a loop factor $\mathcal{O}(10^{-3} - 10^{-4})$. We then impose the following relation between the hidden gauge coupling g_h and the kinetic mixing χ

$$\chi = \frac{g_Y g_h}{16\pi^2}\ \kappa, \tag{1}$$

where κ is $\sim \mathcal{O}(1)$ and depends on the masses of the particles in the loop.

For the most simple hidden sector with just an extra U(1) symmetry and the corresponding hidden photon γ', the low energy effective Lagrangian describing the kinetic mixing with the photon is then given by

$$\mathcal{L} = -\frac{1}{4}F_{\mu\nu}F^{\mu\nu} - \frac{1}{4}X_{\mu\nu}X^{\mu\nu} - \frac{\chi}{2}X_{\mu\nu}F^{\mu\nu} + \frac{m_{\gamma'}^2}{2}X_\mu X^\mu + g_Y j^\mu_{\rm em} A_\mu, \tag{2}$$

where $F_{\mu\nu}$ is the field strength of the ordinary electromagnetic field A_μ and $X_{\mu\nu}$ is the field strength of the hidden U(1) gauge field X_μ. A mass $m_{\gamma'}$ for the hidden photon can be generated either from the Higgs mechanism or from the Stückelberg mechanism. In both cases, masses around the GeV-scale can be obtained naturally but much smaller values are also possible 5). Masses in the GeV range can be tested and constrained especially by electron beam dump experiments. This has been studied in 6) for past beam dump experiments at SLAC and Fermilab and further in 7) by taking into account the experimental acceptancies and two additional experiments at KEK and in Orsay. An overview of all current experimental constraints on the hidden photon for the MeV to GeV mass range is given in 7, 8).

In general, the hidden sector can contain not only gauge but also matter fields. The attractive possibility of DM in the hidden sector interacting via a hidden photon has been studied in various models for different ranges of DM and hidden photon masses, in particular, GeV-scale dark forces 2, 3, 9, 10) but also massless U(1)s 11).

This paper summarizes the current status of limits on hidden photons from electron beam dump experiments in Sec. 2, based on the results presented in 7). In Sec. 3, a toy-model as well as several supersymmetric models for DM interacting via a hidden photon are discussed regarding the DM relic density and signatures in direct detection experiments, following the analysis of 9).

2 Hidden photons in electron beam dump experiments

Hidden photons are produced in a process similar to ordinary bremsstrahlung off an electron beam incident on a target. They are emitted at a small angle in forward direction and carry most of the beam energy, cf. Fig. 1 (left). Due to their feeble interaction with SM particles they can traverse the dump and be observed in the detector through their decay into fermions, e.g., into e^+e^-.

The production cross section of hidden photons is roughly given by

$$\frac{d\sigma}{dx_e} \simeq 4\alpha^3\chi^2\,\xi(E_e, m_{\gamma'}, Z, A)\sqrt{1-\frac{m_{\gamma'}^2}{E_e^2}}\;\frac{1-x_e+\frac{x_e^2}{3}}{m_{\gamma'}^2\frac{1-x_e}{x_e}+m_e^2 x_e}\,. \tag{3}$$

where $x_e = E_{\gamma'}/E_e$ is the fraction of the incoming electron's energy E_e carried by the hidden photon, m_e is the electron mass and $\xi(E_e, m_{\gamma'}, Z, A)$ is an effective flux of photons that takes into account atomic and nuclear form factors and is approximately proportional $\xi \sim Z^2$ for the mass range of interest.

For the thick target experiments under consideration, the number of hidden photon events observable via the decay products can be estimated as

$$N \simeq \frac{N_e N_0 X_0}{A}\int dE_{\gamma'}\int dE_e\int dt\left[I_e\frac{1}{E_e}\left.\frac{d\sigma}{dx_e}\right|_{x_e=\frac{E_{\gamma'}}{E_e}} e^{-\frac{L_{\rm sh}}{l_{\gamma'}}}\left(1-e^{-\frac{L_{\rm dec}}{l_{\gamma'}}}\right)\right]{\rm BR}_{l\bar{l}}, \tag{4}$$

where N_e is the number of the incident electrons, N_0 is Avogadro's number, X_0 is the unit radiation length of the target material, $L_{\rm sh}$ and $L_{\rm dec}$ are the lengths of the target plus shield and of the decay region, respectively, and ${\rm BR}_{l\bar{l}}$ is the branching ratio of those decay products that the detector is sensitive to, i.e., e^+e^-, $\mu^+\mu^-$ or both. The energy distribution $I_e(E_0, E_e, t)$ describes that the initial energy E_0 of the electrons in the beam is degraded as they pass through the target. Detailed calculations and expressions are given in [6, 7].

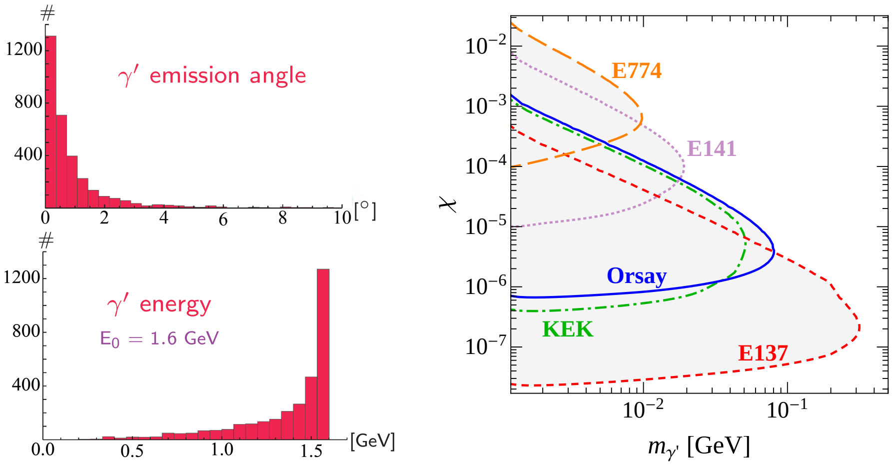

Figure 1: *left:* Hidden photon emission angle *(top)* and energy *(bottom)* from Monte Carlo simulations with MadGraph for a beam energy of 1.6 GeV, $\chi = 10^{-5}$ and a total of 3200 hidden photons with a mass of 50 MeV produced. *right:* Limits on hidden photons from electron beam dump experiments at SLAC (E141, E137), Fermilab (E774), KEK and in Orsay [7].

With the partial decay width into leptons given by [1]

$$\Gamma_{\gamma' \to l^+ l^-} = \frac{\alpha \chi^2}{3} m_{\gamma'} \left(1 + 2\frac{m_l^2}{m_{\gamma'}^2}\right) \sqrt{1 - 4\frac{m_l^2}{m_{\gamma'}^2}} \,, \tag{5}$$

the decay length $l_{\gamma'} = \gamma \beta c \tau_{\gamma'}$ can be estimated as

$$l_{\gamma'} \simeq \frac{3E_{\gamma'}}{\alpha \chi^2 m_{\gamma'}^2} \simeq 8 \text{ cm} \frac{E_{\gamma'}}{1 \text{ GeV}} \left(\frac{10^{-4}}{\chi}\right)^2 \left(\frac{10 \text{ MeV}}{m_{\gamma'}}\right)^2 . \tag{6}$$

For large values of χ and/or $m_{\gamma'}$ this is much shorter than the minimum length of the dump required to suppress the SM background, so that electron beam dump experiments can not access the corresponding region in the parameter space.

In an earlier analysis 6), limits from the E141 and E137 experiments at SLAC and the Fermilab E774 experiment have been determined. We extended their analysis by two more experiments at KEK in Japan 12) and at the Orsay Linac in France 13). Additionally, in order to derive constraints from Eq. (4), we included the acceptances for the different experiments, taking into account the geometry of the detector and possible energy cuts. For this purpose, we compared the experimental specifications with the events obtained from Monte Carlo simulations with MadGraph for the hidden photon production in bremsstrahlung followed by the decay, see 7) for details. The limits we obtain for all five electron beam dump experiments are presented in Fig. 1 (right). A comparison with others constraints is given in 7, 8). An overview of future searches that can further probe the parameter space is presented in 14).

3 Hidden sectors with dark matter interacting via hidden photons

In this section we consider the possibility that the hidden sector also contains DM in addition to the hidden photon. We first discuss the resulting DM relic density and direct detection cross sections in a toy-model and then turn to a more complete supersymmetric realization. The results of this section have been presented in detail in 9).

3.1 Toy-model: Dirac fermion as dark matter candidate

The simplest possible hidden sector assumed in the following contains despite the hidden photon just one Dirac fermion as DM candidate, cf. 3) for similar models. Applying the relation given in Eq. (1) we fix the hidden sector gauge coupling as a function of the kinetic mixing χ and determine the DM relic abundance and direct detection rate for fixed κ. Depending on the masses of both particles the DM annihilation can proceed either in a s-channel diagram through the hidden photon into SM particles or in a t-channel diagram into two hidden photons. While the former is present for the entire mass range and resonant at $m_{\gamma'} = 2m_{\mathrm{DM}}$, the latter is accessible (and dominant) only for $m_{\mathrm{DM}} > m_{\gamma'}$. For a DM mass of 6 GeV and $\kappa = 0.1$, we find that in the dark green band in Fig. 2 (left) the correct relic abundance can be obtained while in the light green area the contribution to the total DM density is only subdominant. Increasing κ pushes the dark green horizontal band upwards to higher values of χ, while it moves down to smaller χ when κ is decreased. The appearance of the resonance at 12 GeV results from the s-channel annihilation. The spin-independent scattering on nuclei is also mediated by the hidden photon and turns out to give cross sections compatible with the ones required to explain the CoGeNT signal for a Standard Halo Model. This is shown in Fig. 2 (left) as a purple band (90% CL lighter, 99% CL darker purple) in which the cross sections for subdominant DM have been rescaled by the actual relic abundance. For a DM mass as light as 6 GeV, there are no constraints from CDMS or XENON. The areas in grey are excluded by the electron beam dump experiments discussed in Sec. 2 and various other constraints summarized in [7, 8].

Scanning over the DM mass as a free parameter and keeping κ fixed to $\kappa = 1$ leads to the scatter plots in Fig. 2 (right) where the upper one is for a

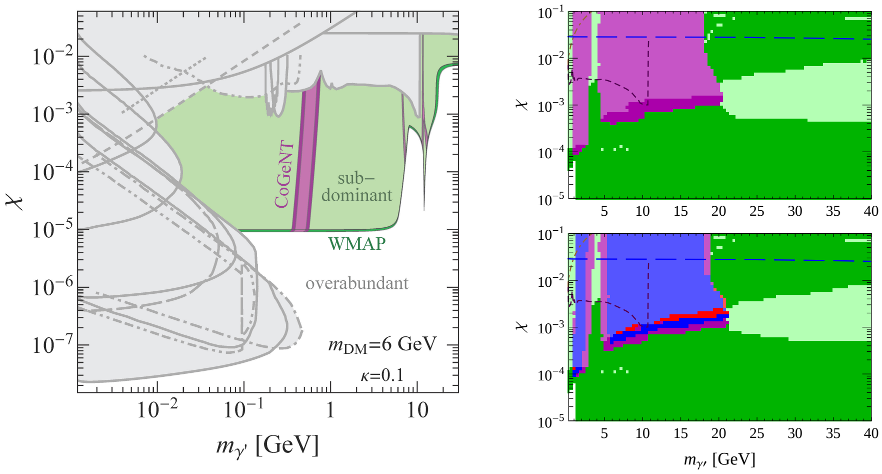

Figure 2: Hidden sector toy-model with Dirac fermion as DM candidate [9]. *left:* Viable DM relic abundance (dark green within the WMAP range, light green for subdominant DM) and region where the direct detection rate can explain CoGeNT (purple) for $m_{\mathrm{DM}} = 6$ GeV, $\kappa = 0.1$. Grey areas are excluded by the beam dump experiments of Fig. 1 (right) and other limits cf. [7, 8]. *right:* Scatter plot scanning over the DM mass for the Standard Halo Model *(top)* and an Einasto profile *(bottom)* for $\kappa = 1$. Purple regions are compatible with CoGeNT, red with DAMA, blue with both.

Standard Halo Model and the lower one for an Einasto profile. In both plots, DM in the dark green regions gives the correct relic abundance and in the light green ones a subdominant contribution. The resulting spin-independent scattering cross sections are in agreement with CoGeNT in the purple areas, with DAMA in the red ones and with both experiments in the blue ones (all points shown are in agreement with all other DD limits). For more details and other results please refer to 9). Thus, for a wide range of parameters, the toy-model provides a Dirac fermion as valid DM candidate with the possibility of explaining certain direct detection claims.

3.2 Supersymmetric model: Majorana and Dirac fermion dark matter

Embedding the idea of a hidden sector with DM into a more sophisticated and better motivated framework, we construct the simplest anomaly-free supersymmetric model which is possible without adding dimensionful supersymmetric quantities. The corresponding superpotential $W \supset \lambda_S S H_+ H_-$ contains one dimensionless coupling λ_S and three chiral superfields S, H_+, H_- where H_+ and H_- are charged under the hidden U(1). In the entire analysis, we assume the MSSM in the visible sector, but our results are largely independent of this choice. We consider two mechanisms by which the hidden gauge symmetry is broken and show their different implications on the DM phenomenology.

In the first case, the effective Fayet-Iliopoulos term, which is induced in the hidden sector through kinetic mixing with the visible Higgs D-term, breaks the hidden gauge symmetry. We find that then the DM candidate can be either a Dirac or a Majorana fermion. As in the previous subsection, the Dirac fermion possesses spin-independent scattering on nuclei and thus exhibits a similar phenomenology as the toy-model. This is shown in the scatter plot of Fig. 3 (left) where we scanned both over the DM mass and the parameter κ in the range $0.1 \leq \kappa \leq 10$. Again, the dark green points give the correct relic abundance and for those in purple the direct detection rate is consistent with CoGeNT when a Standard Halo Model is assumed. The plot only contains points for which the scattering cross section is in agreement with constraints from direct detection experiments. In difference to the toy-model, the lower part of the scatter plot can not be filled since the DM particle can not be heavier than the hidden photon and therefore the t-channel annihilation is not possible. The Majorana fermion, on the other hand, due to its axial coupling, possesses mostly spin-dependent scattering which is less constrained by direct detection experiments. Spin-independent scattering is possible also for the Majorana fermion thanks to the Higgs-portal term, but the cross sections are tiny, several orders of magnitude below current limits and without any hope of explaining direct detection claims.

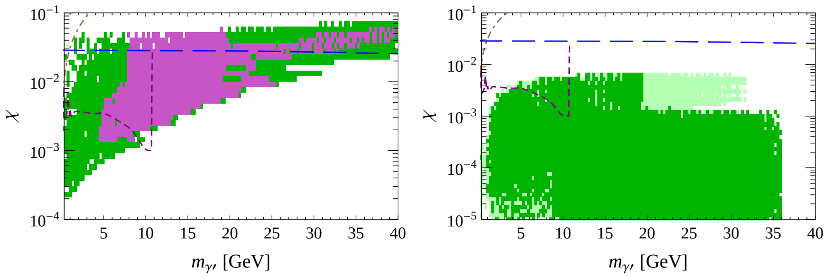

Figure 3: Scatter plots for the supersymmetric hidden sector with hidden gauge symmetry breaking induced by the visible sector *(left)* or radiatively *(right)* for $0.1 \leq \kappa \leq 10$ 9). The scattering of the Dirac fermion DM candidate in the left plot is spin-independent while the one of the Majorana fermion in the right plot is mostly spin-dependent. Dark green points give the correct DM relic abundance, light green ones a subdominant contribution and purple ones have spin-independent scattering cross sections in agreement with CoGeNT.

In the second case, the running of the Yukawa coupling λ_S induces the breaking of the hidden gauge symmetry. The DM candidate turns out to be a Majorana fermion which again, because of its mostly spin-dependent scattering, can not account for the claims in spin-independent direct detection experiments. Scanning over the parameter space and κ in the range $0.1 \leq \kappa \leq 10$ we find points that can give the correct relic abundance or a subdominant contribution as shown in the scatter plot in Fig. 3 (right) in dark and light green, respectively. All points shown are in agreement with the limits arising from spin-dependent direct detection experiments.

Thus, also supersymmetric hidden sector models can give valid dark matter candidates which, in certain cases, have some similarities to the phenomenology that was obtained in the toy-model. Results for other parameter settings and plots of the scattering cross sections in the different scenarios compared to experimental limits are given in 9).

4 Conclusions

The existence of a hidden sector with a dark force is well motivated from a top-down (string theory, SUSY) and a bottom-up ($g-2$, DM) point of view. Because of the weak interactions with the SM, such scenarios are not much constrained, and we presented here new limits from past electron beam dump experiments on the hidden photon mass and kinetic mixing. If the hidden sector also contains DM, we showed that a toy-model with Dirac fermion DM gives the right relic abundance and spin-independent scattering cross sections able to explain claims in direct detection experiments. For a more sophisticated supersymmetric hidden sector with hidden gauge symmetry breaking induced by the visible sector, we find a Dirac fermion DM candidate with similar phenomenology. A Majorana fermion with mostly spin-dependent scattering can also be the DM candidate in this scenario or when the hidden gauge symmetry is broken radiatively. Our supersymmetric models with gravity mediation have therefore proven to provide viable DM candidates with interesting potential for direct detection experiments.

5 Acknowledgments

This work has been done in collaboration with Mark Goodsell, Carsten Niebuhr, and Andreas Ringwald.

References

1. M. Pospelov, Phys. Rev. D **80**, 095002 (2009) [arXiv:0811.1030].

2. P. Fayet, Phys. Rev. D **75**, 115017 (2007) [arXiv:hep-ph/0702176]. N. Arkani-Hamed, D. P. Finkbeiner, T. R. Slatyer and N. Weiner, Phys. Rev. D **79**, 015014 (2009) [arXiv:0810.0713]. C. Cheung, J. T. Ruderman, L. T. Wang and I. Yavin, Phys. Rev. D **80**, 035008 (2009) [arXiv:0902.3246].

3. M. Pospelov, A. Ritz and M. B. Voloshin, Phys. Lett. B **662**, 53 (2008) [arXiv:0711.4866]. E. J. Chun, J. C. Park and S. Scopel, JHEP **1102**, 100 (2011) [arXiv:1011.3300]. Y. Mambrini, JCAP **1107**, 009 (2011) [arXiv:1104.4799]. D. Hooper, N. Weiner and W. Xue, Phys. Rev. D **86**, 056009 (2012) [arXiv:1206.2929].

4. B. Holdom, Phys. Lett. B **166**, 196 (1986).

5. M. Goodsell, J. Jaeckel, J. Redondo and A. Ringwald, JHEP **0911**, 027 (2009) [arXiv:0909.0515]. M. Cicoli, M. Goodsell, J. Jaeckel and A. Ringwald, JHEP **1107**, 114 (2011) [arXiv:1103.3705].

6. J. D. Bjorken, R. Essig, P. Schuster and N. Toro, Phys. Rev. D **80**, 075018 (2009) [arXiv:0906.0580].

7. S. Andreas, C. Niebuhr and A. Ringwald, Phys. Rev. D **86**, 095019 (2012) [arXiv:1209.6083].

8. S. Andreas, [arXiv:1211.5160]. S. Andreas, [arXiv:1110.2636].

9. S. Andreas, M. D. Goodsell and A. Ringwald, to appear in Phys. Rev. D [arXiv:1109.2869].

10. D. Feldman, B. Kors and P. Nath, Phys. Rev. D **75**, 023503 (2007) [arXiv:hep-ph/0610133]. E. J. Chun and J. C. Park, JCAP **0902**, 026 (2009) [arXiv:0812.0308]. A. Katz and R. Sundrum, JHEP **0906**, 003 (2009) [arXiv:0902.3271]. D. E. Morrissey, D. Poland and K. M. Zurek, JHEP **0907**, 050 (2009) [arXiv:0904.2567]. T. Cohen, D. J. Phalen, A. Pierce and K. M. Zurek, Phys. Rev. D **82**, 056001 (2010) [arXiv:1005.1655]. Z. Kang, T. Li, T. Liu, C. Tong and J. M. Yang, JCAP **1101**, 028 (2011) [arXiv:1008.5243]. N. Fornengo, P. Panci and M. Regis, Phys. Rev. D **84** (2011) 115002 [arXiv:1108.4661].

11. R. Foot, Phys. Rev. D **78**, 043529 (2008) [arXiv:0804.4518]. L. Ackerman, M. R. Buckley, S. M. Carroll and M. Kamionkowski, Phys. Rev. D **79**, 023519 (2009) [arXiv:0810.5126]. J. L. Feng, M. Kaplinghat, H. Tu and H. B. Yu, JCAP **0907**, 004 (2009) [arXiv:0905.3039]. X. Chu, T. Hambye and M. H. G. Tytgat, JCAP **1205**, 034 (2012) [arXiv:1112.0493].

12. A. Konaka *et al.*, Phys. Rev. Lett. **57**, 659 (1986).

13. M. Davier and H. Nguyen Ngoc, Phys. Lett. B **229**, 150 (1989).

14. J. L. Hewett *et al.*, [arXiv:1205.2671].

Frascati Physics Series Vol. LVI (2012)
DARK FORCES AT ACCELERATORS
October 16-19, 2012

HEAVY PHOTON SEARCH

John Jaros for the HPS Collaboration
SLAC National Accelerator Laboratory,
2575 Sand Hill Road, Menlo Park, CA 94025, USA

Abstract

The Heavy Photon Search Experiment (HPS) is a new experiment at Jefferson Lab designed to look for massive vector gauge bosons (heavy photons) in the mass range 20-1000 MeV/c^2 which couple to electrons with couplings α'/α in the range 10^{-5} to 10^{-10} . The experiment utilizes a compact forward spectrometer employing silicon microstrip detectors for vertexing and tracking and a $PbWO_4$ electromagnetic calorimeter for fast triggering, and is designed to measure the invariant mass and decay vertex location of electro-produced heavy photons. As its first stage, the HPS Collaboration mounted the HPS Test Run Experiment, which ran parasitically in Hall B at JLAB during Spring 2012. The run demonstrated the technical feasibility of the design and confirmed critical background assumptions. On the basis of this successful test run, the experiment has been approved for physics running. The experimental design and results from the Test Run are discussed, along with the collaboration's plans for stage two, the full HPS experiment.

1 Introduction

The Heavy Photon Search (HPS) is a new, dedicated experiment at Jefferson Laboratory designed to search for a heavy photon (aka A', dark photon, or hidden sector photon) in the mass range 20-1000 MeV/c^2 and coupling ϵe to electric charge, where $\alpha'/\alpha = \epsilon^2$ is in the range 10^{-5} to 10^{-10}. The search enjoys unique sensitivity by employing both invariant mass and secondary decay vertex signatures, and will explore virgin territory in heavy photon parameter space. Experimentally, HPS explores new territory as well, looking at very forward angles, large acceptances, and high rates in fixed target electroproduction.

HPS, like other experiments described at this workshop, is motivated by the possibility that there exist sectors of particles and interactions which are essentially hidden from us by virtue of their weak couplings to ordinary matter. Hidden sector photons are of especial interest because they are expected on very general theoretical grounds in many Beyond Standard Model theories, could explain the presently observed discrepancy between the experimental and theoretical values for the muon's anomalous magnetic moment, and may even explain the unexpectedly high flux of electrons and positrons recently seen in the cosmic rays (see 1) for a recent review). Through kinetic mixing, heavy photons are expected to mix with the Standard Model photon, which induces their weak couplings to electric charge 2, 3). So heavy photons couple to electrons, can be produced by electron bremsstrahlung off heavy nuclear targets, and can decay to e^+e^- pairs. Since the coupling of heavy photons to e^+e^- pairs is much weaker than the canonical electromagnetic coupling, heavy photon production is buried in a huge background of pairs from massive virtual photons (QED tridents). The weak coupling is also responsible for the heavy photon's very narrow decay width. Consequently, a heavy photon would appear as a very sharp mass resonance above the QED background, and, for a wide range of coupling strengths, have a distinct secondary decay vertex. HPS exploits both signatures.

These signatures will uncover some bread and butter physics as well. QED predicts the existence of as yet unseen atoms comprised of bound μ^+ and μ^- mesons 4), and it predicts their production at levels sufficient for detection in HPS 5). True Muonium decays to e^+e^- pairs with a decay signature just like the heavy photon's, a sharp mass bump (at $2m_\mu$) and a finite decay length.

It offers additional physics for HPS, and a perfect heavy photon calibration signal.

The idea for HPS came from a seminal paper by Bjorken, Essig, Schuster, and Toro 9) which explored the phenomenology of heavy photons in fixed target experiments, capitalizing on the interest stirred by papers which proposed Dark Matter annihilating to pairs of heavy photons as the source of the e^+ excess in the cosmic rays 6), 7). Besides setting exclusion limits in the mass/coupling parameter space by reinterpreting existing results, the authors suggested a number of search strategies. HPS derives from the vertexing concept put forward in their paper.

HPS was presented to the Jefferson Laboratory Program Advisory Committee in December, 2010 as a two staged proposal 8). The first, the HPS Test Run, a minimalist version of the experiment to demonstrate the technological approach, confirm background estimates, and begin the search, was approved early in 2011, and was subsequently proposed and funded by DOE HEP. It was installed at JLAB in April 2012, commissioned and run. The second stage, HPS proper, was approved conditionally, contingent on the outcome of the Test Run. A subsequent Program Committee reviewed the Test Run results in 2012. Since then, the HPS Collaboration has revised the design of the second stage experiment, proposed it to DOE HEP 10) and begun long lead-time preparations. Stage II HPS will be reviewed by DOE in July, 2013. With approval and funding, HPS plans to be ready for installation at Hall B at JLAB in September, 2014, have a commissioning run late 2014, and take data in 2015.

This paper will review and motivate the design of the experiment, present results from the HPS Test Run experiment, outline the revised design of Full HPS, and give its reach. The HPS design has evolved since the time this work was presented at the Dark 2012 Workshop. The current version is included here.

2 HPS Design Considerations

As emphasized in 9), fixed target experiments enjoy a considerable luminosity advantage over colliding beam experiments in searching for heavy photons in the mass range 20-1000 MeV/c^2. Since it is this range that has been largely unexplored, and since this is the mass range preferred by models attributing high energy electrons and positrons in the cosmic rays to dark matter annihilations, it is natural to conduct a fixed target search. Electron bremsstrahlung provides a natural production mechanism, shown in fig.1 for signal and virtual photon background. The kinematics of A' bremsstrahlung, reviewed in $^{9)}$, dictate the experimental design. For A' masses well above the electron mass, the A's are radiatively produced at very forward angles with nearly the full energy of the electron beam. Their decay products are boosted forward with typical polar angles $\approx m_{A'}/E_{beam}$, so good forward acceptance is a design prerequisite. Bump hunting requires good momentum and angular resolution, which is most easily accomplished with charged particle spectrometry, and vertex detection requires the first sensor layers be relatively close to the target, to minimize extrapolation errors. So the HPS apparatus places its detectors as close to the beamline as possible to maximize acceptance, just downstream of the target to optimize vertex resolution, and within a magnet to make a precise momentum measurement. Silicon microstrip sensors are chosen as the tracking detectors, providing optimal spatial resolution, high rate capability, and good radiation hardness. Downstream of the analyzing magnet, the magnetic field has bent the electrons and positrons respectively to beams right and left as they enter an electromagnetic calorimeter, providing charge discrimination. The ECal, using an array of $PbWO_4$ crystals, provides a fast trigger on events with both an electron and a positron.

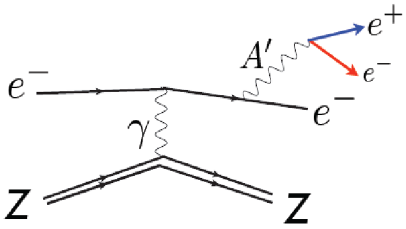

Figure 1: *Feynman diagram for radiative A' electro-production. Radiative QED background arises from a similar diagram, with the A' replaced by a virtual photon, $\gamma*$. The QED Bethe-Heitler diagram also contributes to the background.*

The viability of the experiment depends on generating large integrated luminosities, because the A' production cross section is small and the trident background comparatively huge. The radiative cross section for A' production on a tungsten target with a 2 GeV electron is roughly a nanobarn for a coupling $\alpha'/\alpha \approx 10^{-6}$ and mass 100 MeV/c^2, but falls (rises) by a decade as the mass doubles (halves). Getting luminosities high and keeping occupancies low is best done by running with essentially 100 % duty factor and with sensors which have very short response times. The CEBAF accelerator at Jefferson Laboratory provides nearly DC beam (beam bunches every 2 ns), a range of beam energies from 2-11 GeV, and excellent beam quality. Silicon microstrip detectors and $PbWO_4$ crystals readout by APDs can be run at very high rates, are radiation hard, and have pulse lengths $\approx$ 60 ns, so can handle very high rates. High rate data acquisition is also required, and available.

Target thickness plays an important role in maximizing the detector's capabilities. By minimizing target thickness, but boosting beam current to keep their product constant, one minimizes multiple Coulomb scattering of beam electrons in the target, and thereby minimizes occupancies and trigger rates. HPS uses 4 - 8 μm tungsten targets and currents in the range of 100-400 nA to accumulate large luminosity samples which don't overwhelm trigger rates. Beam spot sizes and halo are also important. Small beam spots offer important constraints which help improve track angular resolution, boost vertex resolution, and thereby reduce tails in the vertex distribution. Since detectors are placed close to the beam (the first layer of the tracker is a mere 1/2 mm from the beamline), beam stability is at a premium. Excess beam halo would contribute to detector occupancy; spurious tracks would add to tracking confusion. CEBAF beams can have transverse sizes as small as 40 μm × 200 μm, have halo at the level of 10^{-5} and below, and have excellent stability, so are well suited to HPS needs.

The experiment demands excellent control of beam-induced backgrounds. Beam electrons passing through the target inevitably multiple Coulomb scatter, so detectors must be placed well beyond the rms multiple Coulomb scattering angle. By staying outside of a 15 mrad cone, the apparatus avoids all but the tails of the multiply scattered beam. The beam may also interact in the target, radiating bremsstralung photons in the forward direction. They too must be avoided. The electrons which have radiated, now degraded in energy, are swept into the horizontal plane by the magnetic field of the analyzing magnet, producing what is called “the sheet of flame,” a horizontal swath of extremely high background. The apparatus avoids it entirely by staying outside of a “dead zone,” defined by $\theta_y < 15$ mrad (y is the vertical dimension). This splits the apparatus into upper and lower halves. Finally, the passage of an intense electron beam through air, or even helium gas, generates an unacceptably large number of delta rays, resulting in high occupancy and tracking confusion. HPS avoids this background by situating the tracker in vacuum, and passing the electron beam in vacuum throughout its passage through the apparatus. The costs are the added complications of connecting power, data cables, and cooling lines through vacuum feedthroughs; of providing remote vertical motion for the sensors (needed to position them close to the beam); and of selecting materials that are vacuum compatible. The benefit is a significant reduction of beam backgrounds.

3 The HPS Test Run Apparatus

Application of the design principles discussed above led to the HPS Test Run apparatus, shown in fig.2. The electron beam enters from the left and is transported everywhere in vacuum. It impinges on a thin W foil target located 10 cm before the silicon tracker within the magnet vacuum chamber, which in turn is situated in a dipole analyzing magnet roughly a meter in length. Motion controls on the upstream end of the vacuum chamber allow the tracker modules to be moved close to the beam.

The Silicon Vertex Tracker (SVT) for the HPS Test Run is shown in fig.3. It uses Hamamatsu microstrip sensors readout by APV25s, the readout chip developed by CMS for operations at the LHC. Signal to noise is ≈ 25, which should result in ≈ 6 μm spatial resolution. Analogue readout proceeds at 40 MHz into a 3 microsecond pipeline. A trigger selects 6 consecutive pulse heights correlated to the event time, and initiates sending them to the data acquisition system. The multiple measurements allow a pulse shape to be fit, and the precise time of the hit to be determined within ± 2 ns. Altogether there are 5 layers of sensors, split top-bottom to avoid the dead zone, each layer comprised of two sensors, one measuring the vertical coordinate, the other at small angle stereo (50 or 100 mrad) to measure the bend plane coordinate. Care is taken to minimize the sensor thickness in order to minimize multiple Coulomb scattering

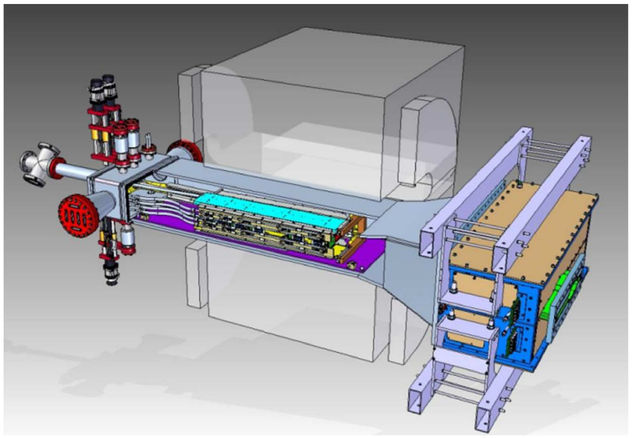

Figure 2: *The HPS Test Run apparatus*

in the sensors. The 5 layers are mounted on top and bottom support plates which are hinged at the downstream end and can be precisely positioned at the upstream end. Cooling for the readout chips is provided, both to remove the heat generated and to improve the radiation hardness of the sensors.

The electromagnetic calorimeter is shown in fig.4. It is a $PbWO_4$ crystal calorimeter, consisting of separate top and bottom modules, each arranged in 5 layers. There are 442 crystals in all. The front face of each crystal is 1.3 cm × 1.3 cm; the crystals are 16 cm long. The crystals are readout with APDs; output pulses are shaped and preamplified, and sent to a JLAB FADC250, a 250 MHz flash ADC, which records them in an 8 sec pipeline. The FADC also provides inputs to the trigger every 8 ns. A thermal enclosure keeps temperature constant to about 1°C to stabilize the ECal gain.

High rate data acquisition is essential for HPS to handle the high luminosity and expected trigger rates. Detailed simulation studies lead us to calculate trigger rates in the range of 25-50 kHz at the planned luminosities. These triggers are dominated by accidentals involving scattered beam electrons, but there is a substantial contribution from QED tridents, both radiative and Bethe-Heitler, as well. The experiment has separate data acquisition systems for the SVT and ECal. The SVT uses the SLAC ATCA-based architecture. Trigger selected data from the APV25 readout chip is sent to the Cluster on

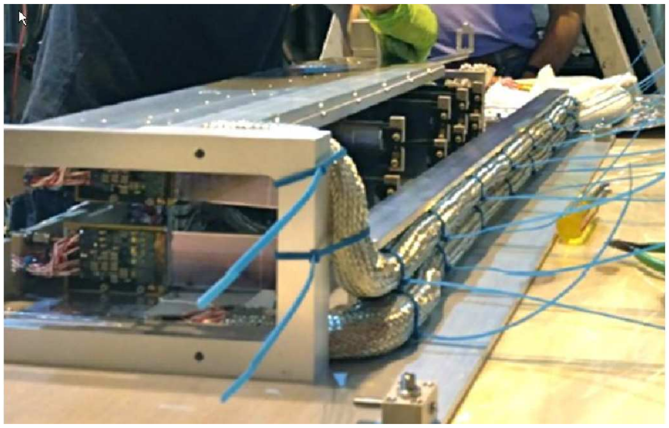

Figure 3: *The HPS Test Run silicon vertex tracker, looking upstream. The structure is split top-bottom.*

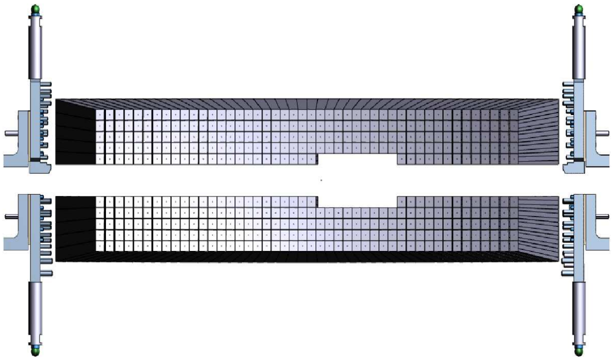

Figure 4: *Beam's eye view of the HPS Test Run Electromagnetic Calorimeter. Like the tracker, it is split top-bottom. The missing crystals accommodate the passage of the electron beam.*

Board (COB) ATCA module. The COB provides digitization, threshold setting, and data formatting, and in turn sends formatted data to be melded with ECal data to the JLAB DAQ. A single ATCA crate with two COBs handled the full HPS Test Run SVT with its 20 sensors and roughly 12k channels.

The ECal DAQ and Trigger utilize the JLAB FADC250, which is packaged 16 to a VXS module. Every 8 ns, the FADC transfers pulse height and time information from each channel to the Crate Trigger Processor, which identifies clusters of energy deposition in the top and bottom modules, then passes the cluster information to the Sub System Processor, which looks for pairs of clusters, one from each of the two modules, which satisfy energy and position criteria designed to select heavy photon decays and minimize background QED processes. Once a trigger is generated, a signal is sent back to the readout chips of the SVT and to the FADCs to initiate transfer of the raw data associated with that trigger. The ECal DAQ system can operate well over the 50 kHz limit which is imposed by the overall data transfer capability at JLAB.

4 HPS Test Run Results

The Test Run apparatus was designed to be run with electron beams, but scheduling conflicts at JLAB prevented our getting dedicated electron beam time. Instead, we ran parasitically with the HDice experiment using their several GeV photon beam in the Spring of 2012. A thin Au converter $\approx$ 70 cm upstream of our detector served as our target and produced a modest rate of e^+e^- pairs. This photon running was in fact adequate for commissioning the entire detector and DAQ, and let us demonstrate its technical feasibility. A dedicated photon run during the last 8 hours of CEBAF 6 running provided us high quality data, much lower backgrounds, and the opportunity to measure normalized trigger rates. These data let us demonstrate the performance potential of the detector, and most significantly, let us conclude that the backgrounds *expected in electron running* are also understood and under control.

Performance of the SVT was very good. About 97 % of channels worked as advertized and had a signal to noise ratio $\approx$ 25. In good channels, the efficiency for mips exceeded 98 %, and track time resolution was better than 3 ns. Tracks were reconstructed with high efficiency and good purity. Even with preliminary alignment constants, tracks were extrapolated to the target with few mm resolution, in agreement with Monte Carlo expectation. Residuals were also as expected from simulation. The extrapolated track position at the converter has a resolution of a few mm, in agreement with the simulation which assumes perfect alignment.

The ECal provided a reliable trigger. Only about 10 % of channels failed to report good data because of HV distribution and noise problems, so large regions of the detector performed as expected. Pre-run gain adjustments provided adequate energy scale uniformity for trigger purposes. An energy calibration was derived by extrapolating tracks of known momentum into the ECal. After accounting for channel to channel threshold and gain non-uniformities, the observed cluster energy distribution was in reasonable agreement with Monte Carlo.

One critical goal of the Test Run was to confirm the level of backgrounds expected in electron running. These backgrounds, which simulation has shown to be due to the tails of the multiple Coulomb scattering of beam electrons in the target, determine both the occupancy levels in the silicon detectors and the trigger rate in the ECal. Confirming the simulations quantitatively was critical to establishing that HPS can run at the proposed luminosities with electron beams. It was possible to do so with photon running because e^+e^- pairs which are produced in the conversion target are subject to essentially the same multiple Coulomb scattering as beam electrons in electron running. The angular distribution of the outgoing pairs is in fact the convolution of two distributions, first the intrinsic angular distribution associated with pair creation, then the multiple Coulomb scattering of the pairs as they exit the target. Since HPS is only sensitive to scatters beyond the dead zone of 15 mrad, it is primarily the tails of the intrinsic angular distribution and the multiple Coulomb scattering distributions which come into play. EGS5 accurately simulates both multiple Coulomb scattering and pair creation and has been verified with data. It was used to simulate the integrated trigger rates expected in the HPS Test Run configuration for three different converter thicknesses, 0.18 %, 0.45 %, and 1.60 % X_0. The trigger rate is given by integrating the observed angular distribution over the acceptance and normalizing to the integrated beam current, and is dominated by hits just beyond $\theta_y = 15$ mrad. As shown in fig.5, the data is in good agreement with the EGS5 prediction, and substantially lower than predicted by GEANT4. So the EGS5 simulation is confirmed; consequently estimates of HPS occupancies and trigger rates using EGS5 for electron beam running are reliable. HPS is ready for electron beams.

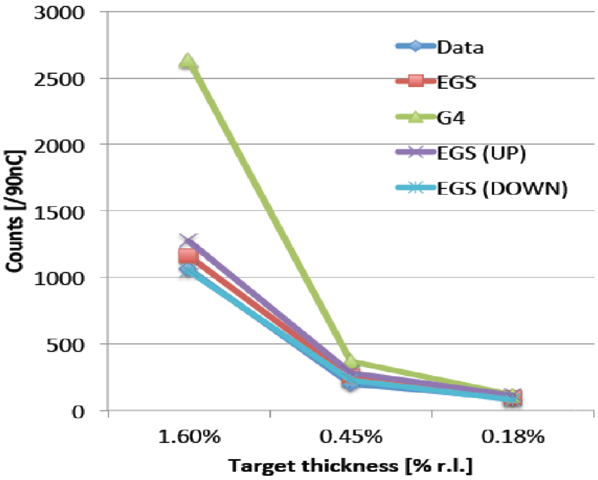

Figure 5: *Normalized trigger rates (number of triggers/90 nC of electrons on target) versus the converter target thickness. The data are in good agreement with the EGS5 prediction.*

5 The HPS Experiment

Since the time of the Dark 2012 Conference, the HPS Collaboration has revised its original design, in part to benefit from lessons learned with the test run, and in part to simplify the design so it could be proposed, funded, and built in time for a scheduling opportunity at JLAB appearing late 2014 and early 2015. The new design, described in the proposal to DOE 10), and shown schematically in fig.6, uses the existing ECal design, but incorporates fixes to the problems encountered and new preamplifiers to get better sensitivity to very small pulse heights. The SVT has been extended from 5 layers to 6, and layers 4, 5, and 6 have been doubled in width to improve acceptance. The greater length and extra layer also improve momentum resolution and track purity. A new support scheme will provide better rigidity, planarity, and cooling to the SVT modules, and the readout will be modified to handle the near doubling in channel number. The SVT DAQ, which had limited trigger rates to 16 kHz in the Test Run, is being modified to handle 50 kHz. The TDAQ, which will still use the JLAB FADC250, is undergoing trigger logic

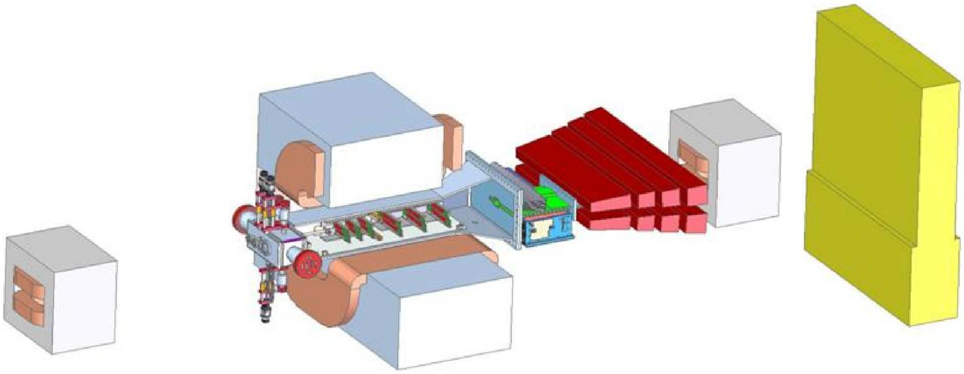

Figure 6: *The full HPS experiment. The six-layer tracker is located inside the good field region of the analyzing dipole in the magnet vacuum chamber. The ECal is positioned just downstream, followed by the muon system.*

and trigger monitoring revisions to supply robust trigger diagnostics. A muon system is being incorporated into the design, which will roughly double HPS acceptance for heavy photons beyond dimuon threshold and allow the first searches for heavy photon decays in the dimuon channel in HPS parameter space. Finally, the beamline is being equipped with beam diagnostics and protection collimators which will insure the safety of the detectors which are placed so close to the incident electron beam.

The performance expected from HPS has been studied extensively with full Monte Carlo simulations. The trigger simulation, for example, includes a faithful representation of all physics and background channels, electrons, photons, hadrons, and even x-rays and synchrotron radiation, and incorporates the time development of pulses from all the detectors, fully simulating the impact of out of time beam backgrounds. Trigger rates at the canonical currents and target thicknesses proposed are ≈ 20 kHz, easily within the capability of the DAQ. Similarly, extensive studies of pattern recognition and track reconstruction with full Monte Carlo overlaid with backgrounds, has demonstrated that tracking is ≈ 98 % efficient, and only 5 % of tracks have hits not correctly associated with the track. These miss-hits can cause large tails in the vertex resolution along the beam direction. A series of track quality and anti-confusion cuts will suppress these tails by three or more orders of magnitude, and make it possible to distinguish a genuine secondary vertex from the tails of the trident vertex distribution beyond 1.0-1.5 cm.

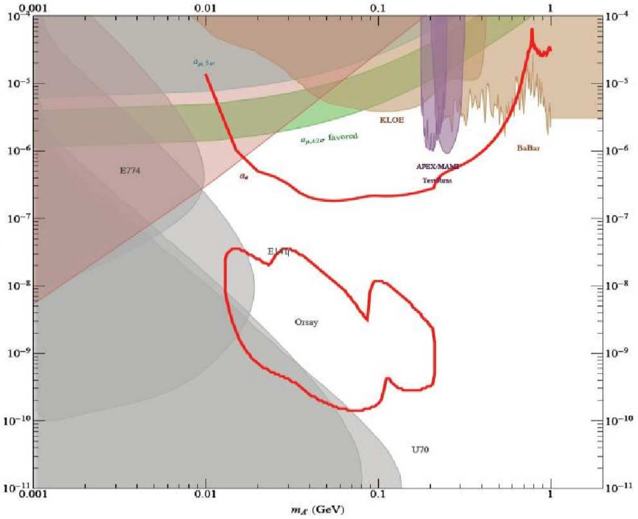

Figure 7: *Reach of the HPS Experiment with running at 1.1 GeV (1 week), 2.2 GeV (3 weeks), and 6.6 GeV (3 weeks). HPS also plans additional running.*

The reach of HPS is shown in fig.7. This is the data that we plan to take in a commissioning run late in 2014 and a regular data taking run in 2015. We plan additional running in 2016 and beyond.

6 Conclusions

The HPS Collaboration has designed, built, installed, and commissioned its first stage, the HPS Test Run, at JLAB. The experiment incorporates several design features to accommodate running a large acceptance, forward spectrometer in an intense electron beam. The detector and DAQ capabilities needed to search for heavy photons have been demonstrated. In addition, EGS5 simulations of multiple Coulomb scattering tails have been confirmed with Test

Run data, leading to a good understanding of the backgrounds that will be presented by electron beams. A proposal for Stage II, the full HPS experiment, has been submitted to DOE. A revised version of that proposal will be reviewed in Summer, 2013. With funding expected soon afterwards, HPS plans to complete construction in time for installation in the Fall 2014, with subsequent commissioning and data taking.

7 Acknowledgements

The work presented here is that of the HPS Collaboration. Support from DOE HEP at SLAC is gratefully acknowledged. Special thanks to Sho Uemura for his help in preparing this paper for publication.

References

1. J. L. Hewett, H. Weerts, R. Brock, J. N. Butler, B. C. K. Casey, J. Collar, A. de Govea and R. Essig *et al.*, arXiv:1205.2671 [hep-ex].
2. B. Holdom, Phys. Lett. B **166** (1986) 196.
3. P. Galison and A. Manohar, Phys. Lett. B **136** (1984) 279.
4. S. J. Brodsky and R. F. Lebed, Phys. Rev. Lett. **102**, 213401 (2009) [arXiv:0904.2225 [hep-ph]].
5. A. Banburski and P. Schuster, Phys. Rev. D **86**, 093007 (2012) [arXiv:1206.3961 [hep-ph]].
6. N. Arkani-Hamed, D. P. Finkbeiner, T. R. Slatyer and N. Weiner, Phys. Rev. D **79** (2009) 015014 [arXiv:0810.0713 [hep-ph]].
7. M. Pospelov and A. Ritz, Phys. Lett. B **671** (2009) 391 [arXiv:0810.1502 [hep-ph]].
8. A. Grillo *et al.* [HPS Collaboration], HPS Proposal to JLab PAC37 PR-11-006, http://www.jlab.org/exp_prog/PACpage/PAC37/proposals/Proposals/
9. J. D. Bjorken, R. Essig, P. Schuster and N. Toro, Phys. Rev. D **80**, 075018 (2009) [arXiv:0906.0580 [hep-ph]].

10. P. Hansson Adrian *et al.* [HPS Collaboration], Heavy Photon Search Experiment at Jefferson Laboratory: Proposal for 2014-2015 Run, https://confluence.slac.stanford.edu/display/hpsg/Project+Overview

Frascati Physics Series Vol. LVI (2012)
Dark Forces at Accelerators
October 16-19, 2012

THE DARKLIGHT EXPERIMENT - A STATUS REPORT

James R. Boyce
On behalf of the DarkLight Collaboration
Jefferson Lab, Newport News, VA 23606, USA

Abstract

Interest in probing physics Beyond the Standard Model (BSM), has led to incorporating accelerator technologies such as Superconducting RF (SRF) and Energy Recovery Linacs (ERL) into experiments searching for evidence of dark matter in laboratory settings. Three experiments will use JLab's accelerators, CEBAF and FEL, to explore complimentary regions of parameter space seeking evidence of a hypothesized gauge boson, the A'. This is a status report on the DarkLight effort using the FEL.

1 Introduction

As summarized by Jaeckel 4) and illustrated in Figure 1, many groups have searched for evidence of dark matter. In early 2006 the LIPSS Collaboration 1) showed that Jefferson Lab's accelerators, using superconducting RF (SRF) and

Energy Recovery Linac (ERL) technologies, could be used to explore regions of parameter space heretofore unreachable.

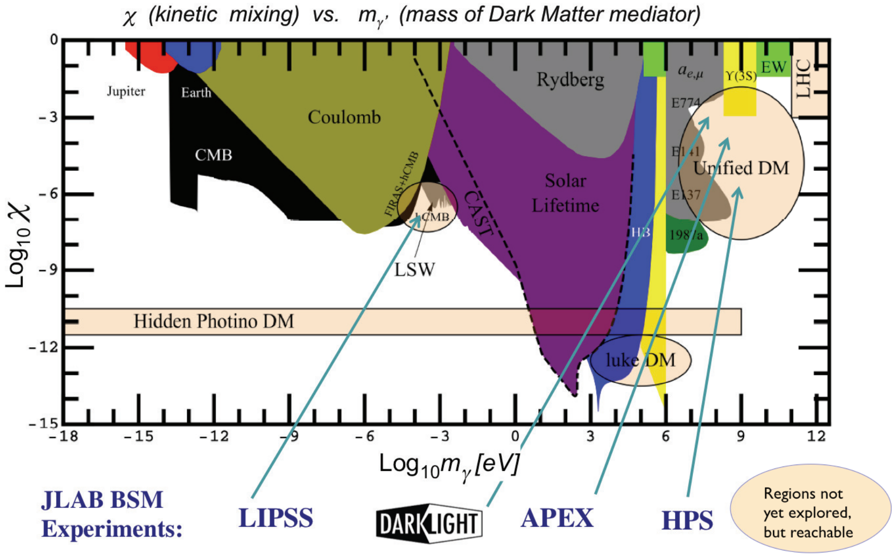

Figure 1: *Many experiments have explored parameter space and have established regions - in color - where dark matter evidence is excluded. Jefferson Lab experiments examine the regions indicated by light blue arrows.*

The high quality electron beam capabilities of JLab's accelerators, CEBAF and FEL, 5) have been incorporated into proposals based on predictions of Freytsis. 3) These experiments will search for the A′ scalar boson in the mass region 10 MeV to 1.0 GeV. Three collaborations (APEX, HPS, and DarkLight) are setting up to explore complementary parameter space regions indicated in Figure 1. The DarkLight Collaboration [1] search for the A′ 2)

---

[1] J. Balewski, J. Bernauer, W. Bertozzi, J. Bessuille, B. Buck, R. Cowan, K. Dow, C. Epstein, P. Fisher, S. Gilad, E. Ihloff, Y. Kahn, A. Kelleher, J. Kelsey, R. Milner, C. Moran, L. Ou, R. Russell, B. Schmookler, J. Thaler, C. Tschalaer, C. Vidal, A. Winnebeck *Laboratory for Nuclear Science, Massachusetts Institute of Technology, Cambridge, MA 02139, USA and the Bates Research and Engineering Center, Middleton MA 01949 USA*

will use the electron beam of the FEL facility to scatter off a gaseous hydrogen target.

2 DarkLight - The Basic Idea

The DarkLight experiment will use the FEL facility's high current (≈ 10mA), low energy (≈ 100 MeV) electron beam to scatter off a diffuse hydrogen gas target. Figure 2 shows the interaction diagram, parameter space to be explored by DarkLight, and the experiment concept. Hydrogen gas is fed into a gas chamber with coaxial windowless entrance and exit channels. Hydrogen gas escaping the chamber into the vacuum beam pipe is removed by pumping stations before and after the interaction region. Electron beam bunches are focused through the channels, interact with the hydrogen gas, and reaction products are recorded for analysis. Evidence for the hypothesized $A^{'}$ would consist of a narrow resonance on a large QED cross section.

S. Benson, C. Gould, G. Biallas, J.R. Boyce, J. Coleman, D. Douglas, R. Ent, P. Evtushenko, H. C. Fenker, J. Gubeli, F. Hannon, J. Huang, K. Jordan, R. Legg, M. Marchlik, W. Moore, G. Neil, M. Shinn, C. Tennant, R. Walker, G. Williams, S. Zhang *Jefferson Lab, 12000 Jefferson Avenue, Newport News, VA 23606, USA*

M. Freytsis *Physics Dept., U.C. Berkeley, Berkeley, CA, USA*

R. Fiorito, P. OShea *Institute for Research in Electronics and Applied Physics University of Maryland, College Park, MD, USA*

R. Alarcon, R. Dipert, *Physics Department, Arizona State University, Tempe, AZ, USA*

G. Ovanesyan *Los Alamos National Laboratory, Los Alamos NM, USA*

T. Gunter, N. Kalantarians, M. Kohl, *Physics Dept., Hampton University, Hampton, VA, USA*

I. Albayrak, M. Carmignotto, T. Horn *Physics Dept., Catholic University of America, Washington, DC 20064, USA*

D. S. Gunarathne, C. J. Martoff, D. L. Olvitt, B. Surrow, X. Li *Physics Dept., Temple University, Philadelphia, PA 19122 USA*

E. Long *Physics Dept., Kent State University, Kent, OH, 44242 USA*

R. Beck, R. Schmitz, D. Walther, *University Bonn, D - 53115 Bonn Germany*

K. Brinkmann, H. Zaunick II. *Physikalisches Institut Justus-Liebig-Universitt Giessen, D-35392 Giessen Germany*

W.J.Kossler *Physics Dept., College of William and Mary, Williamsburg VA 23185, USA*

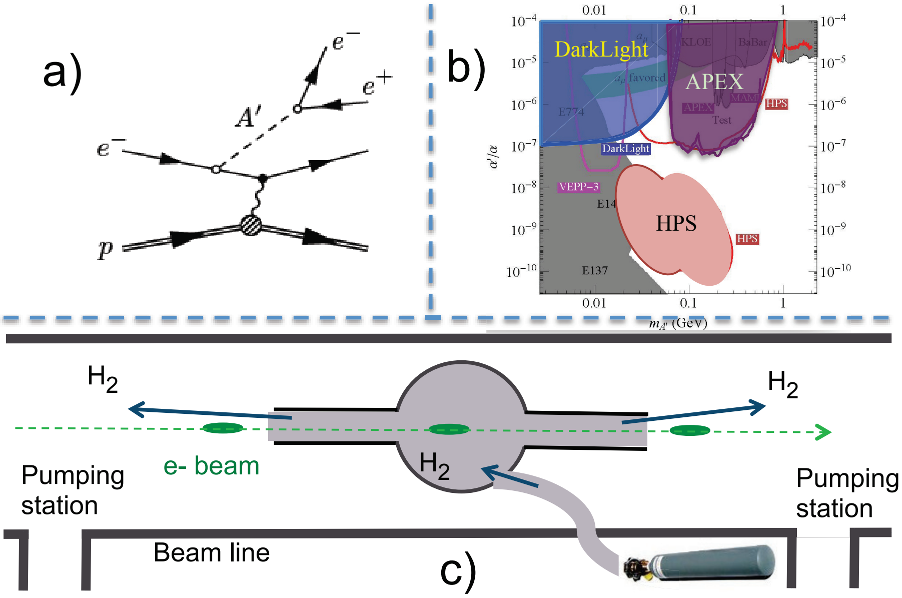

Figure 2: a) The hypothesized reaction, b) the parameter space to be explored by upcoming JLab experiments DarkLight, APEX and HPS, and c) The DarkLight experiment concept.

3 Proposed Detector System Design

The detector system for the DL experiment surrounds the windowless gas target and is inside a 0.5 T solenoid magnet surrounding the electron beam line, detectors, and windowless gas chamber at the interaction region. A candidate location for this system is in the the FEL's UV beam line, indicated in Figure 3, which is a schematic layout of the FEL's ERL accelerator system. TheDarkLight system is contained in a cylindrical space about 1.7 meters long and 1 meter in diameter fitting around the the accelerator beam line. Figures 4 and 5 show the present detector system design concept. The diameter of the input and output channels ($\approx$ 2 mm) was chosen by balancing the requirement of a constant density of Hydrogen in the interaction chamber, against the need to maintain good vacuum in the accelerator beam line. Hence the pumping stations before and after the DL system.

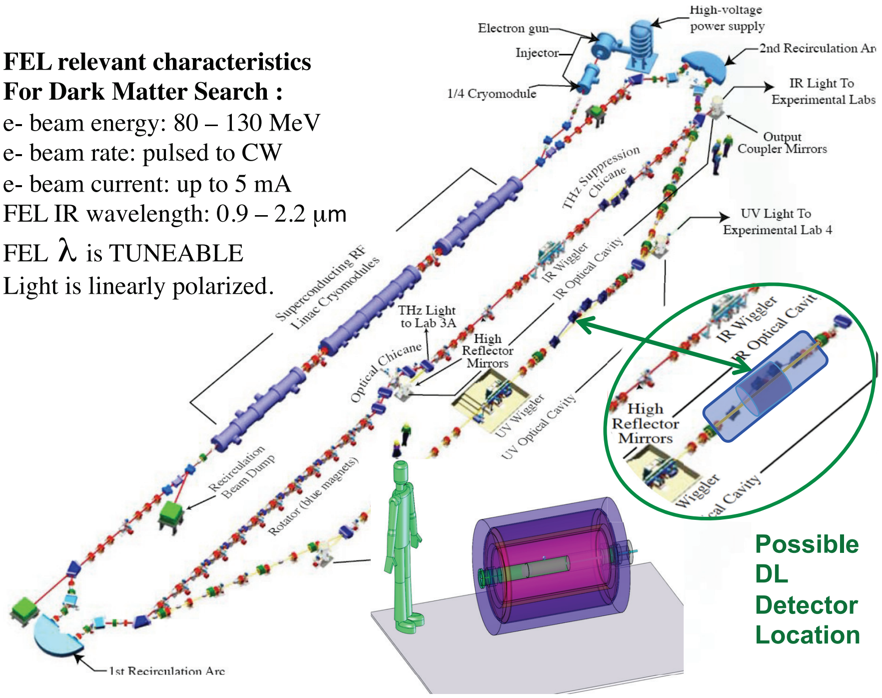

FEL relevant characteristics
For Dark Matter Search :
e- beam energy: 80 – 130 MeV
e- beam rate: pulsed to CW
e- beam current: up to 5 mA
FEL IR wavelength: 0.9 – 2.2 μm
FEL λ is TUNEABLE
Light is linearly polarized.

Figure 3: Jefferson Lab's FEL is an Energy Recovering Linac (ERL) in a 60 meter long racetrack configuration. An inset cartoon illustrates the size of the DarkLight detector system relative to a green manikin. Also shown a location for the DarkLight Experiment and relevant FEL characteristics for Dark Matter experiments.

However, this design calls for clean transmission of 10 mA of a 100 MeV electron beam through the DL system. Cleanly threading a 1 MW beam and then cleanly maintaining it through such a system has never been done before and is a challenging task for the FEL beam opticians and operators.

Prior to more detailed design considerations, three topics needed further examination: 1) background ambient radiation in the detector location, 2) radiation caused by scraping of the electron bunch along the in/out channels, and 3) excessive RF heating of the target region induced by the beam. These topics were addressed in 2012 by extensive modeling and by measurements with the FEL.

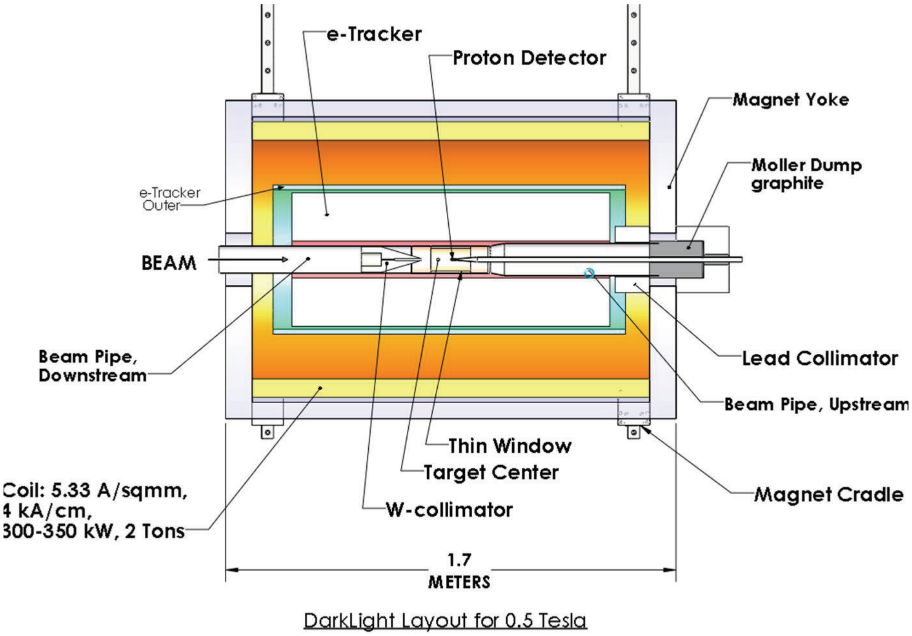

Figure 4: A cross section of the DL system shows the solenoid surrounding detectors surrounding the windowless gas chamber - the interaction region.

4 Background Radiation

Ambient vault radiation was measured outside the vacuum beam line while the beam-target interaction studies required installing an insertable system in the beam-line. Results of these studies will be used to establish shielding requirements and beam bunch size requirements.

4.1 Beam-Target radiation.

The 2-mm diameter constraints on the entrance/exit channels along with the beam current and energy means putting 1MW of power through the chamber. Two items of concern needed to be addressed: beam scraping and RF induced hot spots. Figure 6 shows the setup used to address these diameter concerns. A solid block of Al with three holes of progressively smaller diameters (6 mm, 4 mm, and 2 mm) was mounted on a standard vacuum chamber/cube and at-

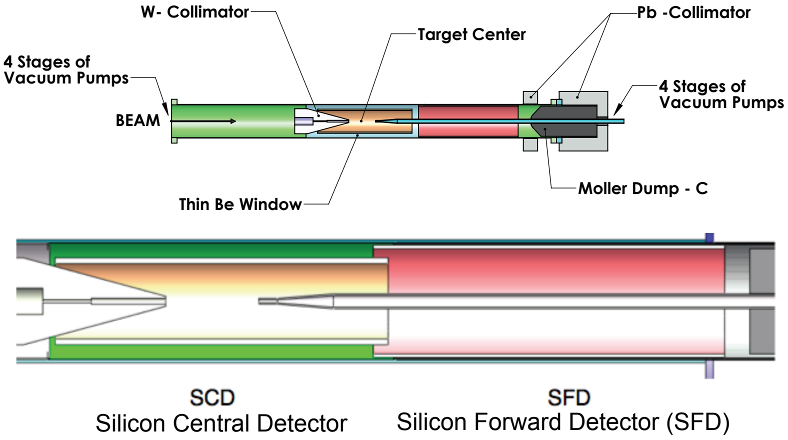

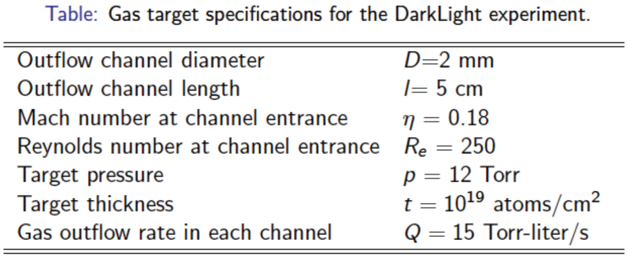
Table: Gas target specifications for the DarkLight experiment.

Outflow channel diameter	D=2 mm
Outflow channel length	l= 5 cm
Mach number at channel entrance	$\eta = 0.18$
Reynolds number at channel entrance	$R_e = 250$
Target pressure	$p = 12$ Torr
Target thickness	$t = 10^{19}$ atoms/cm^2
Gas outflow rate in each channel	$Q = 15$ Torr-liter/s

Figure 5: An enlarged view of the target chamber and the initial design considerations.

tached to a remotely controlled precision stepper motor. The cube was then mounted in the IR beam line along with insertable viewers before and after the target block. The beam-target test consisted of sending the the beam through each of the three holes and measuring the temperature and radiation as a function of beam current and hole size. First, with the Al block retracted, the FEL beam was established with low rep rate and bunch charge. Then the block was inserted to each hole's position co-axial to the beam and the beam current was progressively increased while the radiation levels and block temperature were monitored and recorded.

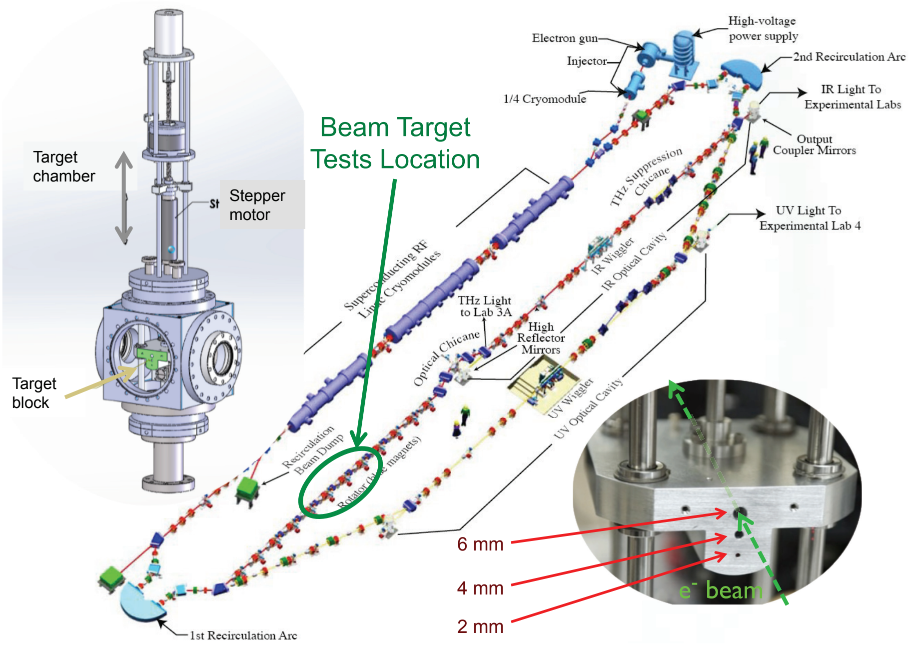

Figure 6: The actual beam-target tests setup. The tests verified that the electron beam can be successfully threaded through input and exit regions of the windowless gas target without excessive scraping off the walls. Radiation from and temperature of the block were recorded as a function of beam conditions.

4.2 Induced RF Heating.

Using an RDT temperature sensor mounted on the Al block, the power deposited in the block was determined by measuring the rise and fall of the Al block temperature. These measurements were taken during an eight hour long run. Bottom Line: there was a loss of between 3 and 7 ppm from a 0.45 MW beam, well below the original tolerable limit of 1E-05 loss due to beam halo scraping.

It is well known that unhealthy levels of radiation can be produced by SRF accelerator cryomodules of the type used in the FEL. Measurements of the vault's ambient radiation was conducted parasitically with an experiment needing UV lasing, i.e., an electron beam of 130 MeV. This would establish an upper limit on the radiation doses of photons and neutrons. Figure 7 shows

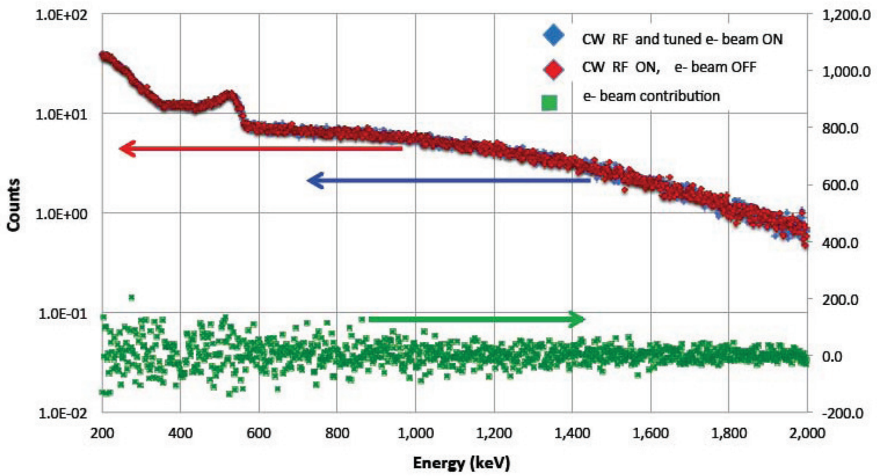

Figure 7: Typical photon spectra in the FEL vault recorded during UV lasing operations. The arrows indicate which scale is appropriate for the data points. The important conclusion from these measurements is that the ambient radiation in the FEL vault is solely from the accelerating cryomodules, providing the electron beam is well tuned and energy recovered.

typical photon spectra taken under these conditions using a NaI/PMT system inside a two-inch thick Pb enclosure. The red spectrum was taken during UV lasing. The blue spectrum was taken immediately after the electron beam was turned off. The green spectra is the difference between the red and blue. These data clearly establish an important fact: a properly tuned electron beam does not contribute to the ambient radiation field in the FEL vault.

In addition to the NaI/PMT detector system, two unshielded, calibrated detector systems measured the flux of neutrons and gammas in the vault. Figure 8 shows the fluxes as function of RF accelerating voltage as the voltage is shut down from the last accelerating cavity back to the injector. At maximum SRF voltages, neutrons contribute about 1/4 of the total radiation. The good news is that since DarkLight does not require maximum SRF voltage, the individual cryomodules can be tuned such that 100 MeV is achieved while at the same time the accelerating SRF voltages are under the threshold for pesky field emission-causing background.

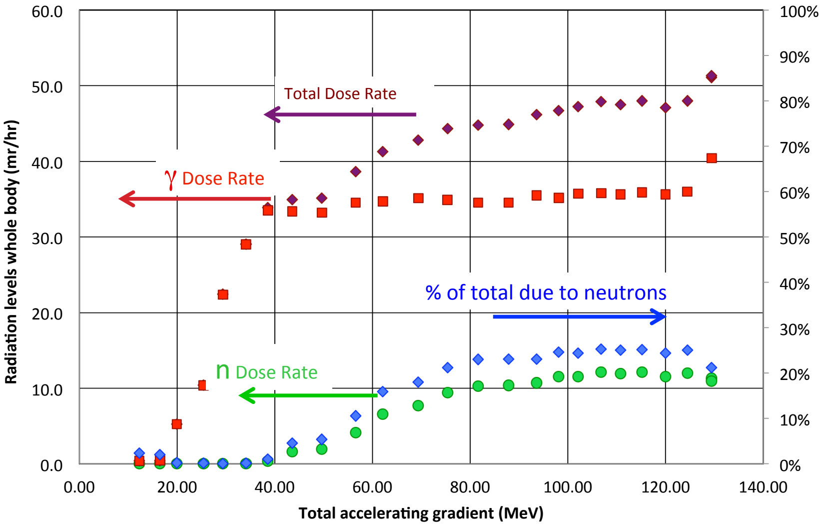

Figure 8: Photon and neutron dose rates recorded during UV lasing operations. The electron beam energy was 130 MeV. These points were recorded as the RF on the three cryomodules was shut down starting with the cavities at the end of the third cryomodule and sequentially shutting down each section back towards the injector. The arrows indicate the appropriate scale for each set of data points.

5 Discussion and Path Forward

To summarize the DarkLight effort to date, we have made background radiation measurements, modeled beam-target and moller scattering, measured actual ambient radiation, designed, constructed, calibrated, and conducted tests with the actual FEL beam. We have established upper level background radiation doses for both neutrons and photons, as well as their sources. We have established that the tight constraints on the electron beam in terms of stability, current, and energy are achievable.

With the successful studies conducted in 2012, the collaboration has the

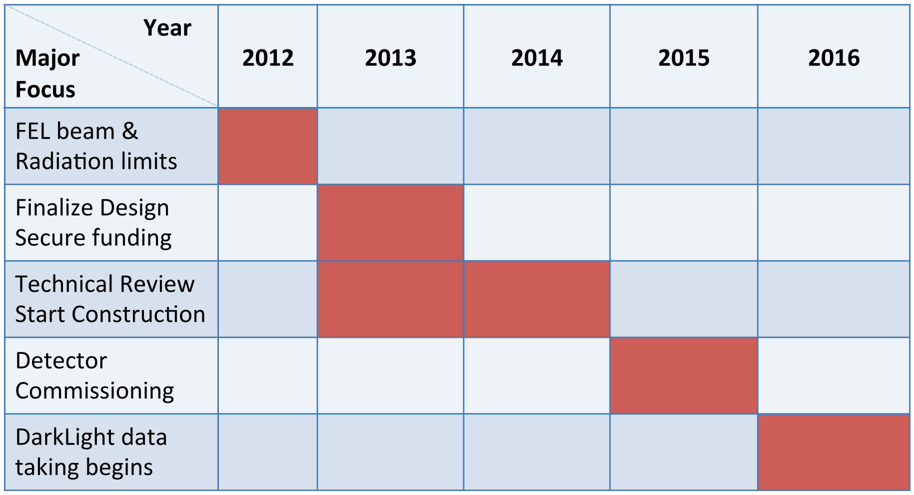

Year / Major Focus	2012	2013	2014	2015	2016
FEL beam & Radiation limits	🟥				
Finalize Design Secure funding		🟥			
Technical Review Start Construction		🟥	🟥		
Detector Commissioning				🟥	
DarkLight data taking begins					🟥

Figure 9: With the information gathered to date, the collaboration's focus for calendar year 2013 will shift over to seeking funding support. Once secured, the design, construction and commissioning of the DarkLight system will start. The estimated start of the experiment will occur in 2016.

information needed to complete the design, construct and commission the the Detector system, and install and run the DarkLight Experiment. The anticipated timeline is shown in Figure 9.

6 Acknowledgements

Notice: Authored by Jefferson Science Associates, LLC under U.S. DOE Contract No. DE-AC05-06OR23177. The U.S. Government retains a non-exclusive, paid-up, irrevocable, world-wide license to publish or reproduce this manuscript for U.S. Government purposes. This work supported by the Commonwealth of Virginia and by DOE under contract DE-AC05-060R23177.

References

1. A. Afanasev, O.K. Baker, K.B. Beard, G. Biallas, J. Boyce, et al. New Experimental limit on Optical Photon Coupling to Neutral, Scalar Bosons. *Phys.Rev.Lett.*, 101:120401, 2008.

2. P. Fisher and Milner R. A proposal for the darklight experiment at the je erson laboratory free electron laser. Program Advisory Committee - 37 PAC PR-11-008, Jefferson Lab, 12000 Jefferson Ave., Newport News, VA 23606, USA, December 2010.

3. M. Freytsis, G. Ovanesyan, and J. Thaler. Dark Force Detection in Low Energy e-p Collisions. *JHEP*, 1001:111, 2010.

4. J. Jaeckel and A. Ringwald. The Low-Energy Frontier of Particle Physics. *Ann.Rev.Nucl.Part.Sci.*, 60:405–437, 2010.

5. G.R. Neil, C. Behre, S.V. Benson, M. Bevins, G. Biallas, et al. The JLab high power ERL light source. *Nucl.Instrum.Meth.*, A557:9–15, 2006.

Frascati Physics Series Vol. LVI (2012)
DARK FORCES AT ACCELERATORS
October 16-19, 2012

U boson search in ϕ Dalitz decays with KLOE

I. Sarra on behalf of the KLOE-2 collaboration
Laboratori Nazionali di Frascati, INFN, Frascati, Italy

Abstract

We have carried out a new search for the existence of a light dark force mediator with the KLOE detector at DAΦ NE. This particle, called U, has been looked for by adding to the already used $\phi \to \eta\, U$, $\eta \to \pi^+\pi^-\pi^0$ and $U \to e^+e^-$, the same decay chain with $\eta \to \pi^0\pi^0\pi^0$. The latter sample (1.7 fb^{-1}) results to have better reconstruction efficiency and reduced background contamination than the previously used sample (1.5 fb^{-1}). No structures are observed in the e^+e^- invariant mass distribution over the background. The resulting exclusion plot, obtained by combining both samples with CLS method, covers the mass range $5 < M_U < 470$ MeV and sets an upper limit at 90% C.L. on the ratio between the U boson coupling constant and the fine structure constant, α'/α, of $\leq 1.7 \times 10^{-5}$ for $30 < M_U < 400$ MeV and $\leq 8.0 \times 10^{-6}$ for $50 < M_U < 210$ MeV. This result assumes the Vector Meson Dominance expectations for the $\phi\eta\gamma^*$ transition form factor. The dependence of this limit on the transition form factor has also been studied.

1 Anomalous experimental results and their possible explanation

A variety of astrophysical observations indicate that 83% of the matter in the Universe is non baryonic and dark, presumably in the form of elementary particles produced in the early Universe. Since no such particles have yet been identified in particle accelerators, these observations require new fundamental particle physics.

Moreover, recent experiments have confirmed the longstanding suspicion that there are more positrons and electrons at 10-100 GeV than can be explained by supernova shocks and interactions of cosmic ray protons with the Interstellar Medium (ISM). The experiments are:

- **Pamela:** The Payload for Antimatter Matter Exploration and Light-nuclei Astrophysics has reported results 1) indicating a sharp upturn in the positron fraction ($\mathrm{e}^+/(\mathrm{e}^+ + \mathrm{e}^-)$) from $10-100$ GeV, contrary to what expected from high-energy cosmic rays interacting with the interstellar medium IMS. One possible explanation for this is dark matter annihilation into e^-e^+.

- **Fermi:** The Fermi Gamma-Ray Telescope can distinguish more than gamma rays. It has now provided the most accurate measurement of the spectrum of cosmic-ray electrons and positrons. These results are consistent with a single power law, but visually they suggest an excess emission from about 100 GeV to 1 TeV 2). The additional source of electrons and positrons could come from nearby pulsars or dark matter annihilation. Dark matter would seem a natural candidate for this as well, with its mass scale determining the cutoff.

- **Integral:** The INTEGRAL satellite 3) observes a 511 keV signal from the galactic core, which suggests the existence of an abundant positron annihilation source, far exceeding what expected from supernovae only.

If we focus only on the high-energy positrons and electrons, there are a number of challenges to any model of dark matter. PAMELA and FERMI signals require a cross section much larger than what allowed by the thermal relic abundance. Boost factors of O(100) or more above what would be expected for a thermal WIMP are required to explain these excesses 4). Moreover:

- *A large cross section into leptons*: typical annihilations via Z bosons produce very few hard leptons. Annihilations into W bosons produce hard leptons, but many more soft leptons through the hadronic shower. Higgs bosons and heavy quarks produce even softer spectra of leptons, all of which seem to give poor fits to the data. At the same time, absent a leptonic gauge boson, it is a challenge to construct means by which dark matter would annihilate directly to leptons.

- *A low cross section into hadrons*: Even if a suitably high annihilation rate into leptons can be achieved, the annihilation rate into hadronic modes must be low. PAMELA measurements of antiprotons tightly constrain hadronic annihilations as well. Consequently, although quark and gauge boson annihilation channels may occur at some level, the dominant source of leptons must arise through some other channel.

The combination of these issues makes the observed high-energy anomalies difficult to explain with thermal dark matter annihilation. However, the inclusion of a new force in the dark sector simultaneously addresses all of these concerns. It is postulated the existence of relatively heavy (~ 1 TeV) Weakly Interacting Massive Particles (WIMPs) states together with at least one relatively light ($\sim$ 1 GeV) vector boson, mediator of a new hidden gauge symmetry.
Although SM particles are not charged under this new symmetry they can still couple with the dark photon through the kinetic mixing mechanism with ordinary SM bosons, and specifically with the photon. The Lagrangian is of the form:

$$\mathcal{L} = \mathcal{L}_{SM} + \mathcal{L}_{Dark} + \mathcal{L}_{mix} \tag{1}$$

where

$$\begin{aligned} \mathcal{L}_{Dark} = \mathcal{L}^{F}_{Dark}(X) \quad &\Rightarrow \quad M_X \sim 100 - 1000\, GeV \;\; WIMP \\ +\mathcal{L}^{B}_{Dark}(U) \quad &\Rightarrow \quad m_U \sim GeV \;\; U\ Boson \\ +\mathcal{L}^{B}_{Dark}(h') \quad &\Rightarrow \quad higgs\ potential\ breaking\ U(1)_D \end{aligned}$$

Typically, the mixing strength is parametrized by a single parameter ϵ_D, whose value has to be determined experimentally. However, in order to better accommodate the above mentioned experimental results, preferred values of ϵ_D are in the ball-park of 10^{-3}. As a consequence of that, the U can be produced and observed at present day colliders depending on its mass and on the value of ϵ_D, as discussed in the next sections.

2 The KLOE detector

DAΦ NE, the Frascati ϕ-factory, is an e^+e^- collider running at center-of-mass energy of $\sim$ 1020 MeV. Positron and electron beams collide at an angle of π-25 mrad, producing ϕ mesons nearly at rest. The KLOE experiment operated at this collider from 2000 to 2006, collecting 2.5 fb^{-1}. The KLOE detector consists of a large cylindrical Drift Chamber (DC), surrounded by a lead-scintillating fiber electromagnetic calorimeter (EMC), all embedded inside a superconducting coil, providing a 0.52 T axial field. The beam pipe at the interaction region is a sphere with 10 cm radius, made of a 0.5 mm thick Beryllium-Aluminum alloy. The drift chamber 6), 4 m in diameter and 3.3 m long, has 12,582 all-stereo tungsten sense wires and 37,746 aluminum field wires, with a shell made of carbon fiber-epoxy composite with an internal wall of $\sim$ 1 mm thickness. The gas used is a 90% helium, 10% isobutane mixture. The momentum resolution is $\sigma(p_\perp)/p_\perp \approx 0.4\%$. Vertices are reconstructed with a spatial resolution of $\sim$ 3 mm. The calorimeter 7), with a readout granularity of $\sim(4.4 \times 4.4)$ cm^2, for a total of 2440 cells arranged in five layers, covers 98% of the solid angle. Each cell is read out at both ends by photomultipliers, both in amplitude and time. The energy deposits are obtained from the signal amplitude while the arrival times and the particles positions are obtained from the time differences. Cells close in time and space are grouped into energy clusters. Energy and time resolutions are $\sigma_E/E = 5.7\%/\sqrt{E\ (\mathrm{GeV})}$ and $\sigma_t = 57\ \mathrm{ps}/\sqrt{E\ (\mathrm{GeV})} \oplus 100$ ps, respectively. The trigger 8) uses both calorimeter and chamber information. In this analysis the events are selected by the calorimeter trigger, requiring two energy deposits with $E > 50$ MeV for the barrel and $E > 150$ MeV for the endcaps. Data are then analyzed by an event classification filter 9), which selects and streams various categories of events in different output files.

3 Searches for a U Boson mediator

The astrophysical observations suggest the existence of a WIMP dark matter particle and of a secluded gauge sector U(1)$_D$ under which the SM particles are uncharged. The abelian gauge field weakly interacts with the U(1)$_Y$ of the SM4 by an invariant kinetic mixing term:

$$\Delta\mathcal{L} = \epsilon_D F^{Y,\mu\nu} F_{D,\mu\nu} \tag{2}$$

The mixing parameter ϵ is of the order of 10^{-4} - 10^{-2}. The Feynman diagram is showed in figure 1. The vector boson U has mass near the GeV scale.

Figure 1: The U boson can communicate with the SM through a kinetic mixing term describing the interaction of the U boson with SM photon. In this case the parameter ϵ_D should be smaller than 10^{-2}.

These hypothesis lead to the consequence that observable effects can be induced in $\mathcal{O}$(GeV) energy e$^+$e$^-$ colliders such as DAΦNE or present and/or future B factories. The U boson can be also produced in electron collisions on a fixed target, such as MAMI 16), in a process analogous to ordinary bremsstrahlung. In this case, production cross sections are much higher with respect to e$^+$e$^-$ processes. However backgrounds, both from ordinary QED reactions and from possible beam related sources are also higher.

The U boson can be produced in e$^+$e$^-$ collisions via the radiative reaction e$^+$e$^-$ $\rightarrow$ Uγ, with subsequent decay of the U into a lepton pair. If the two leptons are charged, the U can be observed as a resonant peak of the lepton pair invariant mass distribution over the standard continuous QED background.

A further line of search available at e$^+$e$^-$ colliders is the study of the decays of a vector meson into a pseudo-scalar and a U, as suggested by Reece and Wang 10). This decays should occur at a rate suppressed by a factor ϵ with respect to the standard radiative ones, which have typical branching ratios of $\sim$

1%. In particular Reece and Wang have focussed their attention on the channel $\phi(1020) \to \eta U$. With the statistics acquired so far by the KLOE experiment at the DAΦNE facility in Frascati, they have argued that one could probe mixing parameters down to 10^{-3}, for U masses below $\mathrm{m}_\phi - \mathrm{m}_\eta \sim 470$ MeV. This search has actually been performed by the KLOE-2 Collaboration, as described in the remaining of this paper.

4 Event selection

To improve the search for the U boson, we have carried out the analysis of the process $\phi \to \eta U$, $U \to e^+e^-$, adding the decay channel $\eta \to \pi^0\pi^0\pi^0$ to the previously used, $\eta \to \pi^+\pi^-\pi^0$. The new search has been performed on a data sample of 1.7 fb^{-1}, corresponding approximately to 6×10^9 produced ϕ mesons. The Monte Carlo (MC) simulation for the $\phi \to \eta U$ decay has been developed according to 10), with a flat distribution in the e^+e^- invariant mass, M_{ee}, while the irreducible background $\phi \to \eta e^+e^-$, $\eta \to \pi\pi\pi$, has been simulated according to a Vector Meson Dominance parametrization 11). All MC productions, including all other ϕ decays, take into account changes in DAΦ NE operation and background conditions on a run-by-run basis. Corrections for data-MC discrepancies in cluster energies and tracking efficiency, evaluated with radiative Bhabha scattering and $\phi \to \rho\pi$ event samples, respectively, have been applied.

As a first analysis step for the neutral η decay channel, a preselection is performed requiring:

1. two opposite charge tracks with point of closest approach to the beam line inside a cylinder around the interaction point (IP), of 4 cm transverse radius and 20 cm length;
2. six prompt photon candidates, *i.e.* energy clusters with $E > 7$ MeV not associated to any track, in an angular acceptance $|\cos\theta_\gamma| < 0.92$ and in the expected time window for a photon ($|T_\gamma - R_\gamma/c| < \mathrm{MIN}(3\sigma_t, 2\,\mathrm{ns})$);
3. a loose cut on the six-photon invariant mass: $400 < M_{6\gamma} < 700$ MeV.

After this selection, a peak corresponding to the η mass is clearly observed in the distribution of the recoil mass against the e^+e^- pair, $M_{\mathrm{recoil}}(ee)$ (Fig. 2). The second peak at $\sim$ 590 MeV is due to $K_S \to \pi^+\pi^-$ decays with wrong

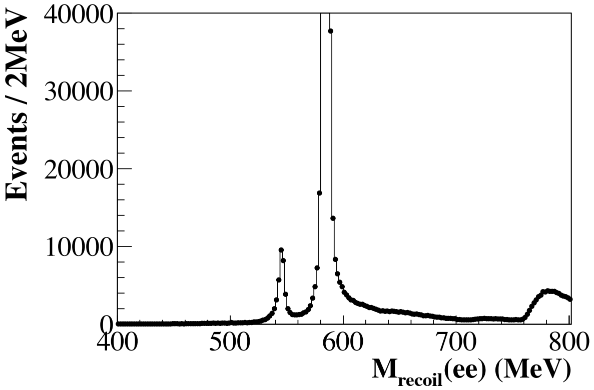

Figure 2: Recoiling mass against the e^+e^- pair for the data sample after preselection cuts. The $\phi \to \eta\, e^+e^-$ signal is clearly visible as the peak corresponding to the η mass.

mass assignment. To select $\phi \to \eta\, e^+e^-$ events, a 3σ cut is applied on this variable, $536.5 < M_{\mathrm{recoil}}(ee) < 554.5$ MeV. The retained sample has $\sim 20\%$ residual background contamination, constituted by $\phi \to \eta\gamma$, $\phi \to K_S K_L$ and $e^+e^- \to \omega\pi^0$ (about 50%, 35% and 15% of the whole background contribution, respectively). In Fig. 3, the comparison between data and Monte Carlo events for the M_{ee} and $\cos\Psi^*$ distributions is shown at this analysis level. The Ψ^* variable is the angle between the directions of the η and the e^+ in the e^+e^- rest frame. Photon conversion events are concentrated at $M_{ee} \sim 30$ MeV and $\cos\Psi^* < 0.6$, while the other backgrounds cover the $M_{ee} > 300$ MeV region and are uniformly distributed in $\cos\Psi^*$.

The $\phi \to \eta\gamma$ background contamination is mainly due to events where a photon converts to an e^+e^- pair on the beam pipe (BP) or drift chamber walls (DCW). After tracing back the tracks of the two e^+/e^- candidates, these events are efficiently rejected by reconstructing the invariant mass (M_{ee}) and the distance (D_{ee}) of the track pair both at the BP and DCW surfaces. Both variables are expected to be small for photon conversion events, so that this

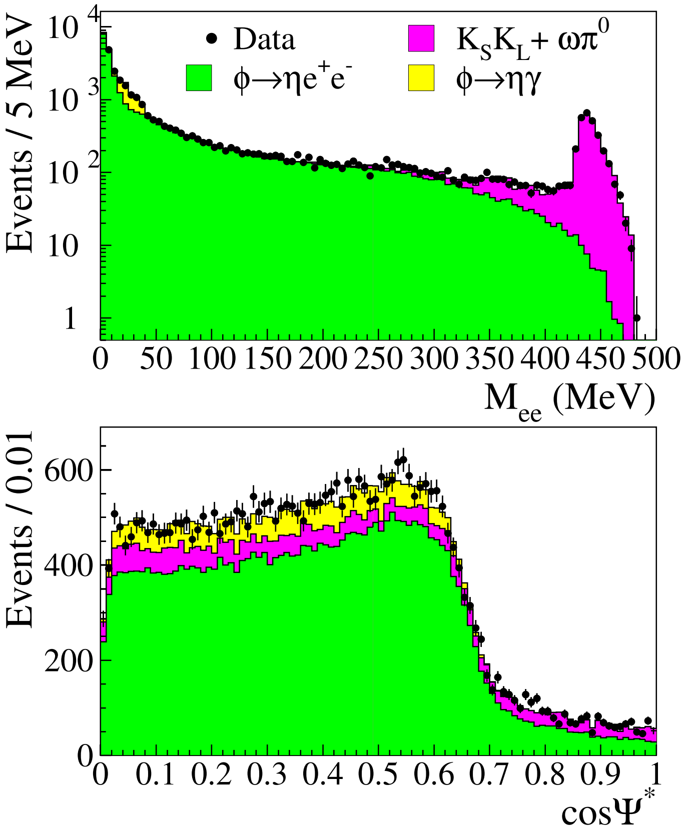

Figure 3: $\phi \to \eta\, e^+e^-$, $\eta \to \pi^0\pi^0\pi^0$ events: data-MC comparison for M_{ee} (top) and $\cos\Psi^*$ distributions (bottom) after the $M_{\rm recoil}(ee)$ cut.

background is removed by rejecting events with: [$M_{ee}(BP) < 10$ MeV and $D_{ee}(BP) < 2$ cm] or [$M_{ee}(DCW) < 120$ MeV and $D_{ee}(DCW) < 4$ cm].

At this stage of the analysis, the surviving background is dominated by events with two charged pions in the final state, and it is rejected by exploiting the timing capabilities of the calorimeter. When an energy cluster is associated to a track, the time of flight (ToF) to the calorimeter is evaluated both using the track trajectory ($T_{\text{track}} = L_{\text{track}}/\beta c$) and the calorimeter timing (T_{cluster}). The $\Delta T = T_{\text{track}} - T_{\text{cluster}}$ variable is then evaluated in the electron hypothesis (ΔT_e). In order to be fully efficient on signal, events with either an e^+ or an e^- candidate inside a 3σ window around $\Delta T_e = 0$ are retained for further analysis.

At the end of the analysis chain, 30577 events are selected, with $\sim 3\%$ background contamination (Fig. 4). The analysis efficiency, defined as the ratio between events surviving analysis cuts and generated events, is $\sim 15\%$ at low e^+e^- invariant masses, increasing up to 30% at higher M_{ee} values.

The analysis of the decay channel $\eta \to \pi^+\pi^-\pi^0$ is the same as described in 12), with the addition of a cut on the recoil mass to the $e^+e^-\pi^+\pi^-$ system, which is expected to be equal to the π^0 mass for signal events. In Fig. 5 top, data-MC comparison shows some residual background contamination in the tails of the distribution, which are not well described by our simulation. A cut $100 < M_{\text{recoil}}(ee\pi\pi) < 160$ MeV is then applied. The effect of this cut on the M_{ee} variable is shown in Fig. 5 bottom. The total number of selected events is 13254, with $\sim 2\%$ background contamination.

5 Upper limit evaluation on *U* boson production

The upper limit on the U boson production in the $\phi \to \eta U$ process is obtained combining the two η decay channels. The resolution of the e^+e^- invariant mass has been evaluated with a Gaussian fit to the difference between the reconstructed and generated mass for Monte Carlo events, providing $\sigma_{M_{ee}} \leq 2$ MeV over the whole M_{ee} range. The determination of the limit is done by varying the M_U mass, with 1 MeV step, in the range between 5 and 470 MeV. Only five bins (5 MeV width) of the reconstructed M_{ee} variable, centered at M_U are considered. For each channel, the irreducible background, $b(M_U)$, is extracted directly from our data after applying a bin-by-bin subtraction of the non-irreducible backgrounds and correcting for the analysis efficiency. The M_{ee} distribution is then fit, excluding the bins used for the upper limit evaluation. The parametrization of the fitting function has been taken from Ref. 11). The $\phi\eta\gamma^*$ transition form factor is parametrized as

$$F_{\phi\eta}(q^2) = \frac{1}{1 - q^2/\Lambda^2} \tag{3}$$

with $q = M_{ee}$. Free parameters are Λ and a normalization factor. The spread of the extracted parameters is contained within the statistical error of the fit

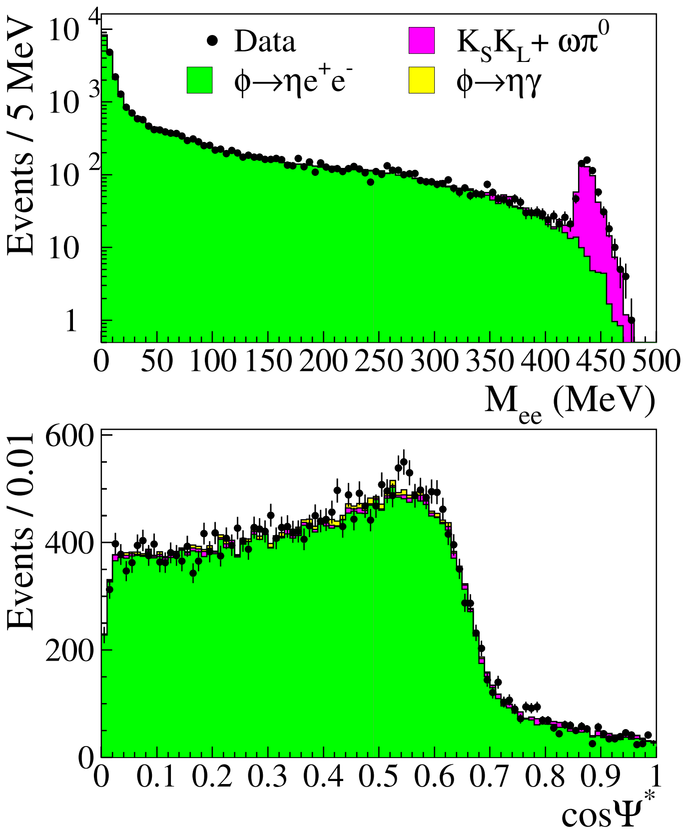

Figure 4: $\phi \rightarrow \eta\, e^+e^-$, $\eta \rightarrow \pi^0\pi^0\pi^0$ events: data-MC comparison for M_{ee} (top) and $\cos\Psi^*$ distributions (bottom) at the end of the analysis chain.

done on the whole M_{ee} mass range, shown in Fig. 6, as expected from the overall good description of the M_{ee} shape for both η decay channels.

The exclusion limit on the number of events for the $\phi \rightarrow \eta U$ signal as a function of M_U is obtained with the CL$_\text{S}$ technique $^{13)}$, using the M_{ee} spectra before background subtraction. The limit is extracted both for each η decay channel and in a combined way. For the combined procedure, the CL$_\text{S}$

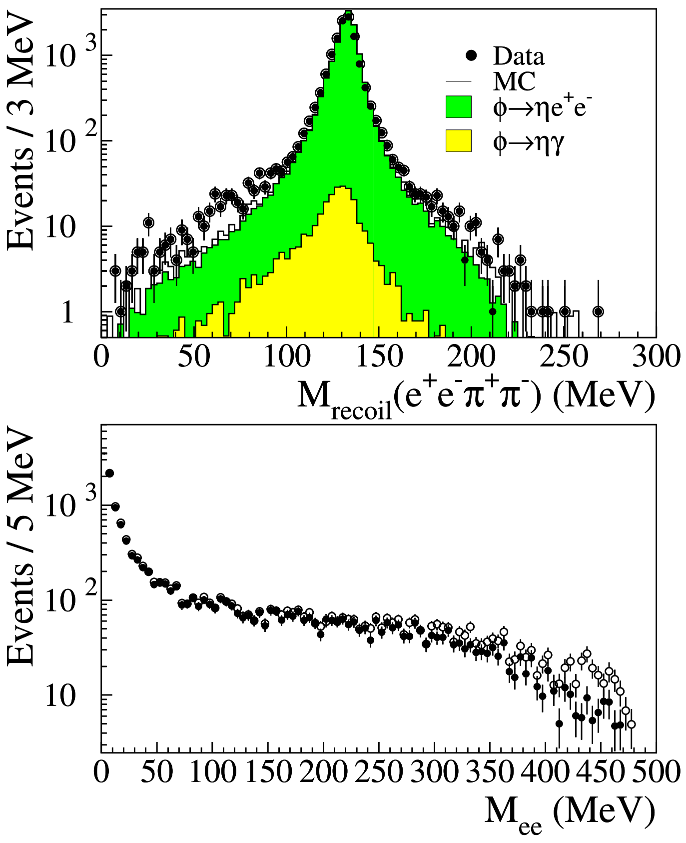

Figure 5: $\phi \to \eta e^+e^-$, $\eta \to \pi^+\pi^-\pi^0$ analysis. Top: data-MC comparison for the recoil mass against the $e^+e^-\pi^+\pi^-$ system. Bottom: M_{ee} distribution before (open circles) and after (black dots) the cut on $M_{\mathrm{recoil}}(ee\pi\pi)$.

evaluation is done by summing values over all bins of the two decay channels, taking into account the different luminosity, efficiency and relative branching ratios of the two samples. The systematic error on the background knowledge $\Delta b(M_{ee})$ is evaluated, for each M_U value, changing by one standard deviation the two fit parameters and has been taken into account while evaluating $\mathrm{CL_S}$,

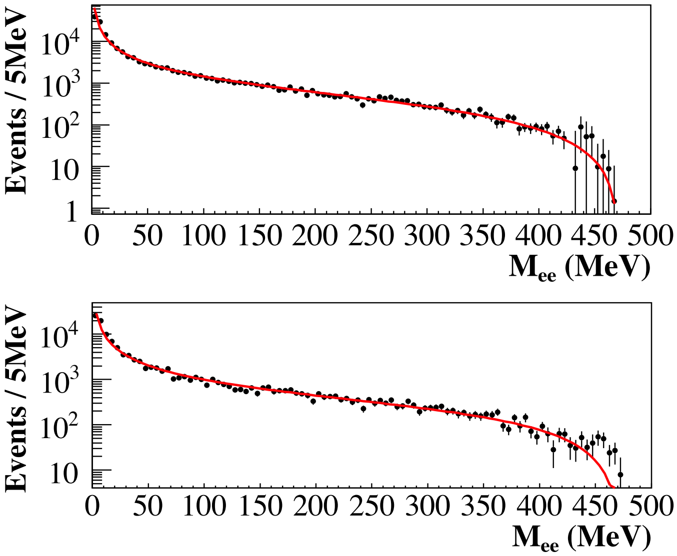

Figure 6: Fit to the corrected M_{ee} spectrum for the Dalitz decays $\phi \to \eta\, e^+e^-$, with $\eta \to \pi^0\pi^0\pi^0$ (top) and $\eta \to \pi^+\pi^-\pi^0$ (bottom).

applying a Gaussian spread of width $\Delta b(M_{ee})$ on the background distribution. In Fig. 7 top, the upper limit at 90% C.L. on the number of events for the decay chain $\phi \to \eta U$, $U \to e^+e^-$, is shown for both $\eta \to \pi^0\pi^0\pi^0$ and $\eta \to \pi^+\pi^-\pi^0$, separately evaluated. In Fig. 7 bottom, the smoothed upper limit on the branching fraction for the process $\phi \to \eta U$, $U \to e^+e^-$, obtained from the combined method is compared with evaluations from each of the two decay channels. In the combined result, the upper limit on the product $\mathrm{BR}(\phi \to \eta U) \times \mathrm{BR}(U \to e^+e^-)$ varies from 10^{-6} at small M_U to $\sim 3 \times 10^{-8}$ at 450 MeV.

The exclusion plot in the $\alpha'/\alpha = \epsilon^2$ *vs* M_U plane, where α' is the coupling of the U boson to electrons and α is the fine structure constant, has been finally

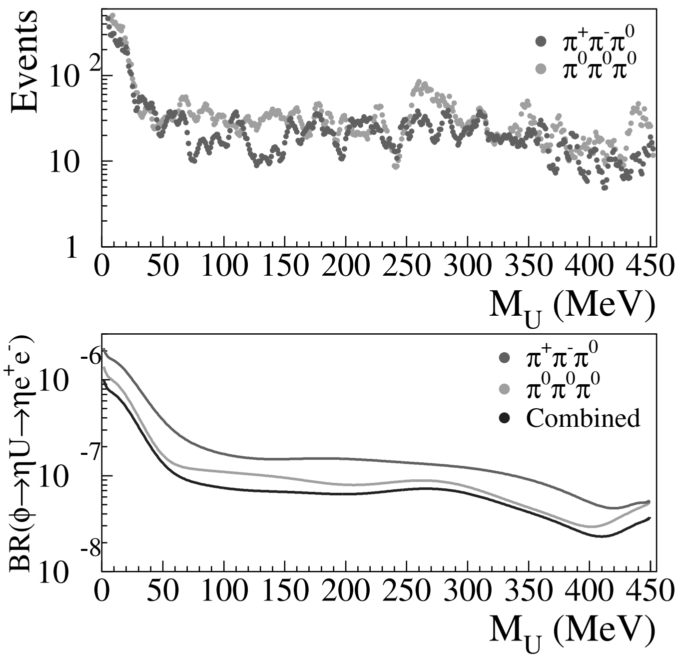

Figure 7: Top: upper limit at 90% C.L. on the number of events for the decay chain $\phi \to \eta U$, $U \to e^+e^-$, with $\eta \to \pi^0\pi^0\pi^0$ and $\eta \to \pi^+\pi^-\pi^0$. Bottom: smoothed upper limit at 90% C.L. on $\mathrm{BR}(\phi \to \eta U) \times \mathrm{BR}(U \to e^+e^-)$, obtained separately for the two η decay channels and from the combined analysis.

derived assuming the relation $^{10)}$:

$$\sigma(e^+e^- \to \phi \to \eta U) = \epsilon^2 \, |F_{\phi\eta}(m_U^2)|^2 \, \frac{\lambda^{3/2}(m_\phi^2, m_\eta^2, m_U^2)}{\lambda^{3/2}(m_\phi^2, m_\eta^2, 0)} \, \sigma(e^+e^- \to \phi \to \eta\gamma) \,, \tag{4}$$

with $\lambda(m_1^2, m_2^2, m_3^2) = [1 + m_3^2/(m_1^2 - m_2^2)]^2 - 4m_1^2 m_3^2/(m_1^2 - m_2^2)^2$. We assume that the U boson decays only to lepton pairs, with equal coupling to e^+e^- and $\mu^+\mu^-$.

The extraction of the limit on the α'/α parameter is related to the parametrization of the form factor (Eq. 4), and thus to the Λ parameter in Eq. 3.

The SND experiment measured the form factor slope, $b_{\phi\eta} = dF/dq^2|_{q^2=0} = \Lambda^{-2}$, obtaining $b_{\phi\eta} = (3.8 \pm 1.8)$ GeV^{-2} 14), with a central value different from theoretical predictions based on VMD ($b_{\phi\eta} \sim 1$ GeV^{-2}) 15), although in agreement within the error. In Fig. 8 the smoothed exclusion plot at 90% C.L. on α'/α is compared with existing limits in the same region of interest 16, 17, 18). The evaluation is done using both the experimental and the theoretical values of the form factor slope. The two resulting curves overlap at low M_{ee} values, while the limit obtained using the SND measurement gives an increasingly larger exclusion region up to ∼ 400 MeV, moving closer to the other curve at the end of the phase space.

Having the experimental value of $b_{\phi\eta}$ an uncertainty of ∼ 50%, we conservatively use the curve obtained with theoretical predictions, resulting in a limit of: $\alpha'/\alpha < 1.7 \times 10^{-5}$ for $30 < M_U < 400$ MeV, and even better for the sub-region $50 < M_U < 210$ MeV: $\alpha'/\alpha < 8.0 \times 10^{-6}$. Comparing our result with the previous KLOE measurement, reported as the dotted line in Fig. 8, we improve the upper limit of about a factor of two when using the same parametrization of the form factor. This result reduces the region of the U boson parameters that could explain the observed discrepancy between the measurement and Standard Model prediction of the muon anomalous magnetic moment, a_μ, ruling out masses in the range 60–435 MeV.

6 Acknowledgements

We warmly thank our former KLOE colleagues for the access to the data collected during the KLOE data taking campaign. We thank the DAΦNE team for their efforts in maintaining low background running conditions and their collaboration during all data taking. We want to thank our technical staff: G.F. Fortugno and F. Sborzacchi for their dedication in ensuring efficient operation of the KLOE computing facilities; M. Anelli for his continuous attention to the gas system and detector safety; A. Balla, M. Gatta, G. Corradi and G. Papalino for electronics maintenance; M. Santoni, G. Paoluzzi and R. Rosellini for general detector support; C. Piscitelli for his help during major maintenance periods. This work was supported in part by the EU Integrated Infrastructure Initiative Hadron Physics Project under contract number RII3-CT- 2004-506078; by the European Commission under the 7th Framework Programme through the 'Research Infrastructures' action of the 'Capacities' Programme, Call: FP7-

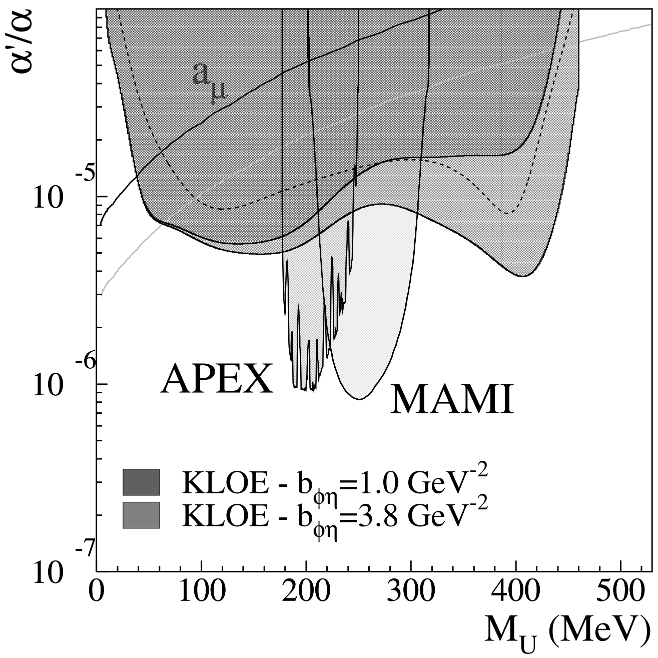

Figure 8: Exclusion plot at 90% C.L. for the parameter $\alpha'/\alpha = \epsilon^2$, compared with existing limits from the muon anomalous magnetic moment and from MAMI/A1 and APEX experiments. The gray line represents the expected values of the U boson parameters needed to explain the observed discrepancy between measured and calculated a_μ values. The dotted line is the previous KLOE result, obtained with the $\eta \to \pi^+\pi^-\pi^0$ channel only.

INFRASTRUCTURES-2008-1, Grant Agreement No. 227431; by the Polish National Science Centre through the Grants No. 0469/B/H03/2009/37, 0309/B/H03/2011/40, DEC-2011/03/N/ST2/02641,
2011/01/D/ST2/00748 and by the Foundation for Polish Science through the MPD programme and the project HOMING PLUS BIS/2011-4/3.

References

1. *An anomalous positron abundance in cosmic rays with energies 1.5–100 GeV*, O. Adriani et al., Nature 458-607 (2009);

2. *Measurement of the Cosmic Ray $e^+ + e^-$ Spectrum from 20 GeV to 1 TeV with the Fermi Large Area Telescope*, A. Abdo et al., Phys. Rev. Lett. 102, 181101 (2009);

3. *Early SPI/INTEGRAL measurements of 511 keV line emission from the 4th quadrant of the Galaxy*, P. Jean et al., Astron. Astrophys. 407, L55 (2003);

4. *Model-independent implications of the $e^{\pm}$, $\bar{p}$ cosmic ray spectra on properties of Dark Matter*, M. Cirelli et al., Nuclear Physics B 813 (2009);

5. M. Adinol et al., Nucl. Inst. and Meth. A 488, 51 (2002);

6. M. Adinolfi et al., Nucl. Inst. and Meth. A 488, 51 (2002).

7. M. Adinolfi et al., Nucl. Inst. and Meth. A 482, 364 (2002).

8. M. Adinolfi et al., Nucl. Inst. and Meth. A 492, 134 (2002).

9. F. Ambrosino et al., Nucl. Inst. and Meth. A 534, 403 (2004).

10. M. Reece, L.T. Wang, JHEP 07, 051 (2009).

11. L.G. Landsberg, Phys. Rep. 128, 301 (1985).

12. F. Archilli et al., Phys. Lett. B 706, 251 (2012).

13. T. Junk, Nucl. Instr. Meth. A 434, 435 (1999).

14. M. N. Achasov et al., Phys. Lett. B 504, 275 (2001).

15. N. N. Achasov and A. A. Kozhevnikov, Sov. J. Nucl. Phys. 55, 449 (1992).

16. H. Merkel et al., Phys. Rev. Lett. 106, 251802 (2011).

17. S. Abrahamyan et al., Phys. Rev. Lett. 107, 191804 (2011).

18. M. Pospelov, Phys. Rev. D 80, 095002 (2009).

Frascati Physics Series Vol. LVI (2012)
Dark Forces at Accelerators
October 16-19, 2012

SEARCH FOR A NEW GAUGE BOSON IN π^0 LEPTONIC DECAYS WITH WASA-AT-COSY

CARL-OSCAR GULLSTRÖM *
for the WASA-at-COSY Collaboration
Department of Physics and Astronomy Uppsala University

Abstract

The WASA-at-COSY detector has recorded a high statistic run of π^0 decays. A search for a new vector boson in the e^+e^- invariant mass spectrum of $\pi^0 \to e^+e^-\gamma$ decay has been done. No new boson has been found and an upper limit has been set in the mass range 30-100 MeV. Also a search for the rare decay $\pi^0 \to e^+e^-$ was carried out. Here 15 event candidates were found.

1 Introduction

Several astrophysical observations of positron excess 1) - 4) suggest that a new gauge boson 5) could exist in the MeV scale since no muon/pion excess has been found at the same time. Leptonic decays of π^0 are a good place to look for such a new boson since one can create e^+e^- pairs abundantly with low background and compare a well formulated theory . The energy range of

Table 1: *BR of observed π^0 decays* 6)

	BR
2γ	$(98.823 \pm 0.034)\%$
$e^+e^-\gamma$ (dalitz decay)	$(1.174 \pm 0.035)\%$
$e^+e^-e^+e^-$ (double dalitz decay)	$(3.34 \pm 0.16)10^{-5}$
e^+e^-	$(6.46 \pm 0.33)10^{-8}$

e^+e^- pairs from π^0 also covers the region where a new boson could explain the discrepancy between the standard model prediction and experimental data of the muon g-2.

2 Theory

2.1 π^0 meson

The π^0 meson is the lightest known hadron and hence it only decays via electroweak interaction. The most common decay is the decay to 2γ (see tab. 1). Other known decays proceed via one or two virtual photons to electron positron pairs. The π^0 meson is a pseduscalar and hence the decay to only one e^+e^- pair is rare since it has to go via a two photon process. More common are decays via one virtual photon i.e. $e^+e^-\gamma$.

2.2 New Boson

The large amount of virtual photons in its decays makes the π^0 a good candidate for looking for a new vector boson. In the simplest model this boson is a U(1) boson with weak coupling to the ordinary photon 5). Extensive searches have been done for this "dark photon" by many experiments and an upper limits have been set in a wide mass range. A new light dark boson is not necessarily a vector particle. Other theories use an axial vector instead. The boson would then not bee seen as a mass peak in the lepton-antilepton invariant mass but could still enhance BR if it's involved in decays of the π^0. The discrepancy between the value found by the KTeV experiment $(7.48 \pm 0.29_{stat} \pm 0.25_{syst}) \times 10^{-8}$ 7) and the SM prediction $(6.23 \pm 0.09) \times 10^{-8}$ 8) of the $\pi^0 \rightarrow e^+e^-$ BR might be due to this new boson.

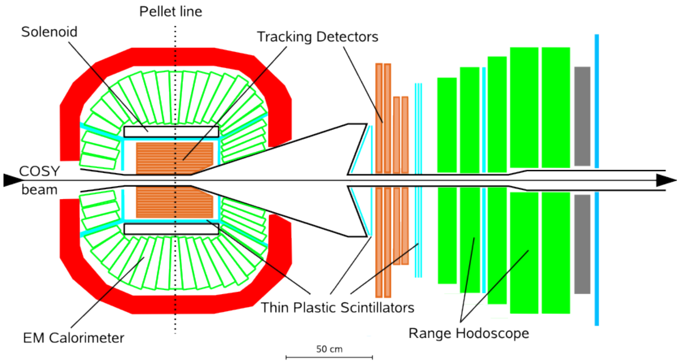

Figure 1: *Wasa-at-Cosy setup*

3 WASA-at-COSY

The WASA detector setup [9] is located at the COSY accelerator in Jülich Germany [10]. The accelerator has the possibility to accelerate protons and deuterons up to 3.7 GeV. For π^0 production the kinetic energy has been chosen to be 550 MeV. This is to maximize the production cross-section (1.12 mbarn) below the two pion threshold in pp collisions. Small pellets of frozen hydrogen serves as internal target. The advantage of pellets is to minimize external photon conversion in the target. The WASA detector consists of a forward detector (FD) for scattering products and a central detector (CD) for measurement of decays (see fig. 1). The FD measures kinetic energy in the range hodoscope, ΔE and time by plastic scintillators and angles by tracking detectors. In the CD energy are measured by the electromagnetic calorimeter, ΔE and time by plastic scintillators and the Tracking detector (MDC) measures charge, angles and momentum.

4 Results

4.1 $\pi^0 \to e^+e^-\gamma$

4.1.1 Data selection

To obtain an e^+e^- invariant mass spectrum of the $\pi^0 \to e^+e^-\gamma$ decay one could look for the $e^+e^-\gamma$ invariant mass and pp missing mass spectra respectively.

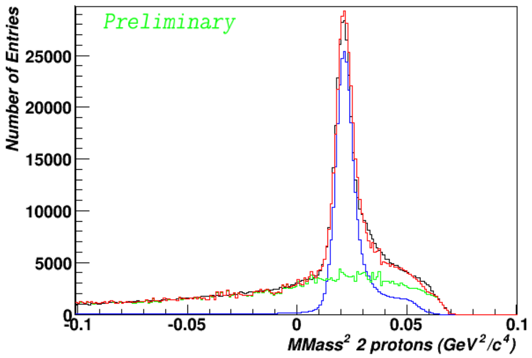

Figure 2: *Missing Mass with respect to two protons identified in the Forward Detector. Black: data, Blue: MC simulations of* $\pi^0 \to e^+e^-\gamma$*, Green MC coincidence of two elastic pp events, Red: MC sum.*

Such control samples have been selected (see fig. 2 and 3). However a larger event sample is obtained with only 1 proton in the FD, e^+e^- in the CD and no constraints on neutral tracks. The full e^+e^- mass spectrum (fig. 4) then contains $1.2 * 10^6$ $\pi^0 \to e^+e^-\gamma$ events with a background of similar size from external conversion in the decay $\pi^0 \to 2\gamma$. Background from random coincidence events with a miss identification of π^+ as e^+ is only important above 100 MeV.

The background from external conversion can be significantly reduced by the fact that almost no conversion take place in the target but most of the seen one are produced in the beryllium beam-pipe. The beam-pipe is located at a radius of 30 mm away from the target so conversion events can be suppressed by choosing tracks that intersect closer than 22 mm from the target (see fig. 5) and the e^+e^- invariant mass calculated at the beamtube should be larger than zero. The final spectrum (fig. 6) contains 500k $\pi^0 \to e^+e^-\gamma$ decays that can be used to set an upper limit for the decay $\pi^0 \to U\gamma$.

4.1.2 New boson search

The invariant mass spectrum in figure 7 does not contain any signal from a new boson and a new upper limit can bee set. The latest attempt to find the decay $\pi^0 \to \gamma U$ was done by the SINDRUM collaboration [11]. The upper

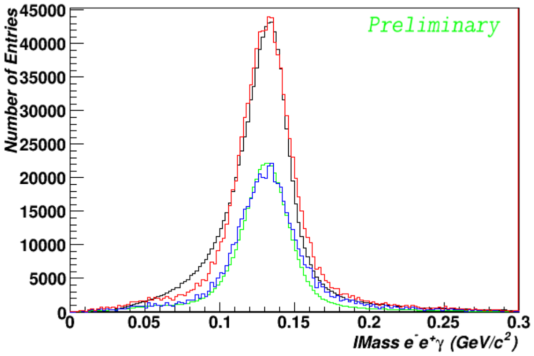

Figure 3: *Invariant Mass* γe^+e^-. *Black: data, Green: MC simulations of* $\pi^0 \to e^+e^-\gamma$, *Blue: MC pair production in* $\pi^0 \to 2\gamma$ *decay, Red: MC sum.*

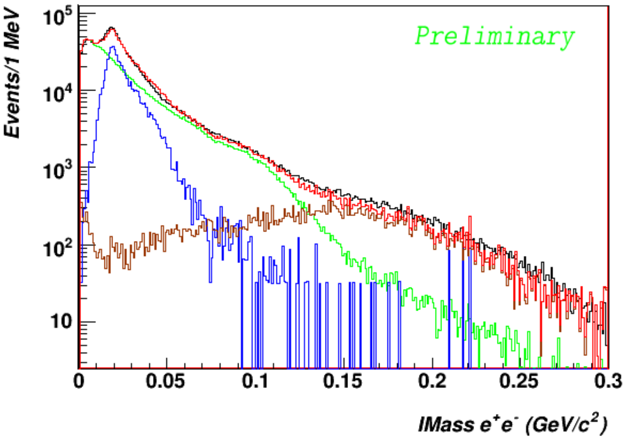

Figure 4: *Invariant Mass of* e^+e^-. *Black: data, Green: MC simulations of* $\pi^0 \to e^+e^-\gamma$, *Blue: MC pair production in* $\pi^0 \to 2\gamma$ *decay, Brown: MC Coincidence of* $\pi^0 \to e^+e^-\gamma$ *and* π^+ *decays when* π^+ *is miss identified as a positron, Red: MC sum.*

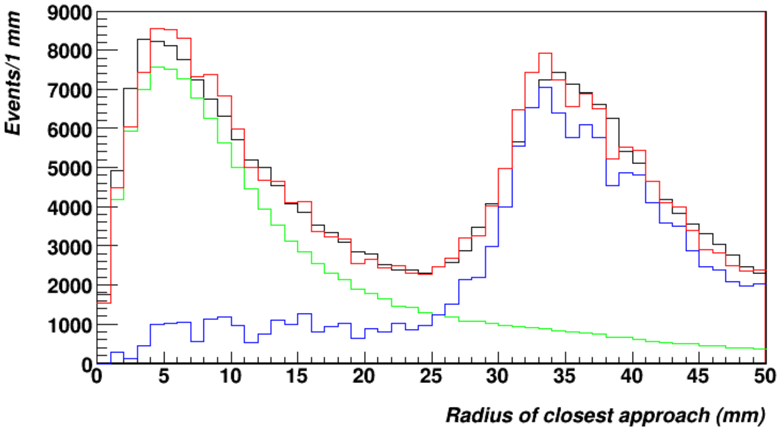

Figure 5: *Distance from target position to closest approach of an* e^+e^- *pair in MDC. Black: data, Green: MC simulation of* $\pi^0 \rightarrow e^+e^-\gamma$*, Blue: MC pair production from* $\pi^0 \rightarrow 2\gamma$ *decay, Red: MC sum.*

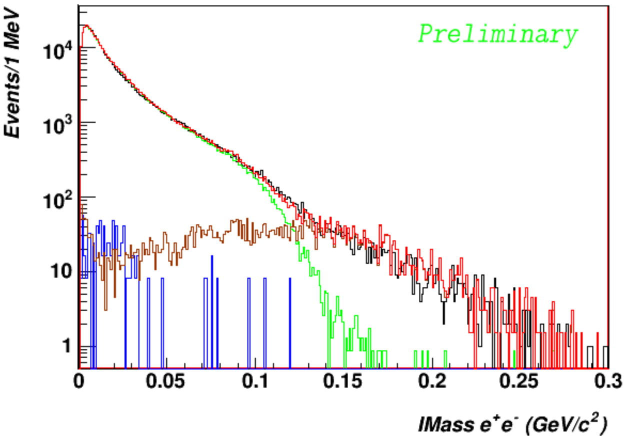

Figure 6: *Invariant Mass of* e^+e^- *after conversion reduction cuts. Black: data, Green: MC simulation of* $\pi^0 \rightarrow e^+e^-\gamma$*, Blue: MC pair production from* $\pi^0 \rightarrow 2\gamma$ *decay, Brown: MC Coincidence of* $\pi^0 \rightarrow e^+e^-\gamma$ *and* π^+ *decays when* π^+ *is misidentified as a positron, Red: MC sum.*

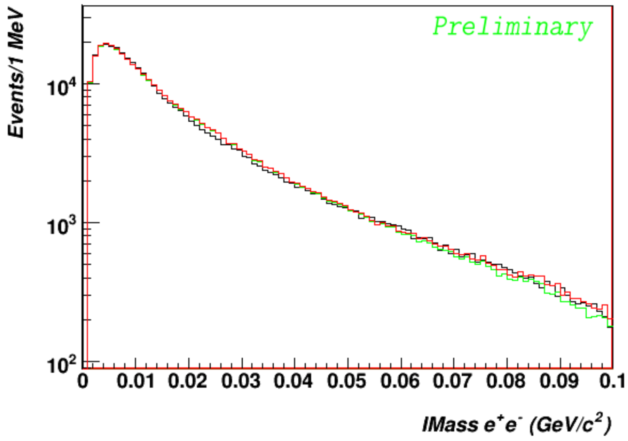

Figure 7: *Invariant Mass of* e^+e^- *after conversion reduction cuts in the range 0-100* MeV/c^2*. Black: data, Green: MC simulation of* $\pi^0 \to e^+e^-\gamma$*, Blue: MC pair production from* $\pi^0 \to 2\gamma$ *decay, Brown: MC coincidence of* $\pi^0 \to e^+e^-\gamma$ *and* π^+ *decays when* π^+ *is misidentified as a positron, Red: MC sum.*

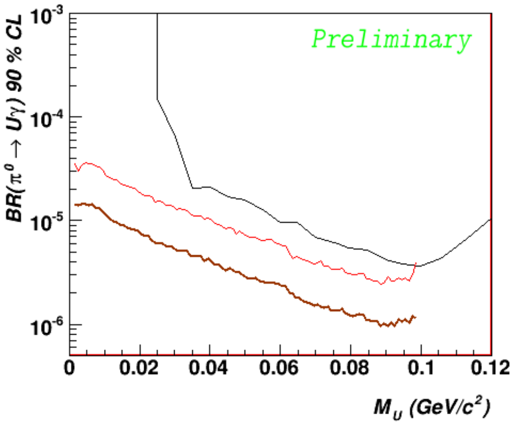

Figure 8: *U.L. for the decay* $\pi^0 \to U\gamma \to e^+e^-\gamma$*. Black: Sindrum* [11]*, Red: WASA 2010, Brown: WASA 2012 (expected).*

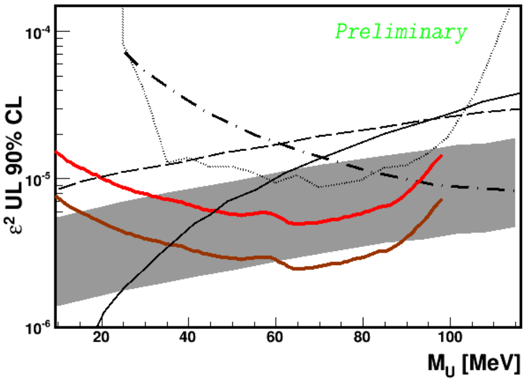

Figure 9: *U.L* ϵ^2*. Dotted: Sindrum* $^{11)}$*, Red: WASA 2010, Brown: WASA 2012 (expected) Dashed: muon g-2* $^{13)}$ *Black: electron g-2* $^{13)}$ *Dotted dashed: KLOE* $^{14)}$*. Grey region: Motivated region within* 2σ *by discrepancy between experiment and SM prediction of muon g-2* $^{13)}$*.*

limit then was based on a lower statistics sample only for events above 25 MeV/c^2. The new upper limit derived from this work is shown in figure 8. The WASA collaboration has also a larger data sample recorded in 2012 that are under investigation. Also a new upper limit expectation based on the known statistical improvement are presented in fig 8. The branching ratio $\pi^0 \to \gamma U$ is related to ϵ^2 by $^{12)}$:

$$\frac{\Gamma(\pi^0 \to \gamma U)}{\Gamma(\pi^0 \to \gamma\gamma)} = \epsilon^2 |F(M_U^2)|^2 \left(1 - \frac{M_U^2}{M^2}\right)^3 \tag{1}$$

where $|F(M_U^2)|^2$ is the Formfactor for the new boson. If one assumes the Formfactor to be 1 one get a new upper limit in the range 45-90 MeV.

4.2 $\pi^0 \to e^+e^-$

The decay $\pi^0 \to e^+e^-$ have a low BR. The cylindrical shape of the MDC gives an angular dependence of resolution. Choosing a limited part of the detector and cross check with the vertex resolution gives the desired resolution below 2.5%. The reconstruction efficiency are however the same as $\pi^0 \to e^+e^-\gamma$.

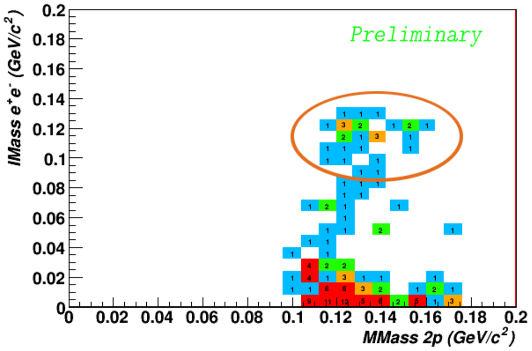

Figure 10: *Missing mass with respect to two protons in FD vs Invariant Mass of* e^+e^- *for events with no photon and high resolution.*

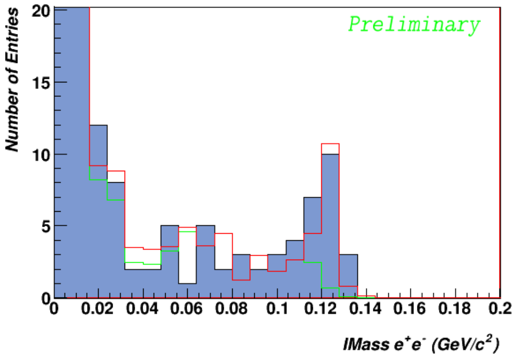

Figure 11: *Invariant Mass of* e^+e^- *after conversion reduction cuts. Blue filled: data, Green: MC simulation* $\pi^0 \to e^+e^-\gamma$*, Red: MC sum* $\pi^0 \to e^+e^-\gamma$ *and* $\pi^0 \to e^+e^-$.

This is because in $\pi^0 \to e^+e^-\gamma$ the e^+e^- lies to close to be separated from each other in a large part of phase space. The 2010 data sample contains 15 candidates. Unfortunately a to low sample to draw any conclusion so far. The sample are sensitive to calibration of the tracking device in the CD. So with the new higher statistical run from 2012 and extra effort in calibration it would be possible to find a sample in the range 75-300.

References

1. O.Adriani et al., Nature **458**, 607 (2009).
2. J.Chang et al., Nature **456**, 362 (2008).
3. F.Aharonian et al., Phys. Rev. Lett. **101**, 261104 (2008).
4. P.Jean et al., Astron. Astrophys. **407**, L55 (2003).
5. C. Boehm and P.Fayet, Nucl. Phys. B **683** (2004) 219.
6. J. Beringer et al. (Particle Data Group), Phys. Rev. **D86**, 010001 (2012).
7. E. Abouzaid *et. al*, Phys. Rev. D **75** (2007) 012004.
8. A. Dorokhov, M. A. Ivanov, Phys. Rev. D **75** (2007) 114007.
9. C. Bargholtz *et. al*, Nucl Instrum Meth A 594 (2008) 339
10. R. Maier *et. al*, Nucl Instrum Meth A 390 (1997) 1.
11. R. Meijer Drees et al. (SINDRUM 1 Collaboration), Phys.Rev.Lett. **68**(1992) 3845.
12. M. Reece and L.-T. Wang JHEP **07.051** (2009).
13. M. Endo, K. Hamaguchi, G. Mishima, Phys.Rev. **D86** (2012) 095029.
14. F. Archilli, D. Babusci, D. Badoni, I. Balwierz, G. Bencivenni, et al. Phys.Lett. **B706** (2012) 251-255

Frascati Physics Series Vol. LVI (2012)
DARK FORCES AT ACCELERATORS
October 16-19, 2012

SEARCHING FOR A LIGHT NEUTRAL AXIAL-VECTOR BOSON IN ISOSCALAR NUCLEAR TRANSITIONS

A. Krasznahorkay, J. Gulyás, M. Csatlós, A. Vitéz, T. Tornyi, L. Stuhl,
L. Csige, Z. Gácsi, A. Krasznahorkay, Jr., M. Hunyadi
Inst. for Nucl. Res., Hung. Acad. of Sci. (MTA Atomki),
H-4001 Debrecen, P.O. Box. 51 Hungary
T.J. Ketel
Department of Physics and Astronomy, VU University,
Amsterdam, The Netherlands

Abstract

The electron-positron angular correlations within the pairs created in the decay of the 17.6-MeV ($J^\pi = 1^+$, $T = 1$) and the 18.12-MeV ($J^\pi = 1^+$, $T = 0$) *isovector and isoscalar magnetic dipole* transitions in ^{8}Be were measured. A sharp maximum was found at large angles in the isoscalar transition(s), which indicates that, in an intermediate step, a neutral isoscalar particle with a mass of 13.45(30) MeV/c^2 and $J^\pi = 1^+$ was created with a confidence level of 3σ. This particle may be identified with U, the supersymmetrical gauge boson, and may be related to dark-matter particles in the **u**niverse.

1 Introduction

In a recent series of papers the intriguing possibility was explored that the cosmic dark matter consists of new elementary particles with masses in the MeV range, which could be searched for in nuclear physics laboratories. Such particles are not excluded by any obvious laboratory measurements or astrophysical arguments. There are even some experimental indications for a light neutral boson with a mass of around 9 MeV/c^2.

The signature of the new particle is the very characteristic angular correlation of the e$^+$e$^-$ pairs from their decay. Quantum electrodynamics (QED) predicts 1, 2) that the angular correlation between the e^+ and e^- emitted in the internal pair creation (IPC) drops rapidly with the separation angle θ. In striking contrast, when the transition takes place by emission of a short-lived ($\tau < 10^{-13}$ s) neutral particle annihilating into an e^+e^- pair, the angular correlation becomes sharply peaked at larger angles. In the center-of-mass system this emission takes place back to back at 180°. In the laboratory system the angle is smaller due to the Lorentz boost.

A light and weakly coupled neutral spin-1 gauge boson U was predicted by Fayet 3) and revisited by Boehm and Fayet 4). It was argued by Boehm *et al.* 5), by Fayet 6) and Beacom 7) that light dark-matter particles decaying through such bosons into e^+e^- pairs may be the source of the observed 511-keV emission line in the galactic bulge 8). In a renormalizable theory, some particle must mediate $\chi\ \bar{\chi} \rightarrow e^+e^-$ annihilation. The simplest possibility is to introduce a light, spin-1 boson, coupling to both e^+e^- and $\chi\bar{\chi}$ states. In a recent paper the mass of such a dark matter candidate was estimated to be m$_e$ $\leq$m$_\chi$ $\leq$ 20 MeV/c^2 9).

In 1988 de Boer and van Dantzig 10) analysed emulsion data obtained from relativistic heavy ion reactions in which e^+e^- pairs were observed at short but non-zero distances from the interaction vertices. These events were attributed to the emission and subsequent decay of a light neutral boson with a mass of around 9 MeV/c^2 and lifetime of about 10^{-15} s. These parameters fall within the allowed mass–lifetime window: 5 MeV/$c^2 \leq m_X \leq$20 MeV/c^2, 10^{-16} s $\leq \tau \leq 10^{-13}$ s 11). This finding motivated a systematic search for anomalous IPC in transitions between the levels of ^{8}Be and ^{12}C 14). The e^+e^- pair decay from ^{8}Be*(17.6, 18.15) $J^\pi = 1^+$ and the ^{12}C*(17.2) $J^\pi = 1^-$ levels was measured. Whereas for the E1 decay (^{12}C) at large correlation angles no deviation is found from internal pair conversion (IPC), surprisingly the M1 angular correlation deviated from IPC at the 4.5σ level. While an anomaly is seen in the pair production, the overall results are not consistent with the involvement of a neutral boson [12, 13, 14]. A limit of $\leq 4.1\times10^{-4}$ was obtained for the boson to γ-ray branching ratio [12, 13, 14, 15].

The aim of the present work is to re-evaluate the anomaly that de Boer et al. observed in pair production and to search for signatures of the assumed boson.

2 Experiments

To populate the 17.6, and 18.12 MeV 1^+ states in ^{8}Be strongly and selectively, we used the ^{7}Li(p,γ)^{8}Be reaction at E_p=0.44, and 1.03 MeV [15], and detected the angular correlation of the the e^+e^- pairs. The experiments were performed at the 5-MV Van de Graaff accelerator of ATOMKI with a typical beam current of 1.0 μA. LiF$_2$ and LiO$_2$ of about 1-mg/cm^2 targets were used on a thin 40-μg/cm^2 C backing.

The e^+e^- pairs were detected by five plastic ΔE–E detector telescopes similar to those built by Stiebing *et al.* [16], but we used larger telescope detectors in combination with position sensitive detectors to increase the coincidence efficiency by about a factor of 600. ΔE detectors of $38\times45\times1$ mm^3 and the E detectors of $78\times60\times70$ mm^3 were used perpendicular to the beam direction and at azimuthal angles of 0°, 60°, 120°, 180° and 270° around the beam pipe. These angles were chosen to obtain a homogeneous acceptance as a function of the correlation angle of the e^+e^- pairs. The positions of the hits were registered by a multiwire proportional counters (MWPC) [17] inserted between the ΔE and E detectors. The anode plane of the MWPC was a set of parallel 10-μm thick gold-plated tungsten wires put equidistantly by 2 mm. There were two cathode planes spanned by 0.1-mm thick silver-plated copper wires separated by 1.27 mm. The two cathode planes, with wirings perpendicular to each other to detect the x and y coordinates, flanked the anode plane at distances of 7 mm. Delay-line read-out (2 ns/taps) was used for the signal (cathode) wires. Ar(50%)+C$_2$H$_6$(50%) counting gas was flowing across the detector volume at an atmospheric pressure. The accuracy of the (x, y) coordinates implies an angular resolution of FWHM$\leq$2° in θ in the 70°–110° angular range. The angular resolution of the set-up is increased by multiple scattering of low energy electrons in the wall of the vacuum chamber and in the plastic ΔE detectors.

The target was tilted by 45° with respect to the beam direction. The telescope detectors were placed around the vacuum chamber made of a carbon fiber tube 16). Apart from e^+e^- pairs, also γ rays were detected. A Ge clover detector with active volume of about 470 cm^3 and equipped with a BGO anti-coincidence shield 18) was put perpendicular to the beam and at a distance of 25 cm from the target.

The electron energy calibration was made with respect to e^+e^- pairs of the 6.05-MeV transition in ^{16}O, and of the 4.44-MeV and 15.11-MeV transitions in ^{12}C excited in the ^{11}B(p,γ)^{12}C reaction with the same setup.

3 Experimental results

Figure 1 shows γ-ray spectra measured at proton absorption resonances at E$_p$=0.441 MeV and 1.03 MeV.

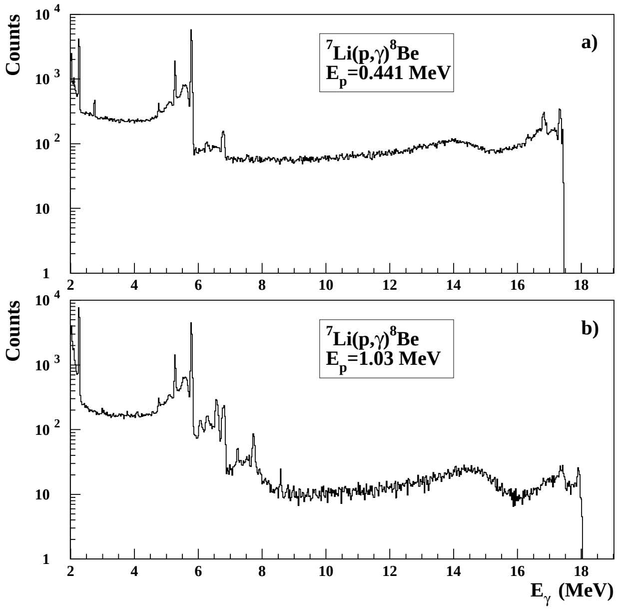

Figure 1: *γ-ray spectra measured at E_p= 0.441 MeV (a) and E_p=1.03 MeV (b).*

The 17.6 ($1^+ \rightarrow 0^+$) and 18.12 ($1^+ \rightarrow 0^+$) MeV photopeaks and their single escape peaks are clearly visible. The double escape peaks are suppressed by the anti-compton shield. The broad peaks at 14-15 MeV correspond to transitions to the first excited 2^+ level at $E_x = 3.0$ MeV, which has a width of $\Gamma = 1.5$ MeV $^{15)}$. This broad peak is more prominent with the 18.1 MeV excitation at E_p=1.03 MeV. The branching ratios of γ-transition to the ground state and to the 2^+ are, respectively, about 30% and 70% for the 18.15 MeV 1^+ state and 70% and 30% for the 17.6 MeV 1^+ state $^{15)}$.

Figure 2 shows the total energy spectra of e^+e^- pairs measured at the proton absorption resonances at E_p=0.441 MeV and 1.03 MeV.

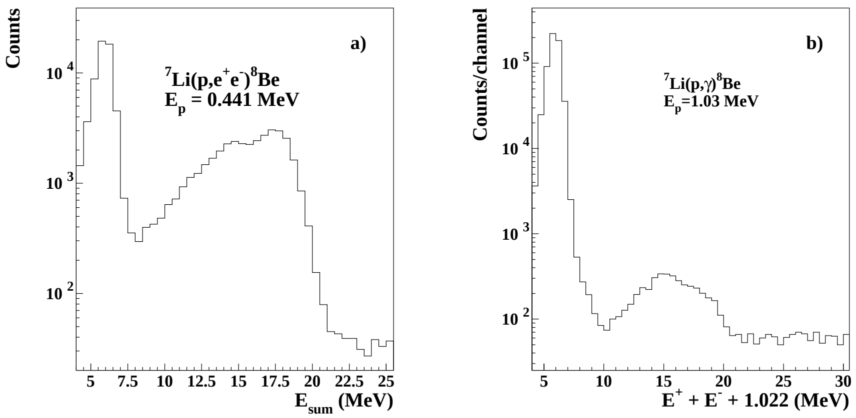

Figure 2: *Total energy spectra of e^+e^- pairs measured at E_p= 0.441 MeV (a) and E_p=1.03 MeV using LiF_2 targets.*

The spectra, especially measured at E_p=1.03 MeV, are dominated by a strong 6.05-MeV peak from the $^{19}F(p,\alpha)^{16}O$ reaction followed by the 100% IPC transition ($0^+ \rightarrow 0^+$, E0). Later on we prepared LiO_2 target with only a thin layer of LiF_2 cover to keep the 6.05-MeV peak at reduced counting rate for energy calibration and for efficiency monitoring of the detector system.

The γ-ray background in the E detectors originating from the target is suppressed by a factor of about 10^{-4} by requiring ΔE–E coincidences in addition to the coincidence between the two telescopes.

The efficiency calibration of the telescopes was made by using the same dataset but with uncorrelated e^+e^- pairs coming from different events. In order to check the calibration, the IPC line of the 6.05-MeV transition in ^{16}O, which is a pure E0 transition, was investigated in the ^{19}F(p,α)^{16}O reaction, and compared to the results of the simulation in Fig. 3.

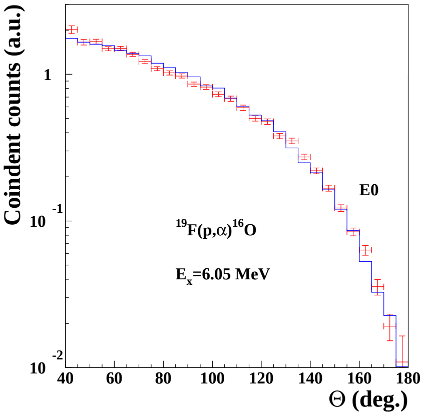

Figure 3: *Measured angular correlation of the* e^+e^- *pairs originated from the 6.05 MeV* $0^+ \rightarrow 0^+$ *E0 transition excited in* ^{16}O *by the* $^{19}F(p,\alpha)$ *reaction (red) compared to the simulated one (blue).*

4 Monte-Carlo simulations

In order to investigate deviations from normal internal pair conversion, a thorough understanding of the spectrometer and the detector response are needed. Besides the IPC process, the background of γ-radiation, external pair creation (EPC) and multiple lepton scattering were considered in extended simulations and calibration procedures.

Extensive Monte Carlo (MC) simulations of the experiment were performed using the GEANT3 code with target chamber, target backing, windows, detector geometries included, in order to model the detector response for e^+e^- pairs and also for γ-rays. In this way the scattering of e^+e^- pairs and the effects of the external pair creation in the surrounding materials could also be investigated. The event files created by the simulation were analysed with the same codes as the experimental data. The efficiency of the setup was calculated from single electron measurements and the results of the simulations was always normalized to that efficiency curve. Very nice agreement has been obtained between the experimental data and the simulations as shown in Fig. 3, indicating our understanding of the set-up.

The instantaneous e^+e^- decay of a hypothetical boson emitted isotropically from the target has also been simulated together with the normal IPC emission of e^+e^- pairs. Figure 4 shows the results of these simulations for the 17.6 MeV M1 transition.

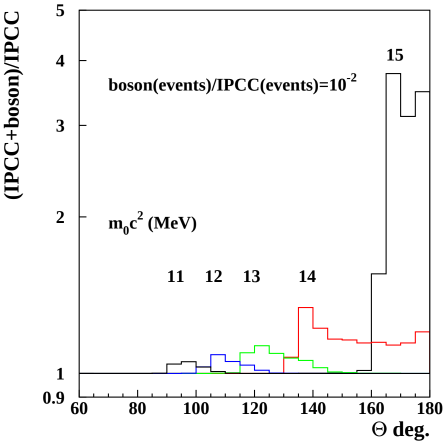

Figure 4: *Simulated angular correlations of IPC and of 1% boson decay* e^+e^- *pairs for boson masses indicated with the different curves.*

The numbers of simulated events are 10^8 for IPC and 10^6 for the decay of the boson. Even for this (very) small branching ratio the effect of the boson is clearly seen, as the IPC correlation drops (very) fast with angle. In this way the method is very sensitive to any boson contribution. The sensitivity is the largest if the mass of the boson is close to the energy of the transition.

5 Experimental results for the angular correlations

The results obtained for the e^+e^- angular correlation at the E$_p$= 0.441 MeV resonance for the total energy range including the broad resonance at 14 MeV and the 17.6 MeV (both 14.7 and 17.6 MeV M1 transitions in ^{8}Be) is shown in Fig. 5a together with the simulated distribution for M1 IPC. One can observe relative excess intensities compared to the simulations at large angles above 110° as it was also mentioned by de Boer et al. [14].

In Fig. 5b the excess is even larger for the transitions deexciting the E$_p$= 1.03 MeV resonance. This resonance at 18.1 MeV is much broader, Γ= 138 keV [15], than the one at 17.6 MeV, Γ= 10.7 keV and its strength is more distributed.

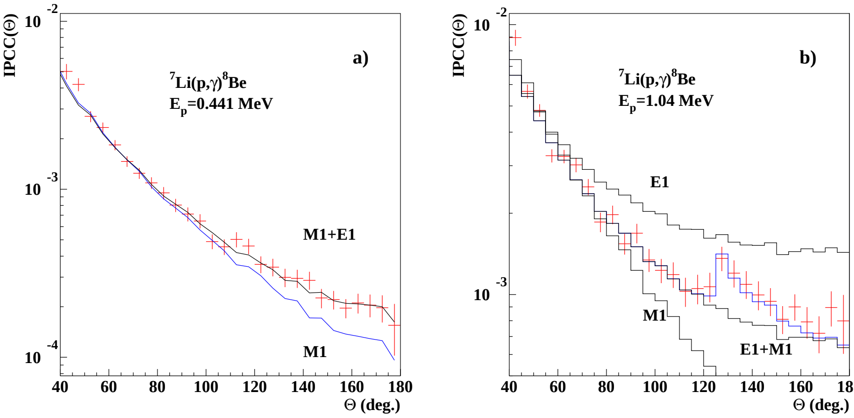

Figure 5: *Measured angular correlation of the* e^+e^- *pairs originated from the decay of the 17.6 MeV resonance (a) and from the 18.15 MeV resonance (b) (red dots with error bars) compared with the simulated ones assuming pure M1 and E1 transitions and M1+E1 mixed transitions. The contribution of a 13.5 MeV boson is shown in blue.*

De Boer et al. [12, 13, 14] assumed always pure M1 transitions from the decay of the 17.6 and 18.15 MeV resonances. It is fine for the resonances itself, but not for the underlying direct background, which is reasonably small (but not negligible) for the 17.6 MeV resonance, but much larger for the 18.15 MeV one. The background originates from the direct (non-resonant) proton capture and its multipolarity is (mostly) E1. It is mainly due to the low-energy tail of the giant dipole resonance 19) and it adds to the M1 decay of the resonances. The contribution of the direct capture depends on the target thickness, if the energy loss in the target is larger than the width of the resonant state. It is especially the case for the 17.6 MeV state.

As shown in Fig. 5 b), the slope of the E1 angular correlation is much smaller compared to the slope of the M1 one, so by mixing in even a small amount of E1 radiation the angular correlation at large angles can be modified considerably. The black simulated curve in Fig.5 a) is calculated by assuming a small (≈5%) E1 contribution to the dominantly M1 one, which explains well the experimental data.

The situation is more complicated in case of the 18.15 MeV resonance. The black (M1+E1) curve in Fig. 5 b) describes the experimental data only up to $\approx 120^\circ$. The deviations at larger angles might be explained by creation and subsequent decay of a new particle, introduced in Ref. 10). The blue curve in Fig. 5 b), which fits the data well, is calculated by assuming the contribution of a boson as well to the IPC process with 13.5 MeV energy and with a branching ration of 3.0×10^{-5} compared to the γ-decay.

The results of the full χ^2 analysis as a function of the mass of the assumed particle is shown in Fig. 6. The experimental results can be explained best if the mass of the particle is 13.45 ± 0.30 MeV/c^2.

6 Conclusion

We have measured the differential internal pair creation coefficients for the the M1 transitions depopulating the 17.6 and 18.12 MeV states in ^{8}Be. Similar deviations were observed at large opening angles, especially in case of the 18.12 case like de Boer 14) did.

The deviations could mostly be explained by the contribution of the direct proton capture which creates mostly E1 transitions. As the angular dependence of the IPC process for E1 transition is much less, compared to the M1 transition, a small mixing of E1 radiation can modify the the IPCC drastically at large angles.

Taking into account the E1 mixing properly, the IPCC of the 17.6 MeV

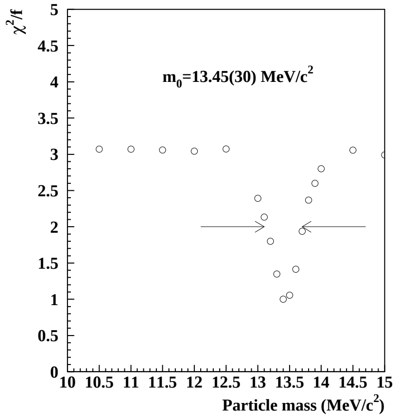

Figure 6: *Determination of the mass of the new particle by the* χ^2/f *method, by comparing the experimental data with the results of the simulations obtained for different masses.*

transition could be well explained. However, it was not the case for the 18.12 MeV transition. The deviation between the experimental and theoretical IPC shows peak like structures in that case, which can be explained only by assuming the creation and decay of a 13.45(30) MeV boson. The branching ratio of the boson creation compared to the γ-decay should be about 3.0×10^{-5} to explain the deviations. Such branching ratio is about 10 times smaller than de Boer 14) published earlier. The detailed χ^2/f analysis showed a 3σ confidence for the new particles. More precise (at least 3 times more statistics) experimental data is needed to clarify the existence of such assumed particles.

7 Outlook

The recent challenges created by astrophysical observations and theoretical predictions for the existence of a low-mass neutral particle motivated us to search for such particles in nuclear transitions. It turned out, however, that presently no spectrometer exists which could be used for serious searches. That is the reason why we started to build a compact positron-electron spectrometer (COPE), by using EU FP7 ENSAR supports, for studying the internal pair creation process of high energy nuclear transitions precisely.

The electrons and positrons will be bent in a toroidal magnetic field created by strong ($Nb_2Fe_{14}B$) permanent magnets and their bending radius will be measured by special time projection chambers like at the ATLAS Experiment at the CERN Large Hadron Collider, but at a 100 times smaller scale.

The energy and angular resolution of such spectrometer is expected to be much better than the present one, which would allows us to make our search more sensitive in the close future.

8 Acknowledgements

The authors are grateful to Fokke de Boer for suggesting the above studies and motivating us to improve the quality of the experimental data. Unfortunately, he left us before obtaining the present results. We regret the loss of our fine colleague. This work has been supported by the Hungarian OTKA Foundation No. K106035, and by the European Community FP7 - Contract ENSAR n° 262010.

References

1. M.E. Rose, Phys. Rev. **76**, 678 (1949).
2. P. Schlter, G. Soff, W. Greiner, Phys. Rep. 75 (1981) 327.
3. P. Fayet, Nucl. Phys. B **187**, 184 (1981).
4. C. Boehm and P. Fayet, Nucl. Phys. B **683**, 219 (2004).
5. C. Boehm *et al.*, Phys. Rev. Lett. **92**, 101301 (2004); Phys. Rev. D **69**, 101302 (2004).
6. P. Fayet, Phys. Rev. D **70**, 023514 (2004).
7. J.P. Beacom *et al.*, astro-ph/0409405, (2004).
8. J. Knodlseder *et al.* astro.-ph/0309442 (to be published); P Jean *et al.* Astron. Astrophys. **407** L55 (2003).
9. N. Borodatchenkova, D. Chouudrhurly and M. Drees, Phys.Rev.Lett. **96** 141802 (2006).

10. F.W.N. de Boer and R. van Dantzig, Phys. Rev. Lett. **61**, 1274 (1988).
11. A. Bross et al., Phys. Rev. Lett. **67**, 2942 (1991).
12. F.W.N. de Boer *et al.*, Phy. Lett. B **388**, 235 (1996)0.
13. F.W.N. de Boer *et al.* J. Phys. G **23**, L85 (1997).
14. F.W.N. de Boer *et al.* J. Phys. G **27** L29 (2001).
15. D.R. Tilley et al., Nucl. Phys. A745 (2004) 155.
16. K.E. Stiebing *et al.*, J. Phys. G **30**, 165 (2004).
17. G. Charpak, F. Sauli, Nucl. Instr. and Meth. **162**, 405 (1979).
18. Z. Elekes *et al.*, Nucl. Instr. and Meth. **503**, 580 (2003).
19. G.A. Fisher et al., Phys. Rev. **C14** (1976) 28.

Frascati Physics Series Vol. LVI (2012)
DARK FORCES AT ACCELERATORS
October 16-19, 2012

SEARCHES FOR DARK PHOTONS AT BABAR

Elisa Guido (on behalf of the *BABAR* Collaboration)
Istituto Nazionale di Fisica Nucleare - Sezione di Genova

Abstract

We present the results of several searches for a narrow resonance, that can be reinterpreted as a dark photon, produced in e^+e^- collisions and decaying into leptons, hadrons, or invisible final states.

1 Introduction

Although the existence of the dark matter is attested by several astrophysical observations, its nature and origin are still not understood. Terrestrial and satellite experiments have recently obtained results motivating the proposal of a hidden gauge sector. This new sector introduces charged WIMP-like dark matter particles 1, 2, 3) with a mass at the TeV scale, and an additional massive photon-like vector - the dark photon A' - responsible for the coupling between this dark sector and the Standard Model (SM), through a kinetic mixing with the SM hypercharge fields [4], in the form $\Delta\mathcal{L}_{mix} = \epsilon F^{\mu\nu} B_{\mu\nu}$, where ϵ represents the mixing angle. The dark photon acquires a charge $e\epsilon$, and, assuming that no light dark fermions exist, it has to decay back to SM particles. The coupling of A' to SM fermions is described by $\alpha' = \epsilon^2\alpha$, and its lifetime is usually small enough so that its decay is prompt. Depending on A' mass, different decays are dominant, either to leptonic or to hadronic final states.

In such a scenario, dark matter particles could annihilate into pairs of dark photons, subsequently decaying to SM fermions. Several astrophysical constraints [5, 6] allows for a small mixing angle between dark sector and SM, thus restricting the possible A' mass to the region of hundreds of MeV to a few GeV.

In a minimal model [7], a dark Higgs boson (h') can also exist, being responsible for the generation of the mass of the dark photon. The mass hierarchy of the two particles is actually not constrained, and the dark Higgs boson could be light as well.

No conclusive proof of the existence of dark forces may come from indirect astrophysical signatures, and only reproducible terrestrial experiments might prove the existence of the dark sector. Actually, these new MeV-GeV scale forces would provide a number of possible new phenomena: high-lepton multiplicity events at the B-factories, high-lepton multiplicity decays of heavy flavors, and even lepton jets at the hadron colliders. In particular, the B-factories, being low-energy and high-luminosity e^+e^- colliders, offer a low background environment for searching for hidden sector signatures at the MeV-GeV scale.

2 Potentialities in searches for the dark sector at $\mathrm{e^+e^-}$ colliders.

At low energy $\mathrm{e^+e^-}$ colliders several searches for the dark sector are possible:

- searches for a dark photon in events of the type $e^+e^- \to \gamma A'$, with $A' \to e^+e^-$, $\mu^+\mu^-$ or $\pi^+\pi^-$;
- searches for a dark photon in meson decays: $\pi^0 \to \gamma l^+l^-$, $\eta \to \gamma l^+l^-$, $\phi \to \gamma l^+l^-$, etc.;
- searches for dark bosons in events of the type $e^+e^- \to A'^* \to W'W'$, or $e^+e^- \to \gamma A'^* \to W'W''$;

- searches for a dark scalar (s) or a dark pseudoscalar (a) in events of the type $B \to K^{(*)}s \to K^{(*)}l^+l^-$, $B \to K^{(*)}a \to K^{(*)}l^+l^-$, $B \to ss \to 2(l^+l^-)$, $B \to 4(l^+l^-)$;
- searches for a dark Higgs boson in events of the type $e^+e^- \to h'A'$, with $h' \to A'A'$;
- searches for an invisible dark photon in events of the type $e^+e^- \to \gamma A'$, with $A' \to$ invisible final states;
- searches for dark hadrons, such as a dark pion π_D, in events of the type $e^+e^- \to \pi_D X$, with $\pi_D \to e^+e^-$, $\mu^+\mu^-$, and X representing any charged state.

At *BABAR* some of these searches have been already performed 9, 10), or are under study. In this paper, we focus on the *BABAR* searches for a dark photon.

3 *BABAR* searches for a dark photon

The *BABAR* detector is described in detail elsewhere 11). It collected data mostly at the $\Upsilon(4S)$ resonance, but also at the $\Upsilon(3S)$ and $\Upsilon(2S)$ peaks, as well as off-resonance data. The total integrated luminosity available is of ~ 521 fb^{-1}, of which ~ 28 fb^{-1} (~ 14 fb^{-1}) were collected at the $\Upsilon(3S)$ ($\Upsilon(2S)$). This large data sample allows for several searches in the dark sector.

The *BABAR* experiment has performed several searches for a possible light pseudoscalar Higgs boson (A^0), which is introduced in the Next to Minimal Supersymmetric SM 12). The reinterpretation of these analyses in terms of dark photon searches is feasible, taking into account a caveat: A^0 is a pseudoscalar, while A' is a vector, therefore any limit should be affected by a change in the efficiency. Despite this, all the searches presented here give a good estimate for the order of magnitude of the corresponding limit in the dark photon search.

3.1 $\Upsilon(3S, 2S) \to \gamma A^0$, $A^0 \to \mu^+\mu^-$

In this search 13), we select events with exactly two oppositely-charged tracks and a single energetic photon with a center-of-mass (CM) energy $E^*_\gamma \geq 0.2$

GeV. At least one of the tracks has to be identified as a muon, and the dimuon candidate and the photon have to be back-to-back in the CM frame. Backgrounds are dominated by QED processes, in the form of "continuum" events $e^+e^- \to \gamma\mu^+\mu^-$, and initial state radiation (ISR) production of light mesons (ρ^0, ϕ, J/ψ, $\Psi(2S)$ and $\Upsilon(1S)$). The signal yield is searched as a function of the A^0 mass in the interval $(0.212-9.3)$ GeV, with a set of unbinned maximum likelihood fits to the reduced mass distribution, defined as: $m_R = \sqrt{m^2_{\mu\mu} - 4m^2_\mu}$. The reduced mass spectra for data at the $\Upsilon(2S)$ and at the $\Upsilon(3S)$ are shown in Fig. 1 a) and b), respectively. The scan is performed in steps of 2-5 MeV, for a total of 1951 mass values, while excluding regions in the vicinity of the J/ψ and $\Psi(2S)$ resonances. The typical signal resolution is of 2-10 MeV, increasing with mass. No significant excess of events is observed above the background in the entire mass range. Bayesian upper limits (ULs) at the 90% of confidence level (CL) are set on the product of branching fractions (BFs) of the decay $(\mathcal{B}(\Upsilon(nS) \to \gamma A^0) \times \mathcal{B}(A^0 \to \mu^+\mu^-) = \mathcal{B}(\Upsilon(nS) \to \gamma A^0) \times B_{\mu\mu})$, in the range $(0.3 - 8.3) \times 10^{-6}$, as shown in Fig. 2. Also, a combined UL on the quantity $f^2_\Upsilon B_{\mu\mu}$ is given, with f_Υ representing the effective coupling of A^0 to the b-quark.

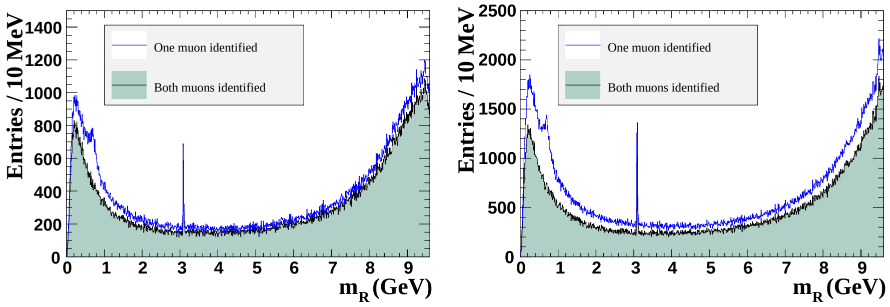

Figure 1: Distribution of the reduced mass m_R in *a)* the $\Upsilon(2S)$ data and *b)* the $\Upsilon(3S)$ data. Open (filled) histograms show the distributions for the selection in which one of (both) the tracks are positively identified as a muon. The ISR-produced J/ψ and $\Upsilon(1S)$ resonances are visible [13].

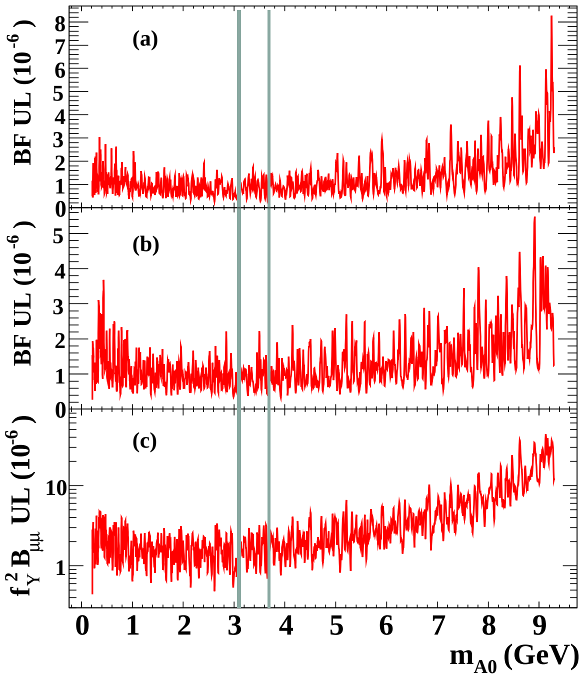

Figure 2: 90% CL ULs on (a) $\mathcal{B}(\Upsilon(2S) \to \gamma A^0) \times B_{\mu\mu}$, (b) $\mathcal{B}(\Upsilon(3S) \to \gamma A^0) \times B_{\mu\mu}$, and (c) effective coupling $f^2_\Upsilon B_{\mu\mu}$, as a function of A^0 mass. The shaded grey vertical areas are the excluded regions around the J/ψ and $\psi(2S)$ resonances [13].

3.2 $\Upsilon(3S) \to \gamma A^0$, $A^0 \to \tau^+\tau^-$

In this search [14], we select events with exactly two oppositely-charged tracks and a single energetic photon with CM energy $E^*_\gamma \geq 0.1$ GeV. Both the τ leptons are required to decay leptonically, either $\tau \to e\nu_e\bar{\nu_\tau}$ or $\tau \to \mu\nu_\mu\bar{\nu_\tau}$, thus leading to three possible final states. Backgrounds are dominated by $e^+e^- \to \gamma\tau^+\tau^-$ events, and other higher-order QED processes, as well as by $\Upsilon(3S)$ decays and $e^+e^- \to q\bar{q}$ events. Any signal peak in the recoil mass ($m_{\tau\tau}$) would translate to a peak in the photon energy distribution. The signal is actually searched for as an excess in a narrow region of the E_γ spectrum. The photon energy spectra of the three different final states are shown in Fig. 3. The range analyzed corresponds to $4.03 < m_{\tau\tau} < 10.10$ GeV, excluding the region of the decays $\Upsilon(3S) \to \gamma\chi_{bJ}(2P)$, $\chi_{bJ}(2P) \to \gamma\Upsilon(1S)$, where $J = 0, 1, 2$, due to the irreducible photon backgrounds. No evidence for a narrow resonance is found in all the mass range, and 90% CL ULs on the product of BFs of the decay $(\mathcal{B}(\Upsilon(nS) \to \gamma A^0) \times \mathcal{B}(A^0 \to \tau^+\tau^-))$ are set in the range $(1.5 - 16) \times 10^{-6}$, as shown in Fig. 4.

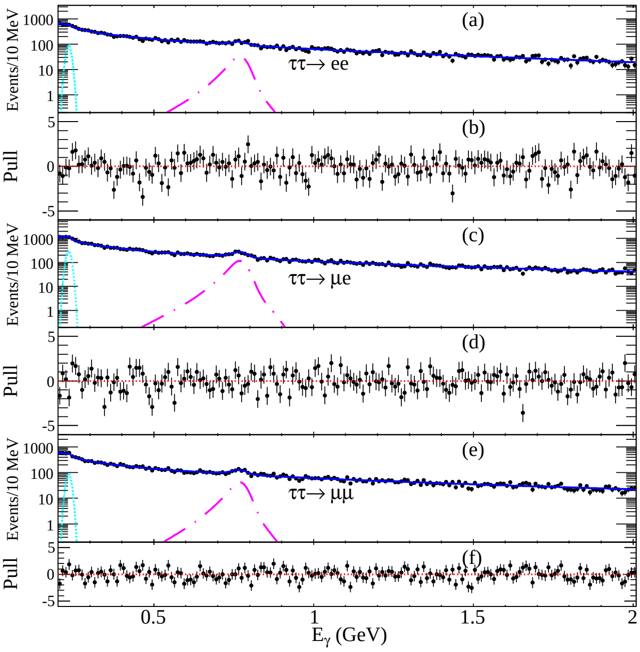

Figure 3: Distribution of the photon energy, E_γ, for each $\tau\tau$-decay modes. Filled circles are data, dotted and dotted-dashed lines represents peaking background contributions, while solid blue lines are the total background functions. Under each plot, the corresponding pull distribution is shown (14).

3.3 $\Upsilon(3S, 2S) \to \gamma A^0$, $A^0 \to$ hadrons

This search (15) looks for hadronic events with the full event energy reconstructed, with at least two charged tracks, and the radiative photon from the $\Upsilon(3S)$ ($\Upsilon(2S)$) with CM energy $E^*_\gamma \geq 2.2(2.5)$ GeV. Background events arise

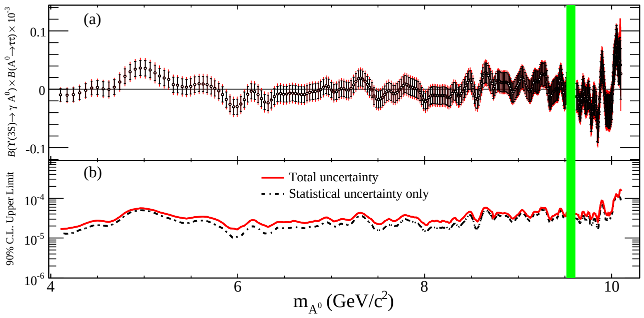

Figure 4: (a) Product BFs and (b) 90% CL ULs on the product of BFs, as a function of A^0 mass. The green vertical region is the excluded range corresponding to the $\chi_{bJ} \to \gamma\Upsilon(1S)$ states [14].

from radiative Bhabha events ($e^+e^- \to \gamma e^+e^-$) or radiative production of muon pairs ($e^+e^- \to \gamma\mu^+\mu^-$), as well as by a light vector meson or a non-resonant hadron, either produced in ISR events or via an $\Upsilon(nS)$ decay. The analysis is performed both in the hypothesis of a CP-odd A^0, and without any specific requirement on the CP values ("CP-all"). A signal would show up as a narrow peak in the candidate mass spectrum, which is analyzed in the range ($2m_\pi$-7 GeV). The candidate mass spectra, before and after the "continuum" background subtraction, are shown in Fig. 5. The signal presence is evaluated in 1 MeV steps, for a total of $\sim$ 6700 mass hypotheses. Being in the absence of a significant signal, 90 % CL ULs on the product of BFs of the decay ($\mathcal{B}(\Upsilon(nS) \to \gamma A^0) \times \mathcal{B}(A^0 \to \text{hadrons})$) are set in the range $(1-80) \times 10^{-6}$, as shown in Fig. 6.

3.4 $\Upsilon(3S) \to \gamma A^0$, $A^0 \to$ invisible final state

The light Higgs boson A^0 could have an invisible decay of the type $A^0 \to \chi^0\bar{\chi}^0$, where χ^0 is the lightest supersymmetric particle, if $m(A^0) > 2m(\chi^0)$. Also the dark photon can decay invisibly in several scenarios, such as light dark matter [16].

For this search [17], we select events with a single energetic photon: two regions are defined, high- and low-energy, with the requirement $E^*_\gamma \geq$ 3.0 GeV and $\geq$ 1.5 GeV, respectively. No tracks originating from the e^+e^-

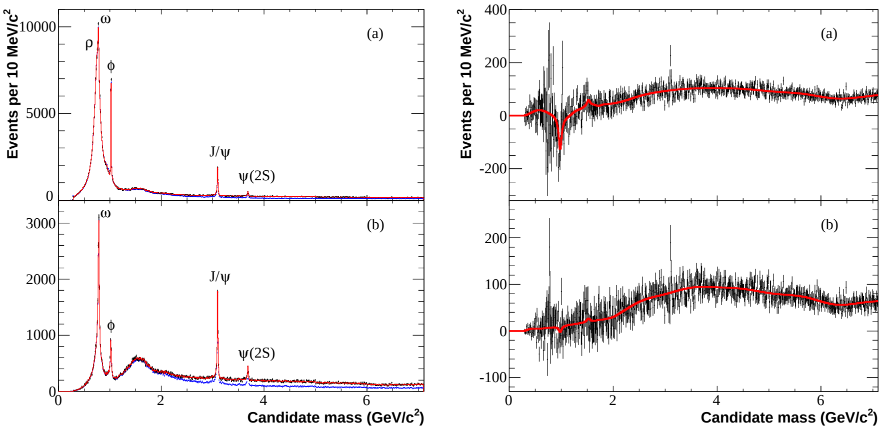

Figure 5: Candidate mass spectrum (left) before, (right) after the "continuum" background subtraction, (a) in the "CP-all" and (b) "CP-odd" hypothesis [15]. The data are shown in black, the background fit function in red, and the "continuum" component in blue.

interaction region must be present in the event. The dominant background in the high-energy region arise from the QED processes $e^+e^- \to \gamma\gamma$, and from the radiative Bhabha events $e^+e^- \to \gamma e^+e^-$ in the low-energy region. We search for a monochromatic peak in the squared missing mass distribution, defined as $m_X^2 = m(\Upsilon(3S))^2 - 2E_\gamma^* m(\Upsilon(3S))$. Two examples of this distribution for the high-energy and the low-energy regions are shown in Fig. 7. A set of maximum likelihood fits to the mass distribution is performed, without finding any evidence for a signal in the range (0-7.8) GeV. Bayesian ULs on the product of BFs of the decay $(\mathcal{B}(\Upsilon(nS) \to \gamma A^0) \times \mathcal{B}(A^0 \to \text{invisible}))$ are set at the 90% CL, in the range $(0.7 - 31) \times 10^{-6}$, as shown in Fig. 8.

4 Conclusions

Several searches performed by the *BABAR* experiment and presented here can be reinterpreted as searches for a dark photon. Until now, only the $\Upsilon(3S) \to \gamma A^0$, $A^0 \to \mu^+\mu^-$ analysis has been reinterpreted for this purpose [8]. Extending to all the *BABAR* data sample, and analyzing all the possible final

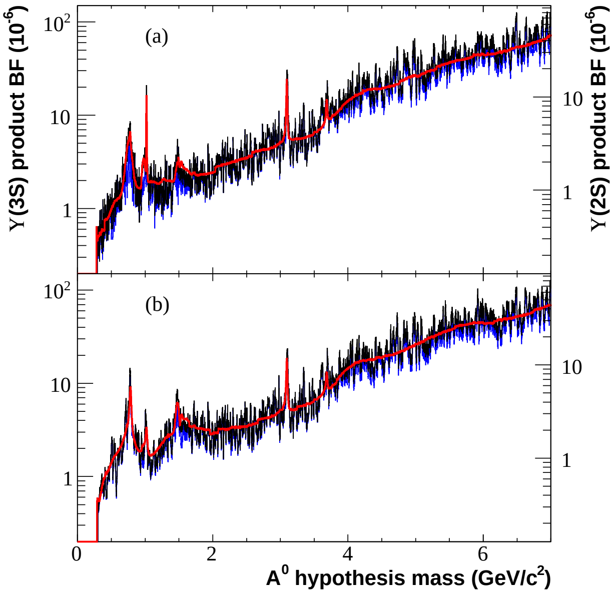

Figure 6: 90% CL ULs on product BFs for (a) "CP-all", and (b) "CP-odd" analysis [15]. The expected ULs are shown in red, while the observed ULs in blue.

states would lead to tighter constraints on the mixing strength between the dark sector and the SM.

References

1. P. Fayet, Phys. Rev. D **75**, 115017 (2007).
2. M. Pospelov, A. Ritz, and M. B. Voloshin, Phys. Lett. B **662**, 53 (2008).
3. N. Arkani-Hamed *et al.*, Phys. Rev. D **79**, 015014 (2009).
4. B Holdom, Phys. Lett. B **166**, 196 (1986).
5. O. Adriani *et al.* [PAMELA Collaboration], Nature **458**, 607 (2009).

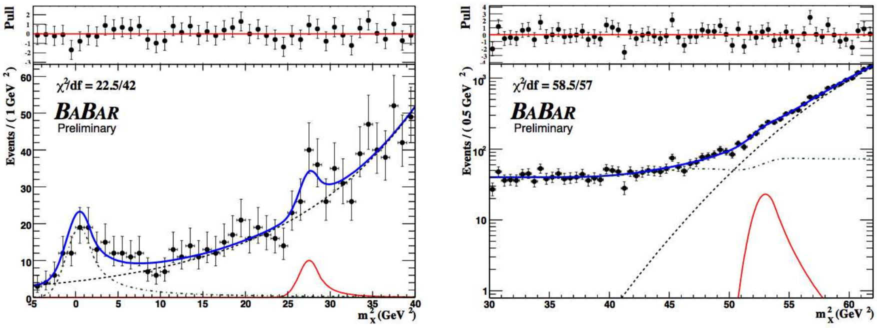

Figure 7: Sample fits to (left) the high-energy and (right) the low-energy region datasets 17). Data are shown by black points, the signal function in solid red, and the total fit function in solid blue, while the green dotted-dashed line represents the QED processes contributing to the background.

6. M. Ackermann *et al.* [Fermi LAT Collaboration], Phys. Rev. D **82**, 092004 (2010).
7. B. Batell, M. Pospelov, and A. Ritz, Phys. Rev. D **79**, 115008 (2009).
8. J. D. Bjorken *et al.*, Phys. Rev. D **80**, 075018 (2009).
9. B. Aubert *et al.* [BABAR Collaboration], arXiv:0908.2821 [hep-ex].
10. J. P. Lees *et al.* [BABAR Collaboration], Phys. Rev. Lett. **108**, 211801 (2012).
11. B. Aubert *et al.* [BABAR Collaboration], Nucl. Instrum. Methods Phys. Res. Sect. A **479**, 1 (2002).
12. R. Dermisek, J. F. Gunion and B. McElrath, Phys. Rev. D **76**, 051105 (2007).
13. B. Aubert *et al.* [BABAR Collaboration], Phys. Rev. Lett. **103**, 081803 (2009).
14. B. Aubert *et al.* [BABAR Collaboration], Phys. Rev. Lett. **103**, 181801 (2009).

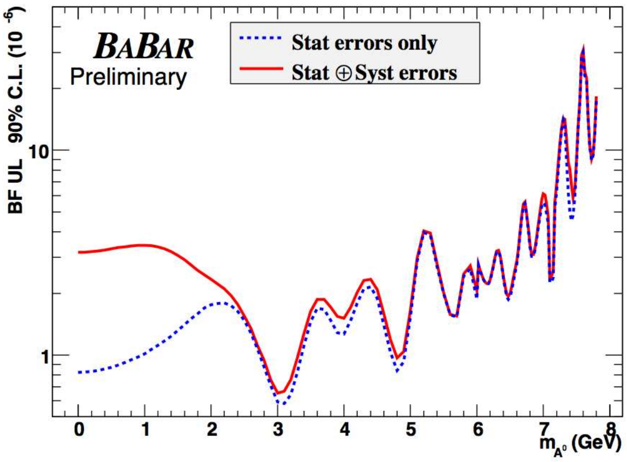

Figure 8: 90% CL ULs on the product BFs, either (dashed blue line) with the statistical uncertainties only, or (solid red line) when considering also systematic uncertainties [17].

15. B. Aubert *et al.* [BABAR Collaboration], arXiv:0808.0017 [hep-ex].

16. J. M. Cline and A. R. Frey, Phys. Rev. D **84**, 075003 (2011).

17. J. P. Lees *et al.* [BABAR Collaboration], Phys. Rev. Lett. **107**, 221803 (2011).

Frascati Physics Series Vol. LVI (2012)
Dark Forces at Accelerators
October 16-19, 2012

U BOSON SEARCH IN THE $e^+ + e^- \to \mu^+\mu^-\gamma$ PROCESS AT KLOE

F. Curciarello
Dipartimento di Fisica e di Scienze della Terra, 98166 Messina, Italy
INFN-Sezione Catania, I-95123, Catania, Italy
On behalf of KLOE/KLOE2 Collaboration [*]

Abstract

Following recent puzzling astrophysical results and recent theoretical studies, a search for a relatively low mass (1 GeV) new vector gauge boson (called the U boson), weakly coupled with SM particles and decaying into lepton pairs, by using the Initial State Radiation (ISR) process, was performed at KLOE. 239.29 pb^{-1} of data were used to search for light vector boson in the $e^+e^- \to \mu^+\mu^-\gamma$ channel. No evidence was found and a preliminary upper limit in the $600 - 1000\,MeV$ mass range was extracted.

---

[*] D. Babusci, D. Badoni, I. Balwierz-Pytko, G. Bencivenni, C. Bini, C. Bloise, F. Bossi, P. Branchini, A. Budano, L. Caldeira Balkeståhl, G. Capon, F. Ceradini, P. Ciambrone, F. Curciarello, E. Czerwiński, E. Dané, V. De Leo, E. De Lucia, G. De Robertis, A. De Santis, P. De Simone, A. Di Domenico, C. Di Donato, R. Di Salvo, D. Domenici, O. Erriquez, G. Fanizzi, A. Fantini, G. Felici, S. Fiore, P. Franzini, P. Gauzzi, G. Giardina, S. Giovannella, F. Gonnella, E. Graziani, F. Happacher, L. Heijkenskjöld, B. Höistad, L. Iafolla, E. Iarocci, M. Jacewicz, T. Johansson, K. Kacprzak, W. Kluge, A. Kupsc, J. Lee-Franzini, F. Loddo, P. Lukin, G. Mandaglio, M. Martemianov, M. Martini, M. Mascolo, R. Messi, S. Miscetti, G. Morello, D. Moricciani, P. Moskal, S. Muller, F. Nguyen, A. Passeri, V. Patera, I. Prado Longhi, A. Ranieri, C. F. Redmer, P. Santangelo, I. Sarra, M. Schioppa, B. Sciascia, M. Silarski, C. Taccini, L. Tortora, G. Venanzoni, R. Versaci, W. Wiślicki, M. Wolke, J. Zdebik

1 Introduction

In the last decades one of the main goal of particle physicists and astrophysicists was to shed light on the possible existence of dark matter and dark energy. Usually, experiments are mainly oriented towards the discovery of new particles at high energy scales, however, a complementary interesting approach is the search for new light particles at relatively low energy scales. Such particles may have remained undiscovered because of their weak coupling to the Standard Model (SM). Moreover, in the last two years striking astrophysical observations, that cannot be interpreted by standard Astrophysics and Particle Physics, have attracted particular attention of the Scientific Community on the study of a hidden low–energy dark sector. Among the most important we remind observations by PAMELA 1), INTEGRAL satellite 2), ATIC 3), Hess 4), Fermi 5) and DAMA/LIBRA 6). The most interesting thing is that all these observations could be explained if one assumes that a dark force gauge boson, mediator of an unknown force with mass less than two proton mass, $M_U < 2\,m_p$, exists. The U boson, also called dark photon, is predicted by several Standard Model Extensions (SME) 7, 8, 9, 10, 11, 12). According to dark force models this dark force gauge boson would be produced during dark matter annihilation processes and then decay into light particles, as leptons, ($\tilde{X} + X \to U + U$, $U \to l^+l^-$, $l = e, \mu$), assuming a mass less than 1 GeV 13). Such dark photon is associated to an abelian gauge symmetry that can communicate with the ordinary SM through a kinetic mixing term that is given by the following relation: 7, 8, 13, 14)

$$L_{mix} = -\frac{\varepsilon^2}{2}\, F_{ij}^{e.m.}\, F_{dark}^{ij} \tag{1}$$

where $\varepsilon^2 = \alpha^{'}/\alpha$ is the kinetic mixing parameter ($\alpha = 1/137$, $\alpha^{'}$ is the U boson coupling constant), $F_{ij}^{e.m.}$ is the electromagnetic tensor, F_{dark}^{ij} is the dark matter hypercharge gauge boson tensor.

Luckily, dark force models make a number of predictions that can be tested by particle physics experiments. Particularly, high luminosity $e^+ - e^-$ collider experiments at GeV scale can be a direct probe of dark forces. At flavour factories a particular clean channel is the production of the U boson plus a photon with the consequent decay of the U boson in a lepton pair:

$e^+e^- \to U\gamma \to l^+l^-\gamma$, where $l = e, \mu$ [13]. The expected U boson signal should have the shape of a Breit-Wigner peak in the invariant mass distribution of the lepton pair. For this reason, about $240\,pb^{-1}$ of KLOE data taken on 2002 were used to analyse the $e^+e^- \to \mu^+\mu^-\gamma$ channel with the aim to search for the light vector gauge boson.

2 KLOE Experimental Set Up

DAΦNE is a $e^+ - e^-$ collider, working at the energy $\sqrt{s} = m_\phi = 1.0195\,GeV$ and it is located at the INFN-LNF of Frascati. The DAΦNE Accelerator Complex consists of a linear accelerator, a damping ring, nearly 180 m of transfer lines, two storage rings that intersect at two points, a beam test area (BTF) and three syncrotron light lines (see Fig.1).

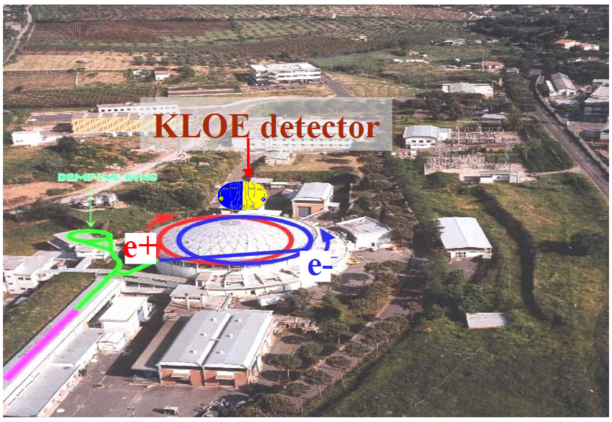

Figure 1: *DAΦNE accelerator complex*

The KLOE detector is made up of a large cylindrical drift chamber (DC, see Fig.2 left side), surrounded by a lead scintillating fiber electromagnetic calorimeter (EMC, see Fig.2 right side). A superconducting coil around the EMC provides a 0.52 T magnetic field. The EMC provides measurement of photon energies, impact point and an accurate measurement of the arrival time of particles. The DC is well suited for tracking of the particles and charged vertices reconstruction. The calorimeter is divided into a barrel and two end–caps and covers 98% of the full solid angle. The modules

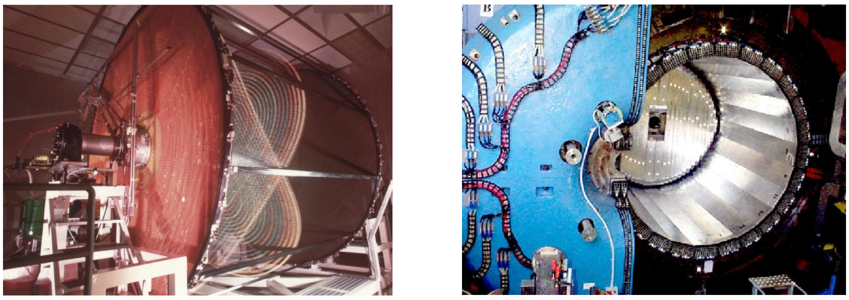

Figure 2: *Left side: KLOE drift chamber Right side: KLOE calorimeter*

are read out at both ends by 4880 photo–multipliers. Energy and time resolutions are $\sigma_E/E = 5.7\%/\sqrt{E(GeV)}$ and $\sigma_t = 57\,ps\,/\sqrt{E(GeV)} \oplus 50\,ps$, respectively. The all-stereo drift chamber, $4\,m$ in diameter and $3.3\,m$ long, is provided of 12000 sense wires, is made of carbon fiber-epoxy composite and operates with a light gas mixture (90% helium, 10% isobutane). The position resolutions are about $\sigma_{xy} = 150\,\mu m$ and $\sigma_z = 2\,mm$. The momentum resolution is $\sigma_{p_\perp}/p_\perp > 0.4\%$ for large angle tracks. Vertices are reconstructed with a spatial resolution of about $3\,mm$.

3 Event Selection

The analysis described in the following is based on the KLOE pion form factor measurement 15). The data sample consists of $239.29\,pb^{-1}$ of data taken in year 2002. The event selection requires:

- two charged tracks with $50° < \theta_\mu < 130°$ (wide cones in Fig.3 a))
- one photon within a cone of $\theta_\gamma < 15°$ ($\theta_\gamma > 165°$) around the beamline (narrow cones in Fig.3 a))

The photon is not detected, its direction is reconstructed from event kinematics: $\vec{p}_\gamma \simeq \vec{p}_{miss} \equiv -\vec{p}_{\mu\mu} = -(\vec{p}_{\mu^+} + \vec{p}_{\mu^-})$. This separation of tracks and photon selection regions in the analysis greatly reduces the contamination from the resonant process $e^+e^- \to \phi \to \pi^+\pi^-\pi^0$, where the π^0 mimics the missing momentum of the photon(s), and from the final state radiation processes: $e^+e^- \to \pi^+\pi^-\gamma_{\mathrm{F}SR}$ and $e^+e^- \to \mu^+\mu^-\gamma_{\mathrm{F}SR}$. Since ISR-photons are mostly

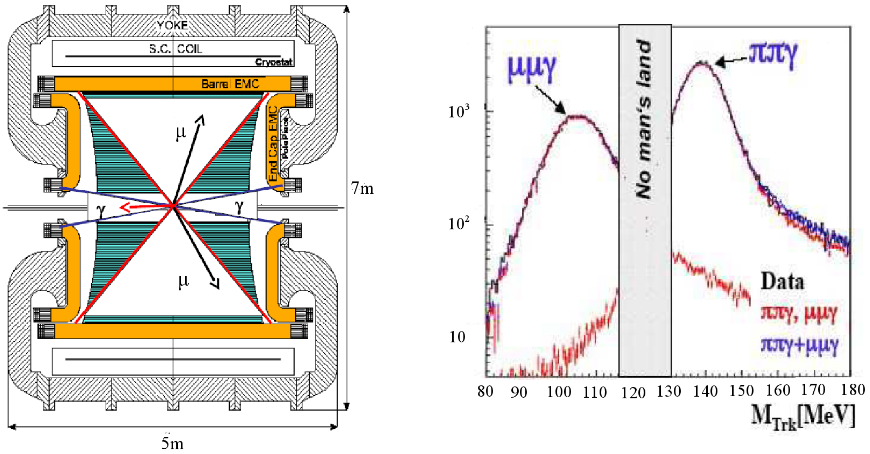

a) b)

Figure 3: *a) Schematic cross-view of KLOE Detector with the selection regions for the missing momentum angle (narrow cones) and for muons track (wide cones) b) Pions and muons separation by cut on M_{Trk} variable*

collinear with the beam line, a high statistics for the ISR signal events remains. Backgrounds contributions coming from:

1. $e^+e^- \to \pi^+\pi^-\gamma(\gamma)$
2. $e^+e^- \to \Phi \to \pi^+\pi^-\pi^0$
3. $e^+e^- \to e^+e^-\gamma(\gamma)$

were separated applying kinematical cuts in the $M_{\mathrm{T}rk} - M^2_{\pi\pi}$ plane (for the definition of M_{trk} variable see later). A particle identification estimator (PID), based on a pseudo-likelihood function using the time-of-flight and calorimeter information, was used to suppress radiative Bhabha events 15, 16, 17). Finally pions and muons are separated by a cut on the trackmass variable $M_{\mathrm{T}rk}$:

- muons are selected with $80 < M_{\mathrm{T}rk} < 115$ MeV,
- pions are selected with $M_{\mathrm{T}rk} > 130$ MeV.

The M_{Trk} variable is computed from energy and momentum conservation, assuming the presence of an unobserved photon and that the tracks belong to particles of the same mass:

$$\left(\sqrt{s} - \sqrt{|\mathbf{p}^{+}|^{2} + M_{\rm Trk}^{2}} - \sqrt{|\mathbf{p}^{-}|^{2} + M_{\rm Trk}^{2}}\right)^{2} - \left(\mathbf{p}^{+} + \mathbf{p}^{-}\right)^{2} = 0 \qquad (2)$$

where $\mathbf{p}^{\pm}$ is the measured momentum of the positive (negative) particle, and only one of the four solutions has physical meaning. In Fig. 3 b) is reported the separation between the $\mu^+\mu^-\gamma$ and $\pi^+\pi^-\gamma$ distributions by M_{Trk} cut. The gap between the two selections has been chosen to reduce the mutual contamination of the two samples.

4 Background Contributions

The contributions of background channels surviving the $\mu^+\mu^-\gamma$ selection, (see section 3), are obtained by fitting in slices of $M^2_{\mu\mu}$ the M_{Trk} distribution for data as a superposition of signal and background distributions.

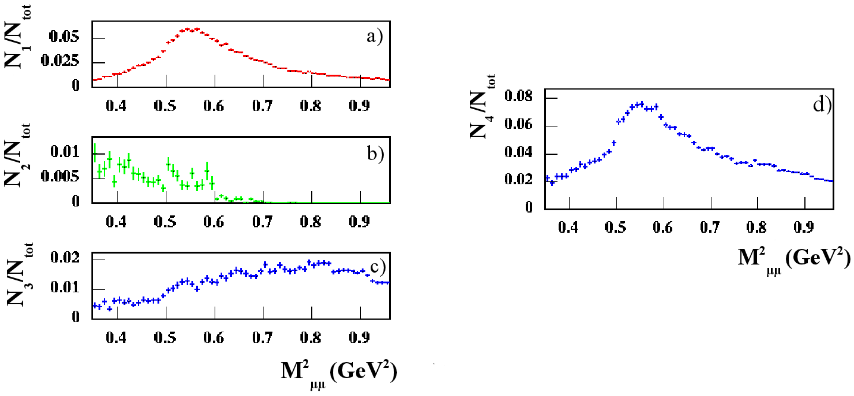

Figure 4: *a) $\pi^+\pi^-\gamma$ background contribution b) $\pi^+\pi^-\pi^0$ background contribution c) $e^+e^-\gamma$ background contribution d) sum of the three relative background contributions a), b) and c). N_1, N_2, N_3 are the background event numbers related to the above mentioned 1., 2., 3. channels, respectively; N_4 represents their sum; N_{tot} is the total number of events found in each bin of $M^2_{\mu\mu}$*

For each background channel, the fit results in normalization parameters, called weights, $w_{ch}(j)$, produced for each slice of $M^2_{\mu\mu}$. The $M_{\mathrm{T}rk}$ distribution for $\mu^+\mu^-\gamma$, $\pi^+\pi^-\gamma$, $\pi^+\pi^-\pi^0$ were extracted by Monte Carlo calculation (MC). Since the $e^+e^-\gamma$ background is much larger, at percent level, its contribution was estimated directly from data. In Fig. 4 the contributions of the three background channels normalized to the total number of events, as well as their sum, are shown. Since in the ρ region the $\pi^+\pi^-\gamma$ cross section is about one order of magnitude greater than the $\mu^+\mu^-\gamma$ one, it is crucial to to keep under control the $\pi^+\pi^-\gamma$ $M_{\mathrm{T}rk}$ tail in the region below $125\,MeV$. For this reason, a tuning of the $M_{\mathrm{T}rk}$ tail using a control sample of $70\,pb^{-1}$ of $\Phi \to \pi^+\pi^-\pi^0$ was also applied.

4.1 Cut on the σ_{MTRK}

A further separation between pions and muons was performed by a cut on the σ_{MTRK} variable which parametrize the quality of the fit of the tracks, as explained in the reference [15]. In Fig. 5a) are reported the $\pi^+\pi^-\gamma$ (black) and

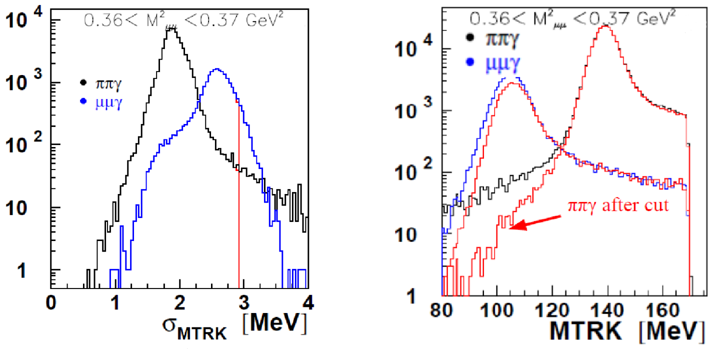

a) b)

Figure 5: *a)* σ_{MTRK} *distribution for one* $M^2_{\mu\mu}$ *slice of* $\pi^+\pi^-\gamma$ *(black) and* $\mu^+\mu^-\gamma$ *(blue); in red a possible cut value is shown b) effect of* σ_{MTRK} *cut on* M_{Trk} *distributions for one slice of* $M^2_{\mu\mu}$*; black and blue histograms represent the* $\pi^+\pi^-\gamma$ *and* $\mu^+\mu^-\gamma$ M_{Trk} *distributions without* σ_{MTRK} *cut; red histograms are obtained after applying* σ_{MTRK} *cut*

$\mu^+\mu^-\gamma$ (blue) σ_{MTRK} distributions for one slice of $M^2_{\mu\mu}$. Figure 5b) shows the effects of σ_{MTRK} cut (red) on $M_{\mathrm{T}rk}$ distribution for one slice of $M^2_{\mu\mu}$. As it is possible to see, there is a significant reduction (up to a factor 2) of the $\pi^+\pi^-\gamma$

contamination in the $\mu^+\mu^-\gamma$ $M_{\mathrm{T}rk}$ region, with a consequent improvement in π/μ separation. The cut was optimized in order to keep the signal ($\mu^+\mu^-\gamma$) at a level of about 70% .

4.2 Absolute Cross Section of $\mu^+\mu^-\gamma$

Once the Data/MC corrections have been applied, the $\mu^+\mu^-\gamma$ cross section was extracted by subtracting the residual background to the observed spectra and dividing it for efficiencies and luminosity.

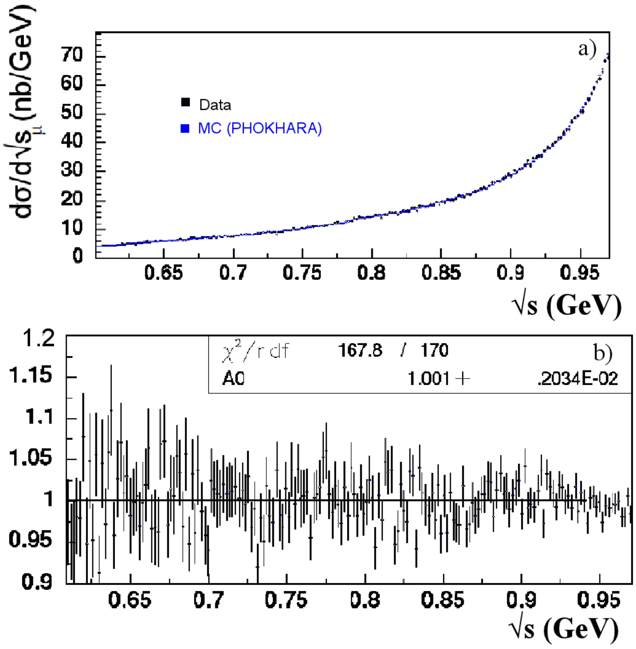

Figure 6: *a) Comparison of data (black points) and MC (blue points) of* $\mu^+\mu^-\gamma$ *absolute cross section b) ratio of data and MC PHOKHARA prediction*

The absolute cross section is in good agreement with the PHOKHARA prediction 18) as reported in Fig. 6.

5 Upper Limit Extraction on ε^2

To extract the upper limit (U.L.) on ε^2 the TLimit Root Class [19], based on the confidence level signal (CLS) technique [20] was used. The observed spectrum, that is the raw spectrum after offline background filter efficiency (`FILFO`) corrections (which are at percent level) and background subtraction, was used as "data" input of TLimit procedure. As "background" input was used the MC PHOKHARA spectrum properly normalized to the raw spectrum. A systematic error of $\sim 2\%$ on background was also applied.

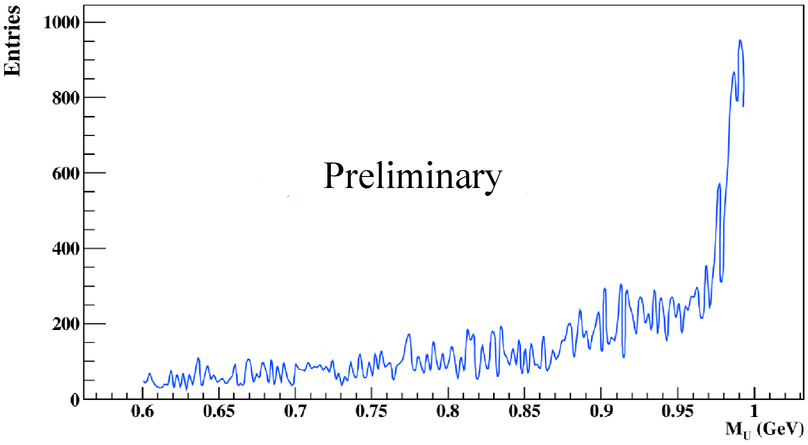

Figure 7: *Exclusion plot on number of signal events at* 90% *of C.L.*

In Fig. 7 the exclusion plot on number of signal events at 90% of confidence level (C.L.) in the energy range between 600 and 1000 MeV is shown.

The U.L. on the kinetic mixing parameter ε^2 was extracted using the following formula [21]:

$$\varepsilon^2 = \frac{\alpha'}{\alpha} = \frac{N_{CLS}/(\epsilon_{eff} \cdot L)}{H \cdot I} \tag{3}$$

where N_{CLS} is the number of entries of signal hypothesis excluded as fluctuations at the 90% C.L.; ϵ_{eff} represents the efficiency and acceptance corrections; L is the integrated luminosity ($L = 239,29\,pb^{-1}$); H is the radiator function given by:

$$H = \frac{d\sigma_{\mu^+\mu^-\gamma}/d\sqrt{s_\mu}}{\sigma(e^+e^- \to \mu^+\mu^-, s_\mu)} \tag{4}$$

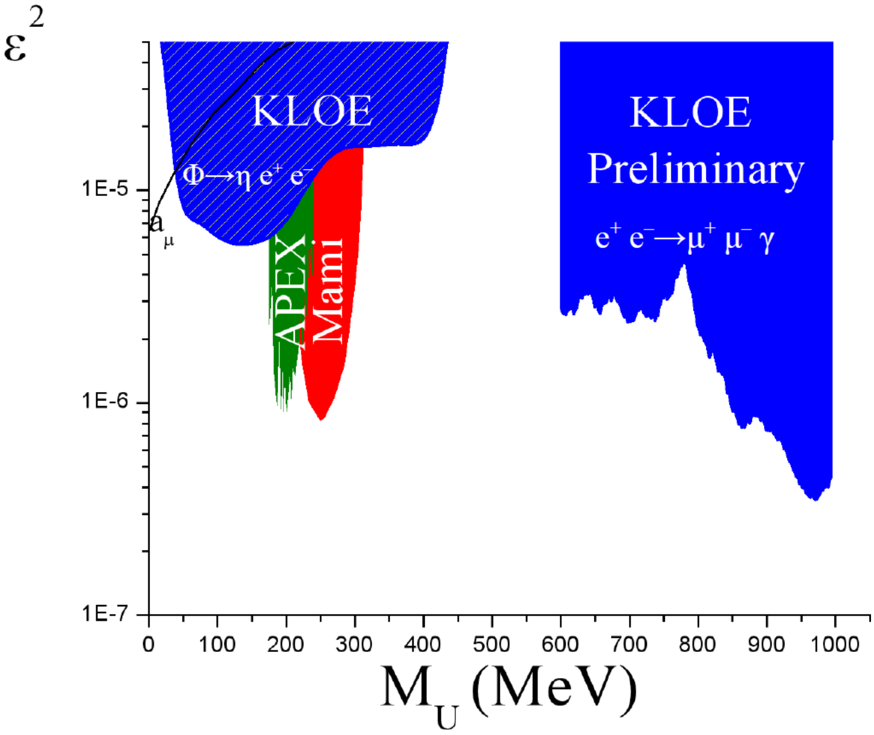

Figure 8: *Exclusion Plot on* ε^2 *in comparison with the existing limits in the* $0-1000\,MeV$ *range*

where $d\sigma_{\mu^+\mu^-\gamma}/d\sqrt{s_\mu}$ is the partial cross section of $e^+e^- \to \mu^+\mu^-\gamma(\gamma)$, s_μ is the invariant mass of muons, $\sigma(e^+e^- \to \mu^+\mu^-, s_\mu)$ is the total cross section of $e^+e^- \to \mu^+\mu^-$ process; the quantity I is given by the following integral:

$$I = \int_i \sigma_U^{\mu\mu}\, ds_i \tag{5}$$

where $\sigma_U^{\mu\mu} = \sigma(e^+e^- \to U \to \mu^+\mu^-, s)$ is the total cross section of U boson production decaying in the $\mu^+\mu^-$ channel, $s = M_U^2$, and i is the mass bin number. In Fig.8 the kinetic mixing parameter ε^2 obtained by formula 3, in the $600-1000\,MeV$ range and the other existing limits are presented. The blue area is the present measurement derived using the $e^+e^- \to \mu^+\mu^-\gamma$ channel, the U.L. is between $2.6\cdot10^{-6}$ and $3.5\cdot10^{-7}$, it is clearly visible the reduction of the sensitivity due to ρ meson at about $0.77\,GeV$. The red area represents the Mami results (22), the dark green area refers to the Apex measure (23) and finally, the blue shaded area shows the KLOE U.L. in the $0 - 460\,MeV$ region calculated using the Dalitz Φ decay (24). The black line represents the ε^2 values consistent with a U boson contribution to the muon magnetic moment anomaly a_μ.

6 Conclusions

$239.29\,pb^{-1}$ of 2002 KLOE data were used to search for light vector boson in the $e^+e^- \to \mu^+\mu^-\gamma$ channel. No U boson evidence was found and an U.L. has been extracted on coupling factor ε^2 in the energy range between 600 and $1000\,MeV$. The preliminary results exclude a possible effect of U boson existence on the a_μ in the investigated energy range between 600 and 1000 MeV. An extension of the muon acceptance selection and full statistics analysis ($2.5\,fb^{-1}$) is planned to have the possibility to explore the muon spectrum at lower invariant mass region, extending the present measurement and increasing the sensitivity of about a factor 3.

References

1. O. Adriani *et al.*, Nature **458**, 607 (2009).
2. P. Jean *et al.*, Astronomy Astrophysics **407**, L55 (2003).
3. J. Chang *et al.*, Nature **456**, 362 (2008).
4. F. Aharonian *et al.*, Phys. Rev. Lett. **101**, 261104 (2008).
5. A. A. Abdo *et al.*, Phys. Rev. Lett. **102**, 181101 (2009).
6. R. Barnabei *et al.*, Eur. Phys. J. C **56**, 333 (2008).
7. C. Boehm, P. Fayet, Nucl. Phys. B **683**, 259 (2004).
8. M. Pospelov, A. Ritz, M.B. Voloshin, Phys. Lett. B **662**, 53 (2008).
9. M. Pospelov, A. Ritz, Phys. Lett. B **671**, 391 (2009).
10. N. Arkani-Hamed, D.P. Finkbeiner, T.R. Slatyer *et al.*, Phys. Rev.D **79**, 015014 (2009).

11. I. Cholis, G. Dobler, D.P. Finkbeiner *et al.*, Phys. Rev. D **80**, 123518 (2009).

12. Y. Mambrini, J. Cosmol. Astropart. Phys. **022**, 1009 (2010).

13. L. Barzè *et al.*, Eur. Phys. J. C **71**, 1680 (2011).

14. B. Holdom, Phys. Lett. B **166**, 196 (1986).

15. D. Babusci *et al.*, arXiv:1212.4524 [KLOE/KLOE2 Collaboration].

16. F. Ambrosino *et al.*, Phys. Lett. B **670**, 285 (2009) [KLOE Collaboration].

17. F. Ambrosino *et al.*, Phys. Lett. B **700**, 102 (2011) [KLOE Collaboration].

18. H. Czyż *et al.*, Eur. Phyis. J. C **39** 411 (2005).

19. http://root.cern.ch/root/html/TLimit.html.

20. G. C. Feldman, R. D. Cousins, Phisical Rev. D **57**, 3873 (1998).

21. G. Venanzoni, KLOE2 Internal Note K2ID-12,

    `http://www.lnf.infn.it/kloe2/index.php?lv1=documents&lv2=list&lv3=private&lv4=k2id.`

22. M. Merkel *et al.*, Phys. Rev. Lett. **106**, 251802 (2011).

23. S. Abrahamyan *et al.*, Phys. Rev. Lett. **107**, 191804 (2011).

24. D. Babusci *et al.*, arXiv:1210.3927 [KLOE/KLOE2 Collaboration].

Frascati Physics Series Vol. LVI (2012)
Dark Forces at Accelerators
October 16-19, 2012

SEARCH FOR DARK SECTOR AT BESIII

Jinlin FU (for the BESIII Collaboration)
Department of Physics, Nanjing University, China

Abstract

With 106M ψ' events collected at BESIII detector, there is no observed signal of light Higgs-like boson A^0 in process $J/\psi \to \gamma A^0$, $A^0 \to \mu^+\mu^-$. The A^0-mass-dependent upper limits at the 90% C.L. of branching fraction for $J/\psi \to \gamma A^0$, $A^0 \to \mu^+\mu^-$ are range from 4×10^{-7} to 2.1×10^{-5}, for $\mathrm{M}(A^0) < 3.0$ GeV/c^2. With 225M J/ψ data sample, there is no obseved signal of light dark matter particles or U boson in invisible decays of η and η'. The upper limits at the 90% C.L. are determined to be 2.6×10^{-4} for the ratio $\frac{\mathcal{B}(\eta\to\text{invisible})}{\mathcal{B}(\eta\to\gamma\gamma)}$ and 2.4×10^{-2} for $\frac{\mathcal{B}(\eta'\to\text{invisible})}{\mathcal{B}(\eta'\to\gamma\gamma)}$. These limits may be used to constrain light dark matter particles or spin-1 U bosons.

1 The BEPC-II collider and BES-III detector

BEPCII/BESIII 1) is a major upgrade of the BESII experiment at BEPC accelerator. The achieved peak luminosity of the double-ring e^+e^- collider, BEPCII, is 0.65×10^{33} cm^{-2} s^{-1} at energy of $\psi(3770)$. The BESIII detector consists of a main drift chamber with momentum resolution 0.5% at 1 GeV/c, an electromagnetic calorimeter with energy resolution 2.5% at 1 GeV/c and a time-of-flight system inside a superconducting solenoidal magnet with a magnetic strength of 1 T. The magnet is surrounded by the muon system made of resistive plate chambers. Based on data samples of 1.06×10^8 ψ' 2) and 2.25×10^8 J/ψ 3), two analyses are performed for dark sector search.

2 Search for a light exotic particle in $J/\psi \to \gamma\mu^+\mu^-$

The HyperCP experiment 4) obsered three anomalous $\Sigma \to p\mu^+\mu^-$ events with $\mu^+\mu^-$ invariant mass around 214.3 MeV/c^2. A particle with these properties could be the pseudoscalar sgoldstino particle 5) in various supersymmetric models 6), a light pseudoscalar Higgs-like boson A^0 7), or a vector U boson 8). No evidence of new physics has been found by studying light dilepton-resonance in $p\bar{p}$ collision, e^+e^- collision and b-quark decays, but it is still important to search for $J/\psi \to \gamma A^0$ to check the possible couples to c-quark and leptons. Theoretically, the branching fraction of $J/\psi \to \gamma A^0$ is about 10^{-9} to 10^{-7} level 9). The upper limits of branching fraction of $J/\psi \to \gamma A^0$ are set by Crystal Ball experiment which are less than 1.4×10^{-5} (90% C.L.) for $M(A^0) < 1.0$ GeV/c^2 10).

The process $\psi' \to \pi^+\pi^- J/\psi$, $J/\psi \to \gamma A^0$, $A^0 \to \mu^+\mu^-$ is used to search for an A^0, and A^0 is assumed as a pseudoscalar (or scalar) particle with narrow width and negligible decay time. Two positive, two negative charged tracks and at least one good photon are required. The events with multiple photons, should be passed through the π^0 veto. The γ with the highest energy is regarded as the photon from J/ψ. The oppositely charged track pair with recoil mass closest to the J/ψ mass is regarded as the π^+ and π^-. The other two charged tracks with at least one satisfying muon identification is assigned as the μ^+ and μ^-. The J/ψ is tagged by constraining $\pi^+\pi^-$ recoil mass within a narrow window. In order to get better mass resolution and suppress backgrounds further, the events are kinematically fitted using energy and momentum conservation constraints under the $\psi' \to \gamma\pi^+\pi^-\mu^+\mu^-$ hypothesis.

The entire $\mu^+\mu^-$ mass range from threshold to 3.0 GeV/c^2 is studied. There is no evidence narrow peak in the mass distribution and only one event with mass of 213.3 MeV/c^2 [shown in Fig.2a]. To set upper limits on the production rates for different masses, the unbinned maximum-likelihood fits are performed to $\sim$300 MeV/c^2-wide ranges of the invariant mass spectrum where the mass of the A^0 peak is restricted to be within a series of 5 MeV/c^2-wide intervals near the center of the range. In each fit, the A^0 signal shape is determined from MC simulation, and the background shape is modeled with a polynomial. The limits on the signal yield in each 5 MeV/c^2 interval are set with Bayesian method at the 90% C.L.. Figure1 shows a typical fit to the $\mu^+\mu^-$ invariant mass spectrum in the 5 MeV/c^2-wide interval centred at 2.43 GeV/c^2. The upper limits at the 90% C.L. on the branching fractions of $J/\psi \to \gamma A^0$, $A^0 \to \mu^+\mu^-$ is calculated with

$$\mathcal{B} < \frac{\mathrm{Nsig(UL)}/\epsilon}{\mathrm{N}(\psi') \times \mathcal{B}(\psi' \to \pi^+\pi^-\mathrm{J}/\psi) \times (1-\sigma)}, \qquad (1)$$

where Nsig(UL), shown in Fig.2b, is the upper limit on the number of signal events in each M($\mu^+\mu^-$) bin; ϵ is the A^0-mass-dependent selection efficiency determined from MC simulation; N(ψ') is the number of ψ' events; $\mathcal{B}(\psi' \to \pi^+\pi^- J/\psi)$ is set at Particle Data Group (PDG) value [11]; and σ is the total systematic error.

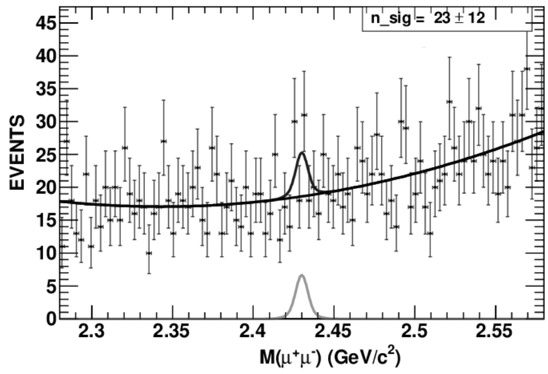

Figure 1: *A typical fit to the invariant-mass spectrum M($\mu^+\mu^-$) in the 5 MeV/c^2 wide interval centered at 2.43 GeV/c^2.*

There is no evidence observed. The A^0-mass-dependent upper limits on the branching fraction for $J/\psi \to \gamma A^0$, $A^0 \to \mu^+\mu^-$ are range from 4×10^{-7} to

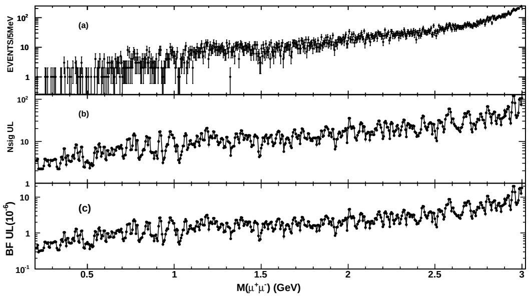

Figure 2: *a) The $\mu^+\mu^-$ invariant mass distribution for the selected $\psi' \to \pi^+\pi^- J/\psi$, $J/\psi \to \gamma\mu^+\mu^-$; b) Upper limits at the 90% C.L. on the number of signal events (Nsig UL) as a function of the $\mu^+\mu^-$ invariant mass; c) Upper limits at the 90% C.L. on the branching fractions (BF UL).*

2.1×10^{-5} [shown in Fig.2c]. Only one event is seen with a $\mu^+\mu^-$ mass of 213.3 MeV/c^2, and the product-branching-fraction upper limit is 5×10^{-7} at the 90% C.L. These limits can rule out much of the parameter space in theoretical models 12).

3 Search for η and $\eta\prime$ invisible decays

Despite of tentative estimation like $\mathcal{B}(\eta(\eta') \to \chi\chi) \approx 1.4\times10^{-4}$ (1.5×10^{-6}) 13), one cannot reliable predict such invisible decay rates of mesons just from the dark matter relic density and annihilation cross section 14). Due to the U boson vectorially coupled to quarks and leptons 15) and more specific case of the U boson coupled to ordinary particles through the electromagnetic current 16), the annihilation process $q\bar{q} \to UU$ may be also a source of invisible meson decays, especially as the invisible decay mode $U \to \chi\chi$ may be dominant 15). Invisible decays of η and η' may originate from $\eta(\eta') \to \chi\chi$ or $U_{\text{inv}}U_{\text{inv}}$. Many searches for invisible decays of π^0, η, η', J/ψ and $\Upsilon(1S)$ have been performed 17, 18, 19, 20, 21). The resulting data can give constraints on different matrix.

The processes $J/\psi \to \phi\eta$ and $\phi\eta'$ are used to study invisible decays of η and η'. The ϕ can be reconstructed with $\phi \to K^+K^-$ decay model. No charged track is required besides those from $\phi \to K^+K^-$. No neutral track is required inside a cone of 1.0 rad around the recoil direction against the ϕ candidate. The reconstructed ϕ particles within a narrow mass window [shown in Fig.3a] are used to tag $\eta(\eta')$. The missing $\eta(\eta')$ can be searched for in the distribution of recoil mass of ϕ candidate.

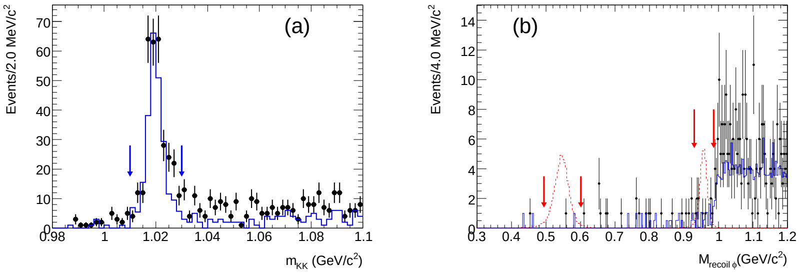

Figure 3: *a) The* K^+K^- *mass distribution. The arrows indicate the signal region of* ϕ *candidates. Points with error bars are data; the histogram is expected background. b) Recoil mass distribution against* ϕ *candidates,* M_ϕ^{recoil}*, for events within* ϕ *mass window. Points with error bars are data; the solid histogram is the sum of the expected backgrounds; the dashed histograms (with arbitrary scale) are signals of* η *and* η' *invisible decays from MC simulations; the arrows indicate the signal regions of the* $\eta(\eta') \to$ *invisible.*

The sources of backgrounds are divided into two classes. Class I: The background is from $J/\psi \to \phi\eta(\eta')$, $\phi \to K^+K^-$ and $\eta(\eta')$ decay into visible states. The expected number of background from Class I is 0.18 ± 0.02 (1.0 ± 0.2) in the signal region for $\eta(\eta')$ case. Class II: The background is from J/ψ decays to final states without $\eta(\eta')$ or without both $\eta(\eta')$ and ϕ. For the η invisible decay, the dominant background is from $J/\psi \to \gamma\eta_c$, $\eta_c \to K^\pm\pi^\mp K_L$. For the η' case, the dominant background is from $J/\psi \to \phi K_L K_L$ and $J/\psi \to \phi f_0(980)$, $f_0(980) \to K_L K_L$. The expected number of background from Class II is 0.8 ± 0.2 (9.4 ± 1.7) in the signal region for $\eta(\eta')$ case.

For η case, only one event [shown in Fig.3b] is seen in the η signal region where 1.0 ± 0.2 backgrounds are expected. The upper limit at the 90% C.L. is $N_{UL}^{\eta} = 3.34$ by using the POLE++ program 23) based on Feldman-Cousins Method 22). For the η' case, an unbinned extended maximum likelihood (ML) fit is performed to the recoil mass distribution against ϕ candidate. The signal shape in the fit, shown in Fig.4, is driven from data sample of $J/\psi \to \phi\eta'$, $\eta' \to \eta\pi^+\pi^-$, $\eta \to \gamma\gamma$. The shape of dominant background $J/\psi \to \phi f_0(980)$, $f_0(980) \to K_L K_L$, is described from MC simulation [shown in Fig.5], in which the parameters of $f_0(980)$ line shape have been determined in the analysis of $J/\psi \to \phi\pi^+\pi^-$ and ϕK^+K^- from BESII data 24). The remaining background from $J/\psi \to \phi K_L K_L$ is modeled with a first-order Chebychev polynomial. In the ML fit [shown in Fig.5], the shapes of signal and dominant background are fixed, the numbers of signal yield and backgrounds are float. The upper limit at the 90% C.L. is $N^{\eta'}_{UL} = 10.1$ with Bayesian method.

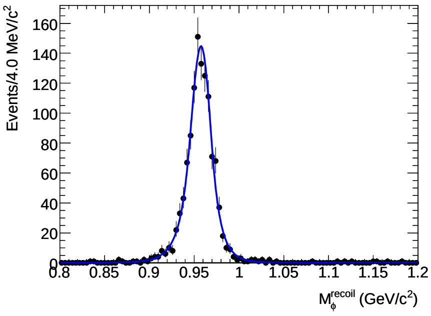

Figure 4: *The M_ϕ^{recoil} distribution for the control sample $J/\psi \to \phi\eta'$, $\eta' \to \pi^+\pi^-\eta(\eta \to \gamma\gamma)$ decay candidates. The solid curve shows the fit results.*

In order to obtain the ratio of $\frac{\mathcal{B}(\eta(\eta')\to\text{invisible})}{\mathcal{B}(\eta(\eta')\to\gamma\gamma)}$, the two-body decays $J/\psi \to \phi\eta(\eta')$, $\eta(\eta') \to \gamma\gamma$ are also studied. The upper limit at the 90% C.L. on the ratio of branching fraction is calculated with

$$\frac{\mathcal{B}(\eta \to \text{invisible})}{\mathcal{B}(\eta \to \gamma\gamma)} < \frac{N^\eta_{UL}/\epsilon_\eta}{N^\eta_{\gamma\gamma}/\epsilon^\eta_{\gamma\gamma}} \frac{1}{1-\sigma_\eta}\,, \tag{2}$$

where N^η_{UL} is the 90% upper limit of the number of observed events for $J/\psi \to \phi\eta$, $\phi \to K^+K^-$, $\eta \to$ invisible decay; ϵ_η is the MC-determined efficiency for the signal channel; $N^\eta_{\gamma\gamma}$ is the number of events for the $J/\psi \to \phi\eta$, $\phi \to K^+K^-$, $\eta \to \gamma\gamma$; $\epsilon^\eta_{\gamma\gamma}$ is the MC-determined efficiency; and σ_η is the total error for the η case. The upper limit for η' case is obtained similarly.

There is no evidence observed for the invisible decays of η and η', The upper limit at the 90% C.L. on the ratio of $\frac{\mathcal{B}(\eta(\eta')\to\text{invisible})}{\mathcal{B}(\eta(\eta')\to\gamma\gamma)}$ is 2.6×10^{-4} ($2.4 \times$

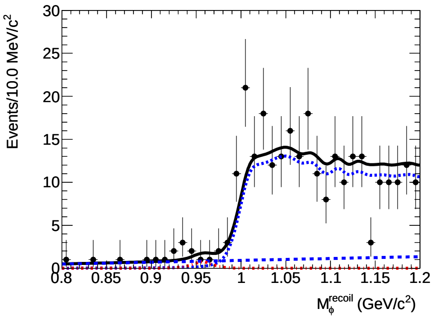

Figure 5: *The M_ϕ^{recoil} distribution with events around the η' mass region. Points with error bars are data. The (black) solid curve shows the result of the fit to signal plus background distributions, the (blue) dotted curve shows the background shape from $J/\psi \to \phi f_0(980)(f_0(980) \to K_L K_L)$, the (blue) dashed curve shows the polynomial function for $J/\psi \to \phi K_L K_L$ background, and the (red) dotted-dash curve shows the signal yield.*

10^{-2}) for $\eta(\eta')$ case. Using the branching fraction values of $\mathcal{B}(\eta(\eta') \to \gamma\gamma)$ from the PDG $^{25)}$, the invisible decays rates are determined to be $\mathcal{B}(\eta \to \text{invisble}) < 1.0 \times 10^{-4}$ and $\mathcal{B}(\eta' \to \text{invisble}) < 5.3 \times 10^{-4}$ at the 90% confidence level. These limits constrain the decays $\eta(\eta') \to UU$, where each U decays invisibly into neutrinos or light dark matter with branching fraction B_{inv}. The resulting $\eta(\eta')$ limits on the U couplings to quarks are improved to be $\sqrt{f_u^2 + f_d^2} < 3 \times 10^{-2}/\sqrt{B_{\text{inv}}}$ and $|f_s| < 4 \times 10^{-2}/\sqrt{B_{\text{inv}}}$, respectively (for $2m_U$ smaller than m_η or $m_{\eta'}$ and not too close to them), f_u, f_d and f_s denoting effective couplings of the U boson to light quarks.

4 Summary

There is no observed signal of light Higgs-like boson A^0 in process $J/\psi \to \gamma A^0$, $A^0 \to \mu^+\mu^-$, based on 106M ψ' data sample. The A^0-mass-dependent upper limits at the 90% C.L. of branching fraction for $J/\psi \to \gamma A^0$, $A^0 \to \mu^+\mu^-$ are range from 4×10^{-7} to 2.1×10^{-5}, for M(A^0) < 3.0 GeV/c^2. There is no obseved signal of light dark matter particles or U boson in invisible decays of η and η', based on 225M J/ψ data sample. The upper limits at the 90% C.L. are determined to be 2.6×10^{-4} for the ratio $\frac{\mathcal{B}(\eta \to \text{invisible})}{\mathcal{B}(\eta \to \gamma\gamma)}$ and 2.4×10^{-2}

for $\frac{\mathcal{B}(\eta'\to\text{invisible})}{\mathcal{B}(\eta'\to\gamma\gamma)}$. These limits may be used to constrain light dark matter particles or spin-1 U bosons.

5 Acknowledgements

We thank the BEPCII group for excellent operation of the accelerator, the IHEP computer group for valuable computing and network support, and all the colleagues contributing on the physical measurements.

References

1. M. Ablikim *et al.* (BESIII Collaboration), Nucl. Instrum. Meth. Methods Phys. Res., Sect. A **614**, 345 (2010).
2. M. Ablikim *et al.* (BESIII Collaboration), Phys. Rev. D **81**, 052005 (2010).
3. M. Ablikim *et al.* (BESIII Collaboration), Chinese Phys. C **36**, 915 (2012).
4. H. K. Park *et al.* (HyperCP Collaboration), Phys. Rev. Lett. **94**, 021801 (2005).
5. D. S. Gorbunov and V. A. Rubakov, Phys. Rev. D **73**, 035002 (2006).
6. J. Ellis, K. Enqvist, and D. Nanopoulos, Phys. Lett. B **147**, 99 (1984); T. Bhattacharya and P. Roy, Phys. Rev. D **38**, 2284 (1988); G. Giudice and R. Rattazzi, Phys. Rep. **322**, 419 (1999).
7. X. G. He, J. Tandean, and G. Valencia, Phys. Rev. Lett. **98**, 081802 (2007).
8. M. Reece and L. T. Wang, J. High Energy Phys. **07**, (2009) 051; M. Pospelov, Phys. Rev. D **80**, 095002 (2009); C.H. Chen, C. Q. Geng, and C.W. Kao, Phys. Lett. B **663**, 400 (2008).
9. R. Dermisek, J. F. Gunion, and B. McElrath, Phys. Rev. D **76**, 051105 (2007).
10. C. Edwards *et al.*, (Crystal Ball Collaboration), Phys. Rev. Lett. bf 48, 903 (1982).
11. K. Nakamura *et al.*, (Particle Data Group), J. Phys. G **37**, 075021 (2010).

12. P. Fayet, Phys. Lett. B **675**, 267 (2009).

13. B. McElrath, arXiv:0712.0016[hep-ph], *Proceedings of the CHARM 2007 Workshop*, Ithaca, NY, August 5-8, 2007.

14. P. Fayet, Phys. Rev. D **81**, 054025 (2010).

15. P. Fayet, Phys. Rev. D **74**, 054034 (2006).

16. P. Fayet, Nucl. Phys. B **347**, 743 (1990).

17. A. V. Artamonov *et al.* (E949 Collaboration), Phys. Rev. D **72**, 091102 (2005).

18. M. Ablikim *et al.* (BES Collaboration), Phys. Rev. Lett. **97**, 202002 (2006).

19. P. Naik *et al.* (CLEO Collaboration), Phys. Rev. Lett. **102**, 061801 (2009).

20. M. Ablikim *et al.* (BES Collaboration), Phys. Rev. Lett. **100**, 192001 (2008).

21. B. Aubert *et al.* (BABAR Collaboration), Phys. Rev. Lett. **103**, 251801 (2009); P. Rubin *et al.* (CLEO Collaboration), Phys. Rev. D **75**, 031104 (2007); O. Tajima *et al.* (Belle Collaboration), Phys. Rev. Lett. **98**, 132001 (2007).

22. G. J. Feldman and R. D. Cousins, Phys. Rev. D **57**, 3873 (1998).

23. J. Conrad, O. Botner, A. Hallgren and C. Peréz de los Heros, Phys. Rev. D **67**, 012002 (2003); http://polepp.googlecode.com/svn/tags/POLEPP-1.1.0.

24. M. Ablikim *et al.* (BES Collaboration), Phys. Lett. B **607**, 243 (2005).

25. J. Beringer *et al.* (Particle Data Group), Phys. Rev. D **86**, 010001 (2012).

Frascati Physics Series Vol. LVI (2012)
DARK FORCES AT ACCELERATORS
October 16-19, 2012

Dark photon search and the Higgs-strahlung channel.

Igal Jaegle for the Belle Collaboration
Department of Physics and Astronomy, University of Hawaǐi at Manoa,
2505 Correa Road, Honolulu 96822, Hawaǐi, USA.

Abstract

The expected sensitivity of Belle is reported for the Dark Photon, A, and Dark Higgs, h' searches, for mass ranges, respectively of $0.27 < m_A < 3$ GeV/c^2 and $0.54 < m_{h'} < 10$ GeV/c^2. The Dark Photon and Dark Higgs was searched for in the Higgs-strahlung channels: $e^+e^- \to Ah'$, with $h' \to AA$ and $A \to l^+l^-$ (with $l = e$ or μ). At the time of writing the results have not yet been unblinded.

1 Introduction

Ordinary matter represents 4 % of the total energy budget of the universe 1).The remainder is believed to be partitioned as either Dark Energy (73%) or Dark Matter (23%), but the nature of those components is unknown. However, experimental results from direct Dark Matter searches, (e.g. DAMA/LIBRA) 2, 3, 4, 5) and other experimental observations that may be interpreted as deviations from the Standard Model (e.g. g-2 measurements 6)), can be explained in Dark Matter (DM) models by the inclusion of an additional interaction, a dark U(1) interaction 7, 8, 9, 10, 11, 12, 13, 14, 15, 16, 17). This interaction, which is mediated by a dark U(1) boson, also known as the "Dark Photon", typically has very small couplings to Standard Model particles.

Dark gauge bosons are postulated to have low masses; of order MeV to GeV due to astrophysical constraints 18, 19). These astrophysical observations include: excesses in the cosmic-ray flux of electrons and/or positrons above expected background beyond normal astrophysical processes and the expected flux of protons and/or anti-protons. Dark matter could be charged under the dark U(1) symmetry group and then the observed excess might correspond to dark matter annihilating into a Dark Photon A, which in turn decays into l^+l^- (with $l = e$ or μ or possibly τ if energetically allowed).

The ideal tools to discover such particles are therefore not the highest energy hadron collider experiments, but lower-energy electron-positron high-luminosity collider experiments such as Belle/BelleII and BaBar, or dedicated fixed target experiments, several of which are planned or already under construction at JLAB (Newport News, USA) or at MAMI (Mainz, Germany), for example. In Belle, work on dark gauge boson searches was started only recently, and has focused on the strategies proposed by 20, 21, 22, 23, 24). The dark U(1) symmetry group could be spontaneously broken, often by a Higgs mechanism, adding a dark Higgs h' (or dark Higgses) to these models. These proceedings will focus on the so-called Higgs-strahlung channel, $e^+e^- \to Ah'$ and in particular the decay modes with $3e^+3e^-$, $3\mu^+3\mu^-$, $2e^+2e^-\mu^+\mu^-$ and $2\mu^+2\mu^-e^=e^-$ final states. The dark photon A can decay into either l^+l^-, hadrons or invisible particles and h' into AA, l^+l^-, hadrons or invisible particles. The decay mode of the A and h' depends of the mass difference between A and h' 22): (a) $m_{h'} < m_A$: $h' \to$ invisible particles, (b) $m_A < m_{h'} < 2m_A$: $h' \to l^+l^-$ or hadrons, (c) $m_{h'} > 2m_A$: $h' \to AA$. Case (c) will be discussed in this proceedings.

The A and h' do not necessarily have prompt decays 22, 25). The decay length of the dark photon is a function of the dark photon coupling strength to Standard Model fermions and is proportional to the inverse of the square of the dark photon coupling. The decay length of the dark Higgs varies for $m_{h'} > 2m_A$ between being prompt and one meter. In the Higgs-strahlung channel, two couplings are involved: the electromagnetic coupling of the dark photon to the Standard Model fermions, α'; and the dark photon coupling to the dark Higgs, α_D. CLOE and BaBar reported their searches on the dark photon and the dark Higgs 26) (contribution of E. Graziani to these proceedings) and 27) (see also contribution of A. Gaz to these proceedings). CLOE focused their search on $m_{h'} < m_A$ (A and h' not prompt) and BaBar on $m_{h'} > 2m_A$ (with A and h' prompt), but no signal was found. BaBar and CLOE set limits respectively for low mass range, $2m_\mu < m_A < 1GeV/c^2$ and $m_{h'} < m_A$; and for highest mass range, $0.8 < m_{h'} < 10.0$ GeV/c^2 and $0.25 < m_A < 3.0$ GeV/c^2. BaBar looked at two types of final states, fully reconstructed ($3l^+l^-$, $2l^+2l^-\pi^+\pi^-$ and $2\pi^+2\pi^-l^+l^-$ where $l = e, \mu$); and partially reconstructed ($2\mu^+2\mu^-X$ and $e^+e^-\mu^+\mu^-X$, where X denotes any final state other than a pair of pions or leptons). The reason to look for partially reconstructed final states is that above $m_A > 1$ GeV/c^2, final states with hadrons dominate assuming $BF(A \rightarrow e^+e^-) + BF(A \rightarrow \mu^+\mu^-) + BF(A \rightarrow hadrons) = 1$ and that $\frac{BF(A\rightarrow hadrons)}{BF(A\rightarrow\mu^+\mu^-)} = R$, where R is the hadronic cross section ratio, $R = \frac{\sigma(e^+e^-\rightarrow hadrons)}{\sigma(e^+e^-\rightarrow\mu^+\mu^-)}$. BaBar reported six candidate events detected: one $4\mu2\pi$, two $4\pi2\mu$, two $4\pi2e$ and one $4\mu X$ events, in a $\sim$ 500 fb-1 data set. There were no candidates in the final states with six leptons. The number of events detected were consistent with background expectations.

For low mass range of the dark photon: $1 < m_A < 300$ MeV/c^2, part of the coupling strength to Standard Model fermions versus dark photon mass have been excluded by Beam dump experiments 28, 29, 30, 31, 32, 33, 34) by looking at reaction $pp \rightarrow AX$ for example. Furthermore, limits could be set for the dark photon between a few MeV/c^2 and 10 GeV/c^2 by reinterpreting the limit on the CP odd Higgs of BaBar 35, 36), CLEO 37) and the upcoming Belle results on $e^+e^- \rightarrow \Upsilon$(1 or 3 S)$\rightarrow \gamma A^0$. As explained by P. Fayet in 38, 39, 40): the U(1) boson likes to couple to SM fermions via electromagnetic currents which make it by definition a dark photon. But more generally, the U(1) boson can have different vectorial couplings and also axial couplings which make searching for it similar to Next-to-Minimal Supersymmetric Standard Model (NMSSM). Hence the limit can be expressed for a pseudoscalar or for a dark vector gauge boson.

2 Experimental setup

The Belle detector is a large-solid-angle magnetic spectrometer, which consists of a silicon vertex detector (SVD), a central drift chamber (CDC), an array of aerogel threshold Cerenkov counters (ACC), a barrel-like arrangement of time-of-flight scintillation counters (TOF), and an electromagnetic calorimeter (ECL) composed of CsI(Tl) crystals located inside a super-conducting solenoid that provides a 1.5 T magnetic field. An iron flux-return (KLM) located outside the coil is optimized to detect K_L^0 mesons and to identify muons. A detailed description can be found in 41). Belle is currently being upgraded to Belle II, an upgraded detector for operation at SuperKEKB, which will have 40 times higher luminosity than KEKB 42). The KEKB collider 43), located in Tsukuba, Japan, is the world's highest-luminosity electron-position collider. KEKB has produced more than one ab^{-1} of data at center-of-mass energies corresponding to the Υ(1S) to Υ(5S) resonances, and in the nearby continuum.

3 Particle and reaction identification

The sub-systems used to identify the electrons are primarily the ECL, which measured the energy and the CDC, which measured the momentum 44). The muons are identified by using the KLM and an analysis combining the measurements of penetration depth, the charged track, and the muon cluster matching 45).

Events with six charged tracks with three pairs of opposite charges are considered for this analysis. Furthermore, in order to maintain a high detection efficiency we require that at least three out of the six tracks be identified as leptons for the six electrons or six muons final states. For 4e2μ and 4μ2e final states respectively, at least five and at least three, out the six tracks have to be identified as leptons.

4 Analysis strategy

Events with six lepton final states from $e^+e^- \rightarrow Ah' \rightarrow AAA \rightarrow 3l^+3l^-$ (l = e or μ) are reconstructed. Energy and momentum conservation is required. The invariant mass for each combination of leptons is required to be consistent with three distinct $A \rightarrow l^+l^-$. Combinations with three "equal" masses (m_{ll}^1,

m_{ll}^2 and m_{ll}^3) and $m_{llll} > 2m_{ll}$ are kept. The "equality" is defined as follows: $m_{ll}^{mean} - 3.\sigma(m_{ll}^{mean}) < m_{ll}^{1,2,3} < m_{mean} + 3.\sigma(m_{ll}^{mean})$, with m_{ll}^{mean} the mean mass of the three dark photon candidates and the width (σ) of the signal as function of the dark mass which is taken from Monte Carlo (MC) simulation. The detection efficiency of Belle was modeled with MC simulations based on the GEANT4 package 46). The simulation includes all relevant properties of the sub-systems, including geometrical acceptance, charged particle identification, trigger efficiency, response of all detector modules, and selection criteria. The MC also includes information about inefficient individual detector modules. Belle can achieve, on average, a detection efficiency of 20 % and 40 % respectively for 6 electron and 6 muon final states and of 15 % and 30 % respectively for 4e2μ and 4μ2e.

5 Background estimation

The background estimation is based on a data driven method. In this method, all combinations that have two pairs where the leptons are combined with their wrong-sign partner and one pair with opposite charge, $(l^-l^-)(l^+l^+)(l^+l^-)$, are kept. The three masses are ordered in decreasing order: $m_{ll}^1 > m_{ll}^2 > m_{ll}^3$. The mass difference between the m_{ll}^1, the highest mass, and m_{ll}^3 the lowest mass: $m_{ll}^1 - m_{ll}^3$ is then calculated. Figure 1 shows the mass difference $m_{ll}^1 - m_{ll}^3$ as function of the mass m_{ll}^1 for the 6 electrons (Figure 1-top) and 6 muons (Figure 1-bottom) final states. For conciseness, the following notations are used: "same sign" for $(l^+l^-)(l^+l^+)(l^-l^-)$ and "opposite sign" for $(l^+l^-)(l^+l^-)(l^+l^-)$ (with $l = e$ or μ). The scatter plot for the opposite sign: $(e^+e^-)(e^+e^-)(e^+e^-)$ - Figure 1-top-right and $(\mu^+\mu^-)(\mu^+\mu^-)(\mu^+\mu^-)$ - Figure 1-bottom-right have their signal region blinded (filled bands), since a blind analysis technique is used and not all selection criteria have been validated. The signal region for the same sign scatter plots ($(e^+e^-)(e^+e^+)(e^-e^-)$ - Figure 1-top-left and $(\mu^+\mu^-)(\mu^+\mu^+)(\mu^-\mu^-)$ - Figure 1-bottom-left) is unblinded.

The background is then estimated for different m_{ll}^1 mass regions as illustrated for the $m_{ll}^1 = 1.9 \pm 0.1$ GeV/c^2 band by Figure 2. It is assumed that the backgrounds have the same shape in the side band region of the same sign distribution and the opposite sign distribution but not necessarily the same number of events. Therefore, the same sign distribution is normalized to the opposite sign distribution by a factor calculated for each m_{ll}^1. The expected

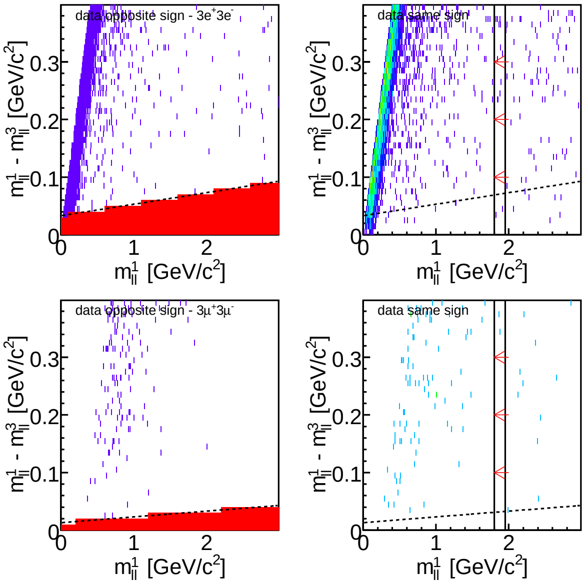

Figure 1: m_{ll}^1 versus $m_{ll}^1 - m_{ll}^3$ for 6e final state (top) and 6μ final state (bottom). Top-left and bottom-left, opposite sign: $(e^+e^-)(e^+e^-)(e^+e^-)$. Top-right and bottom-right, same sign: $(e^+e^-)(e^+e^+)(e^-e^-)$. The 2D histograms are divided into 20 slices, each slice is then projected on the $m_{ll}^1 - m_{ll}^3-$axis. The red arrow (right) shows slice 10, corresponding to m_{ll}^1 = 1.9 ± 0.1 GeV/c^2 and the direction of the projection. The filled box on the left (top and bottom) corresponds to the blinded signal region.

background is then the scaled number of events counted in the signal region of the same sign distribution. The signal obtained in the MC simulation is shown as a black curve in Figure 1 (for the opposite sign).

6 Expected sensitivity

The expected background with no constraint on the impact parameters and the vertex positions is less than 25 events and less than 5 events with a constraint on the impact parameters but no constraint on the vertex positions for the six electron final states. No events are found in the signal box of the same sign distribution for the cases of the six muon, 4e2μ and 4μ2e final states. The case with no constraint on the impact parameter and on the vertex position corresponds to displaced vertex positions up to 80 cm from the interaction

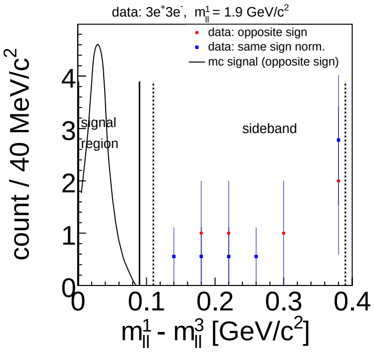

Figure 2: Projection on $m^1_{ll} - m^3_{ll}$ for $m^1_{ll} = 1.9 \pm 0.1$ GeV/c^2. The "same sign"-$(e^+e^-)(e^+e^+)(e^-e^-)$ (black point) distribution has been normalized to the "opposite sign"-$(e^+e^-)(e^+e^-)(e^+e^-)$ (red square) distribution using the side band area.

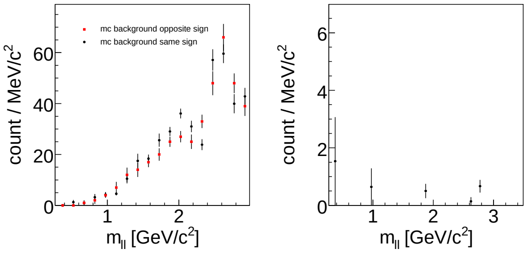

Figure 3: Left, background estimation method verified successfully with MC Right, for experimental data, predicted BG is > 20 events for the electron final state.

point and according to [22, 25] up to $\epsilon \sim 10^{-6}$. Here, $\epsilon = \frac{\alpha'}{\alpha}^2$ is the strength of the dark photon mixing with the Standard Model hypercharge gauge boson and α, the electromagnetic coupling. For the case with a constraint on the impact parameters, the decay length can go up to 6 mm i.e. up to $\epsilon \sim 10^{-4}$.

Figure 3-left shows a MC simulation test of the background estimation method. The interaction $e^+e^- \to 3e^+3e^-$ have been generated with an uniform phase space generator. The background estimated from the same sign distribution is consistent with the number of events counted in the signal region of the opposite sign for all m_A candidates. Figure 3-right shows the expected background deduced from the data same sign analysis.

A statistical method based on the Feldman-Cousins approach [47] is used to then calculate preliminary upper limits (90% CL) for a number of "observed" events equal to the estimated background events for the full luminosity and the prompt case. Figure 4 (left - six electron, right six muons, bottom-left 4e2μ and bottom-right 4μ2e final states) shows the preliminary sensitivity limit for different "Dark Higgs" mass hypotheses compared to the BaBar upper limits [27]. Figure 5 (top-left six electron, top-right six muons, bottom-left 4e2μ and bottom-right 4μ2e final states) shows the preliminary sensitivity limits for different "Dark Photon" mass hypotheses. Due to the expected low level of background the sensitivity scales nearly linearly with the integrated luminosity.

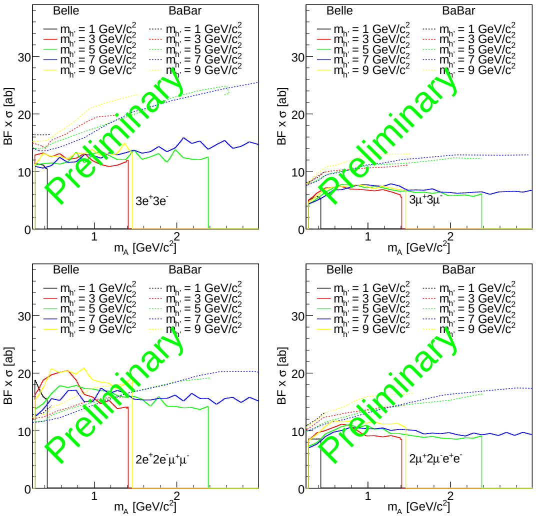

Figure 4: Sensitivity as a function of the "Dark Photon" mass for different "Dark Higgs" mass hypotheses. Top-left: 6e. Top-right: 6μ. Bottom-left: 4e2μ. Bottom-right: 4μ2e. Full line this analysis. Dashed line BaBar upper limit [27].

7 Conclusions

The Dark Photon and the Dark Higgs are searched for in the mass ranges: $0.27 < m_A < 3$ GeV/c^2 and $0.54 < m_{h'} < 10.86$ GeV/c^2. Based on control data samples, it was found that the background is small, implying that the detection sensitivity scales nearly linearly with integrated luminosity. The expected preliminary Belle sensitivities have been shown. At the time of writing

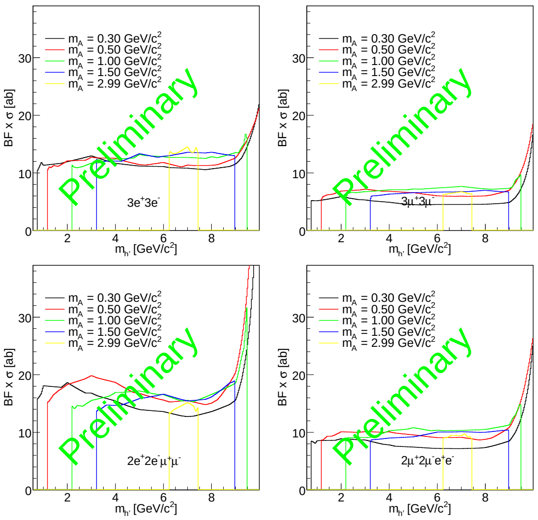

Figure 5: Sensitivity as function of the "Dark Higgs" mass for different "Dark Photon" mass hypothesis. Top-left: 6e. Top-right: 6μ. Bottom-left: 4e2μ. Bottom-right: 4μ2e.

the results have not yet been unblinded.

Acknowledgements

The authors would like to thank the organizers (INFN-Frascati) of the DARK2012, Dark Forces at Accelerators 16-19th October 2012 (Frascati-Italy) for their kind invitation and hospitality and congratulate them for a successful workshop. We acknowledge support from the U.S. Department of Energy under Award Number DE-SC0007852.

References

1. G. Hinshaw et al. The Astr. J. 180, 225 (2009).
2. DAMA Collaboration, R. Bernabei, et al. Eur. Phys. J. C 56 (2008).
3. CDMS-II Collaboration, Z. Ahmed et al., Published Feb 11, 2010, Science 327:1619-1621 arXiv:0912.3592 (2010).

4. XENON Collaboration, E. Aprile, et al. Phys. Rev. Lett. 105:131302 (2010).
5. CoGeNT collaboration, C.E. Aalseth et al. arXiv:1002.4703 (2010).
6. Muon g-2 Collaboration, G. W. Bennett et al., Phys. Rev. D73 072003 (2006).
7. M. Pospelov, A. Ritz and M. Voloshin, arXiv:0711.4866 (2007).
8. N. Arkami-Hamed, D. Finkbeiner, T. Slatyer and N. Weiner, arXiv:0810.0713 (2008).
9. E. J. Chun and J. C. Park, arXiv:0812.0308 (2008).
10. C. Cheung, J. Ruderman, L.T. Wang, and I. Yavin, arXiv:0902.3246 (2009).
11. A. Katz and R. Sundrum, arXiv:0902.3271 (2009).
12. D. Morrissey, D. Poland and K. Zurek, arXiv:0904.2567 (2009).
13. M. Goodsell, J. Jaeckel, J. Redondo, and A. Ringwald, arXiv:0909.0515 (2009).
14. M. Baumgart, C. Cheung, L.-T. Wang, J. Ruderman, I. Yavin, arXiv:0901.0283 (2009).
15. Y. Nomura and J. Thaler, arXiv:0810.5397 (2008).
16. D. Alves, S. Behbabani, P. Schuster, and J. Wacker, arXiv:0903.3945 (2009).
17. J. Jaeckel, A. Ringwald, Ann. Rev. Nucl. Part. Sci. 60 405 (2010).
18. PAMELA - O. Adriani et al., Nature 458, 607-609 (2009)
19. Fermi LAT. Collaboration, M. Ackermann et al., Phys Rev. D 82, 092004 (2010)
20. M. Reece and L. T. Wang, JHEP 0907, 051 (2009)
21. R. Essig, P. Schuster, and N. Toro, arXiv:0903.3941 (2009).
22. B. Batell, M. Pospelov, and A. Ritz, arXiv:0903.0363 (2009).

23. F. Bossi, arXiv:0904.3815 (2009).

24. P.-f. Yin, J. Liu, and S.-h. Zhu, arXiv:0904.4644 (2009).

25. R. Essig, et al. arXiv:1008.0636v1 (2010).

26. Simona Giovannella, J. Phys.: Conf. Ser. 335 012067 (2011).

27. J. P. Lees et al (BaBar Collaboration), Phys. Rev. Lett. 108, 211801 (2012).

28. J. Blumlein, *et al.*, Int. J. Mod. Phys. A **7** 3835 (1992).

29. J. Blumlein, *et al.*, Z. Phys. C **51** 341 (1991).

30. L. Barabash, *et al.*, Phys. Lett. B **295** 154 (1992).

31. J. Blumlein and J. Brunner, arXiv:1104.2747 (2011).

32. J. D. Bjorken, S. Ecklund, W. R. Nelson, A. Abashian, C. Church, B. Lu, L. W. Mo, T. A. Nunamaker et al., E137 collaboration, Phys. Rev. D38 (1988) 3375.

33. E. M. Riordan, M. W. Krasny, K. Lang, P. De Barbaro, A. Bodek, S. Dasu, N. Varelas, X. Wang et al., E141 collaboration, Phys. Rev. Lett. 59 (1987) 755.

34. A. Bross, M. Crisler, S. H. Pordes, J. Volk, S. Errede, J. Wrbanek, E774 collaboration, Phys. Rev. Lett. 67 (1991) 2942.

35. B. Aubert et al. (BaBar collaboration), PRL 103 (2009) 081803

36. B. Aubert et al. (BaBar collaboration), PRL 103 (2009) 181801

37. W. Love et al. (CLEO collaboration), PRL 101 (2008) 151802

38. P. Fayet NPB 347 (1990) 743

39. P. Fayet PL 95B (1980) 285

40. P. Fayet NPB 187 (1981) 184

41. A. Abashian et al. (Belle Collaboration), Nucl. Instrum. Methods Phys. Res., Sect. A 479, 117 (2002).

42. K. Abe et al. (Belle II Collaboration), Belle II Technical Design Report, KEK Report 2010-1, arXiv:1011.0352v1 (2010)

43. S. Kurokawa, Nucl. Intr. and Meth. A499, 1 (2003).

44. K. Hanagaki et al, NIM A 485, 490 (2002).

45. A. Abashian et al, NIM A 491, 69 (2002).

46. R. Brun et al., GEANT, Cern/DD/ee/84-1, (1986).

47. G.J. Feldman and R.D. Cousins Phys. Rev. D 57, 38733889 (1998)

Frascati Physics Series Vol. LVI (2012)
DARK FORCES AT ACCELERATORS
October 16-19, 2012

SEARCH FOR DARK PHOTONS AND DARK HIGGS AT BABAR

Alessandro Gaz
University of Colorado, Boulder, Colorado 80309, USA
on behalf of the BABAR Collaboration

Abstract

We report on a search for dark photons A' and dark Higgs h' through the higgs-strahlung process $e^+e^- \to A'^*,\ A'^* \to A'h'$ using the BABAR detector at the PEP-II asymmetric energy e^+e^- collider. This search is motivated by the results of astrophysical and terrestrial experiments. We analyze the full BABAR dataset (516 fb^{-1}) and find no significant signal, thus we proceed to set 90% confidence level upper limits on the product of the Standard Model-dark sector mixing angle and the dark sector coupling constant.

1 Introduction

While the evidence of the existence of dark matter has become overwhelming in the past decade, its nature still remains unclear. Among the different models that have been proposed, the scenario in which the dark matter is made of

Weakly Interacting Massive Particles (WIMPs) seems particularly appealing. The generic Lagrangian that incorporates the Standard Model (SM) and the dark sector can be written as:

$$\mathcal{L} = \mathcal{L}_{SM} + \mathcal{L}_{WIMP} + \mathcal{L}_{mediator} \,, \tag{1}$$

where the mediator between the SM and the WIMP sector can be either a SM particle (gauge boson, Higgs), or a yet to be discovered kind of particle.

The models of *secluded* $U(1)_D$, in which the additional gauge field mixes kinetically with the SM hypercharge $U(1)_Y$ are particularly interesting for the investigation at colliders $^{1)}$. In such scenarios, WIMP particles can annihilate into the mediator particle A' (which we will refer to as the dark photon), which then couples to the SM particles. If $m(A') \sim 1$ GeV $\ll m(WIMP)$, this naturally leads to an enhancement of the WIMP annihilation cross-section in the center of the galaxy, and a larger branching fraction to leptons, consistent with the observations of PAMELA $^{2)}$, ATIC $^{3)}$, and INTEGRAL $^{4)}$. In addition, this could also explain the annual modulation observed by the DAMA/LIBRA Collaboration $^{5)}$.

In this search we focus on models in which a dark Higgs h' is responsible for the spontaneous symmetry breaking of the secluded $U(1)_D$. In general the A' and h' states are predicted to be narrow, so the favored production mechanism at e^+e^- colliders is the so called higgs-strahlung process: $e^+e^- \to A'^* \to A'h'$ $^{6,\ 7)}$. If $m(h') > 2m(A')$, as we will assume in this analysis, the h' dominantly decays to a pair of dark photons, which always decay with sizable branching fraction to pairs of leptons. In the higgs-strahlung process, we would therefore expect a very clear signature of three pairs of leptons in the final state.

2 The BABAR experiment at the PEP-II e^+e^- collider

The BABAR detector is described in detail elsewhere $^{8)}$. The tracking system is composed by a five-layer silicon vertex tracker (SVT) and a drift chamber (DCH) which operates using a mixture of helium and isobutane. The measurement of the energy loss through the silicon and the gaseous mixture provides useful information for particle identification, particularly at low momentum. A detector of internally reflected Cherenkov light (DIRC) is used for particle identification (PID) purposes, particularly for separating charged kaons from charged pions at high momentum. A tallium-doped CsI calorimeter (EMC) measures the energy deposited by electromagnetic showers and the interaction of neutral particles, while the detectors (resistive plate chambers or limited streamer tubes) of the instrumented flux return (IFR) provide the detection of muons and neutral kaons.

Particularly important, for this analysis, are the PID capabilities of the detector. The PID algorithms that have been developed in the last years of the experiment are based on Error Correcting Output Code (ECOC) 9), and combine all the relevant information from the five subdetectors. For this analysis, it is important to maximize the selection efficiency, rather than keeping the mis-identification rate low. With the selectors employed in this analysis we select electrons (muons) with an average efficiency of $\sim 98\%$ ($\sim 90\%$), with a pion mis-identification rate of $\sim 0.4\%$ ($\sim 4\%$).

The PEP-II e^+e^- asymmetric energy collider has operated for a decade, mostly as a $\Upsilon(4s)$ factory. In the last months of data-taking runs at the energy of the $\Upsilon(3s)$ and $\Upsilon(2s)$ have been taken, and throughout the whole history of the experiment data at energies away from the resonances have been collected, in order to study the continuum $e^+e^- \to q\bar{q}$, $q = u, d, s, c$ background. For the purposes of this analysis, all data can be used: the total dataset has a corresponding integrated luminosity of 516 fb^{-1}.

3 Search for dark Higgs and dark photons with the Higgs-strahlung mechanism

We search for the higgs-strahlung process in the full BABAR dataset 10). We limit ourselves to the ranges $0.8 < m(h') < 10$ GeV and $0.25 < m(A') < 3.0$ GeV, requiring $m(h') > 2m(A')$. For these masses and kinetical mixing strength $\varepsilon \geq 10^{-4}$, these particles are expected to decay promptly. We consider the A' decaying to pairs of electrons, muons, and pions. We search for the higgs-strahlung process either in the *exclusive modes*, in the order: 6μ, $4\mu 2e$, $2\mu 6e$, $4\mu 2\pi$, $2\mu 2e 2\pi$, $4e 2\pi$, $2\mu 4\pi$, $2e 4\pi$, or the *inclusive modes*: $4\mu + X$, $2\mu 2e + X$. The order is chosen to minimize the cross-feed between channels and the loss of efficiency due to mis-classification. The remaining possible final states are neglected because their contribution to the final result is expected to be marginal.

We optimize the selection using $\sim 10\%$ of the data; these data are then discarded for the actual analysis. For the exclusive modes, we require the event to contain exactly 6 tracks, accounting for at least 95% of the colliding e^+e^- energy. The tracks are also required to originate from the same vertex (the vertex probability has to be $\geq 10^{-5}$), and the largest mass difference ΔM between two A' candidates has to be less than 10-240 MeV, depending on the final state. For the inclusive modes we require the four tracks to originate from the same vertex (probability $\geq 10^{-5}$) and the masses of the A' candidates have to be compatible within uncertainties. Moreover, the knowledge of the beam energies allows us to derive the mass of the recoiling system X (and require it to be compatible with the mass of the other A' candidates). Figure 1 shows the ΔM distribution for signal Monte Carlo (MC) and the data. To increase the data statistics, we also consider the *same-sign* sample, obtained by requiring the presence of two pairs of particles having the same electric charge (e.g. $(\mu^+\mu^+)(e^-e^-)$). The signal is clearly peaking at low values of ΔM, while the background has a much broader distribution. Opposite-sign and same-sign data give compatible predictions for the amount of background expected in the analysis.

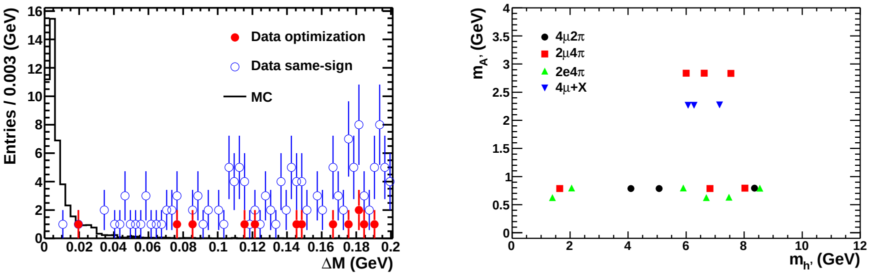

Figure 1: Left plot: ΔM distributions for (black histogram) signal MC ($m(h') = 3.0$ GeV, $m(A') = 0.5$ GeV), (red filled circles) data used for the optimization, (open blue circles) same-sign data. Right plot: distribution in the $(m(h'), m(A'))$ plane of the six events observed in the dataset used in the analysis. For each event there are three different combinations of A' candidates than can be assigned as daughters of the h' candidate.

Six events pass our selection in the dataset used in the analysis, four of which lie on the band $m(A') \sim 0.7 - 0.8$ GeV, consistent with the decay of ρ and ω mesons. This is fully compatible with our SM background predictions.

In order to establish 90% confidence level (CL) upper limits on the cross-sections of the higgs-strahlung process, we conservatively assume that each event is a potential signal event. We scan the $(m(h'), m(A'))$ plane at steps of 10 MeV along each axis, defining as signal region the interval $m(X) - 5\sigma_{m(X)} < m(X) < m(X) + 3\sigma_{m(X)}$, where X is either A' or h'. The signal efficiency (accounting for acceptance, trigger, and selection) is determined from MC for several signal points and then interpolated through the plane. The results of this scan are presented in Fig. 2.

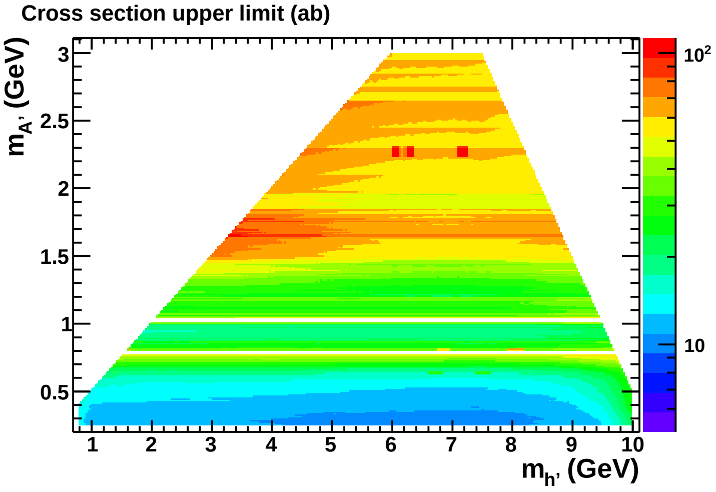

Figure 2: Cross section upper limits (in ab) for the higgs-strahlung process. We conservatively assume that each event is a potential signal event.

The dominant systematic uncertainty comes from the interpolation procedure of the signal efficiency (1-8%); other major contributions arise from PID (1.5-4.5%) and the modeling of A' decays to hadrons (4%).

We translate these cross-section upper limits into upper limits on the product $\alpha_D \varepsilon^2$, where $\alpha_D = g_D^2/4\pi$ is the gauge coupling of the dark sector. These upper limits are displayed on Fig. 3. Assuming $\alpha_D = \alpha$, these limits translate into upper limits on the kinetic mixing ε, which are in the range $10^{-3} - 10^{-4}$, significantly tighter than those previously presented.

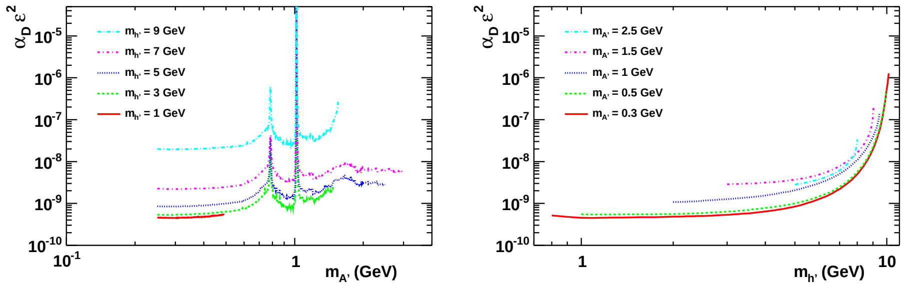

Figure 3: 90% CL upper limits on the product $\alpha_D\varepsilon^2$. On the left plot we show the exclusion curves as a function of $m(A')$ for different $m(h')$ hypotheses, whereas on the right plot the curves are as a function of $m(h')$ for different values of $m(A')$.

4 Conclusions

In conclusion, we have performed a search for the higgs-strahlung process $e^+e^- \rightarrow A'h'$, with the dark Higgs h' decaying to a pair of dark photons A'. Using the full BABAR dataset, we found no signal and set upper limits on the dark coupling constant that are significantly tighter than corresponding limits previously presented by other experiments.

References

1. M. Pospelov, A. Ritz, M. Voloshin, Phys. Lett. B **662**, 53 (2008).
2. O. Adriani *et al.*, Nature **458**, 607 (2009).
3. J. Chang *et al.*, Nature **456**, 362 (2008).
4. A.W. Strong *et al.*, Astron. Astrophys. **444**, 495 (2005).
5. R. Bernabei *et al.*, Eur. Phys. J. C **56**, 333 (2008).
6. B. Batell, M. Pospelov, A. Ritz, Phys. Rev. D **79**, 115008 (2009).
7. R. Essig, P. Shuster, N. Toro, Phys. Rev. D **80**, 115003 (2009).
8. BABAR Collaboration, Nucl. Instrum. Meth. A, **479**, 1 (2002).

9. T.G. Dietterich and G. Bakiri, J. Artif. Intell. Res., **2**, 263 (1995).
10. BABAR Collaboration, Phys. Rev. Lett, **108** 211801 (2012).

Frascati Physics Series Vol. LVI (2012)
Dark Forces at Accelerators
October 16-19, 2012

SEARCH FOR DARK HIGGSSTRAHLUNG PROCESSES AT KLOE

Enrico Graziani
INFN sezione di Roma Tre, Roma, Italy
on behalf of the KLOE/KLOE2 Collaboration [*]

---

[*] D. Babusci, D. Badoni, I. Balwierz-Pytko, G. Bencivenni, C. Bini, C. Bloise, F. Bossi, P. Branchini, A. Budano, L. Caldeira Balkeståhl, G. Capon, F. Ceradini, P. Ciambrone, F. Curciarello, E. Czerwiński, E. Dané, V. De Leo, E. De Lucia, G. De Robertis, A. De Santis, P. De Simone, A. Di Domenico, C. Di Donato, R. Di Salvo, D. Domenici, O. Erriquez, G. Fanizzi, A. Fantini, G. Felici, S. Fiore, P. Franzini, P. Gauzzi, G. Giardina, S. Giovannella, F. Gonnella, E. Graziani, F. Happacher, L. Heijkenskjöld, B. Höistad, L. Iafolla, E. Iarocci, M. Jacewicz, T. Johansson, K. Kacprzak, W. Kluge, A. Kupsc, J. Lee-Franzini, F. Loddo, P. Lukin, G. Mandaglio, M. Martemianov, M. Martini, M. Mascolo, R. Messi, S. Miscetti, G. Morello, D. Moricciani, P. Moskal, S. Muller, F. Nguyen, A. Passeri, V. Patera, I. Prado Longhi, A. Ranieri, C. F. Redmer, P. Santangelo, I. Sarra, M. Schioppa, B. Sciascia, M. Silarski, C. Taccini, L. Tortora, G. Venanzoni, R. Versaci, W. Wiślicki, M. Wolke, J. Zdebik

Abstract

We searched for the existence of a Higgstrahlung process in a secluded sector, possibly leading to a dark photon and a dark Higgs final state. Using the KLOE detector at the DAΦNE e^+e^- collider in Frascati, we investigated the case in which the dark Higgs boson h' is lighter than the dark photon U and thus escapes detection, showing up as a missing energy, and the dark photon U decays in a muon pair. We found no evidence of the process and set tight upper limits to its parameters.

1 Introduction

In recent years, several unexpected astrophysical observations have failed to find a common interpretation in terms of standard astrophysical or particle physics sources. A non exhaustive list of these observations include the 511 keV gamma-ray signal from the galactic center observed by the INTEGRAL satellite 1), the excess in cosmic ray postirons reported by PAMELA 2), the total electron and positron flux measured by ATIC 3), Fermi 4), and HESS 5, 6), the annual modulation of the DAMA/LIBRA signal 7, 8) and the low energy spectrum of nuclear recoil candidate events observed by CoGeNT 9).

Although there are alternative explanations for some of these anomalies, they could be all explained with the existence of a dark matter weakly interacting massive particle, WIMP, belonging to a secluded gauge sector under which the Standard Model (SM) particles are uncharged 10−19) An abelian gauge field, the U boson with mass near the GeV scale, couples the secluded sector to the SM through its kinetic mixing with the SM hyper-charge gauge field. The kinetic mixing parameter ϵ is expected to be of the order $10^{-4} - 10^{-2}$ 11−20) so that observable effects can be induced in O(GeV)-energy e^+e^- colliders 20−24) and fixed target experiments 25−28) .

The U boson can be produced at e^+e^- colliders via different processes: $e^+e^- \to U\gamma$, $e^+e^- \to Uh'$ (dark Higgsstrahlung), where h' is a Higgs-like particle responsible for the breaking of the hidden symmetry, and $V \to P\gamma$ decays, where V and P are vector and pseudoscalar mesons, respectively. In this work we study the Higgsstrahlung process $e^+e^- \to Uh'$ using data collected by the KLOE experiment at the e^+e^- collider DAΦNE at Frascati, both at a center of mass energy of $\sim$ 1019 MeV, the mass of the Φ meson (on peak sample), and at a center of mass energy of $\sim$ 1000 MeV (off peak sample).

The process $e^+e^- \to Uh'$ is one of the most interesting reactions to study at an e^+e^- collider because, differently from the other final states listed above, is suppressed by a single factor of ϵ. There are two very different scenarios depending on the masses of the dark photon and of the dark Higgs boson. For Higgs boson mass $m_{h'}$ larger than two dark photon masses m_U, the dark Higgs boson would decay dominantly and promptly to a U boson pair, thus giving rise to a six charged particle final state (this case was recently investigated by the BaBar experiment 29)); while Higgs bosons lighter than the dark photon would have, in most of the parameter space region, such a large lifetime to escape undetected, showing up as a missing energy signature. In this work we study only the so called "invisible" dark Higgs scenario, thus confining our search to the case $m_{h'} < m_U$.

The lifetime of the dark Higgs boson depends on the kinetic mixing parameter ϵ, the boson masses $m_{h'}$ and m_U and the dark coupling constant α_D. For masses of the order of 100 MeV and $\alpha_D = \alpha_{em}$ the dark Higgs boson lifetime would be $\sim 5\mu s$ for $\epsilon \sim 10^{-3}$, corresponding, for KLOE energies, to a decay length of $\sim$ 100 m. The dark Higgs boson would be invisible up to $\epsilon \sim 10^{-2} \div 10^{-1}$, depending on the h' mass.

We limit our search to the decay of the U boson in a muon pair: our final state signature is then a couple of opposite charge muons plus missing energy. The measurement is thus performed in the range $2m_\mu < m_U < 1000$ MeV with the constraint $m_{h'} < m_U$.

The production cross section of the dark Higgsstrahlung process is proportional to the product $\alpha_D \times \epsilon^2$ and depends on the boson masses 21). Fig.1 shows the expected cross section in the KLOE range of interest, for $\epsilon = 10^{-3}$ and $\alpha_D = \alpha_{em}$, as a function of $m_{h'}$ and m_U. Values as high as hundreds of fb are reachable in this hypothesis. Compared to the B-factory case 29), KLOE benefits of the 1/s factor and of the resonance-like behaviour expected for the producion cross section 21).

2 The KLOE detector

The KLOE experiment operated from 2000 to 2006 at DAΦNE, the Frascati Φ factory. DAΦNE is an e^+e^- collider running mainly at a center-of-mass energy of ∼1019 MeV, the mass of the Φ meson. Equal energy positron and electron beams collide at an angle of ∼ 25 mrad, producing Φ mesons nearly at rest. The

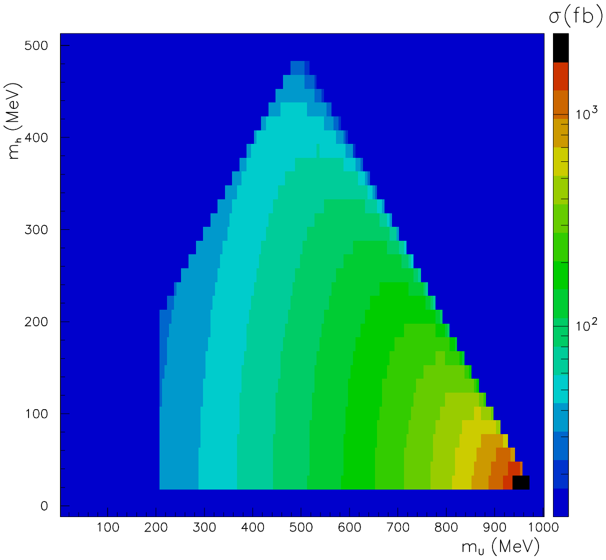

Figure 1: *Dark Higgsstrahlung production cross section for* $\epsilon = 10^{-3}$ *and* $\alpha_D = \alpha_{em}$ *as a function of* $m_{h'}$ *and* m_U.

detector consists of a large cylindrical Drift Chamber (DC), surrounded by a lead-scintillating fiber electromagnetic calorimeter (EMC). A superconducting coil around the EMC provides a 0.52 T field. The beam pipe at the interaction region is spherical in shape with 10 cm radius, it is made of a beryllium-aluminum alloy of 0.5 mm thickness. Low beta quadrupoles are located at about ±50 cm distance from the interaction region. The drift chamber 30), 4 m in diameter and 3.3 m long, has 12,582 all-stereo tungsten sense wires and 37,746 aluminum field wires. The chamber shell is made of carbon fiber-epoxy composite with an internal wall of ∼ 1 mm thickness, the gas used is a 90% helium, 10% isobutane mixture. The spatial resolutions are $\sigma_{xy} \sim 150\mu m$ and $\sigma_z \sim 2$ mm. The momentum resolution is $\sigma_\perp / p_\perp \approx 0.4$ %. Vertexes are reconstructed with a spatial resolution of ∼ 3 mm. The calorimeter 31) is divided into a barrel and two endcaps, for a total of 88 modules, and covers 98% of the solid angle. The modules are read out at both ends by photomultipliers, both in amplitude and time. The readout granularity is $\sim$ (4.4.4) cm^2, for a total of 2440 cells arranged in five layers. The energy deposits are obtained from the signal amplitude while the arrival times and the particles positions are obtained from the time differences. Cells close in time and space are grouped into energy clusters. The cluster energy E is the sum of the cell energies. The cluster time T and position are energy-weighted averages. Energy and time resolutions are $\sigma_E/E = 5.7\%/\sqrt{E(GeV)}$ and $\sigma_t = 57$ ps$/\sqrt{E(GeV)} \oplus$ 100 ps, respectively. The trigger [32] uses both calorimeter and chamber information. In this analysis the events are selected by the calorimeter trigger, requiring two energy deposits with E>50 MeV for the barrel and E>150 MeV for the endcaps. A cosmic veto rejects events with at least two energy deposits above 30 MeV in the outermost calorimeter layer. Data are then analyzed by an event classification filter [33], which selects and streams various categories of events in different output files.

3 Event selection

The analysis of the process $e^+e^- \rightarrow Uh'$, $U \rightarrow \mu^+\mu^-$, h' invisible, has been performed on a data sample of 1.65 fb^{-1} collected during the 2004-2005 KLOE data taking campaign at a center of mass energy of $\sim$ 1019 MeV, corresponding to the mass of the Φ meson (on peak sample), and on a data sample of 0.2 fb^{-1} at a center of mass energy of $\sim$ 1000 MeV (off peak sample), well below the Φ resonance.

The Monte Carlo simulation of the signal process $e^+e^- \rightarrow Uh'$, $U \rightarrow \mu^+\mu^-$, h' invisible, has been produced using an ad hoc generator interfaced with the standard Geanfi KLOE full simulation program. A grid in $m_{h'}$ - m_U masses, with approximate steps of $\sim$ 30 MeV has been generated to cover all the allowed region. The mass resolution was found to be between 0.5 and 2 MeV for m_U (invariant mass of the muon pair) and between 3 and 17 MeV for $m_{h'}$ (missing mass). The signature of the process would thus be the appearance of a sharp peak in the bidimensional distribution $M_{\mu\mu}$ - M_{miss}. We define θ as the polar angle direction of the muon pair momentum (momentum of the U boson, opposite to that of the h', in case of dark Higgsstrahlung events). Contrarily to most of the dominant QED background processes, the signal is predicted to show a large angle production in θ, with two dominant terms proportional to $sin\theta$ and $sin^3\theta$ [21].

As a first step of the analysis, a preselection was performed by requiring:

- events with only two opposite charge tracks, with a reconstructed vertex inside a 4×30 cm cylinder around the interaction point;
- each track must have an associated EMC cluster;
- the visible momentum direction has to be in the barrel: $|cos\theta| < 0.75$;
- the momenta of the two tracks must be individually below 460 MeV;
- the modulus of the missing momentum must exceed 40 MeV.

After this selections (mostly aimed at rejecting QED backgrounds), the hermeticity and tightness of the electromagnetic calorimeter was used as a veto to avoid the presence of photons in the event. It was required to have no unassociated energy deposition with E>15 MeV on EMC. The inefficiency of the calorimeter as a function of the energy was studied with a sample of radiative Bhabhas $e^+e^- \to e^+e^-\gamma$ reconstructed with the DC only, with the missing momentum direction (corresponding to the direction of the photon) pointing to the barrel: $|cos\theta| < 0.75$. It was found that the EMC inefficiency in photon detection started below 10% level at 20 MeV, to fall down to $\sim 1\%$ at ~ 70 MeV and to 0.1% at ~ 200 MeV.

The event selection then proceeded by applying particle identification (PID) algorithms to the two charged tracks. These were almost entirely based on the excellent energy and time resolution of the EMC. A set of neural network, organised for different values of track momentum and polar angle, was trained on simulated Monte Carlo samples to perform muon to electron discrimination. The neural networks used five input variables (three of them related with energy depositions in calorimeter planes, i.e. the longitudinal shower profile, energy to momentum ratio, cluster time, related to the time of flight and thus to the particle velocity) and one output. The PID performances, checked on selected data samples of $e^+e^- \to e^+e^-$, $e^+e^- \to \mu^+\mu^-$, $e^+e^- \to \pi^+\pi^-$ were found to be excellent: the fraction of $e^+e^- \to \mu^+\mu^-$ events, in which both tracks were required to be identified as muons, was measured to be 85%, while the fraction of residual $e^+e^- \to e^+e^-$ events was 10^{-4} and the fraction of doubly tagged $e^+e^- \to \pi^+\pi^-$ was $\sim 50\%$ (muon and pion induced showers look very similar at KLOE energies).

After the missing energy and the PID selections, a huge background from $\Phi \to K^+K^-$, $K^\pm \to \mu^\pm\nu$ events survives in the on peak sample. This corresponds to the fraction of doubly early leptonically decaying charged kaons in the IP region. Charged kaons have in KLOE an average decay length of ~ 90 cm. The reconstructed vertex of the extrapolated muon tracks is thus expected to be displaced from the IP, due to the charged kaon lifetime, and with a bad χ^2 of the fitting procedure. Cuts on the radial and z projections of the distance between the reconstructed vertex and the IP and on the χ^2 of the fit allowed to reduce by a factor ~ 35 the $\Phi \to K^+K^-$, $K^\pm \to \mu^\pm\nu$ background.

Events surviving all the described selections were organized in bidimensional histograms with the muon pair mass $M_{\mu\mu}$ and the event missing mass M_{miss} on the two axes. The binning was chosen such as to keep most of the signal in one bin only. In $M_{\mu\mu}$ a 5 MeV bin width was enough over all the plane; while for M_{miss} a variable binning of 15, 30 and 50 MeV widths was chosen. According to the simulation, a fraction of 90÷95% of the signal was contained in one bin. The selection efficiency, estimated from the Monte Carlo on the generated points of the m_U-$m_{h'}$ grid, was found to be between 15% and 25%, depending on the masses, with most frequent values ∼20%. The efficiency for a generic point on the $M_{\mu\mu}$-M_{miss} plane was then evaluated by linear interpolation between the two closest available generated points lying on opposite sides of the considered one.

Several sources of systematic uncertainties in the signal efficiency evaluation were taken into account. Uncertainties from the PID procedure were estimated by selecting samples of $e^+e^- \to \mu^+\mu^-\gamma$ in data and Monte Carlo, applying the PID algorithms to them and studing the differences between the samples. The results were used first to correct the Monte Carlo efficiency as a function of the track momentum and then to quote a systematic uncertainty, assumed to be of the order of the average correction. An 8% effect was ascribed to this source. The same $e^+e^- \to \mu^+\mu^-\gamma$ samples selected in data and in the simulation were used to evaluate the effect of the cut on the vertex-IP distance. A 12% average difference was found and used to correct the Monte Carlo efficiency. A 3% effect due to the spread of this correction as a function of the missing momentum polar angle direction was assigned to this source. The systematic uncertainty due to the usage of the EMC veto was evaluated by selecting samples of $\Phi \to K^+K^-$, $K^\pm \to \mu^\pm\nu$ in data and Monte Carlo. In this case, the cut on the vertex-IP distance was removed to increase the size of the statistical sample. A 2% difference was observed and used both to correct the Monte Carlo efficiency and to quote a systematic uncertainty due to this source. Finally, a 5% uncertainty was estimated due to interpolation and binning effects in the efficiency evaluation procedure. A total ±10% systematic uncertainty was then evaluated as the quadratic sum of all the above effects.

4 Results

Results are shown in fig.2 for the on peak and off peak samples respectively. In the left plot of fig.2 (on peak sample) several sources of backgrounds are easily distinguishable: $\Phi \to K^+K^-$, $K^\pm \to \mu^\pm\nu$ (triangular region at the left of the populated part of the distribution), $\Phi \to \pi^+\pi^-\pi^0$ (mostly horizontal band, corresponding to events in which both photons from π^0 decay are undetected), continuum backgrounds $e^+e^- \to \mu^+\mu^-$ and $e^+e^- \to \pi^+\pi^-$ (diagonal bands starting from the right-bottom part of the distribution), $e^+e^- \to e^+e^-\mu^+\mu^-$ and $e^+e^- \to e^+e^-\pi^+\pi^-$ (two photon events, top part of the distribution, for $M_{miss} > 350MeV$). In the distribution in the right plot of fig.2 (off peak sample) all the backgrounds from the Φ decays are strongly suppressed.

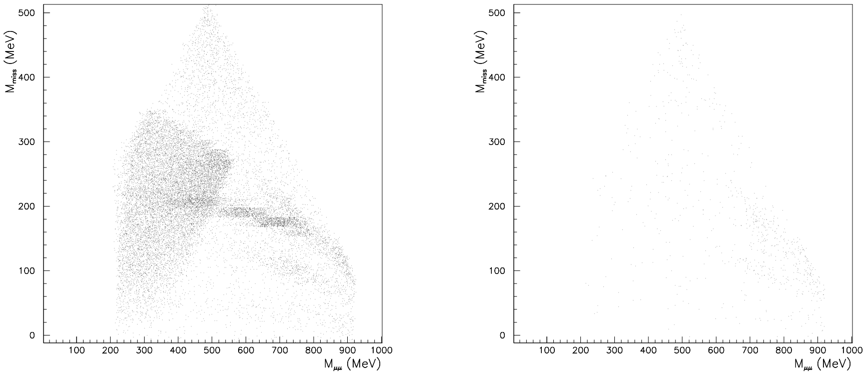

Figure 2: *Results for on peak sample (left plot, 1.65 fb^{-1} integrated luminosity) and off peak sample (right plot, 0.2 fb^{-1} integrated luminosity).*

In order to search for possible signals or to set upper limits to the production of the dark Higgsstrahlung process, an accurate estimate of the background

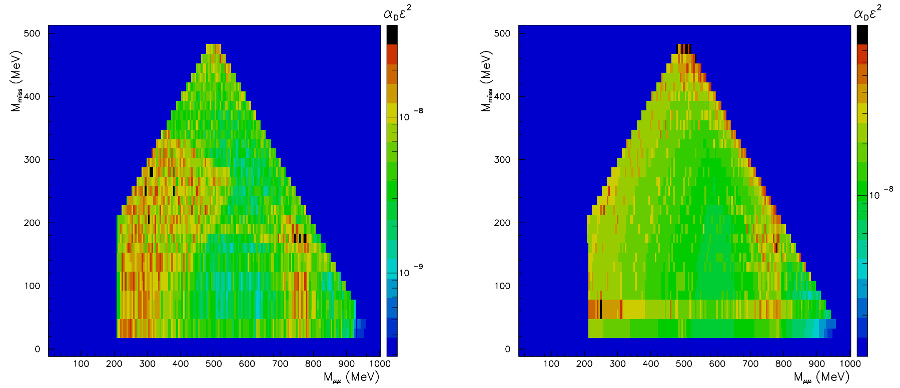

Figure 3: *90% CL upper limits in* $\alpha_D \times \epsilon^2$ *for the on peak sample (left plot) and off peak sample (right plot).*

is needed. At the time of the workshop, mostly for technical problems, a complete Monte Carlo simulation for all the contributing background processes was not available. The background was then evaluated directly on the data. A 5×5 bin matrix in the $M_{\mu\mu}$-M_{miss} plane was built and moved all along the populated regions of fig.2. The average of the content of the 24 bins surrounding the central one, where the presence of a possible signal is checked, was assumed to be an estimate of its background. No evidence of the dark Higgsstrahlung process was found. Using uniform prior distributions, 90% confidence level Bayesian upper limits on the number of events were derived bin by bin, separately for the on peak and off peak samples. These results were then converted in terms of the dark Higgstrahlung production cross section parameters $\alpha_D \times \epsilon^2$ by using:

- the integrated luminosity information;
- the signal efficiency as described above;
- the dark Higgsstralung cross section and the branching fraction of the U boson decay into muon pairs as in reference 21);

The small fraction of the signal outside the central bin of the 5×5 matrix was explicitly taken into account into the likelihood expression. The 10% systematic

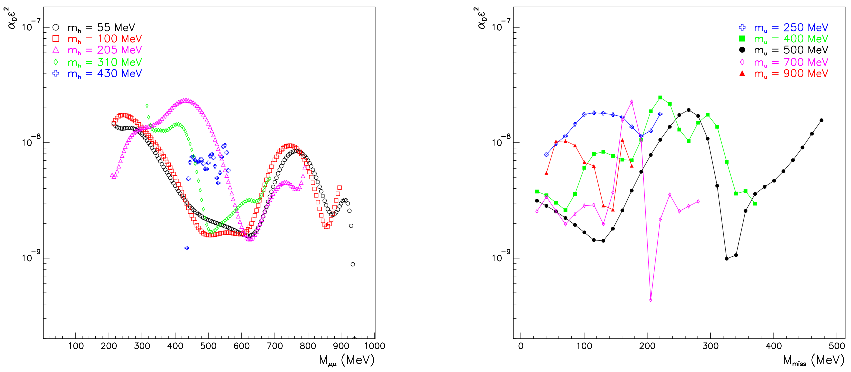

Figure 4: *Combined 90% CL upper limits in $\alpha_D\epsilon^2$ as a function of $M_{\mu\mu}$ for different values of $m_{h'}$ (left plot) and as a function of M_{miss} for different values of m_U (right plot).*

uncertainties on the signal efficiency were taken into account by convolving the likelihood with gaussian distributions with variances set equal to the estimated systematic errors. The $\alpha_D \times \epsilon^2$ 90% CL limits are shown in fig.3 separately for the on peak and off peak sample. These results were then combined by taking into account the different integrated luminosities of the two samples and the expected slightly different signal efficiencies and cross sections due to the different center of mass energies. The combined 90% CL upper limits were then projected in the $M_{\mu\mu}$ and M_{miss} directions and slightly smoothed, just to make them more readable. They are shown in fig.4. These limits are largely dominated by the available data statistics. Values as low as $10^{-9}\div10^{-8}$ in $\alpha_D\epsilon^2$ are excluded at 90% CL for a large range of the dark photon and dark Higgs masses.

5 Conclusions

A search for the dark Higgsstrahlung process has been performed by KLOE in the range $2m_\mu < m_U < 1000$ MeV with $m_{h'} < m_U$. No signal has been observed and upper limits on the product of the mixing angle and the dark coupling constant have been set in the range $10^{-9}\div10^{-8}$ in $\alpha_D\epsilon^2$. Assuming

$\alpha_D = \alpha_{em}$ these measurements translate into limits on the mixing angle in the range $10^{-4}\div10^{-3}$. These results are numerically comparable with those of Babar 29) and complement them as they refer to the same process in a different final state and in a different region of the phase space.

At KLOE2/DAΦNE2 the larger expected integrated luminosity and the presence of a high resolution Inner Tracker detector are expected to improve these results at least by a factor 2, thus allowing a study deep inside the $\epsilon \approx 10^{-4}$ parameter space region.

References

1. P.Jean *et al*, Astron. Astrophys., **407** (2003), p. L55
2. O. Adriani *et al.* Nature, **458** (2009), p. 607
3. J. Chang *et al.* Nature, **456** (2008), p. 362
4. A.A. Abdo *et al.* Phys. Rev. Lett., **102** (2009), p. 181101
5. F. Aharonian *et al.* Phys. Rev. Lett., **101** (2008), p. 261104
6. F. Aharonian *et al.* Astron. Astrophys., **508** (2009), p. 561
7. R. Bernabei *et al.* Int. J. Mod. Phys. D, **13** (2004), p. 2127
8. R. Bernabei *et al.* Eur. Phys. J. C, **56** (2008), p. 333
9. C.E. Aalseth *et al.* Phys. Rev. Lett., **107** (2011), p. 141301
10. M. Pospelov, A. Ritz, M.B. Voloshin Phys. Lett. B, **662** (2008), p. 53
11. N. Arkani-Hamed, D.P. Finkbeiner, T.R. Slatyer, N. Weiner Phys. Rev. D, **79** (2009), p. 015014
12. D.S.M. Alves, S.R. Behbahani, P. Schuster, J.G. Wacker Phys. Lett. B, **692** (2010), p. 323
13. M. Pospelov, A. Ritz Phys. Lett. B, **671** (2009), p. 391
14. J. Hisano, S. Matsumoto, M.M. Nojiri Phys. Rev. Lett., **92** (2004), p. 031303

15. M. Cirelli, M. Kadastik, M. Raidal, A. Strumia Nucl. Phys. B, **813** (2009), p. 1
16. J. March-Russell, S.M. West, D. Cumberbatch, D. Hooper JHEP, **0807** (2008), p. 058
17. I. Cholis, G. Dobler, D.P. Finkbeiner, L. Goodenough, N. Weiner Phys. Rev. D, **80** (2009), p. 123518
18. I. Cholis, D.P. Finkbeiner, L. Goodenough, N. Weiner JCAP, **0912** (2009), p. 007
19. N. Arkani-Hamed, N. Weiner JHEP, **0812** (2008), p. 104
20. R. Essig, P. Schuster, N. Toro Phys. Rev. D, **80** (2009), p. 015003
21. B. Batell, M. Pospelov, A. Ritz Phys. Rev. D, **79** (2009), p. 115008
22. M. Reece, L.T. Wang JHEP, **0907** (2009), p. 051
23. N. Borodatchenkova, D. Choudhury, M. Drees Phys. Rev. Lett., **96** (2006), p. 141802
24. P.F. Yin, J. Liu, S.h. Zhu Phys. Lett. B, **679** (2009), p. 362
25. J.D. Bjorken, R. Essig, P. Schuster, N. Toro Phys. Rev. D, **80** (2009), p. 075018
26. B. Batell, M. Pospelov, A. Ritz Phys. Rev. D, **80** (2009), p. 095024
27. R. Essig, P. Schuster, N. Toro, B. Wojtsekhowski JHEP, **1102** (2011), p. 009
28. M. Freytsis, G. Ovanesyan, J. Thaler JHEP, **1001** (2010), p. 111
29. J.P. Lees *et al.* (BaBar Collab.) Phys. Rev. Lett. **108** (2012) 211801
30. M. Adinolfi *et al.* Nucl. Instr. Meth. A, **488** (2002), p. 51
31. M. Adinolfi *et al.* Nucl. Instr. Meth. A, **482** (2002), p. 364
32. M. Adinolfi *et al.* Nucl. Instr. Meth. A, **492** (2002), p. 134
33. F. Ambrosino *et al.* Nucl. Instr. Meth. A, **534** (2004), p. 403

Frascati Physics Series Vol. LVI (2012)
Dark Forces at Accelerators
October 16-19, 2012

SEARCH FOR LONG-LIVED EXOTIC PARTICLES AT LHCb

V.A.M. Heijne
Nikhef National Institute for Subatomic Physics, Amsterdam, The Netherlands

Abstract

Many beyond the Standard Model theories propose the existence of a long-lived heavy particle decaying into Standard Model particles. The decay of those neutral long-lived particles provides a displaced vertex; a signature which can be detected with the LHCb detector at the Large Hadron Collider. A search has been performed for a Higgs-like boson decaying into two neutralinos, using the dataset collected at the LHCb detector in 2010 corresponding to an integrated luminosity of approximately 35.8 pb^{-1}. The analysis is sensitive to long-lived particle lifetimes from 3 to 25 ps and masses between 30 and 55 GeV. No evidence for the production of these long-lived states is observed, and limits are set on their production rates.

1 Introduction

Although the Standard Model has proven to be a successful description of particle physics, it leaves several fundamental questions unanswered, such as the hierarchy of mass scales, neutrino oscillations, matter-antimatter asymmetry, and the nature of dark matter and dark energy. There exists a wide variety of theoretical models that can solve some of these problems. Several of those models predict the existence of new massive long-lived particles with a measurable flight distance. Those particles would produce vertices displaced from the interaction region, which the LHCb detector can reconstruct efficiently 1).

A first class of models featuring long-lived particles originates in weak scale supersymmetry (SUSY). If R-parity violation in SUSY is allowed, the lightest superpartner decays into Standard Model particles, which leave a displaced vertex signature. A particular model in the framework of minimal supergravity (mSUGRA) R-parity violation models is proposed by Carpenter, Kaplan and Rhee 2). In this model the lightest neutralino $\tilde{\chi}_1^0$ has a mass in the range 20-60 GeV/c^2 and it decays into three quarks through baryon number violation (BV). Such decays give rise to three soft jets with a total invariant mass related to that of the original sparticle 3). This study considers neutralino lifetimes in the range from 3 to 25 ps, compatible with the limits on the baryon number violating couplings λ'' 4) 5). The production of $\tilde{\chi}_1^0$ mainly happens in pairs through the decay of the light Higgs boson h^0 with a mass 110-120 GeV/c^2. At a small value of $\tan\beta$, the SUSY h^0 is essentially equivalent to the Standard Model Higgs, with an expected production cross-section of about 20 pb at 7 TeV pp collisions 6).

A second example is the Hidden Valley (HV) model, in which a new non-abelian gauge group exists, hidden by a large energy scale 7) 8). The Hidden Valley region may be accessible at the LHC, resulting in the decay of hidden particles into Standard Model particles. A Higgs boson may exist which decays with a significant branching fraction as $h^0 \to \pi_\nu \pi_\nu \to b\bar{b}b\bar{b}$, where the π_ν is a new scalar long-lived particle.

2 LHCb Detector

The analysis is performed using data collected by LHCb during 2010, corresponding to an integrated luminosity of 35.8 pb^{-1}.

The LHCb detector 1) is a single-arm forward spectrometer covering the approximate pseudorapidity range $2 < \eta < 5$, designed for the study of particles containing b or c quarks. The detector includes a high precision tracking system with a silicon-strip vertex detector (the VErtex LOcator or VELO) surrounding the pp interaction region, enclosed by an RF-foil shielding the sensors from the radio frequency perturbation produced by the beams. In addition, the tracking system consists of a large-area silicon-strip detector located upstream of a dipole magnet with a bending power of about 4 Tm, and three stations of silicon-strip detectors and straw drift-tubes placed downstream. Charged hadrons are identified using two ring-imaging Cherenkov detectors. Photon, electron and hadron candidates are measured by a calorimeter system. Muons are identified by a muon system composed of alternating layers of iron and multiwire proportional chambers.

3 Simulated Samples

Monte Carlo events are used to investigate the sensitivity of LHCb to the long-lived particle production and decay processes and to provide an estimate of the overall Higgs detection efficiency. This analysis considers the BV48 and HV10 models, assuming a branching fraction of unity for the Higgs decaying into two long-lived particles. The signal events are generated using Pythia 6.423 9). The baryon number violation model BV48 has the following parameters: the lifetime of the long-lived particle (τ_{LLP} = 10 ps), the mass of the long-lived particle (m_{LLP} = 48 GeV/c^2), the Higgs mass (m_{h^0} = 114 GeV), and the standard MSSM parameters (M1 = 62 GeV, M2 = 250 GeV, $\tan\beta = 5$ and μ = 140 GeV). The Hidden Valley model HV10 has the parameters (τ_{LLP} = 10 ps), (m_{LLP} = 35 GeV) and (m_{h^0} = 130 GeV).

For an integrated luminosity of 35.8 pb^{-1}, both models predict about 160 events with at least one reconstructible displaced vertex in the acceptance, and 80 events with at least two vertices. In addition to the signal samples, simulated Standard Model events are used, namely 8.5 M inclusive $b\bar{b}$ events (i.e. events with b-hadrons) with an enhanced contribution of displaced b-hadron decays. The $t\bar{t}$ and $c\bar{c}$ backgrounds are found to be negligible. For the simulation, pp collisions are generated using Pythia with a specific LHCb configuration 10). The interaction of the generated particles with the detector and its response are implemented using the Geant4 toolkit 11) 12) as described in 13).

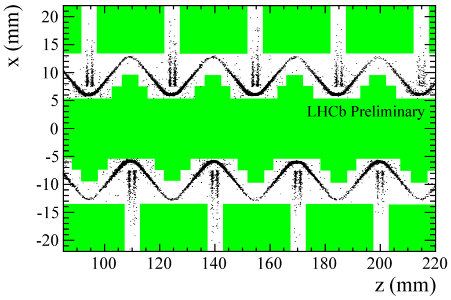

Figure 1: *Distribution in x and z, for $|y| < 1$ mm, of the reconstructed candidate vertices. The visible structures reflect the geometry of the VELO detector, with the doublets of silicon sensors appearing as pairs of vertical bands and the RF foil as the two wave shapes. The green-shaded region represents the fiducial vacuum volume in which displaced vertex candidates are accepted.*

4 Event Selection

4.1 Online Selection

The trigger consists of a hardware stage, based on information from the calorimeter and muon systems, followed by two software stages. The software levels include lines specially defined to select displaced vertices which are reconstructed by a vertexing algorithm in the trigger. The trigger accepts events with two or more displaced vertices, each having no backward going tracks (pseudorapidity in the range $-3.5 < \eta < -1.5$), at least four forward tracks ($2 < \eta < 5$) which form an invariant mass larger than 3 GeV and a distance to the beam-line larger than 0.4 mm. Furthermore there should be at least one primary vertex in the event and at least two candidate vertices downstream of the most upstream primary vertex.

The main source of background arises from particles that have interacted with the detector material. Candidate vertices are required to be in a fiducial volume (of which a slice is shown in fig. 1) defined to exclude the VELO sensors and the RF foil.

A total number of 58,552 events pass the above selection criteria. An identical selection is applied to the signal and background MC samples. Using the measured cross-section $\sigma_{b\bar{b}} = 287 \pm 40\,\mu$b 14) 15) , the analysis of the

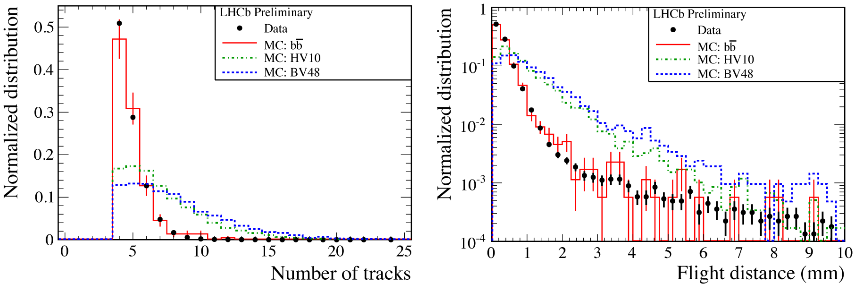

Figure 2: *Number of tracks and flight distance of the long-lived candidates selected at the trigger level.*

inclusive $b\bar{b}$ MC sample predicts $(75 \pm 13) \times 10^3$ events at this stage. Fig. 2 indicates that not only the number of events, but also the distributions in data are compatible with $b\bar{b}$ as the dominant background.

4.2 Offline Selection

The two long-lived particles are expected to travel almost back-to-back in the transverse (x,y) plane, in the absence of radiative effects. Fig. 3 shows the azimuthal angle $\Delta\phi$ between the position vectors drawn from the primary vertex to the displaced vertices. Pairs of candidates with $\Delta\phi > 2.8$ rad are combined to form a parent (Higgs) candidate.

The total number of Higgs-like candidates after the above selection is 13,893 and the resulting invariant mass distribution of candidates is shown in fig. 3. A likelihood fit is performed to the data using the expected shapes of the BV48 signal and of the simulated $b\bar{b}$ events. The fit yields a number of signal events compatible with zero (43 ± 198 signal events with $14,316 \pm 713$ $b\bar{b}$ and a fit χ^2 of 1.4 per degree of freedom). The data are therefore consistent with $b\bar{b}$ background.

The final selection requires at least six tracks and an invariant mass larger than 6 GeV for each candidate. Additionally the displaced vertex position error is required to be $\sigma_r < 0.05$ mm and $\sigma_z < 0.24$ mm. The cuts have been chosen to remove all the Standard Model background, while optimizing the Higgs signal detection efficiency, ϵ. This efficiency can be found in tab. 1 for different stages of the event selection. For the BV48 model $\epsilon = (0.384 \pm 0.017)$ % is

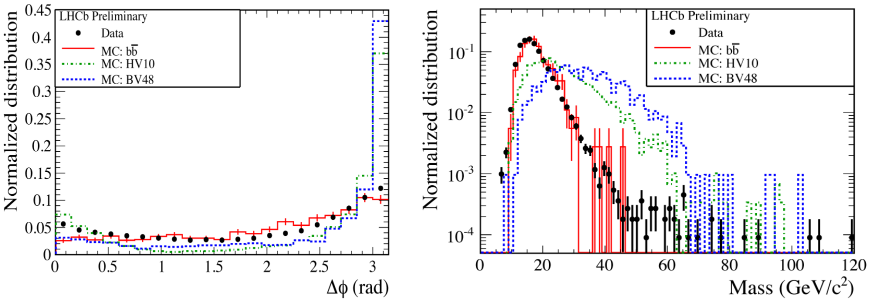

Figure 3: *The azimuthal angle difference and the invariant mass, both normalized to one, of the pairs of long-lived particle candidates selected by the azimuthal angle cut* $\Delta\phi > 2.8$.

predicted, resulting in two expected events in an integrated luminosity of 35.8 pb^{-1}. No data events survive the final selection.

5 Systematic uncertainties

The contributions to the systematic uncertainty are summarized in tab. 2. The uncertainty on the trigger efficiency has been estimated by comparing the number of $b\bar{b}$ events with large time of flight in data and simulation, and agrees within a statistical uncertainty of 15 %. Conservatively this value is adopted as the systematic uncertainty on the trigger efficiency. In addition the results have been cross-checked by using candidates generated in the detector material, and by sampling with independent triggers.

The uncertainty on the total track reconstruction efficiency has been estimated from a comparison of the number of tracks observed in the candidates in data and $b\bar{b}$ MC events. The quoted contribution of 7 % is inferred by artificially varying the track efficiency in simulated events.

The comparison of data and MC distributions gives a calibration uncertainty of 10 % on the measurement of the p_T and the mass of the long-lived particle, and of ±0.01 mm on the vertex position errors σ_r and σ_z. By shifting the cuts by these amounts the quoted contributions of 6 % and 12 % are obtained.

The effect of the fiducial volume requirement has been estimated by taking

Requirement	ϵ (%)
One LLP in acceptance (generator cut)	29.4
LLP preselection	44.1
Trigger	35.5
Fiducial volume	95.8
LLP selection	66.4
Two LLP found	19.1
$\Delta\phi$ cut	68.4
Total	0.384
Total without trigger	0.589

Table 1: *Fraction of the BV48 signal events surviving at different stages of the analysis.*

Source	%
Integrated luminosity	4
Trigger	15
Track reconstruction	7
p_T and mass calibration	6
Vertex reconstruction	12
Fiducial volume	4
Beam-line position	1
Total	22

Table 2: *Systematic uncertainties on the Higgs detection efficiency.*

into account only displaced vertices restricted to a radial distance < 4.5 mm from the beam-line, far from the RF foil.

A possible bias coming from the cut on the radial distance with respect to the beam-line position uncertainty has been estimated to contribute with less than 1 %.

6 Results and Conclusion

Since no events pass the final selection criteria, the analysis for a particular point of the BV model (m_{LLP}=48 GeV, a lifetime of 10 ps, and m_{h^0}=114 GeV) results in a cross-section upper limit of 32 pb at 95 % CL.

A full MC simulation is made for several other points in the BV model parameter space (varying τ_{LLP}, m_{LLP} and m_{h^0}). In order to cover a larger region of the parameter phase space of the theoretical model, a fast simulation program has been developed, which runs over $h^0 \rightarrow \tilde{\chi}_1^0 \tilde{\chi}_1^0$ events generated by PYTHIA 9). The charged particles selected within the LHCb acceptance are fed to a vertex reconstruction algorithm similar to the one for real data. Inefficiencies are parameterized as a function of the vertex position to simulate the fiducial volume requirement.

The procedure is compared with the full simulation and tuned to obtain the correct shape for the most relevant distributions. The systematic uncertainties are assumed to be the same as for the full simulation. The results of the fast simulation, which can be found in 16), correspond well with the sample points of the full simulation.

References

1. LHCb collaboration, A.A. Alves Jr. *et al*, The LHCb detector at the LHC, JINST **3** (2008) S08005.
2. L.M. Carpenter, D.E. Kaplan, and E.-J. Rhee, Six-quark decays of the Higgs boson in supersymmetry with R-parity violation, Phys. Rev. Lett. **99** (2007) 211801, arXiv:hep-ph/0607204.
3. J.M. Butterworth, J.R. Ellis, A.R. Raklev, and G.P. Salam, Discovering baryonnumber violating neutralino decays at the LHC, Phys. Rev. Lett. **103** (2009) 241803, arXiv:0906.072.
4. R. Barbier *et al*, R-parity-violating supersymmetry, Physics Reports **420** (2005) 1, arXiv:hep-ph/0406039
5. H.K. Dreiner, M. Kramer, and B. O'Leary, Bounds on R-parity violation from leptonic and semi- leptonic meson decays, Phys. Rev. **D75** (2007) 114016, arXiv:hep-ph/0612278.
6. LHC Higgs Cross Section Working Group, Higgs cross sections at 7, 8 and 14 TeV, (April 2012), https://twiki.cern.ch/twiki/bin/view/LHCPhysics/.
7. M.J. Strassler and K.M. Zurek, Echoes of a hidden valley at hadron colliders, Phys. Lett. **B651** (2007) 374, arXiv:hep-ph/0604261

8. M.J. Strassler and K.M. Zurek, Discovering the Higgs through highly-displaced vertices, Phys. Lett. **B661** (2008) 263, arXiv:hep-ph/0605193.

9. T. Sjöstrand, S. Mrenna, and P. Skands, PYTHIA 6.4 Physics and manual, JHEP **05** (2006) 026, arXiv:hep-ph/0603175.

10. I. Belyaev *et al*, Handling of the generation of primary events in Gauss, the LHCb simulation framework, Nuclear Science Symposium Conference Record (NSS/MIC) IEEE (2010) 1155.

11. GEANT4 collaboration, J. Allison *et al*, Geant4 developments and applications, IEEE Trans. Nucl. Sci. **53** (2006) 270

12. GEANT4 collaboration, S. Agostinelli *et al*, GEANT4: A simulation toolkit, Nucl. Instrum. Meth. **A506** (2003) 250.

13. M. Clemencic *et al*, The LHCb simulation application, Gauss: design, evolution and experience, Journal of Physics: Conference Series **331** (2011), no. 3 032023.

14. LHCb collaboration, R. Aaij *et al*, Measurement of J/ψ production in pp collisions at $\sqrt{s} = 7$ TeV, Eur. Phys. J. **C71** (2011) 1645, arXiv:1103.0423

15. LHCb collaboration, R. Aaij *et al*, Measurement of $\sigma(pp \to b\bar{b}X)$ at $\sqrt{s} = 7$ TeV in the forward region, Phys. Lett. **B694** (2010) 209, arXiv:1009.2731.

16. LHCb collaboration, R. Aaij *et al*, Search for Higgs-like bosons decaying into long-lived exotic particles (2012), LHCb-CONF-2012-014.

Frascati Physics Series Vol. LVI (2012)
DARK FORCES AT ACCELERATORS
October 16-19, 2012

A force beyond the Standard Model
–
Status of the quest for hidden photons

Joerg Jaeckel
Institut für theoretische Physik, Universität Heidelberg,
Philosophenweg 16, 69120 Heidelberg, Germany

Abstract

In this note we discuss the search for new gauge forces beyond the Standard Model. In particular we give an overview for the simplest case of a new U(1), kinetically mixed with the Standard Model photon (hypercharge boson), a so-called hidden photon (also known as dark photon, heavy photon or A').

1 Introduction

The Standard Model (SM) features three gauge forces, electromagnetism, the weak force and the strong force. The corresponding gauge group is U(1) × SU(2) × SU(3). This is certainly not an obvious structure, and it is therefore only natural to ask if these are the only ones or, if there are additional (gauge) forces.

In this note we concentrate on the simplest case: an extra $\mathrm{U}(1)_X$ kinetically mixed with the electromagnetic/hypercharge U(1) of the Standard Model. This corresponds to an extra photon-like particle, the hidden photon (HP).

Of course, when looking for a new extra force we immediately have to confront the question why we have not seen it. This is directly linked to the properties of the new gauge bosons responsible for the force. In principle there are two ways in which particles can hide from observation in experiments. The first, and so far the most commonly investigated, is that the new particles are very heavy. In this case one needs a lot of energy to create them and forces mediated by them are of extremely short range. Moreover, heavy particles that are not protected by a new symmetry decay very fast. The second option is that the interactions between the new particles and those of the SM are extremely weak. In this case their effects would simply be too feeble to have been observed so far. This is why such particles are often referred to as belonging to a so-called hidden sector. Particles in these hidden sectors could even be very light, potentially even massless.

These two possibilities suggest that exploring new physics is in a sense (at least) two-dimensional. One needs to explore in the direction of higher mass and energy, as well as in the complementary direction of very weak couplings. This suggests two entirely different search strategies. Higher masses can be most directly explored in high energy experiments like, for example, the Large Hadron Collider (LHC) at CERN. Probing very weak couplings requires high precision/intensity/luminosity but can often be done at fairly low energies. Both approaches nicely complement each other as can be seen in the case of an extra U(1) that we discuss in this note.

2 Hidden photons

Let us consider an extra U(1) gauge group. If all Standard Model particles are uncharged under this new gauge group the dominant interaction with ordinary matter is via kinetic mixing 1) with the hypercharge U(1) gauge boson. This is encoded in the following Lagrangian,

$$\begin{aligned}\mathcal{L} \supset\ & -\frac{1}{4}W^a_{\mu\nu}W^{a,\mu\nu} - \frac{1}{4}B_{\mu\nu}B^{\mu\nu} - \frac{1}{4}X_{\mu\nu}X^{\mu\nu} - \frac{\chi_{\scriptscriptstyle Y}}{2}B_{\mu\nu}X^{\mu\nu} \qquad (1)\\ +\ & \frac{m_X^2}{2}X_\mu X^\mu + \frac{1}{2}\frac{m_W^2}{g^2}(-gW^3_\mu + g'B_\mu)^2 + \frac{1}{2}m_W^2(W^1_\mu W^{1,\mu} + W^1_\mu W^{1,\mu})\\ +\ & \text{SM matter and Higgs terms,}\end{aligned}$$

where B_μ and W_μ denote the usual electroweak gauge fields and X_μ denotes the hidden U(1) field with gauge coupling g_X. Importantly the term $\frac{\chi_Y}{2}B_{\mu\nu}X^{\mu\nu}$ introduces a mixing between X_μ and B_μ.

The naive one loop estimate for the mixing parameter is

$$\chi_{\scriptscriptstyle Y} \sim \frac{eg_{\scriptscriptstyle X}}{6\pi^2}\log\left(\frac{m}{\Lambda}\right) \qquad (2)$$

where m is the mass of a heavy particle coupled to both the new U(1) and hypercharge and Λ is some cutoff scale. In general models of field 1) and string theory 2, 3, 4, 5, 6, 7, 8, 9, 10, 11, 12, 13, 14) a wide range of kinetic mixing parameters are predicted, stretching from $\chi \sim 10^{-12}$ to $\chi \sim 10^{-3}$.

In general, the HP mass might result from a Higgs or a Stückelberg mechanism. In the first case a Higgs particle appears in the spectrum, with mass $\sim \sqrt{\lambda}m_X/g_X$ where g_X is the hidden sector gauge coupling and λ the Higgs self-coupling. Even if we take g_X to be relatively small, the Higgs particle phenomenology tightly constrains this scenario, especially for sub-eV values of m_X 15). However, for very small g_X, as one finds in large volume string scenarions 16, 9, 13), viable hidden Higgs models can be realized. The expected regions are shown inside the dotted lines in Fig. 2. The Stückelberg case also occurs naturally in large volume string compactifications 9, 13). Typical expected parameter values are indicated by the dash-dotted lines of Fig. 2.

At energies far below the electroweak scale and for small masses of the new gauge boson, $m_X \ll m_W$, we can consider only the remaining light degrees of freedom and the mixing is directly with the photon,

$$\mathcal{L} \supset -\frac{1}{4}F_{\mu\nu}F^{\mu\nu} - \frac{1}{4}X_{\mu\nu}X^{\mu\nu} - \frac{\chi}{2}F_{\mu\nu}X^{\mu\nu} + \frac{m_X^2}{2}X_\mu X^\mu + j_\mu A^\mu, \qquad (3)$$

where the mixing with the photon is related to that with the hypercharge via

$$\chi = \chi_{\scriptscriptstyle Y}\cos(\theta_W), \qquad (4)$$

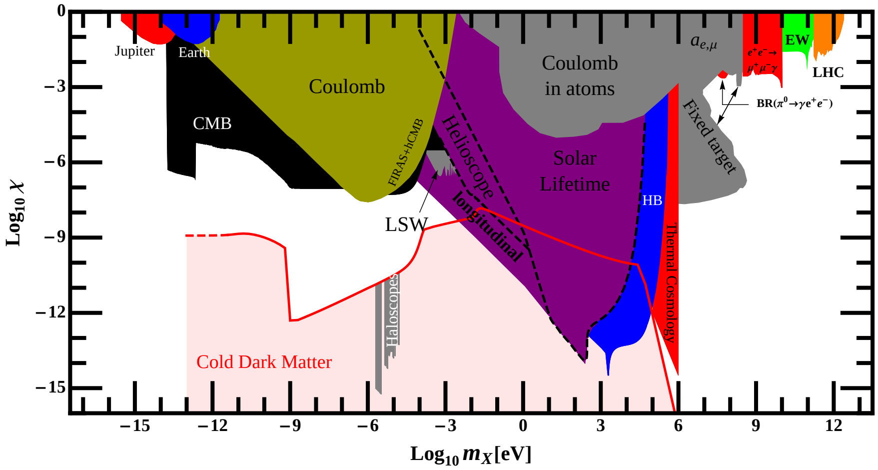

Figure 1: *Limits on the kinetic mixing of a hidden photon with the ordinary photon. Figure updated from* [17] *with new and improved limits from* [18, 19, 20, 21]*. The area shaded in light red gives the area where HPs can be cold dark matter* [22]*.*

where θ_W is the Weinberg angle. For later convenience we have also included the coupling to the electromagnetic current j_μ.

As we can see the kinetic mixing and the mass of the new particle are the only two new parameters. The current constraints are shown in Fig. 1. In the following sections we will sketch some of these constraints as well as prospects for future searches.

3 A matter of convenience: a new force or photon–HP oscillations

In Eq. (3) we have introduced the somewhat unusual kinetic mixing term. To get a better understanding it is convenient to remove this term by a suitable field re-definition. There are two simple field re-definitions that we can use to remove the kinetic mixing term[1]:

(1) $A^\mu \to A^\mu - \chi X^\mu$.

---

[1] Here and in the following we neglect terms of the order of χ^2.

(2) $X^{\mu} \to X^{\mu} - \chi A^{\mu}$.

Although the resulting physics is, of course, completely equivalent, the physical picture resulting from both shifts is somewhat different. Depending on the situation it is often easier to use one or the other picture. Let us now briefly consider both pictures.

3.1 Option (1): A Z' and a new force

Inserting the shift $A^{\mu} \to A^{\mu} - \chi X^{\mu}$ into Eq. (3) removes the kinetic mixing term,

$$\mathcal{L} \supset -\frac{1}{4}F_{\mu\nu}F^{\mu\nu} - \frac{1}{4}X_{\mu\nu}X^{\mu\nu} + \frac{m_X^2}{2}X_{\mu}X^{\mu} + j_{\mu}(A^{\mu} - \chi X^{\mu}). \tag{5}$$

We now have two nicely independent particles. A massless particle A and a massive particle X. X is a massive uncharged vector particle. In that sense it is similar to a Z boson and therefore it is a special case of a so-called Z'.

A is the ordinary photon and couples to the electromagnetic current

$$j^{\mu} = en^{\mu}, \tag{6}$$

where e is the electric charge and n^{μ} is the number current of charged particles with unit charge.

X is the new hidden photon and it couples to ordinary matter via

$$-\chi j_{\mu}X^{\mu} = -\chi e n_{\mu} X^{\mu}. \tag{7}$$

In other words a particle with electromagnetic charge Q now also carries a "hidden charge",

$$Q_X = -\chi Q, \tag{8}$$

coupling it to the hidden photon.

It is now easy to calculate the interaction between two charged particles with charges $q_1 e, q_2 e$ separated by a distance r,

$$V(r) = q_1 q_2 \frac{\alpha}{r}\left[1 + \chi^2 \exp(-m_X r)\right]. \tag{9}$$

The first term is, of course, the ordinary Coulomb interaction. The second is the additional contribution from the "new force" mediated by X.

Let us note that the form of the correction makes both ways of how to hide particles, mentioned in the introduction, explicit. For a fixed resolvable distance $r_{\rm res} > 0$ the new force becomes negligible whenever the mass $m_X \gg 1/r_{\rm res}$. The force has a range shorter than the resolution and is therefore not observed. Alternatively we can make χ very small. In this case the force becomes simply very weak and at some point unobservable even if m_X is small and the range is large.

Eq. (9) also provides a way to search for the new force: we can test Coulomb's law. This can be done at scales of the order of $\sim 10\,\mathrm{cm}$ with Cavendish experiments [23, 24, 25]. The corresponding limit is shown in Fig. 1 labelled "Coulomb" and is currently the best limit in the range of μeV. The precision achieved, about one part in 10^{16}, is remarkable. Nevertheless it is also noteworthy that the best experiment is more than 40 years old. At much smaller scales one can use atomic transitions [25, 26, 27, 28] (see Fig. 1). Following essentially the same arguments one can also look at magnetic fields, which is useful at much larger scales where one can use the magnetic fields of Earth and Jupiter which have been mapped with a good precision. This gives the bounds labelled "Earth" and "Jupiter" [25].

Other experiments do not look for the mediated force, but directly for the new exchange particle. From Eq. (5) and our discussion above it is clear that below the electroweak scale we simply deal with a new massive vector particle that has a coupling to charged particles according to Eq. (8). This particle can then be produced in scattering experiments with charged particles. The production process is similar to that of photons only that the particle is massive and the interaction is suppressed by a factor χ. One incarnation of this are so-called fixed-target experiments [29]. In these experiments a large number of charged particles (often electrons) with a fairly high energy is shot onto a block or a foil (typically of metal). In the interaction between the incident and the target particles Xs are produced. If the mass of X is now larger than $2m_e$, X can and will decay into electron-positron pairs which can then be detected. The produced electron-positron pairs have to be distinguished from those produced in ordinary electromagnetic interactions. This can be done in two ways. First the invariant mass distribution of the electron-positron pairs produced via an X has a clear peak at the mass m_X. Second, for very low values of χ the produced X is very long lived and we therefore have very displaced vertices (sometimes displaced by 100s of meters). Bounds from this type of experiment 29, 30, 31, 18) are typically in the MeV to GeV region as shown in Fig. 1.

Similarly scattering can be done at very high energy colliders such as the LHC where one typically looks for peaks in the invariant mass distribution 32, 19). The only difference is that in this region the mixing is with the hypercharge and we have an effective charge of X,

$$Q_X = \chi_Y g' \left[\frac{\gamma}{\tan^2(\theta_W)} T^3 - (1+\gamma) Q_Y \right], \quad \text{where} \quad \gamma = \tan^2(\theta_W) \frac{m_W^2}{m_X^2 - m_Z^2}. \tag{10}$$

The limits scaled to the electromagnetic mixing parameter are shown at the very high mass end of Fig. 1.

Instead of real particle production we can also look at loop-effects such as (g-2) of the electron and the muon. The tight constraints in the MeV-GeV range from precision measurements of these quantities are shown in Fig. 1, labelled "$a_{e,\mu}$". As is well known, the muon (g-2) has a slight deviation from the SM expectation. HPs in a suitable range, shown red in Fig. 2 can fit this 33). It should be noted that over the last couple of years this region has shrunk considerably due to a renewed experimental and theoretical effort. Note, however, that most of these limits hold only when the dominant decay of the HP is into SM particles. If there are additional "hidden sector" decay modes, fixed target and similar constraints will be relaxed, while it is still possible to fit (g-2).

3.2 Option (2): Photon–hidden photon oscillations

Let us now turn to the second option of dealing with the kinetic mixing term. Before we proceed let us, however, stress again that physical results are, of course absolutely independent of which picture we choose.

Inserting the shift $X^\mu \to X^\mu - \chi A^\mu$ into Eq. (3) we obtain,

$$\mathcal{L} \supset -\frac{1}{4} F_{\mu\nu} F^{\mu\nu} - \frac{1}{4} X_{\mu\nu} X^{\mu\nu} + \frac{m_X^2}{2} \left(X_\mu X^\mu - 2\chi X_\mu A^\mu + \chi^2 A_\mu A^\mu \right) + j_\mu A^\mu. \tag{11}$$

With this shift we have again succeeded in removing the kinetic mixing term. Moreover, charged particles are still charged only under A in contrast to the previous subsection. However, we now have a non-diagonal mass term, mixing X and A. This mass term now leads to $A \leftrightarrow X$ oscillations, in complete analogy to the non-diagonal mass matrices of neutrinos that lead to neutrino flavor oscillations. Indeed this analogy goes even further. In the basis used in this section we are in the interaction eigenbasis and have oscillations. In the previous section we were in the mass eigenbasis and had non-trivial couplings to charged matter, but no oscillations[2].

The interaction basis we are discussing in this section is particularly convenient when the interactions with matter are in some sense "strong". An example are the so-called light-shining-through-walls experiments (LSW). In these experiments a laser is shone onto an opaque wall and one looks for light "coming out of the wall". The idea is that an initial photon oscillates into a hidden photon, which traverses the wall unimpeded and after the wall oscillates back into a photon that is subsequently detected. For this it is convenient to use the interaction basis, as it is only the A component that interacts with the wall (and the laser and the detector) and is completely suppressed (this is the "strong" effect caused by the large amount of interacting particles in the wall). Current limits 34) from "LSW" are shown in Fig. 1.

The centre of stars contains an extremely high number of photons which can oscillate into HPs and then leave the star (the rest of the star is basically a thick wall). This is a very efficient way for stars to loose energy. In this kind of environment the oscillations are modified by the presence of a plasma allowing for resonances (similar to the MSW effect for neutrinos) but also allowing the longitudinal modes to contribute. Limits on an extra energy loss for the sun and horizontal branch stars give extremely tight constraints 35, 21) (cf. Fig 1).

Similarly production of HPs in the early universe plasma either before the CMB release 36) (region "thermal cosmology") or after 37, 38) (region "CMB") benefits from resonances and leads to a very sensitive test.

---

[2] In the mass eigenbasis the "oscillations" appear as follows. Both mass eigenmodes couple to charged particles. Accordingly to know the effect on a charged particle we have to add the amplitudes of both eigenmodes multiplied with their respective couplings. This sum exhibits the oscillatory behavior because the two eigenmodes with different masses acquire different phases when moving in space (similar in frequency).

3.3 Have it your way

As stressed before observables are independent of the chosen picture. But in the above examples the description may be more transparent in one picture. In others no clear preference is obvious.

For example the regions "$BR(\pi^0 \to \gamma e^+ e^-)$" 20) and "$e^+ e^- \to \gamma \mu^+ \mu^-$" arise from decays of pions and decay of Υ resonances 39, 40, 41, 42), respectively. These mesons can decay into two photons. In presence of a kinetically mixed hidden photon we can now have one photon oscillate into a HP which subsequently decays into an electron-positron pair with an invariant mass $\approx m_X$. Alternatively one can take picture (1) and imagine that the meson couples (via the charged quarks) to a photon and a hidden photon.

For the electroweak precision, "EW", constraints 42) arising most notably from the linewidth and lineshape of the Z resonance one has to take into account the full electroweak symmetry breaking and mixing effects.

4 Searching hidden photons: The future

In the previous section we have reviewed existing constraints on hidden photons, spanning a wide range of masses from 10^{-15} eV to more than 10^{12} eV. Yet, the search is far from over. In Fig. 2 we compare the existing constraints (grey areas) with interesting target regions from models of string theory (regions enclosed by dashed, dotted and dashed-dotted lines) 9, 13). The hint from (g-2)$_\mu$ 33) (red) and the region where hidden photons can be dark matter (light red) 22) (and next section). It is obvious that there are large regions that still need to be explored. In this section we look at the near future experimental prospects (shown in different shades of green).

4.1 Low energy probes

A clear step forward in the meV mass range will be the next generation of LSW experiments, most notably ALPS-II 44) (cf. the corresponding region in Fig. 2) and REAPR. These experiments will feature a resonant regeneration scheme 49, 50). In such a setup the light is reflected back and forth in an optical cavity on the production side (this was already pioneered by ALPS-I 51)) as well as on the regeneration side. This enhances the signal by a factor $N_{\rm prod} N_{\rm reg}$ where $N_{\rm prod}$ and $N_{\rm reg}$ are the number of passes on the production

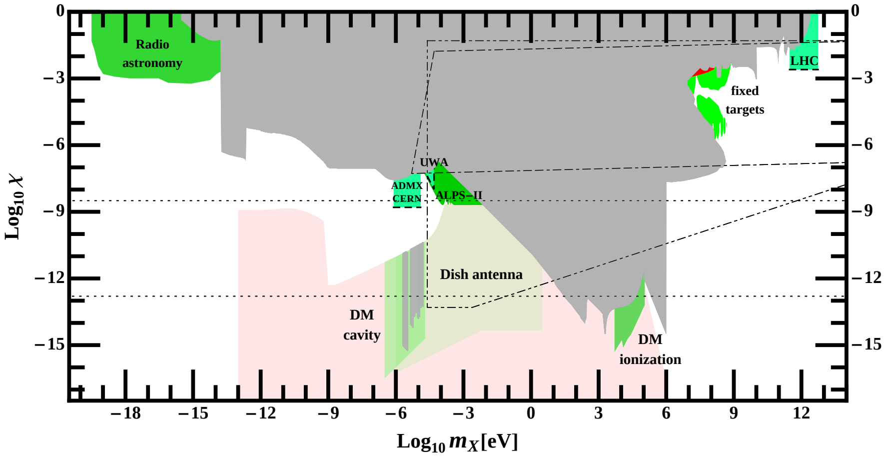

Figure 2: *Prospects for near future searches for hidden photons (shaded green). The regions labeled, ADMX, CERN and UWA are LSW experiments in the microwave range (cf.* 43)*), ALPS-II will operate in the optical regime* 44)*. Radio astronomy searches for a frequency dependence of distant sources could provide sensitivity at very small masses* 45)*. The dish antenna region gives the prospects for a broadband search for dark matter HP according to* 46)*. At higher masses we have fixed target experiments* 43, 47) *and the LHC as well as a detection of ionization signals, caused by HP DM in direct detection experiments for WIMP DM* 48)*. The small red region at high masses corresponds to the* $(g-2)_\mu$ *hint* 33)*.*

and regeneration side, respectively. As ∼ 100000 passes seem feasible this yields an enormous gain in sensitivity. Moreover, ALPS-II will be significantly longer, allowing to probe also smaller masses.

At even smaller masses in the μeV region, LSW with "light" in the microwave range 52, 53) is very promising. Here, resonant regeneration is easier to achieve and first experiments have already been performed 54, 55, 56). Such experiments also benefit from a potentially enormous number of passes of up to 10^{11} in the microwave cavities and very sensitive detection techniques 57). This allows for very interesting sensitivity as shown by the regions "ADMX CERN" and "UWA" in Fig. 2.

At even smaller masses it may also be possible to probe photon-hidden photon oscillations by observing the frequency dependence of well modelled radio signals 45). The frequency dependence of the oscillation probability would lead to structures in the frequency spectrum at a frequency scale $\Delta\omega \sim \omega^2/(m_X^2 L_{\rm source})$ (where $L_{\rm source}$ is the distance to the source) and amplitude $\sim \chi^2$. This will extend sensitivity to extremely small masses as shown by the "Radio astronomy" region in Fig. 2.

In the sub-eV region one can also search for HP dark matter with extremely high sensitivity as we will see in the next section.

4.2 Intermediate energy probes

In the MeV to GeV region the next few years will bring new and improved fixed target experiments. In particular the A1 collaboration with the MAMI and MESA accelerators at Mainz 47) as well as APEX 41), Darklight 58) and HPS 59) at Jefferson Lab will use electrons on various targets whereas the VEPP-3 60) at SLAC intends to use positrons. The region projected to be tested by these experiments is shown as the green "fixed target" region in Fig. 2. It encompasses all of the $(\text{g-2})_\mu$ region. In addition proton fixed target experiments promise additional information 61).

4.3 High energy probes

The LHC will continue to improve the limits on hidden photons in the 100 GeV to multi TeV range over the next years. The first step in the improvement will be the increase in the beam energy from 8 TeV to 13 TeV hopefully even 14 TeV. This will approximately double the mass reach for hidden photons. Increased integrated luminosity collected over the next few years will importantly improve the sensitivity to smaller cross sections and therefore smaller kinetic mixings. Further improvements towards somewhat smaller masses may also come from analyses that include lower energy electrons and muons. An indication of the tested region is the green "LHC" region in Fig. 2.

5 Hidden photon dark matter

In contrast to common belief very light particles can indeed be good dark matter candidates. The crucial aspect is that *very light dark matter particles* *need to be produced non-thermally.* The most famous example is the so-called misalignment mechanism for the axion (62, 63, 64). Its essential features are as follows. In the early Universe the field starts with a non-vanishing expectation value. Because the Hubble constant is much larger than the mass of the field in question, the field is basically stuck at this initial value. This is also the reason why it is not unreasonable to assume a non-vanishing initial value; there is simply no time to relax to the minimum of the potential. Moreover, after inflation the field is smoothed out and basically has the same field value everywhere in space. Once the Hubble value drops below the mass of the field, the field starts to oscillate and one can show that these oscillations behave like non-relativistic matter. This becomes plausible by remembering that the momentum of a particle is essentially the spatial derivative of the field, and a (nearly) homogeneous field configuration therefore corresponds to particles with extremely low momentum.

As argued recently (65, 22) a similar mechanism works also for hidden photons. For the evolution in the early Universe the Hubble constant is larger than the mass. It is therefore reasonable to include additional interactions with gravity,

$$\mathcal{L} = -\frac{1}{4}X_{\mu\nu}X^{\mu\nu} + \frac{m_X^2}{2}X_\mu X^\mu + \frac{\kappa}{12}RX_\mu X^\mu + \mathcal{L}_{\text{kinetic mix}} + \mathcal{L}_{\text{SM}}, \qquad (12)$$

where R is the Ricci scalar[3] and the last two terms indicate the kinetic mixing and the rest of the Standard Model.

As already mentioned in Sect. 2, in general, the HP mass might result from a Higgs or a Stückelberg mechanisms. In the first case, we have to worry when the phase transition happens and also take into account the effects of the Higgs field. As in (65, 22), we focus therefore on the Stückelberg case, which occurs naturally in large volume string compactifications (16, 9, 13). In this case, there is no phase transition.

Let us briefly comment on the equations of motion and in particular determine the behavior of the energy density in the expanding universe. Let us see if we can find the hallmark property of non-relativistic "cold" dark matter:

---

[3] We use a coordinates such that $ds^2 = dt^2 - a^2(t)dx_i^2$, i.e. the metric is $g_{\mu\nu} = \text{diag}(1, -a^2(t), -a^2(t), -a^2(t))$. Moreover, the gravitational part of the Lagrangian is $\mathcal{L}_{\text{GR}} = -R/(16\pi G_N)$.

the energy dilutes like the volume, i.e. $\rho \sim 1/(a(t))^3$ where $a(t)$ is the scale factor.

For simplicity let us focus on the homogeneous solution, $\partial_i X_\mu = 0$. The equation of motion then enforces $X_0 = 0$. As explained in $^{66)}$ the invariant $X^\mu X_\mu = -1/a^2(t) X_i X_i$ is a coordinate independent measure for the size of the vector and it is convenient to introduce $\bar{X}_i = X_i/a(t)$. Using this the equation of motion is,

$$\ddot{\bar{X}}_i + 3H\dot{\bar{X}}_i + \left(m_X^2 + (1-\kappa)(\dot{H} + 2H^2)\right)\bar{X}_i = 0. \tag{13}$$

The energy density is

$$\rho(t) = T_0^0 = \frac{1}{2}\left(\dot{\bar{X}}_i\dot{\bar{X}}_i + m_X^2 \bar{X}_i\bar{X}_i + (1-\kappa)H^2\bar{X}_i\bar{X}_i + 2(1-\kappa)H\dot{\bar{X}}_i\bar{X}_i\right). \tag{14}$$

For $H \ll m_X$ and $\dot{H} \ll m_X^2$ Eq. (13) is that of a weakly damped harmonic oscillator. One can easily see that the amplitude oscillates with frequency m_X and it is damped by a factor $\exp(-3\int H dt/2) \sim 1/a^{3/2}(t)$. Inserting into Eq. (14) we then find that the energy density indeed dilutes like the volume $\sim 1/a^3(t)$. Taking a different point of view: In this limit both expressions (13) and (14) reduce to same form as the equations of motion and the energy momentum tensor of a scalar field (independent of the value of κ) and for such a field we already know (e.g. from the case of axions) that this behaves as non-relativistic matter. For $\kappa = 1$ this equivalence holds true exactly even in the very early Universe where $H \gtrsim m_X$ and/or $\dot{H} \gtrsim m_X^2$.

Now we have seen that an initial field value for hidden photons can nicely behave like cold dark matter. However, there are several questions remaining: 1) How do we get the right abundance. 2) Does it survive? 3) Does it change observation? For a detailed discussion see $^{22)}$ but let us briefly summarize the answers. 1) The abundance is proportional to the initial field value squared. Therefore getting the right abundance requires some amount of fine-tuning or anthropic arguments. For 2) and 3) we have to make sure that the HPs forming do not decay, or spoil observations such as, e.g. the CMB. This leads to upper limits on the kinetic mixing parameter. Heavier HPs can decay into electron-positron pairs via the kinetic mixing interaction. This is quite fast and therefore basically[4] rules out HP dark matter with masses $m_X \gtrsim$ MeV. At lower masses

---

[4] Unless one considers $^{67)}$ incredibly small kinetic mixings $\chi \lesssim 10^{-26}$.

HPs can decay into three photons, but this decay is fairly suppressed by a by a small algebraic factor as well as phase space. Therefore it provides a constraint only at masses just below an MeV. At even smaller masses other evaporation mechanisms originating from photon-HP mixing in the plasma of the early universe and scattering with the electrons in the plasma dominate. This both reduces the condensate as well as transferring energy to the ordinary electrons and producing extra photons. This can lead to observable effects such as distortions in the CMB or a changed number of effective neutrinos. Although all these effects combined set fairly strong constraints, a large and interesting area of viable HP dark matter remains. This is shown as the light red area in Figs. 1 and 2.

5.1 Detecting hidden photon dark matter

Having a viable dark matter candidate it is now desirable to also have ways to detect it.

First of all, let us note that due to the small mass of HP dark matter particles, conventional direct detection methods designed for weakly interacting massive particles (WIMPs) based on nuclear or electronic recoils do not work, the recoil energy is just too small.

Nevertheless, we have a plentiful source of HPs and we have already seen previously that those have a natural tendency to convert into ordinary photons that can be detected. Therefore, in principle we do not need to do anything but simply set up a detector for photons and wait. As dark matter HPs are very slow their energy is essentially given by their mass and therefore we expect a nicely peaked signal of photons with energy/frequency corresponding to the HP mass.

Unfortunately things are not quite as easy since the rate of produced photons is quite small. Therefore we need incredibly good photon receivers as well as shielding of background noise. Moreover, it is desirable to have techniques to enhance the signal. Two options are currently being pursued. The first is based on the haloscope technique originally proposed for axions 68) but it can also be used for detecting hidden photons 22). The idea is to enhance the conversion of HPs into photons by employing a suitable cavity resonant with the HP mass. This is analog to the resonant regeneration scheme discussed above for LSW experiments. The output power is then enhanced by the Q-

factor of the cavity (which is proportional to the number of reflections),

$$P_{\mathrm{out}} \sim \chi^2 m_X \rho_{\mathrm{HP}} Q V \mathcal{G}, \tag{15}$$

where ρ_{HP} is the density of dark matter hidden photons, V the volume of the cavity and $\mathcal{G}$ a geometrical factor encoding properties of the cavity as well as the dark matter configuration. This technique works particularly well in the microwave regime where good cavities as well as excellent detectors exist. This technique has already been employed 69, 70, 71, 72, 73) and further improvements are underway 74, 75, 76). The currently excluded region is the "haloscope region" shaded in grey in Figs. 1 and future prospects are indicated as the "DM cavity" region in Fig. 2.

The cavity technique is sensitive to extremely small couplings but it has two drawbacks. As it relies on the resonant enhancement it requires a slow scan through masses, where each measurement is only sensitive to a small region of masses and then the cavity has to be tuned to a new frequency and another measurement has to be performed. In essence one needs to do a slow and time-consuming scan through the masses. The second issue is that the output power is proportional to the volume of the cavity. With increasing frequency the volume of the cavity goes down, or one has to operate the cavity in a higher mode which often leads to smaller geometrical factors.

Accordingly it would be nice to have a broadband technique without a "volume suppression". One option is to use a "dish antenna" 46). Here the basic idea is as follows. On charged matter the HP dark matter field essentially acts like a small oscillating ordinary electric field. The electrons in a conducting (reflecting) surface then start to oscillate in this field, emitting ordinary photons. One can check that for very slow HPs the produced electromagnetic radiation is emitted perpendicular to the surface. Using a suitable (spherical) surface all radiation from the whole surface is concentrated in a point, the centre, where it can be detected. It is easy to understand that the concentrated power in the centre is proportional to the area A_{dish} of the "antenna",

$$P_{\mathrm{centre}} \sim \chi^2 \rho_{\mathrm{HP}} A_{\mathrm{dish}}. \tag{16}$$

This technique can be used in the radio frequency range but also promises good sensitivity at much higher frequencies in the optical regime. This is indicated as the very light green "Dish antenna" region in Fig. 2.

Finally, experiments for direct detection of WIMPs may also be used [48]. Dark matter HPs with masses in the multi keV may be completely absorbed. This produces an ionization signal that can be detected. A rough estimate for a future sensitivity is shown as "DM ionization" in Fig. 2 (we have assumed that the direct detection experiment is sensitive to an ionization signal from an 0.1 fb cross section at WIMP masses of $\sim 100\,\mathrm{GeV}$; other assumptions as in [48]).

6 Conclusions

New forces are a hallmark feature of many models of physics beyond the Standard Model. A very simple but also very well motivated example is an extra U(1) gauge force kinetically mixed with the electromagnetic or hypercharge U(1) of the Standard Model. In this note we have given overview over past and future searches for such a new force and the corresponding gauge boson, often called hidden photon, heavy photon, dark photon or A'.

The simple example of a hidden photon nicely demonstrates that there are (at least) two directions to explore. The hidden photon could be very light and very weakly coupled, corresponding to a very weak but long range force. Alternatively it could be heavy in which case the interaction is very short range (and weak in this sense).

Searches for hidden photons span a huge range of masses and energies from $10^{-20}\,\mathrm{eV}$ to multi-TeV. Exploring this vast range requires to exploit the complementarity between very different experimental techniques, from low energy ultrahigh precision experiments to high energy colliders. This complementarity can be nicely seen in Fig. 1 where the different energy scales probed by a variety of experiments nicely fit together to cover a large range in masses and couplings.

While significant progress has been made over the past few years, huge regions remain to be explored. Interesting regions are suggested by models of fundamental theories (e.g., string theory) but also by the intriguing possibility that hidden photons form all or part of dark matter. It is therefore very exciting that many experiments, exploring different energy/mass ranges and using a variety of techniques are underway, in construction or in planning, promising new insights into fundamental physics and even the potential for discovering a new force.

7 Acknowledgements

JJ would like to thank Javier Redondo and Andreas Ringwald for joyful long-term collaboration on the subject.

References

1. B. Holdom, Phys. Lett. **B166**, 196 (1986).
2. K. R. Dienes, C. F. Kolda, and J. March-Russell, Nucl. Phys. **B492**, 104 (1997), arXiv:hep-ph/9610479.
3. A. Lukas and K. Stelle, JHEP **0001**, 010 (2000), arXiv:hep-th/9911156.
4. S. A. Abel and B. W. Schofield, Nucl. Phys. **B685**, 150 (2004), arXiv:hep-th/0311051.
5. R. Blumenhagen, G. Honecker, and T. Weigand, JHEP **0506**, 020 (2005), arXiv:hep-th/0504232.
6. S. A. Abel, J. Jaeckel, V. V. Khoze, and A. Ringwald, Phys. Lett. **B666**, 66 (2008), arXiv:hep-ph/0608248.
7. S. A. Abel, M. D. Goodsell, J. Jaeckel, V. V. Khoze, and A. Ringwald, JHEP **07**, 124 (2008), arXiv:0803.1449.
8. M. Goodsell, p. 165 (2009), arXiv:0912.4206.
9. M. Goodsell, J. Jaeckel, J. Redondo, and A. Ringwald, JHEP **11**, 027 (2009), arXiv:0909.0515.
10. M. Goodsell and A. Ringwald, Fortsch. Phys. **58**, 716 (2010), arXiv:1002.1840.
11. J. J. Heckman and C. Vafa, Phys.Rev. **D83**, 026006 (2011), arXiv:1006.5459.
12. M. Bullimore, J. P. Conlon, and L. T. Witkowski, JHEP **1011**, 142 (2010), arXiv:1009.2380.
13. M. Cicoli, M. Goodsell, J. Jaeckel, and A. Ringwald, JHEP **1107**, 114 (2011), arXiv:1103.3705.

14. M. Goodsell, S. Ramos-Sanchez, and A. Ringwald, JHEP **1201**, 021 (2012), arXiv:1110.6901.

15. M. Ahlers, J. Jaeckel, J. Redondo, and A. Ringwald, Phys.Rev. **D78**, 075005 (2008), arXiv:0807.4143.

16. C. P. Burgess *et al.*, JHEP **07**, 073 (2008), arXiv:0805.4037.

17. J. Jaeckel and A. Ringwald, Ann. Rev. Nucl. Part. Sci. **60**, 405 (2010), arXiv:1002.0329.

18. S. Andreas, C. Niebuhr, and A. Ringwald, Phys.Rev. **D86**, 095019 (2012), arXiv:1209.6083.

19. J. Jaeckel, M. Jankowiak, and M. Spannowsky, (2012), arXiv:1212.3620.

20. S. Gninenko, (2013), arXiv:1301.7555.

21. H. An, M. Pospelov, and J. Pradler, (2013), arXiv:1302.3884.

22. P. Arias *et al.*, JCAP **1206**, 013 (2012), arXiv:1201.5902.

23. E. R. Williams, J. E. Faller, and H. A. Hill, Phys. Rev. Lett. **26**, 721 (1971).

24. D. F. Bartlett and S. Loegl, Phys. Rev. Lett. **61**, 2285 (1988).

25. V. Popov, Tr. J. of Physics **23**, 943 (1999).

26. S. Karshenboim, Phys.Rev. **D82**, 073003 (2010), arXiv:1005.4872.

27. S. G. Karshenboim, Phys. Rev. Lett. **104**, 220406 (2010), arXiv:1005.4859.

28. J. Jaeckel and S. Roy, Phys.Rev. **D82**, 125020 (2010), arXiv:1008.3536.

29. J. D. Bjorken, R. Essig, P. Schuster, and N. Toro, Phys. Rev. **D80**, 075018 (2009), arXiv:0906.0580.

30. A1 Collaboration, H. Merkel *et al.*, Phys.Rev.Lett. **106**, 251802 (2011), arXiv:1101.4091.

31. APEX Collaboration, S. Abrahamyan *et al.*, Phys.Rev.Lett. **107**, 191804 (2011), arXiv:1108.2750.

32. M. T. Frandsen, F. Kahlhoefer, A. Preston, S. Sarkar, and K. Schmidt-Hoberg, JHEP **1207**, 123 (2012), arXiv:1204.3839.

33. M. Pospelov, Phys. Rev. **D80**, 095002 (2009), arXiv:0811.1030.

34. K. Ehret *et al.*, Phys.Lett. **B689**, 149 (2010), arXiv:1004.1313.

35. J. Redondo, JCAP **0807**, 008 (2008), arXiv:0801.1527.

36. J. Redondo and M. Postma, JCAP **0902**, 005 (2009), arXiv:0811.0326.

37. J. Jaeckel, J. Redondo, and A. Ringwald, Phys. Rev. Lett. **101**, 131801 (2008), arXiv:0804.4157.

38. A. Mirizzi, J. Redondo, and G. Sigl, JCAP **0903**, 026 (2009), arXiv:0901.0014.

39. B. Echenard, Mod.Phys.Lett. **A27**, 1230016 (2012), arXiv:1205.3505.

40. M. Reece and L.-T. Wang, JHEP **0907**, 051 (2009), arXiv:0904.1743.

41. R. Essig, P. Schuster, N. Toro, and B. Wojtsekhowski, JHEP **1102**, 009 (2011), arXiv:1001.2557.

42. A. Hook, E. Izaguirre, and J. G. Wacker, Adv.High Energy Phys. **2011**, 859762 (2011), arXiv:1006.0973.

43. J. Hewett *et al.*, (2012), arXiv:1205.2671.

44. R. Bähre *et al.*, (2013), arXiv:1302.5647.

45. A. Lobanov, H.-S. Zechlin, and D. Horns, (2012), arXiv:1211.6268.

46. D. Horns *et al.*, (2012), arXiv:1212.2970.

47. H. Merkel *et al.*, PoS **BORMIO2012**, 006 (2012).

48. M. Pospelov, A. Ritz, and M. B. Voloshin, Phys.Rev. **D78**, 115012 (2008), arXiv:0807.3279.

49. F. Hoogeveen and T. Ziegenhagen, Nucl. Phys. **B358**, 3 (1991).

50. P. Sikivie, D. B. Tanner, and K. van Bibber, Phys. Rev. Lett. **98**, 172002 (2007), arXiv:hep-ph/0701198.

51. [ALPS Collaboration], K. Ehret *et al.*, Nucl. Instrum. Meth. **A612**, 83 (2009), arXiv:0905.4159.

52. F. Hoogeveen, Phys. Lett. **B288**, 195 (1992).

53. J. Jaeckel and A. Ringwald, Phys. Lett. **B659**, 509 (2008), arXiv:0707.2063.

54. R. G. Povey, J. G. Hartnett, and M. E. Tobar, Phys. Rev. **D82**, 052003 (2010), arXiv:1003.0964.

55. [ADMX Collaboration], A. Wagner *et al.*, Phys. Rev. Lett. **105**, 171801 (2010), arXiv:1007.3766.

56. M. Betz and F. Caspers, Conf.Proc. **C1205201**, 3320 (2012), arXiv:1207.3275.

57. F. Caspers, J. Jaeckel, and A. Ringwald, JINST **4**, P11013 (2009), arXiv:0908.0759.

58. M. Freytsis, G. Ovanesyan, and J. Thaler, JHEP **1001**, 111 (2010), arXiv:0909.2862.

59. [HPS-Collaboration], https://confluence.slac.stanford.edu/display/hpsg/ .

60. B. Wojtsekhowski, AIP Conf.Proc. **1160**, 149 (2009), arXiv:0906.5265.

61. B. Batell, M. Pospelov, and A. Ritz, Phys.Rev. **D80**, 095024 (2009), arXiv:0906.5614.

62. J. Preskill, M. B. Wise, and F. Wilczek, Phys. Lett. **B120**, 127 (1983).

63. L. F. Abbott and P. Sikivie, Phys. Lett. **B120**, 133 (1983).

64. M. Dine and W. Fischler, Phys. Lett. **B120**, 137 (1983).

65. A. E. Nelson and J. Scholtz, Phys.Rev. **D84**, 103501 (2011), arXiv:1105.2812.

66. A. Golovnev, V. Mukhanov, and V. Vanchurin, JCAP **0806**, 009 (2008), arXiv:0802.2068.

67. C.-R. Chen, F. Takahashi, and T. Yanagida, Phys.Lett. **B671**, 71 (2009), arXiv:0809.0792.

68. P. Sikivie, Phys. Rev. Lett. **51**, 1415 (1983).

69. S. De Panfilis *et al.*, Phys. Rev. Lett. **59**, 839 (1987).

70. W. Wuensch *et al.*, Phys. Rev. **D40**, 3153 (1989).

71. C. Hagmann, P. Sikivie, N. S. Sullivan, and D. B. Tanner, Phys. Rev. **D42**, 1297 (1990).

72. S. J. Asztalos *et al.*, Phys. Rev. **D64**, 092003 (2001).

73. [ADMX Collaboration], S. J. Asztalos *et al.*, Phys. Rev. Lett. **104**, 041301 (2010), arXiv:0910.5914.

74. O. K. Baker *et al.*, Phys.Rev. **D85**, 035018 (2012), arXiv:1110.2180.

75. S. Asztalos *et al.*, Nucl.Instrum.Meth. **A656**, 39 (2011), arXiv:1105.4203.

76. ADMX Collaboration, J. Heilman and K. Tracy, AIP Conf.Proc. **1274**, 115 (2010).

Frascati Physics Series Vol. LVI (2012)
Dark Forces at Accelerators
October 16-19, 2012

THE NEW G-2 EXPERIMENT AT FERMILAB

G. Venanzoni
(On behalf of the Fermilab E989 Collaboration)
Laboratori Nazionali di Frascati dell' INFN, Frascati

Abstract

There is a long standing discrepancy between the Standard Model prediction for the muon g-2 and the value measured by the Brookhaven E821 Experiment. At present the discrepancy stands at about three standard deviations, with comparable accuracy between experiment and theory. Two new proposals at Femilab and J-PARC plan to improve the experimental uncertainty of a factor 4, and there are good motivation to expect a further reduction of the error from the theoretical side. I will review the status of the proposal to Fermilab, E989, and discuss how the goal of 0.14 ppm on the muon anomaly can be achieved, by collecting more than 21 times the statistics of the BNL measurement, and obtaining a factor of 3 reduction in the overall systematic error.

1 Introduction

The muon anomaly $a_\mu = (g-2)/2$ is a low-energy observable, which can be both measured and computed to high precision $^{1)}$. Therefore it provides an important test of the Standard Model (SM) and it is sensitive search for new physics $^{2)}$. Since the first precision measurement of a_μ from E821 experiment at BNL in 2001 $^{3)}$, there has been a discrepancy between its experimental value and the SM prediction. This discrepancy has been slowly growing due to impressive theory and experiment recent achievements. Figure 1 (from $^{4)}$) shows an up-to-date comparison of the SM predictions of different groups and the BNL measurement for a_μ. Evaluation of different groups are in very good agreement, showing a persisting $3\,\sigma$ discrepancy (as, for example, $26.1 \pm 8.0 \times 10^{-10}$ $^{4)}$), despite many changes in the recent history. It should be noted that both theory and experiment uncertainties have been reduced by more than a factor two in the last ten years[1]. The accuracy of the theoretical prediction ($\delta a_\mu^{\rm TH}$, between 5 and 6 $\times 10^{-10}$) is limited by the strong interaction effects which cannot be computed perturbatively at low energies. The leading-order hadronic vacuum polarization contribution, $a_\mu^{\rm HLO}$, gives the main uncertainty (between 4 and 5 $\times 10^{-10}$). It can be related by dispersion integral to the measured hadronic cross sections, and it is known with a fractional accuracy of 0.7%, *i.e.* to about 0.4 ppm. The O(α^3) hadronic light-by-light contribution, $a_\mu^{\rm HLbL}$, is the second dominant error to the theoretical evaluation. It cannot at present be determined from data, and relies on same specific models. Although its value is almost one order of magnitude smaller than $a_\mu^{\rm HLO}$, it is much worse known (with a fractional error of the order of 30%) and therefore it still give a significantly contribution to $\delta a_\mu^{\rm TH}$ (between 2.5 and 4 $\times 10^{-10}$).
From the experimental side, the error achieved by the BNL E821 experiment is $\delta a_\mu^{\rm EXP} = 6.3 \times 10^{-10}$ (0.54 ppm) $^{6)}$. This impressive result is still limited by the statistical errors, and a new experiment, E989 $^{7)}$ at Fermilab, to measure the muon g-2 to a precision of 1.6×10^{-10} (0.14 ppm) has received a CD0 approval, and funding from the DOE has begun. CD1 is expected in mid 2013.

---

[1] In 2001 this discrepancy was $(23.1 \pm 16.9) \times 10^{-10}$ $^{5)}$.

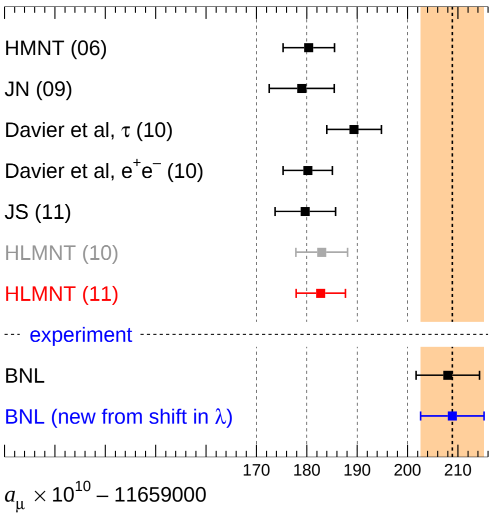

Figure 1: Standard model predictions of a_μ by several groups compared to the measurement from BNL (taken from $^{4)}$).

2 Recent results and expected improvement on the hadronic contribution

Differently from the QED and Electroweak contributions to a_μ, which can be calculated using perturbation theory, and therefore are well under control, the hadronic ones (LO VP and HLbL) cannot be computed reliably using perturbative QCD. The hadronic contribution a_μ^{HLO} can can be computed from hadronic e^+e^- annihilation data via a dispersion relation, and therefore its uncertainty strongly depends on the accuracy of the experimental data. For the Hadronic Light-by-Light contribution a_μ^{HLbL} there is no a direct connection with data and therefore only model-dependent estimates exist. As the hadronic sector dominates the uncertainty on the theoretical prediction a_μ^{TH}, considerable effort has been put by on it by the experimental and theoretical groups, reaching the following main achievements:

- A precise determination of the hadronic cross sections at the e^+e^- colliders (VEPP-2M, DAΦNE, BEPC, PEP-II and KEKB) which allowed a determination of $a_\mu^{\rm HLO}$ with a fractional accuracy below 1%. These efforts led to the development of dedicated high precision theoretical tools, like Radiative Corrections (RC) and the non-perturbative hadronic contribution to the running of α (i.e. the vacuum polarisation, VP) in Monte Carlo (MC) programs used for the analysis of the data 8);

- The use of '*Initial State Radiation*' (ISR) which opened a new way to prcisely obtain the electron-positron annihilation cross sections into hadrons at particle factories operating at fixed beam-energies 9).
- A dedicate effort on the evaluation of the Hadronic Light-by-Light contribution (see for example 10)), where two different groups 11, 12) obtained results consistent on the size of the contribution (with sligthly different errors), and therefore strengthening our confidence in the reliability of these estimates;
- an impressive progress on lattice, where an accuracy of $\sim 2\%$ were reached on on the two-flavor QCD correction to $a_\mu^{\rm HLO}$ 13);
- A better agreement between the e^+e^-– and the τ– based evaluation of $a_\mu^{\rm HLO}$, thanks to improved isospin corrections 14). These two sets of data are eventually in agreement (with τ data moving towards e^+e^-– data) after including vector meson and $\rho - \gamma$ mixing 15, 16, 17).

For sure further improvements are expected on the hadronic contribution to a_μ on the timescale of the new g-2 experiments at Fermilab and J-PARC. On the experimental side more data are expected from current and future e^+e^- colliders. From the theory, the lattice calculation has already reached a mature stage and has real prospects to match experimental precision below 1%. From both activities a further reduction of the error on $a_\mu^{\rm HLO}$ can be expected. What about $a_\mu^{\rm HLBL}$? With the expected reduction of the error on $a_\mu^{\rm HLO}$ and the planned improved precision of the new g-2 experiments, it is clear that it will become the main subject of future theoretical investigations. Although there isn't a direct connection with data, $\gamma - \gamma$ measurements perfomed at e^+e^- colliders will help us to constrain on-shell form factors 18). Lattice calculation would help for the off shell contributions.

3 Measuring a_μ

The measurement of a_μ uses the spin precession resulting from the torque experienced by the magnetic moment when placed in a magnetic field. An ensemble of polarized muons is introduced into a magnetic field, where they are stored for the measurement period. Assuming that the muon velocity is transverse to the magnetic field ($\vec{\beta} \cdot \vec{B} = 0$), the rate at which the spin turns relative to the momentum vector is given by the difference frequency between the spin precession and cyclotron frequencies. Because electric quadrupoles are used to provide vertical focusing in the storage ring, their electric feld is seen in the muon rest frame as a motional magnetic feld that can affect the spin precession frequency. In the presence of both $\vec{E}$ and $\vec{B}$ fields, and in the case that $\vec{\beta}$ is perpendicular to both, the anomalous precession frequency (*i.e.* the frequency at which the muons spin advances relative to its momentum) is

$$\begin{aligned} \vec{\omega_a} &= \vec{\omega_S} - \vec{\omega_C} \\ &= -\frac{q}{m}\Big[a_\mu \vec{B} - \Big(a_\mu - \frac{1}{\gamma^2 - 1}\Big)\frac{\vec{\beta} \times \vec{E}}{c}\Big] \end{aligned} \tag{1}$$

The experimentally measured numbers are the muon spin frequency ω_a and the magnetic field, which is measured with proton NMR, calibrated to the Larmor precession frequency, ω_p, of a free proton. The anomaly is related to these two frequencies by

$$a_\mu = \frac{\tilde{\omega_a}/\omega_p}{\lambda - \tilde{\omega_a}/\omega_p} = \frac{R}{\lambda R}, \tag{2}$$

where $\lambda = \mu_\mu/\mu_p = 3.183345137(85)$ (determined experimentally from the hyperfine structure of muonium), and $R = \tilde{\omega_a}/\omega_p$. The tilde over ω_a means it has been corrected for the electric-field and pitch ($\vec{\beta} \cdot \vec{B} \neq 0$) corrections [3]. The magnetic field in Eq. (1) is an average that can be expressed as an integral of the product of the muon distribution times the magnetic field distribution over the storage region. Since the moments of the muon distribution couple to the respective multipoles of the magnetic field, either one needs an exceedingly uniform magnetic field, or exceptionally good information on the muon orbits in the storage ring, to determine $< B >_{\mu-dist}$ to sub-ppm precision. This was possible in E821 where the uncertainty on the magnetic field averaged over the muon distribution was 30 ppb (parts per billion). The coefficient of the

$\vec{\beta} \times \vec{E}$ term in Eq. (1) vanishes at the "magic" momentum of 3.094 GeV/c where $\gamma = 29.3$. Thus a_μ can be determined by a precision measurement of ω_a and B. At this magic momentum, the electric field is used only for muon storage and the magnetic field alone determines the precession frequency. The finite spread in beam momentum and vertical betatron oscillations introduce small (sub ppm) corrections to the precession frequency. These are the only corrections made to the measurement.

The experiment consists of repeated fills of the storage ring, each time introducing an ensemble of muons into a magnetic storage ring, and then measuring the two frequencies ω_a and ω_p. The muon lifetime is 64.4 μs, and the data collection period is typically 700 μs. The g-2 precession period is 4.37 μs, and the cyclotron period ω_C is 149 ns.

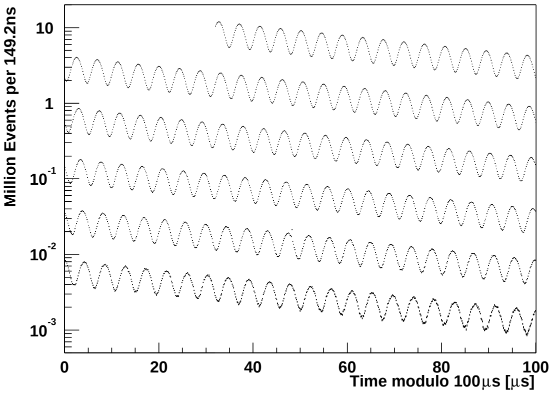

Figure 2: Distribution of electron counts versus time for the 3.6 billion muon decays. The data are wrapped around modulo 100 μs [6].

Because of parity violation in the weak decay of the muon, a correlation exists between the muon spin and the direction of the high-energy decay electrons. Thus as the spin turns relative to the momentum, the number of high-energy decay electrons is modulated by the frequency ω_a, as shown in Fig. 2. The E821 storage ring was constructed as a super-ferric magnet, meaning that the iron determined the shape of the magnetic field. Thus B_0 needed to be well below saturation and was chosen to be 1.45 T. The resulting ring had a central orbit radius of 7.112 m, and 24 detector stations were placed symmetrically around the inner radius of the storage ring. The detectors were made of Pb/SciFi electromagnetic calorimeters which measured the decay electron energy and time of arrival. The detector geometry and number were optimized to detect the high energy decay electrons, which carry the largest asymmetry, and thus information on the muon spin direction at the time of decay. In this design many of the lower-energy electrons miss the detectors, reducing background and pileup.

4 The FERMILAB PROPOSAL: E989

The E989 experiment at Fermilab plans to measure a_μ to an uncertainty of 16×10^{11} (0.14 ppm), derived from a 0.10 ppm statistical error and roughly equal 0.07 ppm systematic uncertainties on ω_a and ω_p.

The proposal efficiently uses the unique properties of the Fermilab beam complex to produce the necessary flux of muons, which will be injected and stored in the (relocated) muon storage ring. To achieve a statistical uncertainty of 0.1 ppm, the total data set must contain more than 1.8×10^{11} detected positrons with energy greater than 1.8 GeV, and arrival time greater than 30 μs after injection into the storage ring. The plan uses 6 out of 20 of the 8-GeV Booster proton batches in 15 Hz operational mode, each subdivided into four bunches of intensity 10^{12} p/bunch. The proton bunches fill the muon storage ring at a repetition rate of 18 Hz, to be compared to the 4.4 Hz at BNL. The proton bunch hits a target in the antiproton area, producing a 3.1 GeV/c pion beam that is directed along a 900 m decay line. The resulting pure muon beam is injected into the storage ring. The muons will enter the ring through a new superconducting inflector magnet, which will replace the existing one, which is wound in such a manner that the coils intercept the beam on both ends of the magnet. The new inflector will result in a higher muon storage efficiency. Once entering the ring, a better optimized pulse-forming network will energize the storage ring kicker to place the beam on a stable orbit. The pion flashes (caused by pions entering the ring at injection) will be decreased by a factor of 20 from the BNL level, and the muon flux will be significantly increased because of the ability to take zero-degree muons. The stored muon-per-proton ratio will be increased by a factor of 5 to 10 over BNL.

The E821 muon storage will be relocated to Fermilab, in a new building with a stable floor and good temperature control, neither of which were available at Brookhaven.

The new experiment will require upgrades of detectors, electronics and data acquisition equipment to handle the much higher data volumes and slightly higher instantaneous rates. A modern data acquisition system will be used to read out waveform digitizer data and store it so that both the traditional event mode and a new integrating mode of data analysis can both be used in parallel. The systematic uncertainty on the precession frequency is expected to improve by a factor 3 thanks to the reduced pion contamination, the segmented detectors, and an improved storage ring kick of the muons onto orbit. The storage ring magnetic feld will be shimmed to an even more impressive uniformity, and improvements in the feld-measuring system will be implemented. The systematic error on the magnetic field is halved by better shimming, relocations of critical NMR probes, and other incremental changes.

In less than two years of running, the statistical goal of 4×10^{20} protons on target can be achieved for positive muons. A follow-up run using negative muons is possible, depending on future scientic motivation. Two additional physics results will be obtained from the same data: a new limit on the muon's electric dipole moment (up to 100 times better); and, a more stringent limit on possible CPT or Lorentz violation in muon spin precession. A technically driven schedule permits data taking to begin in 2016.

5 Conclusion

The measurements of the muon g-2 have been a important benchmark for the development of QED and the Standard Model. In the recent years, following the impressed accuracy (0.54 ppm) reached by E821 experiment at BNL, a worldwide effort from different theoretical and experimental groups have significant improved its SM prediction. At present there appears to be a 3σ difference between the theoretical (SM) and the experimental value. This discrepancy, which would fit well with SUSY expectations, is a valuable constraint in restricting physics beyond the standard model and guiding the interpretation of LHC results. In order to clarify the nature of the observed discrepancy between theory and experiment and eventually firmly establish (or constrain) new physics effects, new direct measurements of the muon g-2 with a fourfold improvement in accuracy have been proposed at Fermilab by E989 experiment, and J-PARC. E989 has received a CD0 approval in September 2012 and the

CD1 is expected in mid 2013. First results could be available around 2017/18.

References

1. F. Jegerlehner, “The anomalous magnetic moment of the muon,” Berlin, Springer (2008) 426 p (Springer tracts in modern physics. 226)
2. D. Stöckinger, “Muon (g-2) and physics beyond the standard model,” In Roberts, Lee B., Marciano, William J. (eds.): Lepton dipole moments 393-438 (Advanced series on directions in high energy physics. 20)
3. H. N. Brown *et al.* [Muon g-2 Collaboration], Phys. Rev. Lett. **86** (2001) 2227
4. K. Hagiwara, R. Liao, A. D. Martin, D. Nomura and T. Teubner, J. Phys. G **38** (2011) 085003
5. J. Prades, hep-ph/0108192.
6. G. W. Bennett *et al.* [Muon G-2 Collaboration], Phys. Rev. D **73** (2006) 072003
7. New Muon (g 2) Collaboration, R.M. Carey *et. al.*, see http://lss.fnal.gov/archive/testproposal/0000/fermilab-proposal-0989.shtml
8. S. Actis *et al.* [Working Group on Radiative Corrections and Monte Carlo Generators for Low Energies Collaboration], Eur. Phys. J. C **66** (2010) 585
9. W. Kluge, Nucl. Phys. Proc. Suppl. **181-182** (2008) 280
10. http://www.int.washington.edu/PROGRAMS/11-47w/
11. J. Prades, E. de Rafael and A. Vainshtein, (Advanced series on directions in high energy physics. 20)
12. F. Jegerlehner and A. Nyffeler, Phys. Rept. **477** (2009) 1
13. X. Feng, K. Jansen, M. Petschlies and D. B. Renner, Phys. Rev. Lett. **107** (2011) 081802

14. M. Davier, A. Hoecker, B. Malaescu and Z. Zhang, Eur. Phys. J. C **71** (2011) 1515

15. F. Jegerlehner and R. Szafron, Eur. Phys. J. C **71** (2011) 1632

16. M. Benayoun, P. David, L. Del Buono and F. Jegerlehner, Eur. Phys. J. C **72** (2012) 1848

17. M. Benayoun, P. David, L. DelBuono and F. Jegerlehner, arXiv:1210.7184 [hep-ph]

18. D. Babusci, *et al.*, Eur. Phys. J. C **72** (2012) 1917

19. G. W. Bennett *et al.* [Muon (g-2) Collaboration], Phys. Rev. D **80** (2009) 052008

Frascati Physics Series Vol. LVI (2012)
Dark Forces at Accelerators
October 16-19, 2012

Dark Matter candidates : Where do we stand?

Celine Boehm
IPPP Ogden Centre, south Road, Durham DH1 3LE, UK

Abstract

The dark matter field has evolved tremendously in ten years. Many new particle candidates have been proposed by theoreticians while dark matter detection experiments have reached an unprecedented degree of precision that allows us to test accurately the WIMP paradigm. In these proceedings, I review the recent evolutions in the field and discuss possible directions in the near future.

1 Introduction

Since the observation of Supernovae of type Ia at 'large' redshift 1) and the results from Cosmological Microwave Background 2, 3), the Cosmology community has succeeded to determine the content of the Universe with an unprecedented degree of precision. While it appears that the Universe is mostly made of two unknown substances (dark matter and dark energy), the energy density associated with dark energy is about three times that of matter. Also it appears that dark matter represent about 80% of the matter content in the Universe. The nature of dark matter is unknown; It is likely to be made of massive neutral stable weakly interacting particles (WIMPs) but the community has now all the experimental tools to either find it or rule out a very important region of the parameter space.

In my opinion, three main changes happened during the last 10 years:

- The field is not 'relic density' driven anymore. Alternative scenarios to thermal Freeze-Out and non resonant self-annihilations have been proposed 4).
- Astrophysical data are now often guiding Particle dark matter model building, cf for example the PAMELA/HEAT anomaly 5, 6).
- Phenomenology overtook the Theory. Supersymmetry has long been seen as a very serious motivation to introduce Weakly Interacting Massive particles but with the lack of new Physics at LHC this is no longer the case (or not to the same extent at least) and models (rather than theories) were proposed.

In the following I will review the key changes in the field and will also discuss some important experimental results.

2 Light mass range

For many decades, the main argument which was used to test whether a particle could be a good dark matter candidate or not was to use the relic density argument. Whatever the nature of these new particles, their energy density today must not exceed the dark matter abundance that is observed.

With the present value of the dark matter cosmological parameter ($\Omega h^2 \simeq 0.1$) and the very small uncertainties (to be improved by the PLANCK experiment), such a constraint turns out to be a killer for many annihilating dark matter models. Indeed this typically implies that the annihilation cross section must have a very precise value which is difficult to achieve in most Particle Physics models, especially once one takes into account constraint from Particle Physics and Astrophysics (the annihilation cross section generally tends to be too small leading to an over abundance of dark matter).

As the relic density constraint enabled one to rule out a large fraction of the Supersymmetric parameter space, new mechanisms have been proposed to either 're-habilitate' some candidates/part of the parameter space 4, 7), making the notion of relic density less essential to model building.

However meanwhile several questions arose:

- Can we consider sub-10 GeV annihilating dark matter particles 8, 9)?
- Can dark matter particles be heavier than a few TeVs?
- Why is not there any signs of Weakly Interacting Massive Particles in the 10 GeV- TeV range?

Some of these questions are supported by anomalies in astrophysical data (the amount of which increased during the last few years). For example, the case for light particles was emphasised after that a 511 keV map was established by the SPectrometer for INTEGRAL on board of the INTEGRAL satellite 10). The latter pointed out that the emission of 511 keV photons (due to positronium formation and the signature of low energy positrons in the Milky Way), was anomalously spherical. This emission was also found to be brighter than what is expected if the positrons originate from Astrophysical sources while the sphericity and brightness could be explained by light annihilating dark matter models 11). Yet not all dark matter models work well: decaying particles fail to describe the morphology of the emission. In fact to fit the data these models require a dark matter halo profile which corresponds to a NFW profile with $\rho = 1.04 \pm 0.3$ 12), a feature which can in principle be used to test these types of models.

Exploring the light mass range implies to overcome the Hut and Lee-Weinberg limit which excludes annihilating dark matter particles lighter than a few GeVs. However this is possible if one considers e.g. either a fermion/scalar particles coupled to a (new) light gauge boson Z' or scalar particles coupled to heavy mediators. In the case of a scalar dark matter coupled to heavy fermions, the annihilation cross section is (almost) independent of the dark matter mass so imposing that such candidates have a relic density equal to the observed dark matter abundance constrains the mass of the mediator rather than the dark matter mass. It also constrains the mediator couplings to the dark matter and Standard Model particles.

In addition, one has to take into account a constraint which comes from the gamma ray emission emanating from such candidates. In particular the exchange of a heavy fermion leads to a constant annihilation cross section into electron-positron that over predicts the gamma-ray emission by five order of magnitudes (if one assumes that one photon is emitted due to final state radiation each time an electron or positron is emitted). To avoid this, the product of the couplings of the heavy mediator to the Standard Model particles and dark matter must be significantly suppressed.

Since the same process is also responsible for the production of low energy positrons in the galaxy, the suppression of the couplings that is required to not over predict the gamma ray flux in the galaxy actually leads to a 511 keV flux prediction that agrees with SPI measurement. This could well be a coincidence but this is puzzling enough to make this model interesting. In this framework, the relic density is actually ensured by the exchange of a light vector boson. However a possible alternative is annihilations into neutrinos 13). In this case, dark matter could give neutrinos a mass providing that they are Majorana particles, a condition which can be experimentally tested in neutrino experiments.

Going back to the model with a new light vector boson (to achieve the correct relic density) and a heavy mediator, it is important to notice that this can be tested by using the experimental value of the anomalous electron g-2 (δa_e). With the present value of δa_e (i.e. $\delta a_e = -0.4(0.88) \times 10^{-12}$) 14), one can exclude heavy mediators exchange as an explanation to the 511 keV line unless there is a compensation between the heavy mediator contribution and that of the Z' or if the dark matter only explains a fraction of the 511 keV emission 15). Such a conclusion however assumes a certain dark matter velocity profile 12) and would probably deserve to be revisited.

3 Heavy mass range

The very heavy mass range has also received a lot of attention recently. In particular, since the observation by the PAMELA experiment of a positron excess in the 10-100 GeV range, many dark matter models with $m_{dm} = 100$ GeV have been proposed. The difficulty in this mass range is to obtain a 'visible' signal in dark matter indirect detection experiments: due to the large mass the dark matter number density is very suppressed and as a consequence one needs to boost the annihilation rate. The resulting boost factor can originate from astrophysical considerations (such as the presence of dark matter clumps near us) or from Particle Physics arguments (such as a Sommerfeld enhancement). Among the most 'successful models' to explain the PAMELA excess, 'leptophilic' dark matter models 16) (which are dominantly coupled to leptons) have received a lot of attention. Those seem to explain successfully the positron excess but they are strongly constrained by the lack of anomaly in the anti-proton data (also collected by the PAMELA experiment) 17, 18).

As a byproduct of these anomalies, there has been many efforts to improve the predictions for positron energy and spatial propagation. Both semi-analytical and numerical methods have been used to make predictions of the flux emission expected in dark matter models. The semi-analytical method solves the diffusion equation in a 'vertical' cylinder (with radius R_{gal} that is large enough to englobe the whole 'visible' galaxy plane) with the help of Bessel and Fourier decomposition. The thickness (height) of the cylinder has direct consequences on the brightness of the signal. A small thickness generally leads to a small flux while, conversely, a large thickness tends to predict very large values of the flux.

While the spatial and energy propagation of cosmic ray has been improved over the last few years, an important issue came up with the problem of subtracting the backgrounds and foregrounds 21). In particular discrepancies in gamma ray (the so-called FERMI bubbles) and submillimetre wavelengths (the so-called 'WMAP haze') have focussed a lot attention and ask the question of whether or not these anomalies could be explained by dark matter particles e.g. 22) (despite constraints from radio emission in the galactic centre 19, 20)). At the same time, providing that one knows the background and foregrounds to a high degree of accuracy and an anomaly does exist, the study of the morphology of the 'dark' emission should provide essential information such as whether dark matter is made of annihilating or decaying particles 23) and what is the value of its mass 24).

4 Intermediate mass range

In absence of strong evidence for dark matter particles in indirect detection experiments, direct detection provides strong constraints on the Vanilla 'WIMP' hypothesis. The XENON100 experiment 25) in particular (along with EDEL-

WEISS (26), CDMS (27) and many other experiments) has unabled to set stringent limits on the dark matter elastic scattering cross section with nucleons. It was found that heavy dark matter (with a mass in the GeV-TeV range) interacts with a cross section that is less than 2 10^{-45} cm^2 if its mass is about 50 GeV, a value which is about ten order of magnitude below expectations if one assumes that the annihilation and elastic scattering cross sections are not too different and which clearly illustrates the experimental breakthrough performed by direct detection experiments.

The XENON100 experiment initially suffered from one drawback due the fact that the response of the detector to dark matter particles strongly depends on the scintillation function (L_{eff}) of liquid Xenon, for which there is no analytical expression. An interpolation to the 'calibration' data has enabled the XENON100 collaboration to establish the recoil energy associated with the primary scintillation signal in the liquid part of the detector but the absence of data below 3 keVnr prevents to accurately model L_{eff} at low energy, while this range is particularly relevant to constrain light WIMPs. To circumvent this problem, XENON100 extrapolated the data at high energy down to lower energies and also 'cut' the too low energies. However uncertainties due to the interpolation should still be present and are not reflected on the corresponding exclusion curve.

While this does not affect the quality of the experiment, the fact that uncertainties are not shown prevents to use these data to accurately constrain light dark matter models (such as those arising from Supersymmetric theories). Also this questions the compatibility between the XENON100 exclusion curve and the CoGeNT (28) and DAMA/LIBRA (29) claims.

However one can reconstruct the experimental uncertainties by repeating a similar analysis as that performed by the XENON100 experiment and not marginalising over L_{eff}. Such a procedure shows that the uncertainties on L_{eff} are large. Hence improving L_{eff} at low energy should really enable the collaboration to obtain very strong constraints on light candidate (30). An additional improvement that one can do to help theorists using the XENON100 data in a more consistent way is to exploit all the information contained in the data. For this one can grid the background events in the plane $(S1, log(S_2/S_1))$ (instead of using bands) as the collaboration did (31). This enables one to improve the constraint by a factor 3-10 (and even more at low energy), using the 100days data and we expect this method to be still very useful using the 225days data.

This has a direct impact on model building. For example in the NMSSM, one finds many dark matter models with a low mass (below 10 GeV) 32). Those are hard to constrain using direct detection experiments but XENON100 does have the potential to exclude them. A proper analysis that would take into account the astrophysical uncertainties is nevertheless still required.

In the 10 GeV-TeV region, the thermal 'freeze-out' relic density argument sets very strong constraints on the parameter space. However it was suggested recently that one could reduce the thermal candidate relic density to a very large degree and nevertheless regenerate the dark matter at a later stage. Such a scenario favours large annihilation cross section but in 33) it was shown that if the cross section is too large, one would actually overproduce gamma rays in the Milky Way. Typically cross section values which are at least thousand times larger than the canonical value ($\sigma v = 3 \ 10^{-26} \mathrm{cm}^3/\mathrm{s}$) are excluded.

Yet there was also a very interesting proposal in this mass range that dark matter can annihilate and produce Higgs bosons in our dark matter halo 34, 35, 36). In particular if the dark matter mass has very specific values (for example $m_{dm} = m_H/2$), one expects the Higgs boson to be produced at rest in the Milky Way 35). The corresponding signature will be the Higgs boson decay into two gammas which in some circumstances can actually be detected. While this applies to the Standard Model Higgs boson, such a technique could be used to exclude light Higgs bosons, such as those predicted in the Next-to-Minimal Supersymmetric extension of the Standard Model.

5 Conclusion

The dark matter field has considerably evolved during the last ten years. While the relic density argument has set very strong constraints on the dark matter annihilation cross section, new directions have been explored where the dark matter could be lighter than a proton or much heavier than a few TeV. Meanwhile indirect detection experiments have collected an impressive amount of data and some anomalies appeared. Those might be indications of dark matter but they could also be related to astrophysical sources. Whatever the origin of these anomalies, these have encouraged the community to propose new dark matter models (including with interactions with leptons only) and explore new directions far away from supersymmetric theories. Since no sign of dark matter particles has been found yet, despite intensive searches at LHC nor in direct detection experiments, it is likely that the dark matter quest continues for at least a few more years. But with the results of the LHC, PLANCK, FERMI-LAT,AMS II, XENON100 and many other experiments delivering their results in the near future, the next ten years should be fascinating!

References

1. S. Perlmutter *et al.* [Supernova Cosmology Project Collaboration], Astrophys. J. **483**, 565 (1997) [astro-ph/9608192].

2. E. Komatsu *et al.* [WMAP Collaboration], Astrophys. J. Suppl. **192**, 18 (2011) [arXiv:1001.4538 [astro-ph.CO]].

3. P. de Bernardis *et al.* [Boomerang Collaboration], Nature **404**, 955 (2000) [astro-ph/0004404].

4. L. J. Hall, K. Jedamzik, J. March-Russell and S. M. West, JHEP **1003** (2010) 080 [arXiv:0911.1120 [hep-ph]].

5. O. Adriani, G. C. Barbarino, G. A. Bazilevskaya, R. Bellotti, M. Boezio *et al.*, Astropart. Phys. **34** (2010) 1 [arXiv:1001.3522 [astro-ph.HE]].

6. M. A. DuVernois, S. W. Barwick, J. J. Beatty, A. Bhattacharyya, C. R. Bower, C. J. Chaput, S. Coutu and G. A. de Nolfo *et al.*, Astrophys. J. **559**, 296 (2001).

7. X. Chu, T. Hambye and M. H. G. Tytgat, JCAP **1205**, 034 (2012) [arXiv:1112.0493 [hep-ph]].

8. C. Boehm, T. A. Ensslin and J. Silk, J. Phys. G G **30**, 279 (2004) [astro-ph/0208458].

9. C. Boehm and P. Fayet, Nucl. Phys. B **683**, 219 (2004) [hep-ph/0305261].

10. J. Knodlseder, V. Lonjou, P. Jean, M. Allain, P. Mandrou, J. -P. Roques, G. K. Skinner and G. Vedrenne *et al.*, Astron. Astrophys. **411**, L457 (2003) [astro-ph/0309442].

11. C. Boehm, D. Hooper, J. Silk, M. Casse and J. Paul, Phys. Rev. Lett. **92**, 101301 (2004) [astro-ph/0309686].

12. Y. Ascasibar, P. Jean, C. Boehm and J. Knoedlseder, Mon. Not. Roy. Astron. Soc. **368**, 1695 (2006) [astro-ph/0507142].

13. C. Boehm, Y. Farzan, T. Hambye, S. Palomares-Ruiz and S. Pascoli, Phys. Rev. D **77**, 043516 (2008) [hep-ph/0612228].

14. T. Aoyama, M. Hayakawa, T. Kinoshita and M. Nio, Phys. Rev. D **85**, 093013 (2012) [arXiv:1201.2461 [hep-ph]].

15. C. Boehm and J. Silk, Phys. Lett. B **661**, 287 (2008) [arXiv:0708.2768 [hep-ph]].

16. M. Cirelli and A. Strumia, PoS IDM **2008**, 089 (2008) [arXiv:0808.3867 [astro-ph]].

17. O. Adriani, G. C. Barbarino, G. A. Bazilevskaya, R. Bellotti, M. Boezio *et al.*, Phys. Rev. Lett. **102** (2009) 051101 [arXiv:0810.4994 [astro-ph]].

18. O. Adriani *et al.* [PAMELA Collaboration], Phys. Rev. Lett. **105** (2010) 121101 [arXiv:1007.0821 [astro-ph.HE]].

19. C. Boehm, J. Silk and T. Ensslin, arXiv:1008.5175 [astro-ph.GA].

20. N. Fornengo, R. A. Lineros, M. Regis and M. Taoso, JCAP **1201**, 005 (2012) [arXiv:1110.4337 [astro-ph.GA]].

21. D. J. Schlegel, D. P. Finkbeiner and M. Davis, Astrophys. J. **500**, 525 (1998) [astro-ph/9710327].

22. D. Hooper, D. P. Finkbeiner and G. Dobler, Phys. Rev. D **76**, 083012 (2007) [arXiv:0705.3655 [astro-ph]].

23. C. Boehm, T. Delahaye and J. Silk, Phys. Rev. Lett. **105**, 221301 (2010) [arXiv:1003.1225 [astro-ph.GA]].

24. T. Delahaye, C. Boehm and J. Silk, Mon. Not. Roy. Astron. Soc. Lett. **422**, 16 (2012) [arXiv:1105.4689 [astro-ph.GA]].

25. E. Aprile *et al.* [XENON100 Collaboration], Phys. Rev. Lett. **109**, 181301 (2012) [arXiv:1207.5988 [astro-ph.CO]].

26. J. Gironnet [EDELWEISS Collaboration],

27. T. Saab [CDMS II Collaboration], PoS IDM **2010**, 010 (2011).

28. C. E. Aalseth *et al.* [CoGeNT Collaboration], arXiv:1208.5737 [astro-ph.CO].

29. R. Bernabei, P. Belli, A. Di Marco, F. Cappella, A. d'Angelo, A. Incicchitti, V. Caracciolo and R. Cerulli *et al.*, arXiv:1301.6243 [astro-ph.GA].

30. J. H. Davis, C. Boehm, N. Oppermann, T. Ensslin and T. Lacroix, Phys. Rev. D **86**, 015027 (2012) [arXiv:1203.6823 [hep-ph]].

31. J. H. Davis, T. Ensslin and C. Boehm, arXiv:1208.1850 [hep-ph].

32. D. A. Vasquez, G. Belanger, C. Boehm, A. Pukhov and J. Silk, Phys. Rev. D **82**, 115027 (2010) [arXiv:1009.4380 [hep-ph]].

33. A. J. Williams, C. Boehm, S. M. West and D. A. Vasquez, arXiv:1204.3727 [hep-ph].

34. C. B. Jackson, G. Servant, G. Shaughnessy, T. M. P. Tait and M. Taoso, JCAP **1004**, 004 (2010) [arXiv:0912.0004 [hep-ph]].

35. N. Bernal, C. Boehm, S. Palomares-Ruiz, J. Silk and T. Toma, arXiv:1211.2639 [hep-ph].

36. C. B. Jackson, G. Servant, G. Shaughnessy, T. M. P. Tait and M. Taoso, arXiv:1302.1802 [hep-ph].

Frascati Physics Series Vol. LVI (2012)
Dark Forces at Accelerators
October 16-19, 2012

DIRECT DETECTION OF DARK MATTER PARTICLES

R. Cerulli
Laboratori Nazionali del Gran Sasso, I.N.F.N., Assergi, Italy

Abstract

Experimental observations and theoretical arguments have pointed out that a large part of the Universe is composed by Dark Matter particles. This motivates experimental efforts to investigate the direct detection of these particles with detectors placed in underground laboratories. In this paper a short review of some used techniques will be presented. Particular care will be given to the results obtained by the DAMA/LIBRA set-up. In addition, experimental and theoretical uncertainties and their implications in the interpretation and comparison of different kinds of results will be shortly addressed.

1 Direct Dark Matter detection

Many experimental observations and theoretical developments have pointed out that most of our Universe is composed by a Dark Matter component largely in form of relic particles. In theories extending the Standard Model of particle physics, many candidate particles have been proposed having different nature and interaction types 1). Often the acronym WIMP is adopted as a synonymous of Dark Matter particle, referring usually to a particle with spin-independent elastic scattering on nuclei. On the contrary, also WIMPs are Dark Matter candidates which can have different phenomenologies and interaction types among them. Moreover, even a suitable particle not yet foreseen by theories could be the solution or one of the solutions.

The DM interaction processes can be of well different nature depending on the candidate; the most considered process is the elastic scatterings on target nuclei but other processes have been proposed in literature and, in particular, some in which also electromagnetic radiation is produced in the interaction 2). Thus, considering the richness of particle possibilities and the existing uncertainties on related astrophysical (e.g. halo model and related parameters, etc.), nuclear (e.g. form factors, spin factors, scaling laws, etc.) and particle physics (e.g. particle nature and interaction types, etc.), a widely-sensitive model independent approach is mandatory. Indeed, most of the activities in the field have based the analysis on a particular "a-priori" assumption on the nature of the DM particle and of its interaction to try to overcome the limitation arising from their large measured counting rate.

In the following some recent achievements obtained by experiments exploiting model-dependent and model independent approaches will briefly summarized.

2 Experiments exploiting model-dependent approach

Originally the so-called "traditional" approach was pursued by simply comparing the measured counting rate with an expectation from an assumed scenario (which implies to adopt many assumptions and approximations). To try to reduce the experimental counting rate, large data selections and several subtraction procedures are often applied to derive a set of recoil-like candidates assuming a priori the interaction type and the nature of the DM candidate. This is the approach pursued by experiments like XENON, CDMS, EDELWEISS, CRESST, etc. Several have been discussed at the Conference 3); here only few are mentioned.

As regard XENON, this project realized so far two set-ups: XENON10 and XENON100 at Gran Sasso Laboratory, using dual phase liquid/gas detectors. Experiments exploiting such technique (like also WARP, ZEPLIN, etc.) perform statistical discrimination between nuclear recoil-like candidates and electromagnetic component of the measured counting rate through the ratio of the prompt scintillation signal ($S1$) and the delayed signal ($S2$) due to drifted electrons in the gaseous phase. The XENON100 experiment has released recently data for an exposure of 224.6 days, using a fiducial volume of 34 kg of Xenon target mass 4). The experiment starts from a relevant counting rate and, in order to try to lower it, needs to apply many data selections, subtractions and handling. Each selection step can introduce systematic errors which can also be variable along the data taking period. Efficiencies of the procedures are not explained in details. After these selections procedures, an analysis based on some discrimination between the electromagnetic radiation and recoiling candidates is applied. Concerns are discussed in literature about the real response of such devices, in particular, to low energy recoils 5, 6). The technical performance of the apparata, confirmed also by similar experiments, has shown that: i) the detectors suffer from non-uniformity; it needs corrections to be evaluated and applied, and systematics to be accounted for; ii) the response of these detectors is not linear, i.e. the number of photoelectrons/keV depends on the energy scale and depends also on the applied electric field; iii) the physical energy threshold is not proved by source calibrations in the energy interval of interest; the calibrations are done with external sources (due to the use of electric fields) and the lowest energy calibration point is 122 keV of ^{57}Co; no calibration is possible at the quoted energy threshold; montecarlo reconstruction of the spectrum is also required; this limits the sensitivity of the method and the reliability of the results; iv) the use of energy calibration lines from Xe activated by neutrons cannot be applied as routine and the studies on a possible calibration with internal sources have not been realized so far; v) despite of the small light response (2.28 photoelectron/keVee), an energy threshold at 1.3 keVee is claimed; vi) the energy resolution is poor; vii) in the scale-up of the detectors the performances deteriorate; viii) the behaviour of the light yield for recoils at low energy is in every case, uncertain.

In the double read-out bolometric technique, the heat signal and the ionization signal are used in order to discriminate between electromagnetic events and recoil-like events. This technique is used by CDMS and EDELWEISS collaborations. CDMS-II detector consists of 19 Ge bolometer of about 230 g each one and 11 Si bolometer of about 100 g each one. The experiment released data for an exposure of about 190 kg × day [7] using only 10 Ge detectors in the analysis (discarding all the data collected with the other ones) and considering selected time periods for each detector. EDELWEISS employs a target fiducial mass of about 2 kg of Ge and has released data for an exposure of 384 kg × day collected in two different periods (July-Nov 08 and April 09-May 10) [8] with a 17% reduction of exposure due to run selection. These two experiments claim to have an "event by event" discrimination between *noise + electromagnetic background* and *recoil + recoil-like (neutrons, end-range alphas, fission fragments,...)* events by comparing the bolometer and the ionizing signals for each event, but their results are, actually, largely based on "a priori" huge data selections and on the application of other preliminary rejection procedures which are generally poorly described and often not completely quantified. An example is the time cut analysis used to remove the so-called surface electrons that are distributed in the electromagnetic band and in the recoiling one, spanning from low to high energy. No detailed discussion about the stability and the robustness of the reconstruction procedure is given; a look-up table to identify such event is used but systematical errors on the stability in time of such table are not discussed. In these experiments few recoil-like events survive the cuts and selection procedures applied in the data analysis. These events are generally interpreted in terms of background. Moreover, most efficiencies and physical quantities entering in the interpretation of the claimed selected events have never been properly accounted. In addition, further uncertainties are present when, as done in some cases, a neutron background modeling is pursued. As regards, in particular, their application to the search for time dependence of the data (such as the annual modulation signature), it would require – among other – to face the objective difficulty to control all the operating conditions – at the needed level ($< 1\%$) – despite of the required periodical procedures e.g. for cooling and for radiation source introduction for calibration as well as of the limitation arising from the reachable duty cycle. The attempt performed by CDMS-II to search for annual modulation in the data have been done by using only 8 detectors over 30 and using data that are not continuous over the whole annual periods considered in the analysis [9]. The use of non-overlapping time periods collected with detectors having background rate within the signal box that differ orders of magnitude cannot allow one to get any reliable result (see e.g. arguments in 10)).

The CRESST experiment exploits the double read-out bolometric technique, using the heat signal due to an interacting particle in the $CaWO_4$ crystals and the scintillation light produced. A statistical discrimination of nuclear recoil-like events from electromagnetic radiation is performed. The detector is placed in the Gran Sasso laboratory. The last data released by the experiment have been collected with 8 detectors of 300 g each one, for an exposure of about 730 kg × day 11). As regards the cuts and selection procedures applied, most of the above discussion also holds. After selections, 67 recoil-like events have been observed in the Oxygen band. The evaluated background contribution can not account for all the observed events. The unexplained excess of events and their energy distribution can be interpreted in terms of a WIMP candidate with spin-independent interaction and a mass in the range of 10-30 GeV. This is compatible with interpretations of the annual modulation result already reported by DAMA in terms of a WIMP candidate and with the hint reported by CoGeNT (see later). Improvement in the radiopurity of the set-up are planned, in order to reduce known source of background. Future results are foreseen.

Other positive hints of a possible light Dark Matter signal have been reported by the CoGeNT experiment 12). The set-up is composed by 440 g, p-type point contact (PPC) Ge diode, with a very low energy threshold at 0.4 keVee. It is located in the Soudan Underground Laboratory. In the data analysis no discrimination between electromagnetic radiation and nuclear recoils is applied. Only noise events are rejected. The experiment observes an excess of events with respect to an estimated background in the energy range 0.4-3.2 keVee. The energy spectrum of the excess is compatible with a signal produced by the interaction of a DM particle with a mass around 10 GeV. In addition in an exposure of 146 kg × days the CoGeNT experiment also reports an evidence at about 2.8σ C.L. of an annual modulation of the counting rate (see later) in (0.5-0.9) keV with phase and period compatible with a Dark Matter signal. The modulation effect observed is similar to that observed with much higher statistical significance by the DAMA collaboration before.

It is worth noting that – in every case – in experiment using discrimination procedures the result will not be the identification of the presence of WIMP elastic scatterings because of the known existing recoil-like indistinguishable background which can hardly be estimated at the needed level of precision. Finally, the electromagnetic component of the counting rate, rejected in this approach, can contain the signal or part of it and will be lost by these approaches.

To search for an elastic scattering WIMP the approach based on the so-called directionality signature can also be considered. It is based on the correlation between the distribution of the recoiling events with the galactic motion of the Earth. In the practice, this approach has some technical difficulties because it is arduous to detect the short recoil track. Different techniques are under consideration but, up to now, they are at R&D stage and have not yet produced competitive results in the field (see e.g. the DRIFT project or the DM-TPC experiment). It has been been suggested also the use of anisotropic scintillator detectors 13). Low background $ZnWO_4$ crystal scintillators have been recently proposed; the features and performances of such scintillators are very promising; a paper exploiting this technique has been recently published 14).

3 Model independent signatures

To obtain a reliable signature for the presence of DM particles in the galactic halo, it is necessary to follow a suitable model independent approach. With the present technology, one feasible and able to test a large range of cross sections and of DM particle halo densities, is the so-called annual modulation signature 15). The annual modulation of the signal rate originates from the Earth revolution around the Sun and offers many peculiarities since the effect induced by DM particles must simultaneously satisfy all the following requirements: (i) the rate must contain a component modulated according to a cosine function; (ii) with one year period; (iii) with a phase roughly around 2^{nd} June; (iv) the modulation must only be found in a well-defined low energy range, where DM particles can induce signals; (v) it must apply just to those events in which only one detector, in a multi-detectors set-up, actually "fires" (*single-hit* events), since the probability that DM particles would have multiple interactions is negligible; (vi) the modulation amplitude in the region of maximal sensitivity has to be $\leq 7\%$ for usually adopted halo distributions, but it can be significantly larger in case of some possible scenarios. To mimic such a signature either spurious effects or side reactions should be able not only to account for the observed modulation amplitude but also to simultaneously satisfy all the requirements. This signature has been exploited with large exposure – using highly radiopure NaI(Tl) as target material – by the former DAMA/NaI experiment and the present DAMA/LIBRA one. In the following the obtained model-independent result will be briefly recalled.

4 The model independent result obtained by the DAMA project exploiting the annual modulation signature

The DAMA/NaI set up and its performances are described in ref. 16, 17, 18, 19), while the DAMA/LIBRA set-up and its performances are described in ref. 20); the recent upgrade of DAMA/LIBRA is presented in ref. 21). The sensitive part of the DAMA/LIBRA set-up is made of 25 highly radiopure NaI(Tl) crystal scintillators placed in a 5-rows by 5-columns matrix; each crystal is coupled to two low background photomultipliers working in coincidence at single photoelectron level. The detectors are placed inside a sealed copper box continuously flushed with HP nitrogen and surrounded by a low background and massive shield. The whole installation is air-conditioned and the temperature is continuously monitored and recorded. The detectors' responses range from 5.5 to 7.5 photoelectrons/keV. Energy calibrations with X-rays/γ sources are regularly carried out down to few keV in the same conditions as the production runs. In the data analysis a software energy threshold of 2 keV is considered.

The DAMA/LIBRA data released so far correspond to six annual cycles for an exposure of 0.87 ton×yr 24). Considering these data together with those previously collected by DAMA/NaI over 7 annual cycles (0.29 ton×yr), the total exposure collected over 13 annual cycles is 1.17 ton×yr; this is orders of magnitude larger than the exposures typically collected in the field. Several analyses on the model-independent DM annual modulation signature have been performed (see Refs. 22, 23) and references therein); here just few arguments are mentioned. In particular, Fig. 1 shows the time behaviour of the experimental residual rates of the *single-hit* events collected by DAMA/NaI and by DAMA/LIBRA in the (2–6) keV energy interval 22, 23). The superimposed curve is the cosinusoidal function: $A \cos \omega(t - t_0)$ with a period $T = \frac{2\pi}{\omega} = 1$ yr, with a phase $t_0 = 152.5$ day (June 2^{nd}), and modulation amplitude, A, obtained by best fit over the 13 annual cycles. The hypothesis of absence of modulation in the data can be discarded 22, 23) and, when the period and the phase are

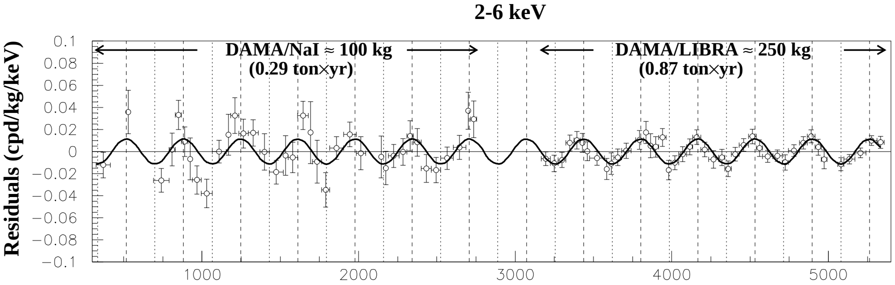

Figure 1: Experimental model-independent residual rate of the *single-hit* scintillation events, measured by DAMA/NaI over seven and by DAMA/LIBRA over six annual cycles in the (2 – 6) keV energy interval as a function of the time [18, 19, 22, 23]. The zero of the time scale is January 1^{st} of the first year of data taking. The experimental points present the errors as vertical bars and the associated time bin width as horizontal bars. The superimposed curve is $A\cos\omega(t-t_0)$ with period $T=\frac{2\pi}{\omega}=1$ yr, phase $t_0=152.5$ day (June 2^{nd}) and modulation amplitude, A, equal to the central value obtained by best fit over the whole data: cumulative exposure is 1.17 ton × yr. The dashed vertical lines correspond to the maximum expected for the DM signal (June 2^{nd}), while the dotted vertical lines correspond to the minimum. See Refs. [22, 23] and text.

released in the fit, values well compatible with those expected for a DM particle induced effect are obtained [23]; for example, in the cumulative (2–6) keV energy interval: $A=(0.0116\pm0.0013)$ cpd/kg/keV, $T=(0.999\pm0.002)$ yr and $t_0=(146\pm7)$ day. Summarizing, the analysis of the *single-hit* residual rate favours the presence of a modulated cosine-like behaviour with proper features at 8.9 σ C.L. [23].

The same data of Fig.1 have also been investigated by a Fourier analysis including the treatment of the experimental errors and of the time binning; a clear peak corresponding to a period of 1 year [23] has been obtained; this analysis in other energy regions has shown instead only aliasing peaks. Moreover, while in the (2–6) keV *single-hit* residuals a clear modulation is present, it is absent at energies just above [23]. In particular, in order to verify absence of annual modulation in other energy regions and, thus, to also verify the absence of any significant background modulation, the energy distribution measured during the data taking periods in energy regions not of interest for DM detection has also been investigated. The data analyses have allowed to exclude the presence of a background modulation in the whole energy spectrum at a level much lower than the effect found in the lowest energy region for the *single-hit* events 23). A further relevant investigation has been done by applying the same hardware and software procedures, used to acquire and to analyse the *single-hit* residual rate, to the *multiple-hits* events in which more than one detector "fires". In fact, since the probability that a DM particle interacts in more than one detector is negligible, a DM signal can be present just in the *single-hit* residual rate. Thus, this allows the study of the background behaviour in the same energy interval of the observed positive effect. A clear modulation is present in the *single-hit* events, while the fitted modulation amplitudes for the *multiple-hits* residual rate are well compatible with zero 23). Similar results were previously obtained also for the DAMA/NaI case 19). Thus, again evidence of annual modulation with proper features, as required by the DM annual modulation signature, is present in the *single-hit* residuals (events class to which the DM particle induced events belong), while it is absent in the *multiple-hits* residual rate (event class to which only background events belong). The obtained result offers an additional strong support for the presence of a DM particle component in the galactic halo further excluding any side effect either from hardware or from software procedures or from background.

The annual modulation present at low energy has also been analyzed by depicting the differential modulation amplitudes, S_m, as a function of the energy. A positive signal is present in the (2–6) keV energy interval, while S_m values compatible with zero are present just above. It has been also verified that the measured modulation amplitudes are statistically well distributed in all the crystals, in all the annual cycles and energy bins; these and other discussions can be found in ref. 23) and ref. therein.

Concluding the data of DAMA/LIBRA and of DAMA/NaI fulfil all the requirements of the DM annual modulation signature.

Sometimes naive statements were put forwards as the fact that in nature several phenomena may show some kind of periodicity. It is worth noting that the point is whether they might mimic the annual modulation signature in DAMA/LIBRA (and former DAMA/NaI), i.e. whether they might be not only quantitatively able to account for the observed modulation amplitude but also able to simultaneously satisfy all the requirements of the DM annual modulation signature; the same is also for side reactions.

Careful investigations on absence of any significant systematics or side reaction able to account for the measured modulation amplitude and to simultaneously satisfy all the requirements of the signature have been quantitatively carried out (see e.g. ref. 18, 19, 22, 25, 26, 27, 28, 29), refs therein). No systematics or side reactions able to mimic the signature (that is, able to account for the measured modulation amplitude and simultaneously satisfy all the requirements of the signature) have been found or suggested by anyone over more than a decade.

5 Comparison

The DAMA obtained model independent evidence is compatible with a wide set of scenarios regarding the nature of the DM candidate and related astrophysical, nuclear and particle Physics. For examples some given scenarios and parameters are discussed e.g. in Refs. 18, 19, 30, 31, 32, 33, 34, 35, 36) and in Appendix A of Ref. 22). Further large literature is available on the topics; other possibilities are open. Here we just recall the recent papers 37, 38) where the DAMA/NaI and DAMA/LIBRA results, which fulfill all the many peculiarities of the model independent DM annual modulation signature, are examined under the particular hypothesis of a light-mass DM candidate particle interacting with the detector nuclei by coherent elastic process. In particular, in Ref. 37) allowed regions are given for DM candidates interacting by elastic scattering on nuclei including some of the existing uncertainties; comparison with theoretical expectations for neutralino candidate and with the recent possible positive hint by CoGeNT 12) is also discussed there (see Fig. 5), while comparison with possible positive hint by Cresst 11) is discussed in Ref. 38).

It is worth noting that no experiment exists, whose result can be directly compared in a model-independent way with those by DAMA/NaI and DAMA/LIBRA.

Other mentioned activities (e.g. 4, 7, 8)) claim model-dependent exclusion under many largely arbitrary assumptions (see for example discussions in 5, 6, 18, 22, 19)); often some critical points also exist in their experimental aspects. Although often the limits achieved by this approach have been presented as robust reference points, it can be easily understood that similar results are quite uncertain not only because of possible underestimated or unknown systematics in the large data selections and in some experimental aspects, but also because the results refer only to a certain (generally largely arbitrary) set of assumptions. The accounting of the many existing experimental and theoretical uncertainties can significantly vary the given model dependent results. In addition implications of the DAMA results are generally presented in incorrect/partial/no-updated way.

6 Conclusions

Large experimental efforts have been done in the investigation of the DM particles in the galactic halo. In particular, several techniques have been used. Some of them have been shortly summarized here. DAMA project reported a model independent evidence for the presence of DM particles in the galactic halo at 8.9σ C.L. (on a cumulative exposure of 1.17 ton×yr i.e. 13 annual cycles of DAMA/NaI and DAMA/LIBRA). Positive hints, compatible in some scenarios with the DAMA results, have been recently reported by CoGeNT and CRESST experiments. Claimed exclusion mentioned have been obtained by neglecting some critical points regarding experimental and theoretical aspects. All the activities mentioned foreseen upgrade of their experimental set-up. Further interesting results are expected.

In particular DAMA/LIBRA will release soon the results of the last annual cycle collected in its phase 1. At present - after the relevant upgrade occurred in 2010 [21)]- it is continuously taking data in the new phase 2.

References

1. D.G. Cerdeno et al., J. Cosm. Astrop. Phys. 06 (2007) 008; A. Bottino et al., Phys. Rev. D 81 (2010) 107302; N. Fornengo et al., Phys. Rev. D 83 (2011) 015001; A. Liam Fitzpatrick et al., Phys. Rev. D 81 (2010) 115005; D. Hooper et al., Phys. Rev. D 82 (2010) 123509; J.F. Gunion et al., arXiv:1009.2555; A.V. Belikov et al., Phys. Lett. B 705 (2011) 82; C. Arina and N. Fornengo., J. High Energy Phys. 0711 (2007) 029; D.G. Cerdeno et al., Phys. Rev. D 79 (2009) 023510; G. Belanger et al., J. High Energy Phys. 1107 (2011) 083. D. Smith and N. Weiner, Phys. Rev. D 64 (2001) 043502; D. Tucker-Smith and N. Weiner, Phys. Rev. D 72 (2005) 063509. R. Bernabei et al., Eur. Phys. J. C 23 (2002) 61. S. Chang et al., Phys. Rev. D 79 (2009) 043513; S. Chang et al., Phys. Rev. Lett. 106

(2011) 011301; S. Chang et al., J. Cosm. Astrop. Phys. 08 (2010) 018. R. Foot, Phys. Rev. D 81 (2010) 087302; R. Foot, Phys. Lett. B 703 (2011) 7; R. Foot, Phys. Rev. D 82 (2010) 095001. Y. Bai and P.J. Fox, J. High Energy Phys. 0911 (2009) 052. J. Alwall et al., Phys. Rev. D 81 (2010) 114027. M.Yu. Khlopov et al., arXiv:1003.1144; M.Yu. Khlopov et al., Int. J. Mod. Phys. D 19 (2010) 1385. S. Andreas et al., Phys. Rev. D 82 (2010) 043522. V. Barger et al., Phys. Rev. D 82 (2010) 035019. P.W. Graham et al., Phys. Rev. D 82 (2010) 063512. B. Batell et al., Phys. Rev. D 79 (2009) 115019. E. Del Nobile et al., Phys. Rev. D 84 (2011) 027301. J.L. Feng et al., Phys. Lett. B 703 (2011) 124; M.T. Frandsen et al., Phys. Rev. D 84 (2011) 041301. M.S. Boucenna and S. Profumo, Phys. Rev. D 84 (2011) 055011; Y.G. Kim and S. Shin, J. High En. Phys. 05 (2009) 036. M.R. Buckley et al., Phys. Lett. B 703 (2011) 343; M.R. Buckley et al., Phys. Lett. B 702 (2011) 216. J.L. Feng et al., Phys. Rev. Lett. 91 (2003) 011302; J.L. Feng et al., Phys. Rev. D 70 (2004) 075019. D.J.H. Chung et al., Phys. Rev. D 64 (2001) 043503. Y. Mambrini, J. Cosm. Astrop. Phys. 07 (2011) 009; Y. Mambrini, J. Cosm. Astrop. Phys. 09 (2010) 022; J. Kopp et al., J. Cosm. Astrop. Phys. 02 (2010) 014; S. Shin, arXiv:1011.6377; C. Arina et al., J. Cosm. Astrop. Phys. 09 (2011) 022; W.Y. Keung et al., Phys. Rev. D 82 (2010) 115019.

2. R. Bernabei et al., Int. J. Mod. Phys. A 22 (2007) 3155; Phys. Rev. D 77 (2008) 023506; Mod. Phys. Lett. A 23 (2008) 2125; Int. J. Mod. Phys. A 21 (2006) 1445.

3. R. Cerulli presentation available in the Conference Site.

4. E. Aprile et al., arXiv:1207.5988.

5. R. Bernabei et al., ”Liquid Noble gases for Dark Matter searches: a synoptic survey”, Exorma Ed., Roma, ISBN 978-88-95688-12-1, 2009, pp. 1–53 [arXiv:0806.0011v2].

6. J.I. Collar and D.N. McKinsey, arXiv:1005.0838; arXiv:1005.3723; J.I. Collar, arXiv:1006.2031; arXiv:1010.5187; arXiv:1103.3481; arXiv:1106.0653; arXiv:1106.3559.

7. Z. Ahmed et al., Science 327 (2010) 1619.

8. E. Armengaud et al., Phys. Lett. B 702 (2011) 329.
9. Z. Ahmed et al., arxiv:1203.1309.
10. J.I. Collar and N.E. Fields, arxiv:1204.3559.
11. G. Angloher et al., arXiv:1109.0702.
12. C.E. Aalseth et al., Phys. Rev. Lett. 106 (2011) 131301; C.E. Aalseth et al., Phys. Rev. Lett. 107 (2011) 141301.
13. P. Belli et al., Il Nuovo Cim. C15 (1992) 475; N.J.C. Spooner at al., IDM Workshop (1997) 481; Y. Shimizu et al., Nucl. Instrum. & Meth. A 496 (2003) 347; R. Bernabei et al., Eur. Phys. J. C 28 (2003) 203.
14. F. Cappella et al., Eur. Phys. J. C 73 (2013) 2276.
15. A.K. Drukier, K. Freese, and D.N. Spergel, Phys. Rev. D 33 (1986) 3495; K. Freese, J. A. Frieman and A. Gould, Phys. Rev. D 37 (1988) 3388.
16. R. Bernabei et al., Il Nuovo Cim. A 112 (1999) 545;
17. R. Bernabei et al., Eur. Phys. J. C 18 (2000) 283.
18. R. Bernabei el al., La Rivista del Nuovo Cimento 26 (2003) 1.
19. R. Bernabei et al., Int. J. Mod. Phys. D 13 (2004) 2127.
20. R. Bernabei et al., Nucl. Instr. & Meth. A 592 (2008) 297.
21. R. Bernabei et al., Journal of Instrumentation 7 (2012) P03009.
22. R. Bernabei et al., Eur. Phys. J. C 56 (2008) 333.
23. R. Bernabei et al., Eur. Phys. J. C 67 (2010) 39.
24. R. Bernabei et al., Eur. Phys. J. C 56 (2008) 333, Eur. Phys. J. C 67 (2010) 39, Eur. Phys. J. C 62 (2009) 327, Eur. Phys. J. C 72 (2012) 1920.
25. R. Bernabei et al., *AIP Conf. Proceed.* **1223**, 50 (2010) [arXiv:0912.0660].
26. R. Bernabei et al., J. Phys.: Conf. Ser. **203**, 012040 (2010) [arXiv:0912.4200]; http://taup2009.lngs.infn.it/slides/jul3/nozzoli. pdf, talk given by F. Nozzoli.

27. R. Bernabei et al., arXiv:1007.0595 to appear on *Proceed. of the Int. Conf. Frontier Objects in Astrophysics and Particle Physics*, May 2010, Vulcano, Italy.

28. R. Bernabei et al., Eur. Phys. J. C 72 (2012) 2064.

29. R. Bernabei et al., arXiv:1210.5501

30. R. Bernabei et al., Phys. Lett. B 389 (1996) 757; Phys. Lett. B 424 (1998) 195; Phys. Lett. B 450 (1999) 448; Phys. Rev. D 61 (2000) 023512; Phys. Lett. B 480 (2000) 23; Phys. Lett. B 509 (2001) 197; Eur. Phys. J. C 23 (2002) 61; Phys. Rev. D 66 (2002) 043503.

31. R. Bernabei et al., Int. J. Mod. Phys. A 21 (2006) 1445.

32. R. Bernabei et al., Eur. Phys. J. C 47 (2006) 263.

33. R. Bernabei et al., Int. J. Mod. Phys. A 22 (2007) 3155.

34. R. Bernabei et al., Eur. Phys. J. C 53 (2008) 205.

35. R. Bernabei et al., Phys. Rev. D 77 (2008) 023506.

36. R. Bernabei et al., Mod. Phys. Lett. A 23 (2008) 2125.

37. P. Belli et al., Phys. Rev. D 84 (2011) 055014.

38. A. Bottino et al., Phys. Rev. D 85 (2012) 095013.

Frascati Physics Series Vol. LVI (2012)
Dark Forces at Accelerators
October 16-19, 2012

SEARCH FOR DARK MATTER IN THE SKY

Aldo Morselli
INFN Roma Tor Vergata

Abstract

Can we learn about New Physics with astronomical and astro-particle data? Since its launch in 2008, the Large Area Telescope, onboard of the Fermi Gamma-ray Space Telescope, has detected the largest amount of gamma rays in the 20MeV 300GeV energy range and electrons + positrons in the 7 GeV-1 TeV range. These impressive statistics allow one to perform a very sensitive indirect experimental search for dark matter. I will present the latest results on these searches and the comparison with LHC searches.

1 Introduction

The Fermi Observatory carries two instruments on-board: the Gamma-ray Burst Monitor (GBM) 1) and the Large Area Telescope (LAT) 2). The GBM, sensitive in the energy range between 8 keV and 40 MeV, is designed to

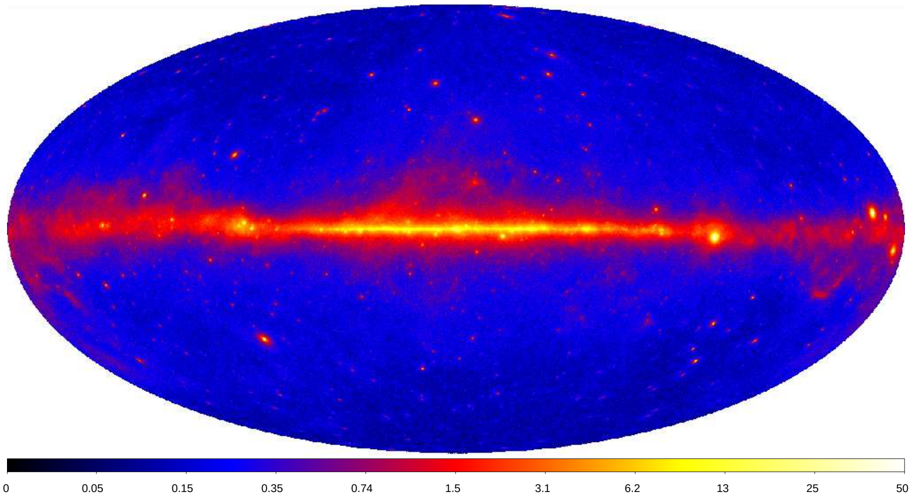

Figure 1: Sky map of the energy flux derived from 24 months of observation. The image shows γ-ray energy flux for energies between 100 MeV and 10 GeV, in units of 10^{-7} erg cm^{-2} s^{-1} sr^{-1}.

observe the full unocculted sky with rough directional capabilities (at the level of one to a few degrees) for the study of transient sources, particularly Gamma-Ray Bursts (GRBs). The LAT is a pair conversion telescope for photons above 20 MeV up to a few hundreds of GeV. The field of view is $\sim$2.4 sr and LAT observes the entire sky every $\sim$ 3 hours (2 orbits). These features makes the LAT a great instrument for dark matter (DM) searches. The operation of the instrument through the first three years of the mission was smooth at a level which is probably beyond the more optimistic pre- launch expectations. The LAT has been collecting science data for more than 99% of the time spent outside the South Atlantic Anomaly (SAA). The remaining tiny fractional down-time accounts for both hardware issues and detector calibrations 3), 4).

More than 650 million gamma-ray candidates (i.e. events passing the background rejection selection) were made public and distributed to the Community through the Fermi Science Support Center (FSSC) [1].

Over the first three years of mission the LAT collaboration has put a

---

[1] The FSSC is available at *http://fermi.gsfc.nasa.gov/ssc*

considerable effort toward a better understanding of the instrument and of the environment in which it operates. In addition to that a continuous effort was made to in order to make the advances public as soon as possible. In August 2011 the first new event classification (Pass 7) since launch was released, along with the corresponding Instrument Response Functions. Compared with the pre-launch (Pass 6) classification, it features a greater and more uniform exposure, with a significance enhancement in acceptance below 100 MeV.

2 The Second Fermi-LAT catalog

The high-energy gamma-ray sky is dominated by diffuse emission: more than 70% of the photons detected by the LAT are produced in the interstellar space of our Galaxy by interactions of high-energy cosmic rays with matter and low-energy radiation fields. An additional diffuse component with an almost-isotropic distribution (and therefore thought to be extragalactic in origin) accounts for another significant fraction of the LAT photon sample. The rest consists of various different types of point-like or extended sources: Active Galactic Nuclei (AGN) and normal galaxies, pulsars and their relativistic wind nebulae, globular clusters, binary systems, shock-waves remaining from supernova explosions and nearby solar-system bodies like the Sun and the Moon.

The Second Fermi-LAT catalog (2FGL) 5) is the deepest catalog ever produced in the energy band between 100 MeV and 100 GeV. Compared to the First Fermi-LAT (1FGL) 6) , it features several significant improvements: it is based on data from 24 (vs. 11) months of observation and makes use of the new Pass 7 event selection. The energy flux map is shown in figure 1 and the sky-distribution of the 1873 sources is shown in figure 2. It is interesting to note that 127 sources are firmly identified, based either on periodic variability (e.g. pulsars) or on spatial morphology or on correlated variability. In addition to that 1170 are reliably associated with sources known at other wavelengths, while 576 (i.e. 31% of the total number of entries in the catalog) are still unassociated.

3 Indirect Dark Matter searches

One of the major open issues in our understanding of the Universe is the existence of an extremely-weakly interacting form of matter, the Dark Matter

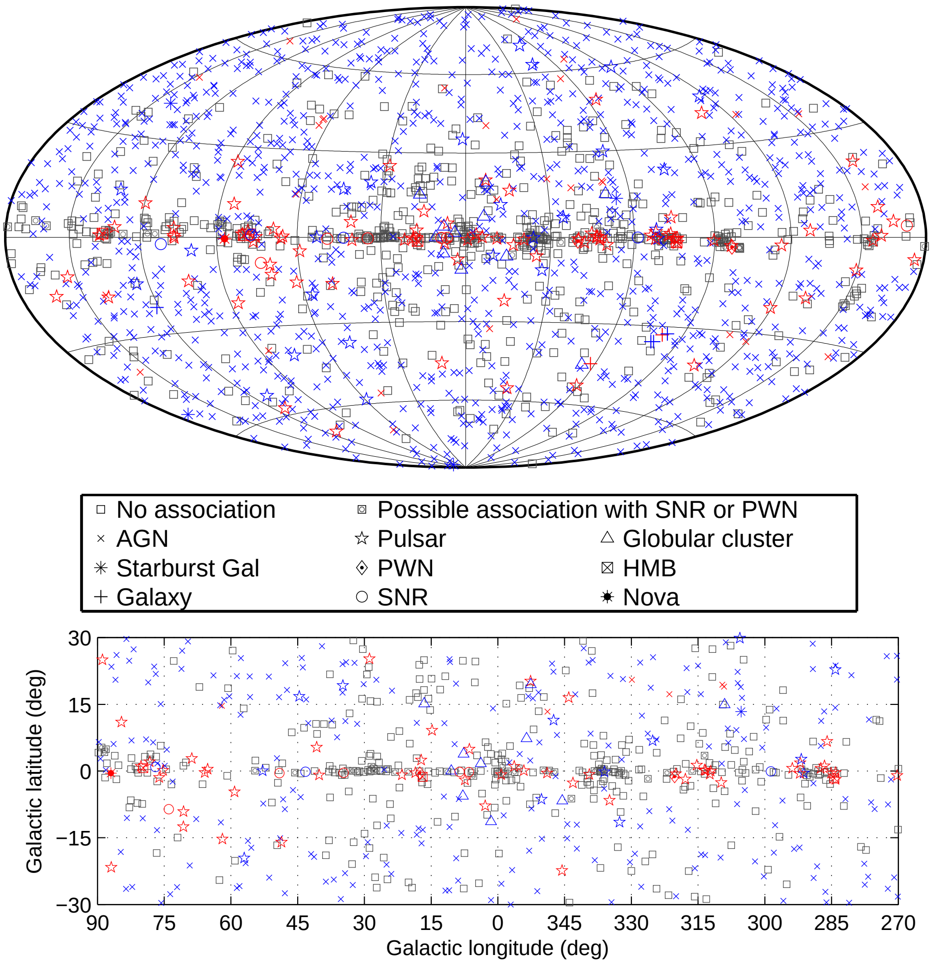

Figure 2: Full sky map (top) and blow-up of the inner Galactic region (bottom) showing sources by source class. Identified sources are shown with a red symbol, associated sources in blue.

(DM), supported by a wide range of observations including large scale structures, the cosmic microwave background and the isotopic abundances resulting from the primordial nucleosynthesis. Complementary to direct searches being carried out in underground facilities and at accelerators, the indirect search for DM is one of the main items in the broad Fermi Science menu. The word indirect denotes here the search for signatures of Weakly Interactive Massive Particle (WIMP) annihilation or decay processes through the final products (gamma-rays, electrons and positrons, antiprotons) of such processes. Among many other ground-based and space-borne instruments, the LAT plays a prominent role in this search through a variety of distinct search targets: gamma-ray lines, Galactic and isotropic diffuse gamma-ray emission, dwarf satellites, CR electrons and positrons.

3.1 Galactic center

The Galactic center (GC) is expected to be the strongest source of γ-rays from DM annihilation, due to its coincidence with the cusped part of the DM halo density profile 7), 8), 9). A preliminary analysis of the data, taken during the first 11 months of the Fermi satellite operations is presented in 10), 11) and it is shown in figures 3 and 4.

The diffuse gamma-ray backgrounds and discrete sources, as we know them today, can account for the large majority of the detected gamma-ray emission from the Galactic Center. Nevertheless a residual emission is left, not accounted for by the above models 10), 11).

Improved modeling of the Galactic diffuse model as well as the potential contribution from other astrophysical sources (for instance unresolved point sources) could provide a better description of the data. Analyses are underway to investigate these possibilities.

3.2 Dwarf galaxies

Dwarf satellites of the Milky Way are among the cleanest targets for indirect dark matter searches in gamma-rays. They are systems with a very large mass/luminosity ratio (i.e. systems which are largely DM dominated). The LAT detected no significant emission from any of such systems and the upper limits on the γ-ray flux allowed us to put very stringent constraints on the parameter space of well motivated WIMP models 12).

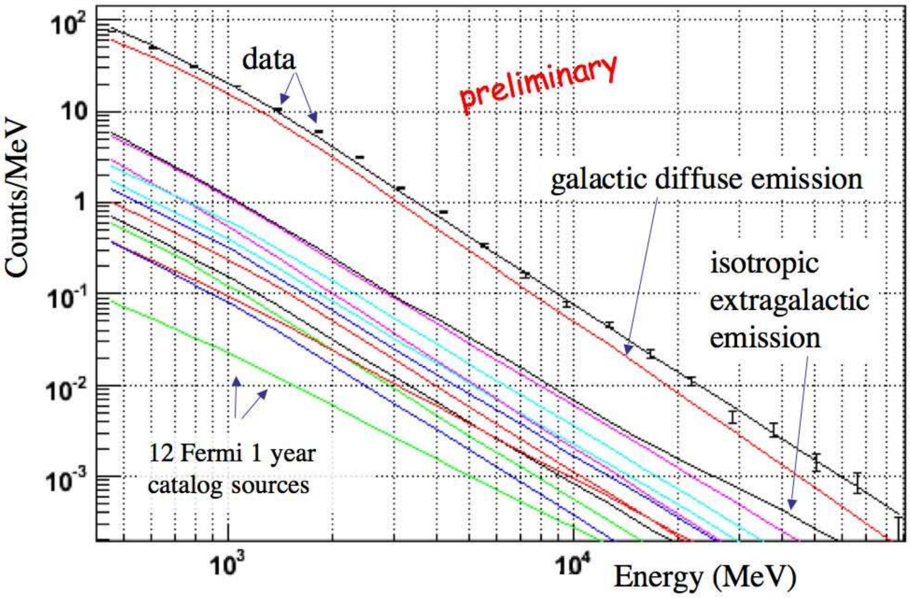

Figure 3: Spectra from the likelihood analysis of the *Fermi* LAT data (number of counts vs reconstructed energy) in a 7°×7° region around the Galactic Center (

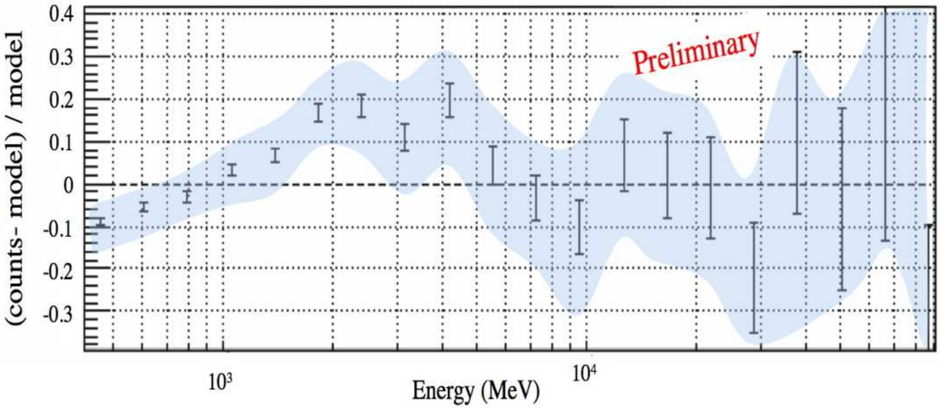

Figure 4: Residuals ((exp.data - model)/model) of the above likelihood analysis. The blue area shows the systematic errors on the effective area.

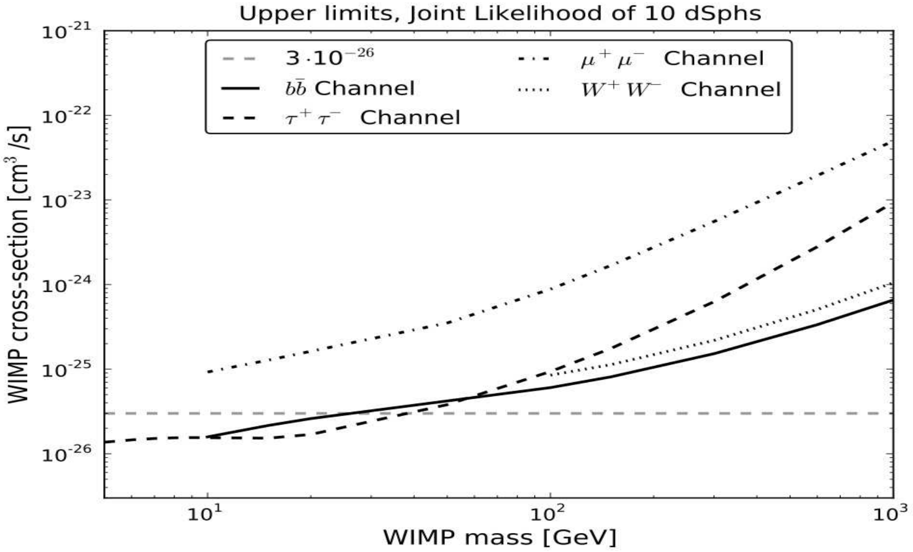

Figure 5: Derived 95% C.L. upper limits on WIMP annihilation cross sections for different channels

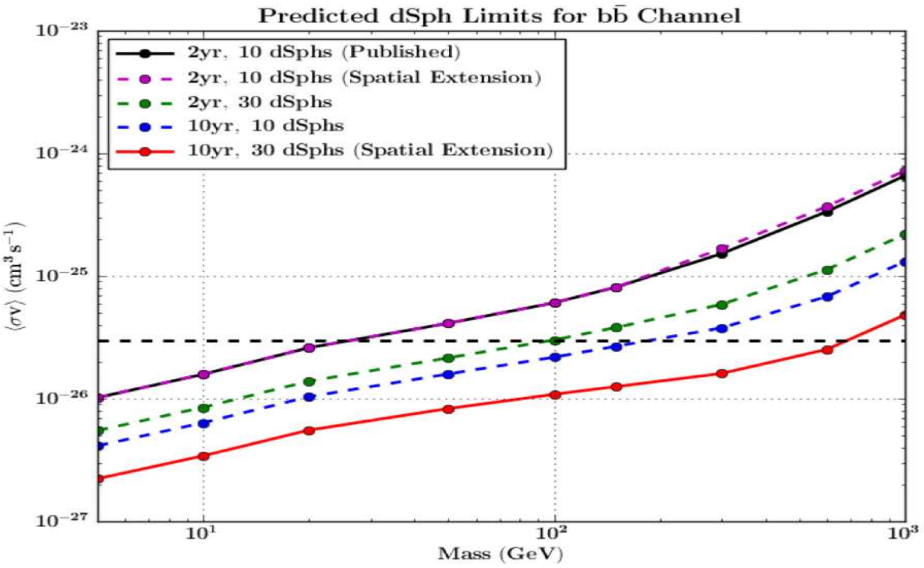

Figure 6: Predicted 95% C.L. upper limits on WIMP annihilation cross sections in 10 years for *bbar* channel.

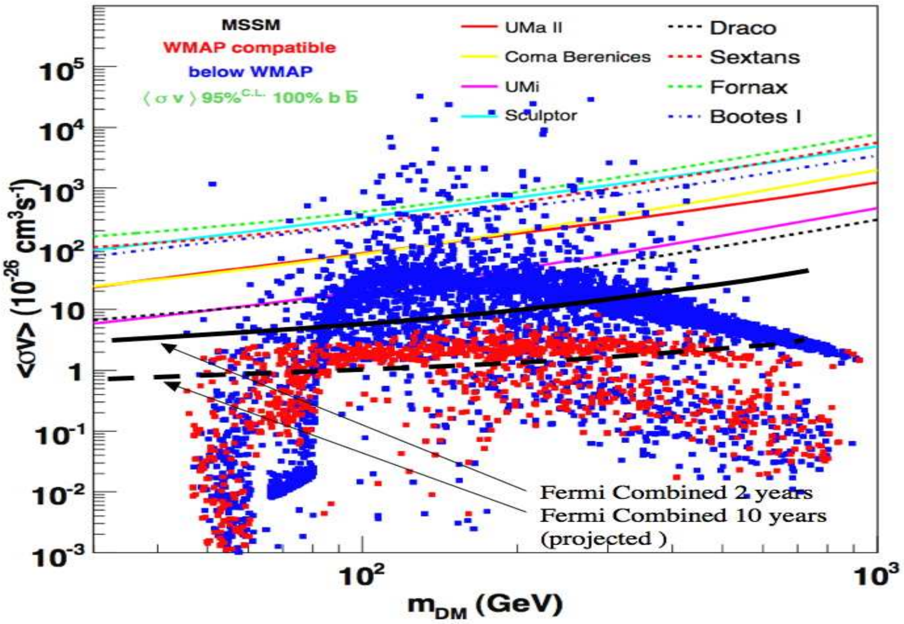

Figure 7: MSSM models in the ($m_{\rm wimp}$,$< \sigma v >$) plane. The models are consistent with all accelerator constraints and red points have a neutralino thermal relic abundance corresponding to the inferred cosmological dark matter density (blue points have a lower thermal relic density, and we assume that neutralinos still comprise all of the dark matter in virtue of additional non-thermal production processes

A combined likelihood analysis of the 10 most promising dwarf galaxies, based on 24 months of data and pushing the limits below the thermal WIMP cross section for low DM masses (below a few tens of GeV), has been recently performed 14).

The derived 95% C.L. upper limits on WIMP annihilation cross sections for different channels are shown in figure 5. The most generic cross section ($\sim 3 \cdot 10^{-26} cm^3 s^{-1}$ for a purely s-wave cross section) is plotted as a reference. These results are obtained for NFW profiles 13) but for cored dark matter profile the J-factors for most of the dSphs would either increase or not change much so these results includes J-factor uncertainties 14).

With the present data we are able to rule out large parts of the parameter space where the thermal relic density is below the observed cosmological dark matter density and WIMPs are dominantly produced non-thermally, e.g. in models where supersymmetry breaking occurs via anomaly mediation (see figure 7 for the MSSM model, updated from 12)).

These γ-ray limits also constrain some WIMP models proposed to explain the *Fermi* LAT and PAMELA e^+e^- data, including low-mass wino-like neutralinos and models with TeV masses pair-annihilating into muon-antimuon pairs.

Future improvements (apart from increased amount of data) will include an improved event selection with a larger effective area and photon energy range, and the inclusion of more satellite galaxies. In figures 6 and 7 are shown the predicted upper limits in the hypothesis of 10 years of data instead of 2; 30 dSphs instead of ten (supposing that the new optical surveys will find new dSph); spatial extension analysis (source extension increases the signal region at high energy $E \geq 10\ GeV, M \geq 200\ GeV$).

Other complementary limits were obtained with the search of possible anisotropies generated by the DM halo substructures 15), the search for Dark Matter Satellites 16) or in the Galactic Halo 17) and a search for high-energy cosmic-ray electrons from the Sun 18).

3.3 Gamma-ray lines

A line at the WIMP mass, due to the 2γ production channel, could be observed as a feature in the astrophysical source spectrum 9). Such an observation would be a “smoking gun” for WIMP DM as it is difficult to explain by a process other than WIMP annihilation or decay and the presence of a feature due to annihilation into γZ in addition would be even more convincing.

Up to now however no significant evidence of gamma-ray line(s) has been found in the first 11 months of data, between 30 and 200 GeV 19) and in the first two years of data from 7 to 200 GeV 20) (see figure 8) and work is ongoing to extend the energy range of the analysis and include more data.

Recently, the claim of an indication of line emission in Fermi-LAT data 21, 22) has drawn considerable attention. Using an analysis technique similar to 19), but doubling the amount of data as well as optimizing the region of interest for signal over square-root of background, 21) found a (trial corrected) 3.2 σ significant excess at a mass of ~ 130 GeV that, if interpreted as a signal

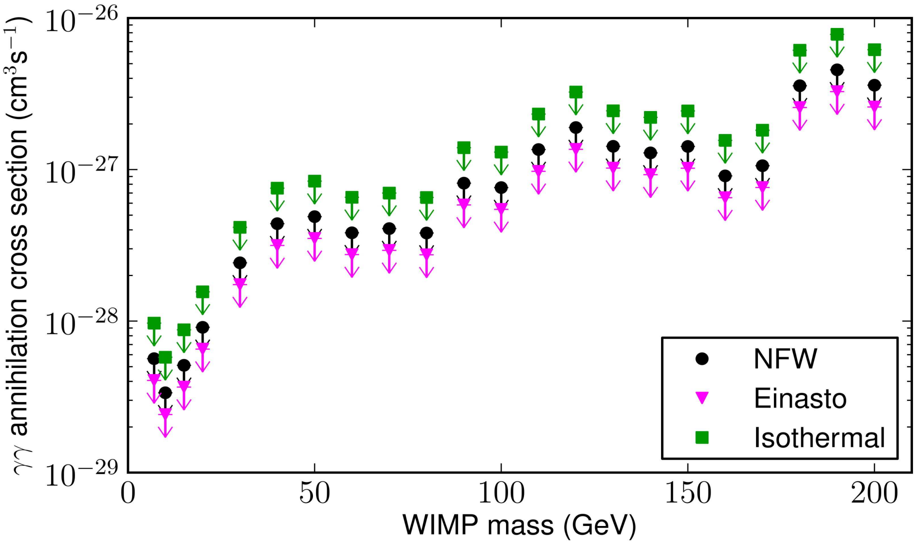

Figure 8: Dark matter annihilation 95% CL cross section upper limits into $\gamma\gamma$ for the NFW, Einasto, and isothermal profiles for the region $|b| > 10°$ plus a $20° \times 20°$ square at the GC

would amount to a cross-section of about $< \sigma v > \sim 10^{-27} cm^3 s^{-1}$.

The signal is concentrated on the Galactic Centre with a spatial distribution consistent with an Einasto profile [23]. This is marginally compatible with the upper limit presented in [20]. The main problems are the limited statistics in the GC sample and the check for any systematic effect that can mimic the line. A new version of the Instrument Response Function (IRF) (called Pass 8) is foreseen soon from the Fermi Lat collaboration. With this new analysis software we should increase the efficiency of the instrument at high energy and have a better control of the systematic effects.

3.4 The Cosmic Ray Electron spectrum

Recently the experimental information available on the Cosmic Ray Electron (CRE) spectrum has been dramatically expanded with a high precision measurement of the electron spectrum from 7 GeV to 1 TeV [24], [25]. The spectrum shows no prominent spectral features and it is significantly harder

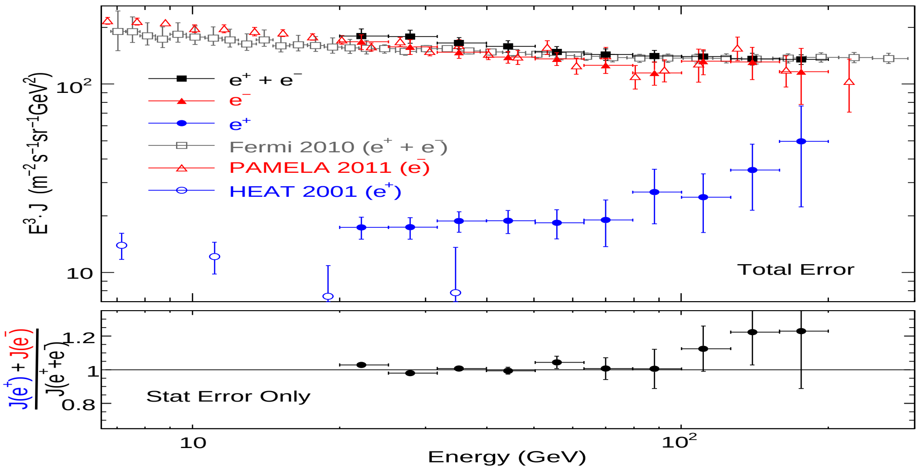

Figure 9: Energy spectra for e$^+$, e$^-$, and e$^+$ + e^- (control region). In the control region where both species are allowed, this analysis reproduces the Fermi LAT results reported previously for the total electron plus positron spectrum 24, 25) (gray). The bottom panel shows that the ratio between the sum and the control flux is consistent with 1 as expected.

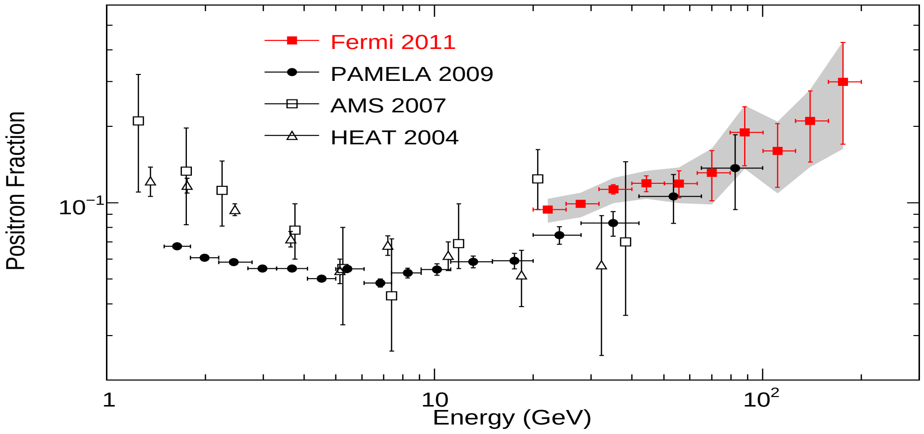

Figure 10: Positron fraction measured by the Fermi LAT and by other experiments 27, 28, 26). The Fermi statistical uncertainty is shown with error bars and the total (statistical plus systematic uncertainty) is shown as a shaded band

than that inferred from several previous experiments. (see figure 9) .

More recently we provided a further, and stronger, evidence of the positron anomaly by providing direct measurement of the absolute e^+ and e^- spectra, and of their fraction, between 20 and 200 GeV using the Earth magnetic field (see figure 9). A steady rising of the positron fraction was observed up to that energy in agreement with that found by PAMELA. In the same energy range, the e^- spectrum was fitted with a power-law with index $\gamma(e^-) = -3.19 \pm 0.07$ which is in agreement with what recently measured by PAMELA between 1 and 625 GeV 26). Most importantly, Fermi-LAT measured, for the first time, the e^+ spectrum in the 20 - 200 GeV energy interval (see figure 10) . The e^+ spectrum is fitted by a power-law with index $\gamma(e^+) = -2.77 \pm 0.14$.

These measurements seems to rule out the standard scenario in which the bulk of electrons reaching the Earth in the GeV - TeV energy range are originated by Supernova Remnants (SNRs) and only a small fraction of secondary positrons and electrons comes from the interaction of CR nuclei with the interstellar medium (ISM). An additional electron + positron component peaked at ~ 1 TeV seems necessary for a consistent description of all the available data sets. The temptation to claim the discovery of dark matter from detection of electrons from annihilation of dark matter particles is strong but there are competing astrophysical sources, such as pulsars, that can give a strong flux of primary positrons and electrons (see 29) and references therein). At energies between 100 GeV and 1 TeV the electron flux reaching the Earth may be the sum of an almost homogeneous and isotropic component produced by Galactic supernova remnants and the local contribution of a few pulsars with the latter expected to contribute more and more significantly as the energy increases. If a single pulsar give the dominant contribution to the extra component a large anisotropy and a small bumpiness should be expected; if several pulsars contribute the opposite scenario is expected.

So far no positive detection of CRE anisotropy was reported by the Fermi-LAT collaboration, but some stringent upper limits were published 30) the pulsar scenario is still compatible with these upper limits.

Forthcoming experiments like AMS-02 and CALET are expected to reduce drastically the uncertainties on the propagation parameters by providing more accurate measurements of the spectra of the nuclear components of CR. Fermi-LAT and those experiments are also expected to provide more accurate measurements of the CRE spectrum and anisotropy looking for features which may give a clue of the nature of the extra component.

4 Conclusions

Fermi turned four years in orbit on June, 2012, and it is definitely living up to its expectations in terms of scientific results delivered to the community. The mission is planned to continue at least four more years (likely more) with many remaining opportunities for discoveries.

5 Acknowledgments

The Fermi LAT Collaboration acknowledges support from a number of agencies and institutes for both development and the operation of the LAT as well as scientific data analysis. These include NASA and DOE in the United States, CEA/Irfu and IN2P3/CNRS in France, ASI and INFN in Italy, MEXT, KEK, and JAXA in Japan, and the K. A. Wallenberg Foun- dation, the Swedish Research Council and the National Space Board in Sweden. Additional support from INAF in Italy and CNES in France for science analysis during the operations phase is also gratefully acknowledged.

References

1. C.Meegan *et al.*, ApJ **702** (2009) 791
2. W.B.Atwood *et al.* [Fermi Coll.] ApJ **697** (2009) 1071-1102 [arXiv:0902.1089]
3. M.Ackermann *et al.* [Fermi Coll.] , Astroparticle Physics **35** (2012) 346353 [arXiv:1108.0201]
4. M.Ackermann *et al.* [Fermi Coll.] , ApJS **203** (2012) 4 [arXiv:1206.1896]
5. A.Abdo *et al.* [Fermi Coll.] ApJS **199** (2012) 31 [arXiv:1108.1435]
6. A.Abdo *et al.* [Fermi Coll.] ApJS **188** (2010) 405 [arXiv:1002.2280]
7. A. Morselli *et al.*, Nucl.Phys. **113B** (2002) 213

8. A.Cesarini, F.Fucito, A.Lionetto, A.Morselli, P. Ullio, Astropart. Phys. **21** (2004) 267 [astro-ph/0305075]

9. E. Baltz *et al.* , JCAP **07** (2008) 013 [arXiv:0806.2911]

10. V. Vitale and A. Morselli for the Fermi/LAT Collaboration, 2009 Fermi Symposium [arXiv:0912.3828]

11. A. Morselli, B.Cañadas, V.Vitale, Il Nuovo Cimento **34** C, N. 3 (2011) [arXiv:1012.2292]

12. A.Abdo *et al.* [Fermi Coll.], ApJ **712** (2010) 147-158 [arXiv:1001.4531]

13. J.Navarro, J.Frenk, S.White Astrophys. J. **462** (1996) 563 [arXiv:astro-ph/9508025]

14. M.Ackermann *et al.* [Fermi Coll.], Phys. Rev. Lett. **107** (2011) 241302 [arXiv:1108.3546]

15. M.Ackermann *et al.* [Fermi Coll.], Phys. Rev. D **85** (2012) 083007 [arXiv:1202.2856]

16. M.Ackermann *et al.* [Fermi Coll.], ApJ **747** (2012) 121 [arXiv:1201.2691]

17. M.Ackermann *et al.* [Fermi Coll.], ApJ **761** (2012) 91 [arXiv:1205.6474]

18. M.Ajello *et al.* [Fermi Coll.], Phys. Rev. D **84** (2011) 032007 [arXiv:1107.4272]

19. A.Abdo *et al.* [Fermi Coll.], Phys. Rev. Lett. **104** (2010) 091302 [arXiv:1001.4836]

20. M.Ackermann *et al.* [Fermi Coll.], Physical Review D **86** (2012) 022002 [arXiv:1205.2739]

21. C. Weniger, JCAP **1208** (2012) 007 [arXiv:1204.2797 [hep-ph]].

22. M. Su and D. P. Finkbeiner, arXiv:1206.1616 [astro-ph.HE].

23. T. Bringmann and C. Weniger, Dark Universe 1 (2012) 194-217 [arXiv:1208.5481]

24. A.A.Abdo *et al.* [Fermi Coll.], PRL **102** (2009) 181101 [arXiv:0905.0025]

25. M.Ackermann *et al.* [Fermi Coll.], Phys. Rev. D **82** (2010) 092004 [arXiv:1008.3999]

26. O.Adriani. *et al.* [PAMELA Coll.], Phys. Rev. Lett. **106** (2011) 201101

27. M. A. DuVernois *et al.*, [HEAT Coll.], ApJ **559** (2001) 296

28. M. Aguilar *et al.*, [AMS Coll.], Physics Reports **366** (2002) 331

29. D. Grasso, S. Profumo, A. W. Strong, L. Baldini, R. Bellazzini, E. D. Bloom, J. Bregeon, G. di Bernardo, D. Gaggero, N. Giglietto, T. Kamae, L. Latronico, F. Longo, M. N. Mazziotta, A. A. Moiseev, A. Morselli, J. F. Ormes, M. Pesce-Rollins, M. Pohl, M. Razzano, C. Sgro, G. Spandre and T. E. Stephens, *Astroparticle Physics* **32** (2009) 140 [arXiv:0905.0636]

30. M.Ackermann *et al.* [Fermi Coll.], Phys. Rev. D **82**, 092003 (2010) [arXiv:1008.5119]

Frascati Physics Series Vol. LVI (2012)
DARK FORCES AT ACCELERATORS
October 16-19, 2012

INDIRECT DARK MATTER SEARCH WITH LARGE NEUTRINO TELESCOPES

Paolo Fermani
on behalf of the ANTARES collaboration
"Sapienza" Università di Roma, P.le Aldo Moro 5, 00185, Roma, Italy
INFN Roma, P.le Aldo Moro 2, 00185, Roma, Italy

Abstract

Dark matter is one of the main goals of neutrino astronomy. At present, there are two big neutrino telescopes based on the Cherenkov technique in ice and water: IceCube at the South Pole and ANTARES in the northern hemisphere. Both telescopes are performing an indirect search for Dark Matter by looking for a statistical excess of neutrinos coming from astrophysical massive objects. This excess could be an evidence of the possible annihilation of dark matter particles in the centre of these objects. In one of the most popular scenarios the Dark Matter is composed of WIMP particles. The analysis and results of the ANTARES neutrino telescope for the indirect detection of Dark Matter fluxes from the Sun are here presented, as well as the latest IceCube published sensitivity results, for different Dark Matter models.

1 Introduction: Dark Matter and the WIMP scenario

In recent years the abundance of cosmological data, such those provided by the WMAP satellite observations 1) or by the studies of Ia supernovae 2), confirmed that only the 26% ($\Omega_m = 0.26$) of the energy balance of the Universe is under the form of matter. Moreover, in this percentage, only the 19% is composed by baryonic matter ($\Omega_b = 0.044$). This means that the 81% of matter in our Universe has a non baryonic nature ($\Omega_{cdm} = 0.21$). This component, called Dark Matter (DM) since not luminous, is necessary to explain a lot of phenomena: among others the rotational curves in spiral galaxies 3) and the Bullet cluster merging 4).

Candidates for DM must be massive, neutral, stable on cosmological time scales and only weakly and gravitationally interacting. Since neutrinos have relativistic velocities they can not be interpreted as possible DM candidates because they were not able to form the current structures of the Universe. Thus, no Standard Model particles share these properties. One of the most popular and tested scenario is that of Dark Matter composed of the Weakly Interacting Massive Particles (WIMPs). The previous listed characteristics can be reproduced in several models 5). In this paper we take into account the two most accredited models: Supersymmetry (SUSY) and Universal Extra Dimensions (UED), in particular their constrained versions: CMSSM and mUED, where the WIMP particles (lightest neutralino and lightest Kaluza-Klein particle) are stable due to the conservation of R-parity and of KK-parity respectively.

There are two ways to experimentally detect WIMPs of our galactic halo 6). The first is the direct search, which aim is to detect the recoil energy of the nuclei; the second is the indirect search, based on the detection of the products of WIMP annihilations in massive celestial bodies (stars, planets, galaxies). WIMPs loose energy through elastic scattering on nuclei and can be gravitationally captured in massive objects like the Sun, where they reach the inner core and there they can self-annihilate (being Majorana particles) producing some Standard Model particles that eventually decay producing neutrinos[1] that can be observed at Earth with large neutrino telescopes.

---

[1] The interaction producing directly neutrinos (of the same energy of the WIMP mass) is suppressed for non relativistic particles in the CMSSM case and permitted in the mUED one.

2 Large neutrino telescopes

Several neutrino telescope have been built in recent years. This kind of telescopes are based on the detection of the Cherenkov light induced by the propagation of relativistic muons generated by neutrino interactions in transparent media like water or ice. Given the small value of neutrino cross-section and the decrease of the flux with the increasing energy, detectors of big mass are necessary. Here we focus on the IceCube and ANTARES experiments.

Since the Earth acts as a shield against all the particles except neutrinos, a neutrino telescope mainly uses the detection of up-going muons as a signature of a muon neutrino (ν_μ) interaction in the Earth below the detector. The muon, travelling in water or ice, induces Cherenkov light that can be detected by the optical modules. The big range of distance covered by muons, permit to observe also interactions that happened hundreds meters far from the detector. Neutrinos of different flavours can also be detected, but with less efficiency and angular precision because the travelled distances of the respective leptons are short. IceCube can detect muons with a minimum energy of 10-20 GeV with the DeepCore extension, while ANTARES is able to detect muons with a minimum energy of 20 GeV and also the neutrino direction with an accuracy of roughly 0.3° for energies beyond 10 TeV.

2.1 The IceCube experiment

IceCube is the largest neutrino observatory in the world 7). It is located at the South Pole immersed in the ice. It consists of 4800 optical sensors or Digital Optical Modules (DOMs) installed on 80 strings between 1450 m and 2450 m below the surface: 1 km of instrumented lines. The in-ice array is complemented by a surface array, IceTop, composed of 160 ice-tanks at the top of the strings. Each tank contains two DOMs. There is also a more dense region of further 6 strings called DeepCore implemented in order to have an improved light collection and a lower energy threshold. The detector construction has been completed in 2011. IceCube covers an area of roughly 1 km^2 and a volume of 1 km^3. Each DOM consists of a 25 cm photomultiplier tube (PMT) in a glass sphere, equipped also with the electronics to perform the digitization and transmission of the signal to the surface such as to operate as a complete and autonomous data acquisition system. For each string there are 60 DOMs with a spacing of 17 m between them. The strings of modules are deployed in ice into holes drilled with hot water. The absolute positioning of the DOMs is measured with the deeper pressure sensor and by the means of laser range at the moment of the deployment. Depths of individual DOMs are determined to an accuracy of 50 cm. The absolute time accuracy on the time of arrival of the signals is guaranteed by a 20 MHz local clock.

2.2 The ANTARES detector

ANTARES is the first and largest submarine neutrino telescope in the Northern hemisphere 8). It was completed in 2008 and located (42° 48' N, 6° 10' E) in the Mediterranean Sea at roughly 2475 m depth, 42 km offshore of the cost of Toulon (France). The detector consists of a three-dimensional array of 885 10" PMTs disposed in 12 vertical strings. These strings are spread over an area of about 0.1 km^2. The basic unit of the detector is the Optical Module (OM), containing one PMT and the associated electronics 9), housed in a pressure resistant glass sphere with a mu-metal cage to minimize the effect of the Earth's magnetic field. The OMs are grouped together in 25 storeys (of three OMs) for each string interconnected via an electro-mechanical cable with the exception of one string which has 20 storeys since the last five are devoted to acoustic measures. The OMs are arranged with the axis of the PMT tubes 45° below the horizontal plane in order to increase the efficiency to detect up-going events. The height of the instrumented strings is 300 m. The distance between two consecutive storeys is 14.5 m. The horizontal distance between two adjacent strings is 60-75 m. There is also one instrumented line for sea environmental measurements. The top of the string consists of a buoy and they are anchored on the sea bed. The absolute position of the detector components as a function of time is obtained through an acoustic triangulation system combined with an orientation system that permit to determine the inclination and orientation of the single storeys 10). The absolute UTC time accuracy is guaranteed by a GPS system and by the 25 MHz clock of the detector.

3 ANTARES search for Dark Matter towards the Sun

Here we present the analysis performed in the ANTARES collaboration to search for a signal towards the Sun with the data taken by the experiment in the period 2007-2008. The Sun is a very interesting source for Dark Matter search.

In fact, the possible signal identification would have a crucial importance: we do not expect such kind of signal arising from the Sun since the solar neutrinos have a lower energy and the neutrinos produced in the Sun's corona by cosmic rays are negligible. References for other analyses with the same data sample performed in the collaboration are 11, 12, 13).

3.1 Data and simulations of signal and background

In the large part of the year 2007 ANTARES was in a 5-lines configuration for a total of 185.5 days of active detector; while in the year 2008 the detector configuration varied: 10,9,12 (since May) lines (for maintenance and repair operations) for a total of 189.8 days of active detector.

The first task in the ANTARES analyses is the discrimination between signal and background events. The main two background sources are the large flux of atmospheric muons and the flux atmospheric neutrinos both produced in the interaction of cosmic rays in the Earth's atmosphere. In order to reduce the first kind of background, the detector is installed at large depth. Moreover, only upgoing events are accepted. Still, a small fraction (but large in absolute number) of atmospheric muons are reconstructed as upgoing. By imposing strict quality cuts in the tracks, they can be further removed. The second background is irreducible since neutrinos can pass trough the Earth detected as up-going events; but we can consider that atmospheric neutrinos are isotropically distributed all over the sky while the signal neutrinos are expected to peak in the Sun direction only, so we are looking for an excess of events over an expected background. In figure 1 an example of data-Monte Carlo comparison where the two kinds of backgrounds are involved it is shown. We have to notice that for the background estimation we used the scrambled data[2] to reduce the effects of the possible systematic uncertainties.

To reconstruct both data and Monte Carlo events a fast and reliable algorithm, called BBFit, has been developed in the ANTARES collaboration 14). This algorithm is based on the multiple coincidences of the Cherenkov photons arriving on the OMs of the apparatus (hits). Then, the minimization of a χ^2 function, containing the difference between expected and measured hits, permits to reconstruct the track of the events with a given quality Q.

---

[2] Scrambled data are obtained randomising the UTC time of the events in the considered data taking period

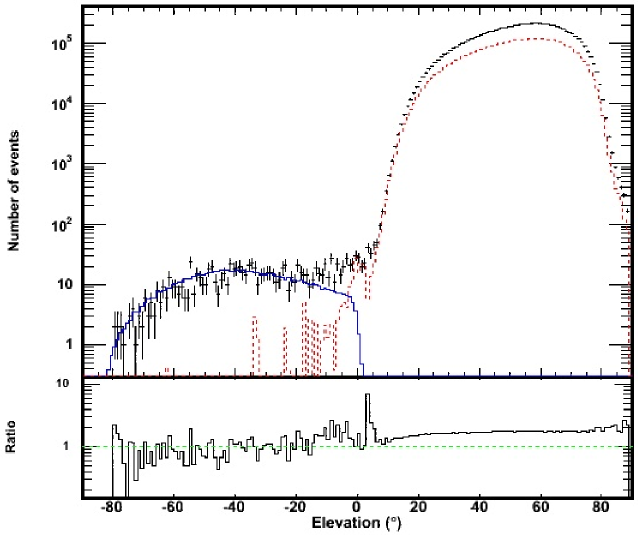

Figure 1: *Comparison between data and simulation for the elevation coordinate of the events. A* $Q < 1.4$ *is applied. The red dashed line represents the simulated atmospheric muons; the blue pointed line shows the simulated atmospheric up-going neutrinos; the black crosses represent scrambled data. The ratio of data over the simulation is shown below the main plot.*

The simulation of signal events from Dark Matter annihilation in the Sun is computed with the WimpSim package [15)], with which we can evaluate the differential neutrino spectra. Several annihilation channels are available for different WIMP masses in order to reproduce any possible Dark Matter model. The neutrino interactions in the Sun medium, the regeneration of τ leptons together with the standard neutrino oscillation scenario has been taken into account. We assume also that capture and annihilation rates are in equilibrium in the Sun. In the CMSSM the main annihilation channels are W^+W^-, $\tau^+\tau^-$ and $b\bar{b}$; for mUED are $c\bar{c}$, $\tau^+\tau^-$, $b\bar{b}$, $t\bar{t}$ and $\nu\bar{\nu}$. Another thing to note is that, although the Sun have a size of roughly half degree, since the annihilation reactions happens in its core, we can consider it as a point source.

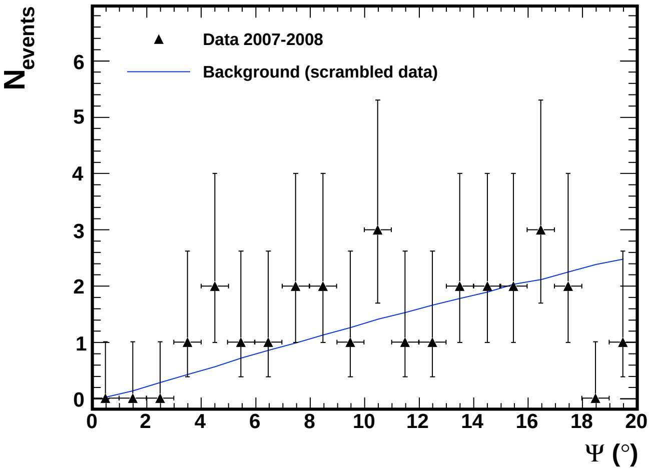

Figure 2: *Distribution of the spatial angle* $\Psi \in [0^\circ, 20^\circ]$ *of the event tracks with respect to the Sun's direction for the expected background computed from the time-scrambled data (solid blue line) compared to the data after the basic selection criteria (black triangles). A* 1σ *Poisson uncertainty is shown for each data point (black crosses).*

3.2 The optimization of the cuts

In the analysis we performed a binned search: it means to count the number of events (signal and background) within an angular bin of given aperture Ψ centred in the Sun position (see figure 2). It is important to note that we followed also a blind[3] procedure to choose the cuts to apply to our data. The optimization of these cuts has been done using the Model Rejection Factor (MRF) method 16). Two parameters were considered for the optimization: the quality of the event reconstruction Q and the half-cone angle aperture around the Sun Ψ. The MRF give us the optimized set of these two parameters to obtain the better average upper limit (at 90% C.L.) on the flux of neutrinos[4]

---

[3] In this way the cuts are selected before to look at the source of interest, avoiding a possible bias.

[4] With neutrinos we means the sum of neutrinos and anti-neutrinos.

arising from Dark Matter annihilation in the Sun. This average flux upper limit can be expressed by:

$$\bar{\phi}_{\nu}^{90\%} = \frac{\bar{\mu}^{90\%}}{A_{eff}(M_{WIMP}) \times T_{eff}} \tag{1}$$

where $\bar{\mu}^{90\%}$ is the average upper limit in the event number, derived from the Feldman and Cousins calculations 17), $A_{eff}(M_{WIMP})$ is the effective area and T_{eff} is the active detector data taking period. This evaluation has been done for each mass and channel of the two models chosen.

3.3 Results and conclusions

Using equation 1 it is possible to evaluate the sensitivity for all the Dark Matter models considered. In figure 3 the average upper limits in the neutrino flux as a function of the WIMP mass are shown. Because of the high dependence of branching ratios over the CMSSM parameter space the different channels are separate; this is not in the mUED case so we can combine the channels conserving a reliable representation. The best limits in CMSSM arise from the W^+W^- and $\tau^+\tau^-$ channels since they have a hard energy spectrum (more neutrino events). For mUED case the channel that most contribute is the $\tau^+\tau^-$ so the total sensitivity is close to the one of that channel of the CMSSM case. We can also pass from these limits on neutrino fluxes to the limits on the spin-dependent cross-section of the WIMPs with protons $\sigma_{H,SD}$. The differential neutrino flux is:

$$\frac{d\phi_\nu}{dE_\nu} = \frac{\Gamma}{4\pi d^2} \sum_f B_f \left(\frac{dN_\nu}{dE_\nu}\right)_f \tag{2}$$

where d is the distance between the Sun and the Earth, $(dN_\nu/dE_\nu)_f$ is the differential number of neutrino events for each channel, B_f the relative branching ratios and $\Gamma \simeq C_\otimes/2$ is the annihilation rate as related to the capture rate $C_\otimes$ assuming the equilibrium of the two rates inside the Sun[5].

---

[5] The capture rate expression, assuming a Navarro Frank and White (NFW) profile for the Dark Matter density and a Maxwell-Boltzmann velocity distribution, is: $C_\otimes \simeq 3.35 \times 10^{18} s^{-1} \times \left(\frac{\rho_{local}}{0.3 GeV cm^{-3}}\right) \times \left(\frac{270 kms^{-1}}{v_{local}}\right) \times \left(\frac{\sigma_{H,SD}}{10^{-6} pb}\right) \times \left(\frac{TeV}{M_{WIMP}}\right)^2$.

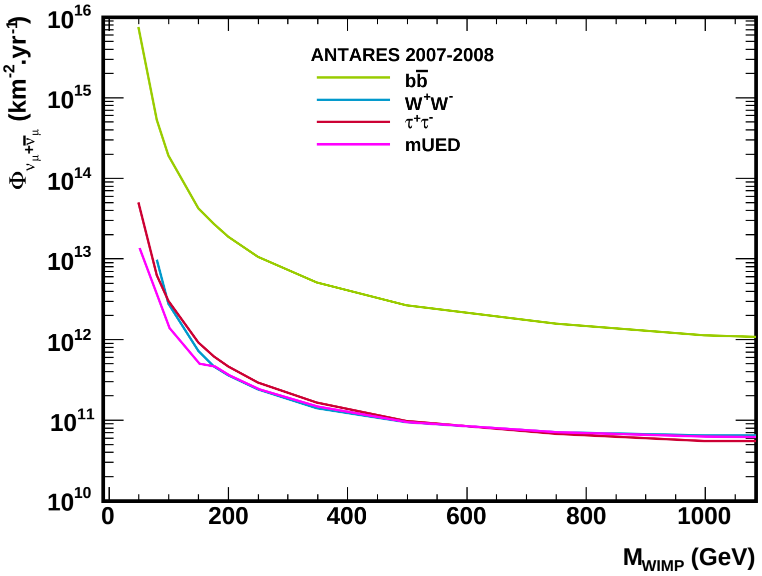

Figure 3: *90% CL upper limit on the neutrino plus anti-neutrino flux as a function of the WIMP mass in the range MWIMP∈[10 GeV;1 TeV] for the three channels $b\bar{b}$, W^+W, $\tau^+\tau$ (CMSSM) and a combination of channels (mUED).*

In figure 4 the limits on the $\sigma_{H,SD}$ values (obtained with a scan of the SuperBayes package [18]) for CMSSM and mUED models can be seen. In the spin-dependent case both ANTARES and IceCube limits are competitive compared with the direct search experiments (this is not in the case for limits on the spin-independent cross-section).

4 Summary of the IceCube Sun analysis

The search for Dark Matter in the IceCube collaboration has given results with the 79-string detector [19] and, for the first time, with the DeepCore expansion

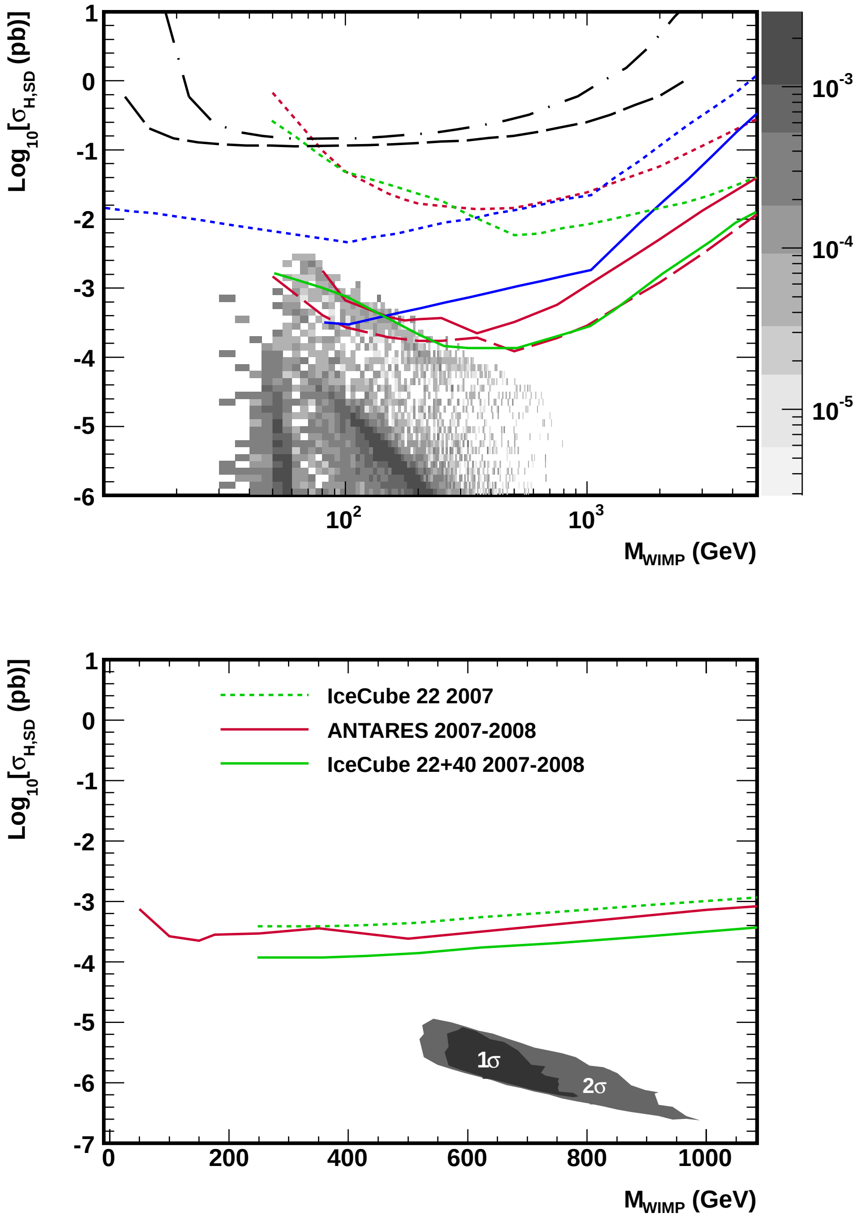

Figure 4: *up) 90% CL upper limits on the spin-dependent WIMP-proton cross-section as a function of the WIMP mass in the range* $M_{WIMP} \in$*[10 GeV;5 TeV], for the three channels:* $b\bar{b}$ *(dotted line),* W^+W *(solid line),* $\tau^+\tau$ *(dashed line), for ANTARES (red line) compared to the results of other indirect search experiments: SuperKamiokande 19962008 (blue line) and IceCube-40 plus AMANDA 2001-2008 (green line) and the results of direct search experiments: KIMS 2007 (black dot-dashed line) and COUPP 2011 (black dashed line); down) The same plot for a combination of channels in the mUED model (red line). Results from IceCube-22 2007 (green dotted line) and IceCube-22+40 2007-2008 (green solid line) are shown for comparison.*

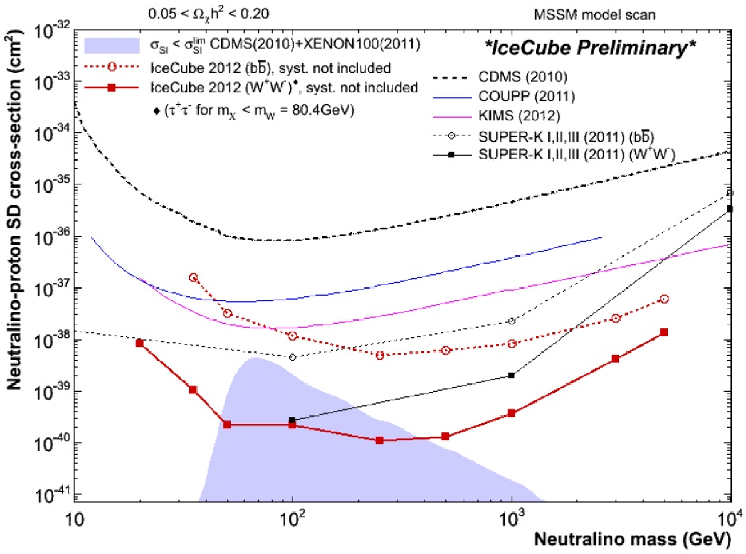

Figure 5: *90% CL upper limits on spin-dependent WIMP-proton cross-section as a function of the WIMP mass for annihilation channels* W^+W^- *(red solid line)* $\tau^+\tau^-$ *(black square and line) and* $b\bar{b}$ *(red dotted line) over a range of WIMP masses. Systematic uncertainties are included. The shaded region represents an allowed MSSM parameter space taking into account recent accelerator, cosmological and direct DM search constraints. Results from Super-K, COUPP, KIMS, CDMS, XENON-100 are shown for comparison* 21).

in the period between June 2010 and May 2011[6]. The total active detector lifetime was of 317 days, with more than 60×10^9 recorded events and roughly 25000 signal-like events in the final state. With DeepCore the analysis has reached neutrino energies of 10-20 GeV. To simulate the signal the packages DarkSusy 20) and WimpSim 15) were used. The search was binned with respect to the Sun position. Comparing signal simulation and data some cuts have been placed to reduce the contamination of atmospheric muon events (requiring a good quality reconstruction and a strong containment detection). To optimize the applied cuts a likelihood analysis was done (with the Feldman and Cousins

---

[6] The data acquisition is divided in two periods: austral summer and austral winter, when the Sun is above and below the horizon respectively

technique [17]). In figure 5 the results of this analysis, as limits on the WIMP-proton spin-dependent cross-section, compared to other experimental limits (for both direct and indirect searches) are shown. For a more complete review on the search for Dark Matter in the IceCube collaboration see the reference [22].

References

1. G. Hinshaw *et al*, WMAP collaboration, Five-Year Wilkinson Microwave Anisotropy Probe Observations: data processing, sky maps, and basic results, Astrophys. J. Supp. **180**, 225-245 (2009).
2. M. Kowalski *et al*, Improved cosmological constraints from new, old and combined supernova data set, Astrophys. J. **686**, 749-778 (2008).
3. T.S. Van Albada *et al*, Distribution of dark matter in the spiral galaxy NGC 3198, Astrophys. J. **395**, 305 (1985).
4. D. Clowe *et al*, A direct empirical proof of the existence of dark matter. Astrophys. J. **648**, 109, (2006).
5. G. Bertone, D. Hooper, J. Silk, Particle dark matter: evidence, candidates and constraints, Phys. Rept. **405**, 279 (2005).
6. Y. Mambrini, C. Muñoz, A comparison between direct and indirect dark matter search, JCAP **410**, 3 (2004).
7. A. Achterberg *et al*, IceCube Collaboration, First Year Performance of the IceCube Neutrino Telescope, Astrop. Phys. **26**, 155-173 (2006).
8. M. Ageron *et al*, ANTARES Collaboration, ANTARES: The first undersea neutrino telescope, Nucl. Instrum. Meth. **A 656**, 11-38 (2011).
9. J.A. Aguilar *et al*, ANTARES Collaboration, Performance of the front-end electronics of the ANTARES Neutrino Telescope, Nucl. Instrum. Meth. **A 622**, 59-73 (2010).
10. S. Adrian-Martinez *et al*, ANTARES Collaboration, The positioning system of the ANTARES neutrino telescope, JINST **7**, T08002 (2012).

11. S. Adrian-Martinez *et al*, ANTARES Collaboration, First search for point sources of high energy cosmic neutrinos with the ANTARES neutrino telescope, Astrophys. J. Lett. **743**, L14-L19 (2011).

12. S. Adrian-Martinez *et al*, ANTARES Collaboration, Search for relativistic magnetic monopoles with the ANTARES neutrino telescope, Astropart. Phys. **35**, 634-640 (2012).

13. S. Adrian-Martinez *et al*, ANTARES Collaboration, Measurement of atmospheric neutrino oscillations with the ANTARES neutrino telescope, Phys. Lett. B **714**, 224-230 (2012).

14. J.A. Aguilar *et al*, ANTARES Collaboration, A fast algorithm for muon track reconstruction and its application to the ANTARES neutrino telescope, Astropart. Phys. **34**, 652-662 (2011).

15. J. Edsjö, WimpSim Neutrino Monte Carlo, http://www.fysik.su.se/∼edsjo/wimpsim/.

16. G.C. Hill, K. Rawlins, Unbiased cut selection for optimal upper limits in neutrino detectors: the model rejection potential technique, Astropart.Phys. **19**, 393-402 (2002).

17. G.J. Feldman, R.D. Cousins, Unified approach to the classical statistical analysis of small signals, Phys.Rev. **D57**, 3873-3889 (1999).

18. F. Feroz *et al.*, Challenges of Profile Likelihood Evaluation in Multi-Dimensional SUSY Scans, JHEP **1106**, 042 (2011).

19. M. Danninger, E. Strahler for the IceCube Collaboration, Searches for Dark Matter Annihilations in the Sun with IceCube and DeepCore in the 79-string Configuration, Proceeding of the 32nd International Cosmic Ray Conference, Beijing, China, 11-18 August (2011).

20. P. Gondolo *et al.*, Darksusy: computing supersymmetric dark matter properties numerically, JCAP **0407**, 008 (2004).

21. M. Danninger for the IceCube collaboration, Search for Dark Matter Captured in the Sun with the IceCube Neutrino Observatory, Talk in 9th International Conference "Identification of Dark Matter, 2012" Chicago, USA, July 23-27, (2012).

22. R. Abbasi *et al*, IceCube collaboration, Multiyear Search for Dark Matter Annihilations in the Sun with the AMANDA-II and IceCube Detectors, Physical Review **D85**, 042002 (2012).

Frascati Physics Series Vol. LVI (2012)
DARK FORCES AT ACCELERATORS
October 16-19, 2012

DEEPLY INELASTIC DARK MATTER: BEAM DUMPS AS WIMP CANNONS

Chris J. Wallace
Institute for Particle Physics Phenomenology,
Durham University, Durham DH1 3LE, UK

Davison E. Soper
Institute of Theoretical Science,
University of Oregon, Eugene, OR 97403, USA

Michael Spannowsky
Institute for Particle Physics Phenomenology,
Durham University, Durham DH1 3LE, UK

Tim M.P. Tait
Department of Physics and Astronomy,
University of California, Irvine, CA 92697, USA

Abstract

We consider a phenomenological approach to constraining dark matter interactions with quarks by the exchange of a light mediator particle. We find that, for low WIMP masses, an old beam dump experiment provides stronger bounds than currently obtainable at the LHC with monojet searches.

1 A toy model for light dark matter

The search for particle dark matter (DM) benefits from many and diverse approaches, both theoretically and experimentally. Recently, there has been much theoretical interest in scenarios for light, "secluded" DM 1), where the DM – generally a hypothesized Weakly Interacting Massive Particle (WIMP) – interacts with the SM only by the exchange of a mediator particle. There are several viable portals for such an interaction. For example, the WIMP candidate could be charged under an additional $U(1)'$ gauge boson which mixes kinetically with the $U(1)_Y$ of the Standard Model (SM) (e.g. (2)).

We propose a phenomenological approach to the mediation of dark matter interactions with the SM, and do not specify a particular portal. We consider Dirac fermionic dark matter (though the analysis is easily extendable to Majorana or scalar DM) which interacts with the SM quarks by the exchange of a mediator particle that is of scalar, vector, pseudo-scalar or axial-vector type. The corresponding interaction terms in the Lagrangian are:

$$\mathcal{L}_{\rm V} = V_\mu \left(g_q \sum_q \bar{q}\gamma^\mu q + g_\chi \; \bar{\chi}\gamma^\mu \chi \right) \; , \qquad \mathcal{L}_{\rm S} = \phi \left(g_q \sum_q \bar{q}q + g_\chi \bar{\chi}\chi \right) , \quad (1)$$

with similar terms for axial-vector and pseudo-scalar mediators[1]. For the vector case, this framework encompasses the physics of the popular kinetic mixing paradigm. As a simplifying assumption, we take the couplings to all quark flavours, g_q, to be equal.

One sensitive testing ground for light dark matter is the current generation of neutrino fixed target experiments (3, 4). Here, we will consider a predecessor to the current facilities, the proton beam dump experiment E613, which ran in the 1980s at Fermilab (5, 6). The relatively high beam energy at E613 (400 GeV) allows the probing of WIMP masses in the $\sim$ few GeV range, whereas the current generation operate at much lower energy (the highest being MINOS which uses the 30 GeV NuMI beamline (7)).

2 Dark matter production and rescattering

WIMP production, $pp \to \chi\bar{\chi}$, in the target proceeds through the s-channel via quark annihilation directly to the mediator particle, which subsequently splits into two WIMPs. We study only the kinematic regime where the mass of the mediator is less than twice the final state mass of the WIMPs, $m_{\rm med} < 2m_\chi$, meaning there is no resonant production. The alternate kinematic regime, $2m_\chi > m_{\rm med}$ was covered in the context of current neutrino experiments recently in (4). The production process was implemented in MadGraph 5 (8).

After production, the WIMPs may rescatter in 15m of iron shielding (atomic number $A_{\rm Fe} = 56$, density $\rho_{\rm Fe} = 7.87$ g/cm^3) before passing through

---

[1] Subject to appropriate factors of γ_5.

Quantity	E613
Beam Energy (E_B)	400 GeV
Protons on Target (POT)	10^{17}
Target Material	tungsten
Target Nucleon Density (n_T)	$1.15 \times 10^{25}/\mathrm{cm}^3$
Target Length (L_T)	43 cm
Distance to Detector (L)	55.8 m
(Effective) Detector Area	1.77 m^2
Detector Length	166 cm

Table 1: Relevant details concerning the E613 experiment 5, 6).

the detector (with a lead-dominated fiducial mass, $A_{\mathrm{Pb}} = 208$, density $\rho_{\mathrm{Pb}} = 11.34\ \mathrm{g/cm}^3$) 56m down the beam tunnel. A WIMP scattering in the detector appears indistinguishably from a neutrino neutral current (NC) event – this allows us constrain the strength of the WIMP interaction with quarks. In lieu of a reliable model of the neutrino NC background, we conservatively require that the predicted number of WIMP NC events is lower than the total number of detected NC events at E613, i.e. less than 156.

The number of WIMPs produced at the target is (see Table 1 for experimental parameters):

$$N_{\mathrm{prod}} = 2 \times \sigma(pp \to \chi\bar{\chi}) \times L_T \times n_T \times \mathrm{POT} \tag{2}$$

The number of expected NC events in the detector from this flux may be found by calculating the probability that the WIMP scatters in the detector, but not in the intervening shielding, i.e.

$$N_{\mathrm{detected}} = \epsilon \times (1 - P_{\mathrm{Fe}}) \times P_{\mathrm{Pb}} \times N_{\mathrm{prod}}\ . \tag{3}$$

The geometric acceptance of the detector is represented schematically by the parameter ϵ, which accounts for the rapidity cut on the WIMPs. In order for a WIMP to hit the detector face, conservatively modelled as a circle of radius 0.75 m, it must be produced with an opening angle of $\Delta\theta = \frac{0.75\ \mathrm{m}}{55.8\ \mathrm{m}} = 0.0134$ radians in the lab frame. The leading-twist probability for a WIMP to scatter is:

$$P = \int_0^L dx\ \frac{1}{\lambda}\ e^{-\frac{x}{\lambda}}\ , \qquad \text{where} \qquad \lambda = \frac{A}{N_A \times \rho \times \sigma\left(\chi N \to \chi N\right)}. \tag{4}$$

N_A is Avagadro's number, 6.022×10^{23}, and $\sigma\left(\chi N \to \chi N\right)$ is the cross section for the deep inelastic scattering of a WIMP from a nucleon, N. λ is the mean free path in a material with atomic mass number A and density ρ.

A Monte Carlo simulation was employed to calculate the number of WIMP NC events expected in the detector. The simulation (implemented in `C++`) accounted for the geometric considerations above and the rescattering in both the shielding and the detector, though it was found that the shielding causes a negligible loss, $(1 - P_{\mathrm{Fe}}) \sim 1$.

3 Results

Figure 1 displays the bounds obtained on the WIMP coupling-mass plane for a mediator particle of mass 1 GeV. Also shown is a bound from the LHC, calculated using the monojet analysis of the CMS collaboration 9). Here, WIMPs are created in a *pp* collision and leave no trace in the detector; the signal is a single jet with missing transverse energy. The CMS analysis permits 660 monojet events above the SM background, from which we derive our bound, which is consistent with other recent work 10).

The constraints from E613 shown in Figure 1 get stronger as the WIMP mass decreases, clearly suggesting the investigation of MeV scale WIMPs, which already well theoretically motivated (e.g. 2)). However, with a 400 GeV proton beam and such light WIMPs, one can run into a region of small Bjorken-x. Here, parton-level deep inelastic scattering is no longer an appropriate description, owing to the gluon saturation of the parton distribution functions. A new model of the nucleus must be employed, whereby the interaction of the mediator and nucleon occurs via a colour dipole 11). With such a model in hand, one could reliably probe MeV-scale WIMP and mediator masses 12).

Acknowledgements

We are very grateful to Paolo Gondolo for suggesting we extend our earlier analysis of MINOS to include beam dump experiments and to Johan Alwall for implementing fixed target kinematics in MadGraph. CJW is grateful to the organisers of the DARK2012 workshop for the opportunity to speak and to the participants for interesting presentations and useful discussions.

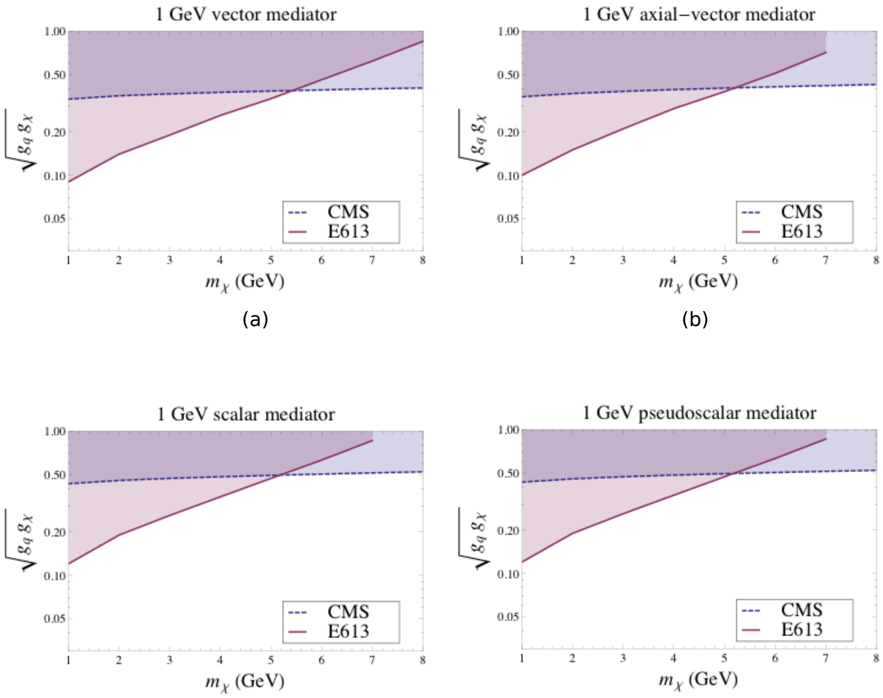

(a) (b)

(c) (d)

Figure 1: Limits on a combination of coupling parameters for 1 GeV (a) vector (b) axial-vector (c) scalar and (d) pseudo-scalar mediators. The shaded regions represent areas of parameter space ruled out by the respective experiment.

References

1. M. Pospelov, A. Ritz and M. B. Voloshin, Phys. Lett. B **662**, 53 (2008) [arXiv:0711.4866 [hep-ph]].
2. C. Boehm and P. Fayet, Nucl. Phys. B **683**, 219 (2004) [hep-ph/0305261].
3. B. Batell, M. Pospelov and A. Ritz, Phys. Rev. D **80**, 095024 (2009) [arXiv:0906.5614 [hep-ph]].
4. P. deNiverville, D. McKeen and A. Ritz, Phys. Rev. D **86**, 035022 (2012) [arXiv:1205.3499 [hep-ph]].
5. T. A. Romanowski, Acta Phys. Polon. B **16**, 179 (1985).

6. M. E. Duffy, G. K. Fanourakis, R. J. Loveless, D. D. Reeder, E. S. Smith, S. Childress, C. Castoldi and G. Conforto *et al.*, Phys. Rev. D **38**, 2032 (1988).

7. http://www-numi.fnal.gov/numwork/tdh/tdh_index.html

8. J. Alwall, M. Herquet, F. Maltoni, O. Mattelaer and T. Stelzer, JHEP **1106**, 128 (2011) [arXiv:1106.0522 [hep-ph]].

9. S. Chatrchyan *et al.* [CMS Collaboration], arXiv:1204.0821 [hep-ex].

10. I. M. Shoemaker and L. Vecchi, Phys. Rev. D **86**, 015023 (2012) [arXiv:1112.5457 [hep-ph]].

11. F. Hautmann, D. E. Soper, Phys. Rev. **D75**, 074020 (2007). [hep-ph/0702077 [HEP-PH]].

12. D. E. Soper, M. Spannowsky, T. M. P. Tait, C. J. Wallace, in preparation.

Frascati Physics Series Vol. LVI (2012)
DARK FORCES AT ACCELERATORS
October 16-19, 2012

Constraining Dark Matter annihilation cross-sections with the Cosmic Microwave Background

Silvia Galli
UPMC Univ Paris 06, UMR7095, Institut d'Astrophysique de Paris, F-75014, Paris, France.
CNRS, UMR7095, Institut d'Astrophysique de Paris, F-75014, Paris, France

Abstract

The injection of secondary particles produced by dark annihilation around redshift ~ 1000 would inevitably affect the process of recombination, leaving an imprint on cosmic microwave background (CMB) temperature and polarization anisotropies. We show that the most recent CMB measurements provided by the WMAP satellite mission and the ACT telescope place interesting constraints on DM self-annihilation rates. Our analysis includes an accurate treatment of the time-dependent coupling of the DM annihilation energy with the thermal gas. We present constraints for specific models of dark matter annihilation channels, as well as a model-independent approach to calculate constraints with future experiments, based on a principal components analysis. We show that current data place already stringent constraints on light DM particles, ruling out thermal WIMPs with mass $m \lesssim 10$GeV annihilating into electrons and WIMPs with mass $m \lesssim 4$GeV annihilating into muons. Finally, we argue that upcoming CMB experiments such as Planck, will improve the constraints by at least 1 order of magnitude, thus providing a sensitive probe of the properties of DM particles.

1 Introduction

The measurements of the Cosmic Microwave Background (CMB) flux provided by a number of different experiments, such as WMAP [1] and ACT [2], have confirmed several aspects of the cosmological standard model and improved the constraints on several cosmological parameters. A key ingredient in the CMB precision cosmology is the accurate computation of the recombination process, occurring at redshift $z_r \sim 1000$. Recombination modeling, while not simple, involves only well-understood conventional physics, and the latest models are thought to be accurate at the sub-percent level required for the future Planck [3] satellite mission [4] [5]. While the attained accuracy on the recombination process is impressive, it should be noticed that non-standard mechanisms could produce percent level modifications that are potentially observable in CMB data.

Dark Matter (DM) annihilation is one of these possible mechanisms, as it produces extra-Lyman-α and ionizing photons that can change the evolution of recombination. This kind of process has received particular attention in the last years as it could be one of the possible origins of the excess of positrons and electrons measured in cosmic rays by different experiments, such as PAMELA [7], ATIC [8] and FERMI [9].

Annihilation of dark matter particles during the epoch of recombination produces high-energy photons and electrons, which heat and ionize the hydrogen and helium gas as they cool. The result is an increased residual ionization fraction after recombination, giving rise to a low-redshift tail in the last scattering surface. The broader last scattering surface damps correlations between temperature fluctuations, while enhancing low multipole correlations between polarization fluctuations. With the WMAP results and the future Planck [3] data, it becomes conceivable these deviations may be detected.

2 Annihilating Dark Matter and CMB

The interaction of the shower produced by dark matter annihilation with the thermal gas has three main effects: i) it ionizes the gas, ii) it induces Ly-α excitation of the Hydrogen and iii) it heats the plasma. The first two modify the evolution of the free electron fraction x_e, the third affects the temperature of baryons. The imprint of self-annihilating dark matter in CMB angular power spectra can be quantified with the annihilation parameter $p_{ann} = f(z) < \sigma v > /m_\chi$ where $< \sigma v >$ is the effective self-annihilation rate, m_χ the mass of our dark matter particle and $f(z)$ indicates the fraction of energy which is absorbed *overall* by the gas, under the approximation that the energy absorption takes place locally. The fraction $f(z)$ depends on redshift, on the dark matter model and on the annihilation channel, and has been calculated by e.g. Slatyer et al. 10) for different cases.

2.1 Constraints with a constant f

In Galli et al. 11) and Galli et al. 12) we reported constraints on the p_{ann} parameter obtained using WMAP data, WMAP plus ACT data and using simulated data for the Planck experiment and for a hypotetical cosmic variance limited experiment, under the simplifying assumption that the fraction $f(z)$ is constant with redshift. This approach has the advantage of being model independent, but is clearly less accurate than implementing the whole redshift dependence of the $f(z)$ parameter, as we will show in the next section. Results for the constant $f(z) = f$ case are reported in Tab. 1. As one can notice, WMAP7 data improve the constraint of a factor ~ 1.4 compared to WMAP5 data, due to a better measurement of the third peak of the temperature power spectrum at $l \sim 1000-1200$ and of the second dip in the temperature-polarization power spectrum at $l \sim 450$. Furthermore, Planck is expected to improve constraints of about an order of magnitude. This is due to the high precision measurement of the CMB polarization that Planck is expected to deliver, and that will be able to break several degeneracies between the annihilation parameter and other cosmological parameters such as the scalar spectral index n_s.

$p_{ann}[cm^3/s/GeV]$ at 95% c.l.	
WMAP5	$< 3.6 \times 10^{-27}$
WMAP7	$< 2.5 \times 10^{-27}$
WMAP7+ACT	$< 2.2 \times 10^{-27}$
Planck	$< 3.1 \times 10^{-28}$
CVl	$< 1.1 \times 10^{-28}$

Table 1: Upper limit on p_{ann} at 95% c.l. from current WMAP observations and future upper limits achievable from the Planck satellite mission and from a cosmic variance limited experiment.

2.2 Constraints with a model dependent f(z)

In Galli et al. 12) we also considered the more accurate case where the fraction f is not just a constant, but it varies with redshift according to the calculations of Slatyer et al. 10). We chose specific values of the mass, model and annihilation channel of the dark matter particle we wanted to test, selected the corresponding $f(z)$ and then calculated the constraints on the annihilation cross-section $< \sigma v >$ with WMAP7 and ACT data. Results for different masses of dark matter particles annihilating in an electron/positron pair are reported in Table 2. Although the implementation of the z-dependence of f clearly leads to more accurate results, we found that taking a simplified analysis with constant f, such that $f(z = 600) = f_{const}$, leads to a difference with respect to the full $f(z)$ approach of less than $\sim 15\%$, depending on the annihilation channel considered.

2.3 A principal component approach

The constraints obtained in the previous section are precise only for specific models of dark matter. In Finkbeiner et al. 13) we proposed an approach to obtain precise model independent constraints, that could however take into account the redshift dependence of the fraction f. The method exploits the fact that the effects of energy deposition by dark matter annihilation at different redshifts on the CMB spectra are not uncorrelated. Any arbitrary energy deposition history can be decomposed into a linear combination of orthogonal basis vectors, with orthogonal effects on the observed CMB power spectra (C_ℓ's). For a broad range of smooth energy deposition histories, the vast majority of the

		$< \sigma v >$ in [cm^3/s] with Variable f	
m_χ[GeV]	channel	WMAP7	WMAP7+ACT
1 GeV	e$^+$e$^-$	$< 2.90 \times 10^{-27}$	$< 2.41 \times 10^{-27}$
100 GeV	e$^+$e$^-$	$< 3.95 \times 10^{-25}$	$< 3.55 \times 10^{-25}$
1TeV	e$^+$e$^-$	$< 4.68 \times 10^{-24}$	$< 3.80 \times 10^{-24}$

		$< \sigma v >$ in [cm^3/s] with Constant $f = f(z = 600)$		
m_χ[GeV]	channel	WMAP7	WMAP7+ACT	$f(z = 600)$
1 GeV	e$^+$e$^-$	$< 2.78 \times 10^{-27}$	$< 2.41 \times 10^{-27}$	0.87
100 GeV	e$^+$e$^-$	$< 3.87 \times 10^{-25}$	$< 3.35 \times 10^{-25}$	0.63
1TeV	e$^+$e$^-$	$< 4.02 \times 10^{-24}$	$< 3.48 \times 10^{-24}$	0.60

Table 2: Upper limits on self-annihilation cross section at 95% c.l. using WMAP7 data and a combination of WMAP7 and ACT data . On the top part of the table we show the results obtained using the proper variable $f(z)$ for each model. On the bottom part, for sake of comparison, we show the results obtained by taking the constraints for a constant generic f reported in Table 1, and then calculating $< \sigma v >$ for each case imposing that f is equal to the corresponding $f(z = 600)$ for each model. We show results for particles annihilating in an electron/positron pair only.

effect on the C_ℓ's can be described by a small number of independent parameters, corresponding to the coefficients of the first few vectors in a well-chosen basis. These parameters in turn can be expressed as (orthogonal) weighted averages of the energy deposition history over redshift. We employ principal component analysis (PCA) to derive the relevant weight functions, and the corresponding perturbations to the C_ℓ spectra. In Fig.1 we show the first three principal components for WMAP7, Planck and a CVL experiment, both before and after marginalization over the cosmological parameters.

For generic energy deposition histories that are currently allowed by WMAP7 data, we find up to 3 principal component coefficients are measurable by Planck and up to 5 coefficients are measurable by an ideal cosmic variance limited experiment. Fig. 2 shows the contraints on the coefficients of the first 3 principal components obtainable from the WMAP7 data, and from

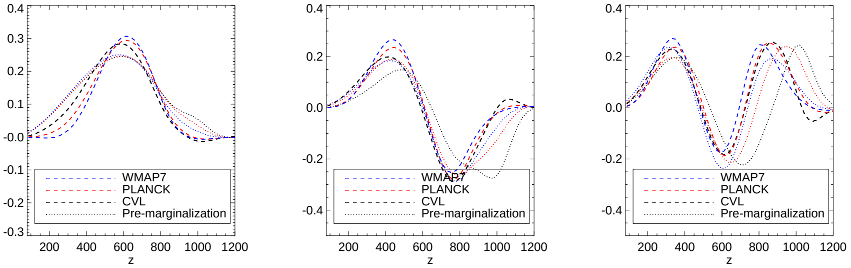

Figure 1: The first three principal components for WMAP7, Planck and a CVL experiment, both before and after marginalization over the cosmological parameters.

simulated data for Planck and a cosmic variance limited experiment, assuming no dark matter annihilation.

References

1. Larson, D., Dunkley, J., Hinshaw, G., et al. 2011, APJS, 192, 16
2. Fowler, J. W., et al. 2010, ApJ, 722, 1148.
3. Planck Collaboration, Ade, P. A. R., Aghanim, N., et al. 2011, AAP, 536, A1
4. Chluba, J., & Thomas, R. M. 2011, MNRAS, 412, 748.
5. Ali-Haïmoud, Y., & Hirata, C. M. 2011, PRD, 83, 043513 .
6. Porter, T. A., Johnson, R. P., & Graham, P. W. 2011, ARAA, 49, 155
7. O. Adriani *et al.* [PAMELA Collaboration], Nature **458**, 607 (2009).
8. J. Chang *et al.*, Nature **456**, 362 (2008).
9. Abdo, A. A., et al. 2009, Physical Review Letters, 102, 181101.
10. Slatyer, T. R., Padmanabhan, N., & Finkbeiner, D. P. 2009, PRD, 80, 043526

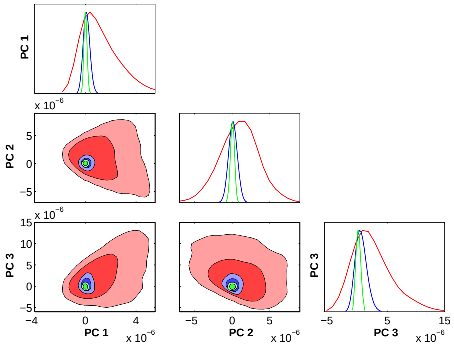

Figure 2: Constraints from the seven-year WMAP7 data (red), and from simulated data for Planck (blue) and a cosmic variance limited experiment (green). The plot shows marginalized one-dimensional distributions and two-dimensional 68% and 95% limits. The mock data for Planck and the CVL experiment assumed no dark matter annihilation. Three Principal Components were used in each run to model the energy deposition from dark matter annihilation. The units of the PC coefficients here are in m^3/s/kg, with $1 \times 10^{-6}\mathrm{m}^3/\mathrm{s}/\mathrm{kg} = 1.8 \times 10^{-27}\ \mathrm{cm}^3/\mathrm{s}/\mathrm{GeV}$.

11. Galli, S., Iocco, F., Bertone, G., & Melchiorri, A. 2009, Phys. Rev. D, **80**, 2.

12. Galli, S., Iocco, F., Bertone, G., & Melchiorri, A. 2011, PRD, 84, 027302

13. Finkbeiner, D. P., Galli, S., Lin, T., & Slatyer, T. R. 2012, PRD, 85, 043522

Frascati Physics Series Vol. LVI (2012)
DARK FORCES AT ACCELERATORS
October 16-19, 2012

SuperB physics opportunities

R. Faccini *Universitá degli Studi "La Sapienza" and INFN Roma*
on behalf of SuperB collaboration

Abstract

The Super*B* project in TorVergata (Italy) aims at investigating flavor physics with a data sample two orders of magnitude larger than the B-Factories that have operated for more than a decade. In the era of LHC this represents a unique opportunity to perform complementary indirect searches for new physics effects. In addition its design characteristics make it a flavor factory with an even broader physics reach. This paper summarizes the host of physics opportunities that will be opened by this experiment and the project status.

1 Introduction

The new Super*B* facility will investigate the consequences for flavor physics of any discoveries at the LHC and search for New Physics (NP) signatures at energy scales that exceed the direct search capabilities of the LHC. A super-flavor factory will also be able to improve the precision and sensitivity of the previous generation of flavor factories by factors of five to ten. The sides and angles of the Unitarity Triangle will be determined to an accuracy of $\sim 1\%$. Limits on Lepton Flavour Violation (LFV) in τ decays will be improved by two orders of magnitude. It will become feasible to search for CP violation (CPV) in charm mixing. Extensive searches for new states in bottomium and charmonium spectroscopy will be achieved. New precision measurements of electroweak properties, such as the running of the weak mixing angle $\sin^2\theta_W$ with energy, should become possible.

Flavor physics is an ideal tool for indirect searches for NP. Both mixing and CPV in B and D mesons occur at the loop level in the Standard Model (SM) and therefore can be subject to NP corrections. New virtual particles occurring in the loops or tree diagrams can also change the predicted branching fractions or angular distributions of rare decays. Current experimental limits indicate NP with trivial flavor couplings has a scale in the 10-100 TeV range, which is much higher than the 1 TeV scale suggested by SM Higgs physics. This means that either the NP scale cannot be seen in direct searches at the LHC or the NP scale is close to 1 TeV and therefore the coupling of NP with flavor must be minimal. In either case, indirect searches provide a way of understanding the new phenomena in great detail.

Super$B$ is an asymmetric e^+e^- collider with a 1.3 km circumference. The design calls for 6.7 GeV positrons colliding with 4.18 GeV electrons at a centre of mass energy $\sqrt{s} = 10.58\,\mathrm{GeV}$. The boost $\beta\gamma = 0.238$ is approximately half the value used at BaBar. The electron beam can be 60%-80% polarized. The design luminosity is $10^{36}\,\mathrm{cm}^{-2}\mathrm{s}^{-1}$ and data taking is expected to start in the latter part of this decade with a delivered integrated luminosity of $75\,\mathrm{ab}^{-1}$ over five years.

In the following sections, the physics potential of SuperB will be reviewed separating the "Golden Modes" from the broader set of physics possible at a flavour-factory. Finally, a comparison with the competitors and the future perspectives will be reported.

2 Physics Potential: Golden Modes

Contrarily to the B-Factories, there is not a single mode that drives the design of the experiment. Tab 1 summarizes the impact on several "Golden Modes" of possibile NP models, impact that is here briefly detailed.

	H^+	MFV	non-MFV	ZP	RH	SUSY models			
						AC	RVV2	AKM	δLL
$\mathcal{B}(\tau \to \mu\gamma)$						L	L	M	L
$\mathcal{B}(B \to \tau\nu, \mu\nu)$	CKM								
$\mathcal{B}(B \to K^{(*)}\nu\overline{\nu})$			M	L		M	M	M	M
$S_{K^0_S\pi^0\gamma}$					L				
Angle β (ΔS)			CKM		L	L	M	M	L
$A_{CP}(B \to X_s\gamma)$			L		M	M	M	M	L
$\mathcal{B}(B \to X_s\gamma)$		L	M		M				
$\mathcal{B}(B \to X_s ll)$			M	M	M				
$A_{FB}(B \to K^{(*)}ll)$						M	M	M	L
Charm mixing						L	M	M	M
CPV in Charm	L								L

Table 1: The golden matrix of observables versus a sample of NP scenarios. H^+ represents the insertion in the model of a charged Higgs Boson; (non-)MFV is a representative (non-)Minimal Flavour Violation model; ZP is NP in Z-penguins; RH corresponds to the introduction of right handed currents. A number of explicit SUSY models are included $^{2)}$. "L" denotes a large effect, "M" a measurable effect and "CKM" indicates a measurement that requires precise measurement of the CKM matrix.

Both BaBar and Belle have successfully measured the CKM Unitarity Triangle angles α, β and γ $^{1)}$. There is an overall agreement with Standard Model expectations although there are a few tensions that might prove to be signs of NP but need smaller statistical uncertainties for confirmation. To this aim SuperB is designed to measure the angles α and γ to $1-2\%$, and β to 0.1%. $|V_{cb}|$ and $|V_{ub}|$ can be measured to 1% and 2% accuracy, respectively, in both inclusive and exclusive semileptonic decays. Figure 1 shows the $\overline{\rho}$-$\overline{\eta}$ plane with current and predicted experimental measurements, assuming the current measurements maintain their central values.

NP can be probed also by comparing the measurements of CKM angles within several modes, leading to a precision measurement of what is traditionally called "ΔS", i.e. the difference in the angle β between $b \to s$ penguin-dominated transitions and $b \to c\bar{c}s$ decays.

In 2-Higgs-doublet (2HDM-II) and Minimal SuperSymmetric (MSSM) models, the decay $B \to \tau\nu$ is sensitive to the presence of a charged Higgs H^-

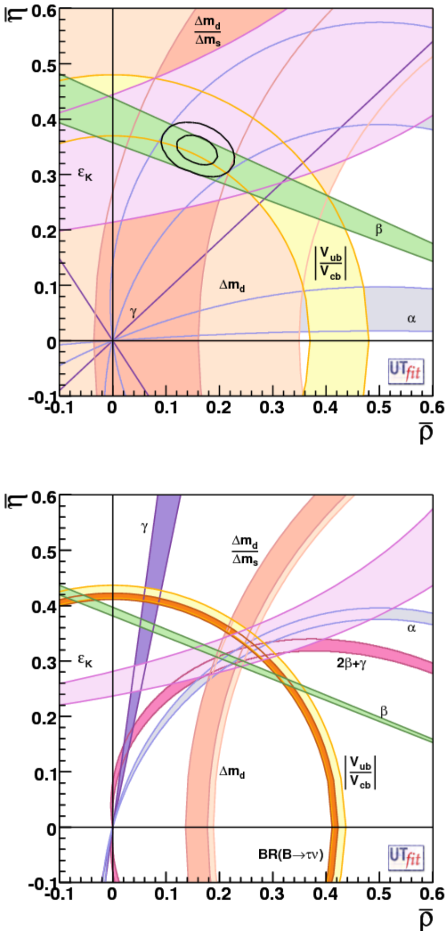

Figure 1: Regions corresponding to 95% probability for $\overline{\rho}$ and $\overline{\eta}$ with current measurements (left) and with Super$B$ precision assuming the current central values (right).

replacing the SM W^-. Super$B$ will be able to exclude masses up to $\sim 2-3\,\mathrm{TeV}$ for values of $\tan\beta$ up to 80.

Super$B$ can access the off-diagonal elements of generic squark mass matrices in the MSSM model using the mass insertion approximation. These cannot be seen by the LHC general purpose detectors. As an example, Super$B$ is sensitive to non-zero values of the matrix element $(\delta^d_{23})_{LL,LR}$ for gluino masses in the 1-10 TeV range through decays such as $b \to s\gamma$ and $b \to sl^+l^-$.

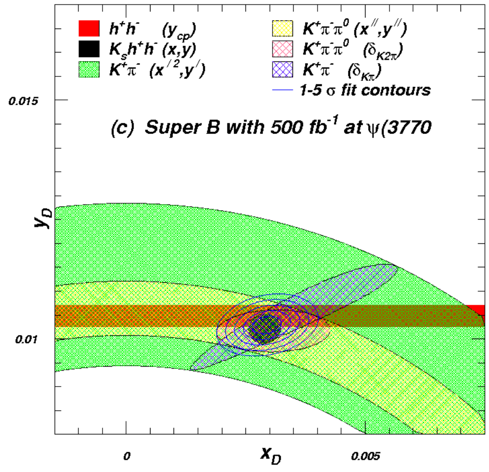

Figure 2: Right: the expected precision on charm mixing parameters from combining BES-III and Super$B$ $\psi(3770)$ and $\Upsilon(4S)$ data.

An almost equal number of $\tau^+\tau^-$ pairs are produced as $B\overline{B}$ pairs at the $\Upsilon(4S)$ resonance. Current experimental 90% confidence level upper limits on τ LFV are in the $10^{-8} - 10^{-7}$ range, depending on the decay. In the very clean environment of Super$B$, upper limits on τ LFV can be achieved down to a level of 2×10^{-10} for $\tau \to \mu\mu\mu$ and Super$B$ can measure the upper limits in ~ 50 other τ decay modes. Background-free modes should scale with the luminosity (L) while other modes will scale with $\sqrt{\mathcal{L}}$ or better, thanks to re-optimized analysis techniques. In $\tau \to \mu\gamma$ for example, LFV is predicted at the level $10^{-10} - 10^{-7}$ depending on the NP model. SU(5) SUSY GUT models predict $\tau \to \mu\gamma$ branching fractions between 10^{-7} and 10^{-9} depending on the NP phase, so the majority of the parameter space is within the expected Super$B$ sensitivity of 2×10^{-9}.

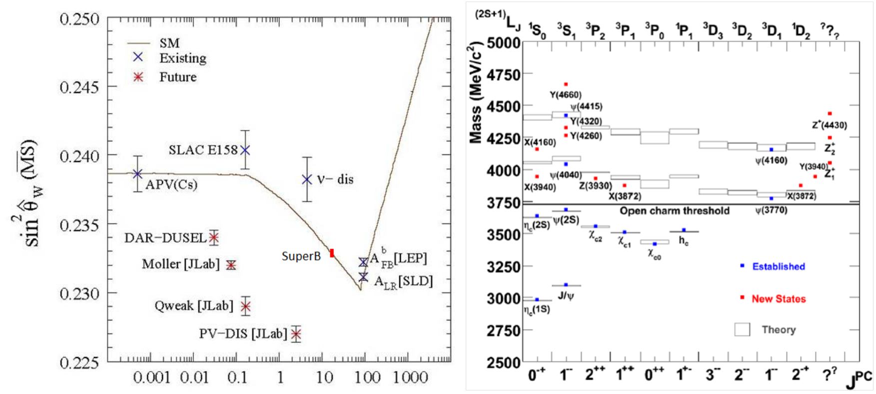

Figure 3: Left: Measurements of $\sin^2\theta_w$ as a function of the center-of-mass energy ($\sqrt{s}$ in GeV). The size of the bar at $\sqrt{s} \sim 10.6\,\mathrm{GeV}$ representing the Super$B$ measurement is approximately the same size as the error. Right: Measured masses of newly observed states positioned according to their most likely quantum numbers.

CPV in charm decays is expected to be very low in the SM ($< 1\%$) so its detection would be a clear indicator of NP. Current values for the mixing parameters x and y from HFAG $^{1)}$ fits give $(0.63 \pm 0.20)\%$ and $(0.75 \pm 0.12)\%$, respectively, allowing for CPV $^{3)}$. At Super$B$, the errors should reduce to 0.07% and 0.02%, respectively. If the results are combined with expected results from BES-III and a dedicated Super$B$ $500\,\mathrm{fb}^{-1}$ run ($\sim$ 4 months running) at the $D\,\overline{D}$ threshold, the BES-III/CLEO-c physics programme can be repeated leading to a further reduction in these errors to 0.02% and 0.01%, respectively. This is shown in Fig. 2.

3 Physics Potential: opportunities from a flavour factory

If a polarised electron beam is available, many of the upper limits on τ LFV modes can be improved by an additional factor of two. The polarisation also allows the search for the τ EDM at a level of $2 \times 10^{-19} e\,\mathrm{cm}$ and the measurement of the τ anomalous magnetic moment $\Delta\alpha_\tau$ with an error of 10^{-6}. The value of $\sin^2\theta_w$ can be measured with an accuracy $\pm 1.8 \times 10^{-4}$ at $Q = 10.58\,\mathrm{GeV}$ and so help understand the discrepancy in the measurements from LEP, SLD and NuTev (5). This is shown in the left-hand plot of Figure 3 where the size of the bar at $Q = 10.58\,\text{GeV}$ represents the expected error on the Super$B$ measurement. It may even be possible to measure $\sin^2\theta_w$ at the $\psi(3770)$ mass if polarisation can be achieved.

The B-Factories and the Tevatron have discovered bound states with a $c\bar{c}$ or a $b\bar{b}$ pair that do not fit into the conventional meson interpretation (see for instance (6) for a review). However, apart from some exceptions like the $X(3872)$, they have only been observed in a single decay channel with a significance only just above 5σ. The right-hand plot of Figure 3 shows some of the newly discovered states. Possible explanations include hybrids, molecules, tetraquarks and threshold effects. Super$B$'s ability to run at the $\Upsilon(nS)$ resonances and charm threshold provides a unique opportunity for testing low- and high-energy QCD predictions. Predicting the expected rates for poorly measured resonances is of course hard and work is on-going to improve the extrapolations. The $B \to X(3872)K$ decays should produce $\sim 2k - 10k$ events in each of their main decay channels. $Y(4260) \to J/\psi\pi^+\pi^-$ will have $\sim 45k$ events, while $\sim 4.5k$ events can be expected for both $Y(4350)$ and $Y(4660)$ decaying to $\psi(2S)\pi^+\pi^-$. It should be possible to confirm the existence of the $Z_1^+(4050)$, $Z^+(4430)$ and $Z_2^+(4430)$ as Super$B$ will collect between $150k - 2M$ events of the relevant fully reconstructed final states $J/\psi\pi^+K$, $\psi(2S)\pi^+K$, and $\chi_{cJ}\pi^+K$.

Other physics opportunities that cannot be detailed here include B_s physics running at the $\Upsilon(5S)$, light meson studies in Initial State Radiation events, $\gamma\gamma$ physics, direct searches for little higgs, Dark Matter, Dark Forces.

4 Competition and status of the project

The strength of SuperB is in the breadth of the physics potential and, in order to achieve it, several features need to be in the design: very high luminosity, possibility to scan from the charm threshold to at least $\sqrt{s} = 11$ GeV, polarized beams at least at the $\Upsilon(4S)$, better if also during the scan, and triggers suited for exotic searches. Tab 2 summarized which research line requires each feature and which are the competitors. It is to be noted that nobody competes on all features.

The physics potential (2), and the detector (4) and accelerator (7) plans have been extensively documented and the activity is currently concentrated

Feature	physics goal	Competitors
high luminosity	precision CKM physics, rare B decays	Belle II (slightly lower luminosity but start earlier)/ LHCb (dirty environment)
Beam Polarization	rare τ decays, EW physics	–
Energy Scan	Exotic Spectroscopy, Charm Physics at threshold	BESIII (up to 4 GeV), Panda (different production)
Devoted Triggers	ISR, $\gamma\gamma$, direct searches	–

Table 2: Features required by each research stream and competitors.

on finalizing its Technical Design Report. Unfortunately, although the Italian government included the experiment among the top priorities of its funded research plan, a detailed spending review that took place in fall 2012 lead to the conclusion that there is not enough funding to pursue the project as described here. Studies are ongoing on how to downgrade the project in order to match the available funds.

References

1. Heavy Flavor Averaging Group (HFAG), www.slac.stanford.edu/xorg/hfag.
2. M. Bona et al., *SuperB Conceptual Design Report*, [arXiv:0709.0451]; D.G. Hitlin et al., *New Physics at the Super Flavor Factory*, [arXiv:0810.1312]; B. O'Leary et al., *SuperB Progress Report – Physics*, [arXiv:1008.1541].
3. C. Amsler et al., J. Phys. **G37**, (2010) 075021.
4. E. Grauges et al., *SuperB Progress Report – Detector*, [arXiv:1007.4241].
5. EW Working Groups, *Precision Electroweak measurements on the Z Resonance*, Phys. Rept. **427**, 257 (2006).

6. N. Drenska, R. Faccini, F. Piccinini, A. Polosa, F. Renga, C. Sabelli, *New Hadronic Spectroscopy* Riv. Nuovo Cim. **033** (2010) 633-712.
7. M.E. Biagini et al., *SuperB Progress Report – Accelerator*, [arXiv:1009.6178].